



POLITECNICO DI TORINO
Repository ISTITUZIONALE

Modeling and Design of Multi-Stable Composite Structures

Original

Modeling and Design of Multi-Stable Composite Structures / DE PIETRO, Gabriele. - (2019 Mar 08), pp. 1-172.

Availability:

This version is available at: 11583/2729360 since: 2019-03-26T16:08:30Z

Publisher:

Politecnico di Torino

Published

DOI:10.6092/polito/porto/2729360

Terms of use:

openAccess

This article is made available under terms and conditions as specified in the corresponding bibliographic description in the repository

Publisher copyright

(Article begins on next page)



ScuDo
Scuola di Dottorato ~ Doctoral School
WHAT YOU ARE, TAKES YOU FAR



Doctoral Dissertation
Doctoral Program in Mechanical Engineering (31st cycle)

Modeling and Design of Multi-Stable Composite Structures

Gabriele De Pietro

* * * * *

Supervisors

Dr. G. Giunta
Prof. E. Carrera
Dr. S. Belouettar

Doctoral Examination Committee:

Dr. Marco Montemurro, Referee, Ars et Métiers Paristech
Dr. Lorenzo Dozio, Referee, Politecnico di Milano
Dr. Eelco Jansen, Leibniz Universität Hannover
Dr. Fiorenzo Fazzolari, University of Liverpool
Dr. Alberto Pirrera, University of Bristol

Politecnico di Torino
March 2019

This thesis is licensed under a Creative Commons License, Attribution - Noncommercial-NoDerivative Works 4.0 International: see www.creativecommons.org. The text may be reproduced for non-commercial purposes, provided that credit is given to the original author.

I hereby declare that, the contents and organization of this dissertation constitute my own original work and does not compromise in any way the rights of third parties, including those relating to the security of personal data.

.....
Gabriele De Pietro
Turin, March 2019

Acknowledgements

This work has been supported by the European Union within the Horizon 2020 research and innovation programme under grant agreement No 642121.

I would like to thank my day-to-day supervisor at Luxembourg Institute of Science and Technology Dr. Gaetano Giunta, who largely contributed to this work and constantly helped me throughout my PhD time. His high-level expertise and full dedication to the job made him a great mentor for me.

I wish to express my sincere gratitude to Prof. Carrera, my academic supervisor at Polytechnic of Turin, whose strong passion for research continuously inspired me over the past three years. I'm glad I could in some small way contribute to the further development of his innovative ideas in the field of computational mechanics.

I would also like to acknowledge Dr. Salim Belouettar from Luxembourg Institute of Science and Technology, who has provided me with great support and enthusiasm during my experience in Luxembourg, Dr. Gaston Rauchs and Dr. Damián Aranda Iglesias for their precious advice and suggestions and also Christelle Vergnat and Sabrina Morais for their great help in the administrative work and organization of my secondments.

Thanks to Dr. Marco Petrolo for being always helpful in managing Fullcomp project activities and to all partners of Fullcomp, which represented for me an amazing adventure as well as a unique opportunity to grow both as a researcher and as a person.

A special thanks to my office mate and friend Yanchuan Hui, who collaborated with me in much of this work and played a fundamental role for the implementation of the ANM-based non-linear solver.

Furthermore, I would like to mention the Fullcompers at Polytechnic of Turin Alberto Garcia de Miguel, with whom I have worked on the extension of Unified Formulation to curved beams, Ibrahim Kaleel and Guohong Li as well as the other members of MUL2 group Dr. Alfonso Pagani, Dr. Matteo Filippi, Dr. Maria Cinefra and Dr. Enrico Zappino who have been always available for assistance and discussion.

I am also grateful to both Dr. Alberto Pirrera and Prof. Paul Weaver who hosted me at University of Bristol and provided me with useful and constructive suggestions about multi-stability.

Finally, I would like to thank my family and Giustina, who patiently assisted and encouraged me. There was never a time when I couldn't count on them.

Summary

Under certain conditions, natural as well as man-made structures can exhibit more than one stable mechanical configuration. Starting from their initial stable state, multi-stable structures can morph into a new stable configuration via a snap-through elastic instability, triggered by an appropriate external energy input. Over the last decades, many researchers have investigated this special class of compliant structures, due to the possibility to harness the snap-through buckling as a source of energy and motion in a wide variety of engineering applications.

A major challenge for the exploitation of multi-stable structures in practical applications is represented by their complex mechanical response resulting in time-consuming design and optimization procedures. Multi-stability phenomena are in fact characterized by large shape changes that call for strongly non-linear structural analyses. Furthermore, the use of composite materials in multi-stable applications yields peculiar kinematic behaviors that call for high-fidelity predictive models, such as two- and three-dimensional finite elements, which result in computationally expensive structural analyses.

To address this issue, the present thesis discusses the studies undertaken to develop a novel reliable yet efficient computational framework for the analysis of bistable composite beams. An advanced structural modeling approach based on a Unified Formulation is adopted. At first, the potential of the formulation in the linear regime is evaluated with regards to mechanical and thermo-mechanical analysis of composite beam structures. At a later stage, since large displacements capabilities are essential for the prediction of bistability phenomena, Green-Lagrange geometric non-linearities are taken into account, in the framework of a total Lagrangian approach.

By means of Unified Formulation, the beam kinematics can be straightforwardly enriched by accounting for additional higher-order terms in the cross-sectional variation of the displacement field. Refined predictions of the stable geometries, snap-through loads and stress fields in bistability analyses can be obtained via the proposed advanced one-dimensional formulation with no loss of accuracy and reduced computational costs when compared to two- and three-dimensional finite elements solutions. Therefore, scope for improvement of the state-of-the-art modeling capabilities is identified and the potential of a versatile modeling framework based on Unified Formulation for a refined analysis of multi-stable composite structures is highlighted.

Sommario

In determinate condizioni, componenti strutturali presenti in natura così come strutture create dall'uomo possono mostrare più di una configurazione meccanica stabile. A partire dalla loro configurazione iniziale, le strutture multi-stabili possono assumere una nuova configurazione stabile a seguito di un fenomeno di instabilità elastica di tipo *snap-through* innescato da un adeguato apporto esterno di energia. Negli ultimi decenni, molti ricercatori hanno studiato questa classe speciale di strutture deformabili, a causa della possibilità di sfruttare il fenomeno di *snap-through* come fonte di energia e movimento in un'ampia gamma di applicazioni.

Un importante ostacolo all'utilizzo di strutture multi-stabili è rappresentato dalla loro complessa risposta meccanica che porta a progettazioni e ottimizzazioni onerose in termini di tempi di calcolo. I fenomeni di multi-stabilità sono caratterizzati da grandi cambiamenti di forma che richiedono analisi strutturali fortemente non-lineari. Inoltre, l'utilizzo di materiali compositi porta a comportamenti cinematici tali da richiedere modelli accurati, come elementi finiti bi-dimensionali e tri-dimensionali, che tuttavia comportano analisi strutturali computazionalmente dispendiose.

Per far fronte a questo problema, la presente tesi discute lo sviluppo di un nuovo modello computazionale affidabile ed efficiente per l'analisi di travi composite bistabili. Un approccio di modellazione strutturale avanzato basato su una formulazione unificata è adottato. In primo luogo, il potenziale di tale formulazione è valutato nel regime lineare, per quanto riguarda l'analisi meccanica e termo-meccanica di strutture composite di tipo trave. Successivamente, poiché la capacità di analizzare strutture in grandi spostamenti è essenziale per la previsione di fenomeni bistabili, non-linearità geometriche di Green-Lagrange sono tenute in conto, nel quadro di un approccio *lagrangiano totale*.

Grazie alla formulazione unificata, il modello cinematico della trave può essere arricchito in maniera semplice, includendo termini aggiuntivi di ordine superiore al primo nell'espressione del campo di spostamenti. Previsioni accurate delle geometrie stabili, dei carichi di *snap-through* e dei campi di stress in analisi di bistabilità possono essere ottenute attraverso la formulazione mono-dimensionale proposta, senza perdita di accuratezza e con costi computazionali ridotti rispetto a soluzioni agli elementi finiti bi- e tri-dimensionali. Per questi motivi, margini di miglioramento delle attuali capacità di modellazione sono identificati e il potenziale del modello proposto per un'analisi accurata di strutture composite multi-stabili è evidenziato.

Contents

List of Tables	XII
List of Figures	XIV
1 Introduction	1
1.1 Outline of the thesis	3
I Literature Review	5
2 Multi-stability: Modeling, Design and Applications	7
2.1 Introduction	7
2.2 Brief theoretical background	7
2.2.1 Definition of multi-stable structure	7
2.2.2 The role of composites in multi-stability	9
2.3 Modeling approaches	9
2.4 Design methodologies	11
2.5 Application concepts	12
2.5.1 Energy harvesters	12
2.5.2 Morphing structures	13
2.5.3 Other proposed applications	14
2.5.4 Bistability in nature: the Venus fly trap	15
3 Mechanics of Composite Multi-Layered Beam Structures: Classical Models and Recent Advances	17
3.1 Introduction	17
3.2 One-dimensional modeling literature review	18
3.2.1 Classical theories	18
3.2.2 Higher-Order Shear Deformation Theories (HSDT)	19
3.2.3 Layer-Wise (LW) models	20
3.2.4 Other modeling approaches	21
3.3 One-dimensional hierarchical models based on Unified Formulation (UF)	22

3.3.1	Variational statements	22
3.3.2	Unified Formulation of the displacement field	23
3.3.3	Variables description level	26
3.3.4	Recent applications of UF-based one-dimensional models	26

II Modeling Methodology 29

4	Hierarchical 1D Finite Elements for Mechanical and Thermal Stress Analysis 31
4.1	Introduction 31
4.2	UF-based displacement field 32
4.3	Geometrical and constitutive equations 32
4.4	Fourier's heat conduction equation 35
4.5	Governing equations and fundamental nuclei 35
4.5.1	Principle of virtual displacements 35
4.5.2	Element stiffness matrix 36
4.5.3	Thermo-mechanical coupling vector 37
4.5.4	Mechanical load vector 38
5	Extension of UF-based Approach to Curved Beam Structures 39
5.1	Introduction 39
5.2	Preliminaries 40
5.3	Geometrical and constitutive relations in local coordinates 41
5.4	Governing equations and fundamental nuclei 43
5.4.1	Strong form Navier-type solution 44
5.4.2	Weak form finite elements solution 47
6	Geometrically Non-Linear Hierarchical Structural Modeling 51
6.1	Introduction 51
6.2	Non-linear strains-displacements relation 52
6.3	Stress notation and constitutive relation 53
6.4	Principle of virtual displacements 53
6.5	UF-based one-dimensional finite element formulation 54
6.6	Tangent stiffness matrix fundamental nucleus 55
6.6.1	Linear contribution 56
6.6.2	Initial-displacement contribution 56
6.6.3	Initial-stress contribution 58
6.7	Locking-free higher-order elements based on MITC 59
6.8	Solution of non-linear algebraic systems 60
6.8.1	Newton-Raphson procedure 60
6.8.2	Arc-length method 61

6.8.3	Path-following solver based on the Asymptotic Numerical Method	63
-------	--	----

III	Numerical Results	67
7	Mechanical and Thermo-Mechanical Analysis	69
7.1	Introduction	69
7.2	Mechanical analysis of sandwich beams	70
7.2.1	Strain energy convergence analysis	71
7.2.2	Shear locking correction	72
7.2.3	Flexural-torsional response	72
7.2.4	Comparison with experiments	75
7.3	Thermal stress analysis	77
7.3.1	Orthotropic laminated beams	77
7.3.2	Functionally graded beams	79
7.4	Mechanical analysis of curved beams	83
7.4.1	Convergence performance	85
7.4.2	Circular thick arch	89
7.4.3	Three-dimensional balcony structure	91
8	Large Deflection and Bistability Analysis	95
8.1	Introduction	95
8.2	Beam-like structures under large deflection	96
8.2.1	Metallic structures	96
8.2.2	Asymmetric laminate	101
8.2.3	Three-layer beam	109
8.3	Bistability analysis of pre-buckled beams	112
8.3.1	Influence of ANM parameters	113
8.3.2	Validation towards literature: bistable air inlet	115
8.3.3	Refined post-buckling and snap-through equilibrium paths	116
8.3.4	Stress prediction in bistable composites	123
9	Conclusions and Outlooks	133
9.1	Concluding remarks	133
9.2	Original contributions	134
9.3	Scope for future research	135
	Curriculum Vitae	137
	Bibliography	141

List of Tables

3.1	Terms of the Taylor's polynomial expansion via Pascal's triangle. . . .	24
3.2	Points of a L4 expansion in natural coordinates.	24
3.3	Points of a L9 expansion in natural coordinates.	25
7.1	Displacements [m] for a very thick doubly-clamped sandwich beam subjected to an off-centric line load.	73
7.2	Stresses $\tilde{\sigma}_{xx}$, $\tilde{\sigma}_{xz}$ and $\tilde{\sigma}_{xy}$ [Pa] for a very thick doubly-clamped sandwich beam subjected to an off-centric line load.	73
7.3	Displacements [m] for a very thick ($l/b = 3$) cantilever two-layer laminated beam. [0/90] stacking sequence.	79
7.4	Axial stress $\tilde{\sigma}_{xx}$ and shear stresses $\tilde{\sigma}_{xy}$ and $\tilde{\sigma}_{xz}$ [Pa] for a very thick ($l/b = 3$) cantilever two-layer laminated beam. [0/90] stacking sequence.	79
7.5	Normal stresses $\tilde{\sigma}_{yy}$, $\tilde{\sigma}_{zz}$ and shear stress $\tilde{\sigma}_{yz}$ [Pa] for a very thick ($l/b = 3$) cantilever two-layer laminated beam. [0/90] stacking sequence. . . .	80
7.6	Elastic and thermal properties of the FGM constituents materials. . . .	83
7.7	Displacements [m] \bar{u}_z , \bar{u}_x and \bar{u}_y . Very thick ($l/b = 5$) metal-ceramic FGM ($n_z = 1$) cantilever beam.	84
7.8	Stresses [Pa] $\bar{\sigma}_{xx}$, $\bar{\sigma}_{xy}$ and $\bar{\sigma}_{xz}$. Very thick ($l/b = 5$) metal-ceramic FGM ($n_z = 1$) cantilever beam.	84
7.9	Stresses [Pa] $\bar{\sigma}_{yy}$, $\bar{\sigma}_{zz}$ and $\bar{\sigma}_{yz}$. Very thick ($l/b = 5$) metal-ceramic FGM ($n_z = 1$) cantilever beam.	85
7.10	Transverse displacement u_ξ [m] versus number of elements N_e . Very thick simply supported circular beam. 2nd-order UF-based model (TE2). . . .	85
7.11	Transverse displacement u_ξ [m] versus number of elements N_e . Very thick simply supported circular beam. 2nd-order UF-based model (TE2). . . .	88
7.12	Dimensionless axial and radial displacements \tilde{u}_s and \tilde{u}_ξ . Thick doubly-clamped circular beam subjected to different in-plane loading conditions. . . .	89
8.1	Displacement components prediction provided by UF-based models and several reference solutions. Thick cantilever beam. $\lambda = 10$	100
8.2	Global Cauchy stresses computed at ($l/4, -h/2$). Thick cantilever beam. $\lambda = 5.20$	100
8.3	Displacement components prediction provided by UF-based models and several reference solutions. Thick doubly-clamped beam. $\lambda = 15.89$. . .	103

8.4	Global Cauchy stresses computed at $(l/4, 0)$. Thick doubly-clamped beam. $\lambda = 11.04$	104
8.5	Displacement components prediction provided by UF-based models and two-dimensional finite elements solutions. Thick simply supported beam. $\lambda = 8.36$	106
8.6	Global Cauchy stresses computed at $(l/4, -h/2)$. Thick simply supported beam. $\lambda = 6.03$	106
8.7	Displacements in a cantilever laminated beam-like structure under large deflection via LW and ESL refined models.	108
8.8	Axial and shear stresses in a cantilever laminated beam-like structure under large deflection via LW and ESL refined models.	108
8.9	Displacement and stress components in a post-buckled simply supported beam. $l/h = 20$. $\lambda_x = 2.1835$	118
8.10	Snap-through load for a pre-buckled doubly-clamped beam structure via UF-based refined one-dimensional models. $l/h = 20$. Pre-compression load $\lambda_x = 2.1835$	120
8.11	Displacement and stress components in a post-buckled clamped-simply supported beam. $l/h = 20$ $\lambda_x = 2.6347$	125
8.12	Snap-through load for a pre-buckled clamped-simply supported beam structure via UF-based refined one-dimensional models. $l/h = 20$. Pre-compression load $\lambda_x = 2.6347$	126

List of Figures

1.1	Snap-through of a bistable pre-buckled beam structure.	2
2.1	Typical equilibrium path of a bistable structure.	8
2.2	Unloading path for a pre-buckled beam with monostable behavior. . . .	9
2.3	Concept of a passively morphing wing flaperon by means of an embed- ded bistable composite plate proposed by Nicassio et al. [121].	13
2.4	Bistable graphene membrane for application in memcapacitors pro- posed by Yamaletdinov et al. [169].	14
2.5	Closure mechanism of the Venus fly trap investigated by Forterre et al. [69].	15
3.1	Coordinate reference system in a beam-like structure.	18
5.1	Three-dimensional curved beam-like structure and Frenet-Serret refer- ence system.	40
7.1	Adopted notation and cartesian coordinate system for sandwich beam- like structures.	70
7.2	Strain energy error as function of the distance between two consecutive nodes.	71
7.3	Locking mitigation by means of selective integration. Simply supported sandwich beam subjected to pressure. B2 elements.	72
7.4	Cross-sectional distribution of the axial displacement u_x [m] at $x =$ $l/4$ via three-dimensional finite elements (left) and 19th-order B4 one- dimensional elements (right). Doubly-clamped sandwich beam ($l/h = 5$) subjected to an off-centric line load.	74
7.5	Cross-sectional distribution of the through-the-width displacement u_y [m] at $x = l/2$ via three-dimensional finite elements (left) and 19th- order B4 one-dimensional elements (right). Doubly-clamped sandwich beam ($l/h = 5$) subjected to an off-centric line load.	74
7.6	Cross-sectional distribution of the through-the-thickness displacement u_z [m] at $x = l/2$ via three-dimensional finite elements (left) and 19th- order B4 one-dimensional elements (right). Doubly-clamped sandwich beam ($l/h = 5$) subjected to an off-centric line load.	75

7.7	Cross-sectional distribution of the axial stress σ_{xx} [Pa] at $x = l/2$ via three-dimensional finite elements (left) and 19th-order B4 one-dimensional elements (right). Doubly-clamped sandwich beam ($l/h = 5$) subjected to an off-centric line load.	75
7.8	Cross-sectional distribution of the shear stress σ_{xy} [Pa] at $x = l/4$ via three-dimensional finite elements (left) and 19th-order B4 one-dimensional elements (right). Doubly-clamped sandwich beam ($l/h = 5$) subjected to an off-centric line load.	76
7.9	Load-displacement response for a sandwich beam with carbon/epoxy composite faces and core layer made of polyurethane foam. Three-point bending test.	76
7.10	Reference system and cross-section of the laminated two-layer beam.	77
7.11	Through-the-thickness variation of the over-temperature $T(z)$ [K] at $x = l/2$ for different slenderness ratios l/b	78
7.12	Cross-sectional distribution of the through-the-thickness displacement u_z [m] at $x = l/2$ via three-dimensional finite elements (left) and 14th-order B4 one-dimensional elements (right). Very thick ($l/b = 3$) laminated cantilever beam.	80
7.13	Cross-sectional distribution of the axial stress σ_{xx} [Pa] at $x = l/2$ via three-dimensional finite elements (left) and 14th-order B4 one-dimensional elements (right). Very thick ($l/b = 3$) laminated cantilever beam.	81
7.14	Cross-sectional distribution of the through-the-thickness normal stress σ_{zz} [Pa] at $x = l/2$ via three-dimensional finite elements (left) and 14th-order B4 one-dimensional elements (right). Very thick ($l/b = 3$) laminated cantilever beam.	81
7.15	Cross-sectional distribution of the through-the-width normal stress σ_{yy} [Pa] at $x = l/2$ via three-dimensional finite elements (left) and 14th-order B4 one-dimensional elements (right). Very thick ($l/b = 3$) laminated cantilever beam.	82
7.16	Adopted reference system and geometry of the FGM beam.	82
7.17	Through-the-thickness profile of the over-temperature $T(z)$ [K] at $x = l/2$ for slender and thick FGM beam-like structures. $n_z = 1$	83
7.18	Shear stress σ_{xy} [Pa] at $x = l/4$. Very thick ($l/b = 5$) metal-ceramic FGM cantilever beam.	86
7.19	Shear stress σ_{yz} [Pa] at $x = l/2$. Very thick ($l/b = 5$) metal-ceramic FGM cantilever beam.	87
7.20	Adopted reference system, geometry and cross-section of a thick arch structure.	88
7.21	Dimensionless axial, radial and shear stress components at $s = l/2$. Thick cantilever circular arch.	90

7.22	Semi-circular three-dimensional balcony structure subjected to a uniform out-of-plane line load.	91
7.23	Longitudinal variation of the transverse displacement u_y . Out-of-plane line load. Three-dimensional semi-circular balcony structure.	92
7.24	Axial and transverse shear stress distributions. Out-of-plane line load. Three-dimensional semi-circular balcony structure.	93
8.1	Locking phenomenon in linear elements for increasing slenderness ratios and effectiveness of the MITC-based correction method. Doubly-clamped boundary conditions. $\lambda = 2$. \hat{u}_z computed at $(l/2, -h/2)$	97
8.2	Convergence analysis for classical and MITC-based cubic one-dimensional finite elements. Simply supported beam ($l/h = 100$). $\lambda = 3$. \hat{u}_z evaluated at $(l/2, h/2)$	98
8.3	Geometrically non-linear response of a slender cantilever beam ($l/h = 100$).	99
8.4	Geometrically non-linear response of a thick cantilever beam ($l/h = 10$).	99
8.5	Through-the-thickness distribution of global Cauchy stresses at $x = l/4$. $\lambda = 5.20$. Thick cantilever beam.	101
8.6	(a) Axial and (b) shear stress components two-dimensional distribution. Thick cantilever beam. $\lambda = 3.79$	102
8.7	Geometrically non-linear response of a slender doubly-clamped beam ($l/h = 100$).	102
8.8	Geometrically non-linear response of a thick doubly-clamped beam ($l/h = 10$).	103
8.9	Through-the-thickness distribution of global Cauchy stresses at $x = l/4$. $\lambda = 5.20$. Thick doubly-clamped beam.	104
8.10	Geometrically non-linear response of a thick simply supported beam ($l/h = 10$).	105
8.11	Through-the-thickness distribution of global Cauchy stresses at $x = l/4$. $\lambda = 6.03$. Thick simply supported beam-like structure.	105
8.12	Through-the-thickness distribution of global Cauchy stresses at increasing load factors λ . Thick simply-supported beam. $x = l/4$	107
8.13	Through-the-thickness profile of (a) axial, (b) normal through-the-thickness and (c) transverse shear stress components via ESL and LW refined models. Two-layer [90/0] laminated beam under large deflection. $x = l/2$	109
8.14	Two-dimensional distribution of dimensionless (a) axial, (b) normal through-the-thickness and (c) transverse shear stress components. Two-layer [90/0] laminated beam under large deflection. $\tilde{\sigma}_{ij} = \sigma_{ij}/p_0$	110
8.15	Through-the-thickness profile of axial and through-the-thickness displacement components in a three-layer beam under large deflection. $\lambda_z = 1$. $x = l$	111

8.16	Evolution of (a) axial, (b) normal through-the-thickness and (c) transverse shear stress profiles from $\lambda_z = 1$ to $\lambda_z = 2$ in a three-layer beam under large deflection. $x = l/4$	112
8.17	Transverse shear stress $\tilde{\sigma}_{xz}$. Three-layer beam under large deflection. $\lambda_z = 2$	113
8.18	Influence of the ANM tolerance parameter in the post-buckling of a simply supported beam. ANM order $n = 10$. $N = 2$ beam model.	114
8.19	Influence of the ANM order parameter in the post-buckling of a simply supported beam. ANM tolerance $\epsilon = 10^{-8}$. Beam model $N = 2$	114
8.20	Graphical sketch of a pre-buckled beam component embedded in a passively actuated shape-adaptive air inlet (Arena et al. [2]).	115
8.21	Equilibrium path of a bistable beam-like air inlet. Uni-directional glass fibre-epoxy resin composite laminate.	116
8.22	Open-closed configurations of a bistable air inlet. Resultant displacement u_{res} [m]. $N = 3$ beam model.	116
8.23	Pre-compression load vs. axial and transverse displacements. Post-buckling response. Simply supported beam. $l/h = 20$	118
8.24	Error trends on displacements, axial and shear stress components via refined UF-based one-dimensional models. Post-buckled simply supported beam. $l/h = 20$. $\lambda_x = 2.1835$	119
8.25	Transverse actuation load vs. axial and transverse displacements. Snap-through behavior of a pre-buckled doubly-clamped beam. $l/h = 20$	119
8.26	Dimensionless resultant displacement \tilde{u}_{res} . Post-buckled and snapped configurations. $l/h = 20$. UF-based one-dimensional model $N = 5$	120
8.27	Dimensionless axial stress $\tilde{\sigma}_{xx}$ distribution in the post-buckled (a,c) and snapped configurations (b,d). $l/h = 20$	121
8.28	Dimensionless normal through-the-thickness stress $\tilde{\sigma}_{zz}$ distribution in the post-buckled (a,c) and snapped configurations (b,d). $l/h = 20$	122
8.29	Dimensionless transverse shear stress $\tilde{\sigma}_{xz}$ distribution in the post-buckled (a,c) and snapped configurations (b,d). $l/h = 20$	123
8.30	Pre-compression load vs. axial and transverse displacements. Post-buckling response. Clamped-simply supported beam. $l/h = 20$	123
8.31	Transverse actuation load vs. axial and transverse displacements. Snap-through behavior of a pre-buckled clamped-simply supported beam. $l/h = 20$	124
8.32	Dimensionless resultant displacement \tilde{u}_{res} . Post-buckled and snapped configurations. Clamped-simply supported beam. $l/h = 20$. UF-based one-dimensional model $N = 5$	124
8.33	Error trends on displacements, axial and shear stress components via refined UF-based one-dimensional models. Post-buckled clamped-simply supported beam. $l/h = 20$. $\lambda_x = 2.6347$	125

8.34	Dimensionless axial stress $\tilde{\sigma}_{xx}$ distribution in the post-buckled (a,c) and snapped configurations (b,d). Clamped-simply supported beam. $l/h = 20$.	126
8.35	Dimensionless normal through-the-thickness stress $\tilde{\sigma}_{zz}$ distribution in the post-buckled (a,c) and snapped configurations (b,d). Clamped-simply supported beam. $l/h = 20$.	127
8.36	Dimensionless transverse shear stress $\tilde{\sigma}_{xz}$ distribution in the post-buckled (a,c) and snapped configurations (b,d). Clamped-simply supported beam. $l/h = 20$.	128
8.37	Transverse actuation load vs. (a) axial and (b) transverse displacements. Snap-through behavior of a pre-buckled pinned-roller composite beam. $l/h = 100$. Uni-directional lay-up.	128
8.38	Through-the-thickness profile of global Cauchy stresses in the pre-buckled and snapped configurations. Pinned-roller composite beam. $l/h = 100$. Uni-directional lay-up.	129
8.39	Through-the-thickness profile of global Cauchy stresses prior to buckling. $\lambda_x = 0.8$. Pinned-roller composite beam. $l/h = 100$. Three-layer cross-ply lay-up.	130
8.40	Through-the-thickness profile of global Cauchy stresses in the pre-buckled and snapped configurations. Pinned-roller composite beam. $l/h = 100$. Three-layer cross-ply lay-up.	131

Chapter 1

Introduction

Conventional engineering structures are designed to be stiff and, therefore, they usually possess a unique shape that does not change when subjected to the external loads. Nevertheless, the same does not always apply to structural elements in nature. For instance, trunk and branches of small trees undergo large deflections when subjected to strong wind, allowing a reduction of the drag force exerted on the tree itself [151] and resulting in a light deformable structural solution able to change its shape to adapt to changing environmental conditions. Compliant structures show a clear potential for re-configuration and, among them, a specific class of structures exhibiting a multi-stable compliant behavior has received special attention in recent years. Multi-stability is an unusual property of structures to inherently possess a certain number of different possible stable shapes. Morphing from one shape to another occurs as a nearly instantaneous configuration change. This is achieved via an elastic instability phenomenon, known as snap-through buckling, triggered by an appropriate external disturbance. A number of materials and structures from nano- to macro-scale exhibiting multi-stability exist, opening up novel opportunities for applications exploiting the high-rate energy and motion released by the snap-through buckling to add shape-adaptivity or functionality. A classical example of bistable structure, i.e. possessing two distinct stable shapes, is obtained by a pre-buckled beam. Starting from a pre-compressed buckled configuration, by means of an external stimulus, the structure can be snapped to a second stable state, as shown in Figure 1.1, and vice-versa. By harnessing the polymorphic behavior of this simple class of compliant structures, a number of fascinating applications can be imagined across multiple length scales, e.g. shape-adaptive structures [2], energy harvesting micro-devices [168] and meta-materials [143]. Nevertheless, the potential of multi-stable compliant structures is yet to be fully exploited in engineering applications. A deeper understanding of their kinematic behavior through the development of high-fidelity predictive models may play a fundamental role in order to enhance their impact on industrial products. As a matter of fact, the prediction of the mechanical response of compliant structures is inherently more complex than in the case of

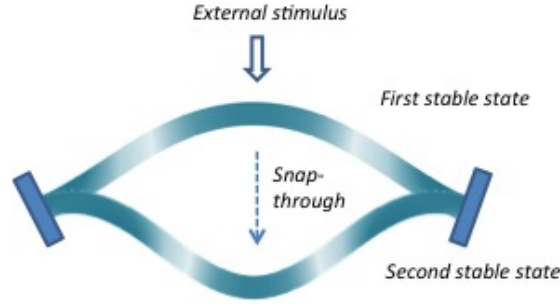


Figure 1.1: Snap-through of a bistable pre-buckled beam structure.

conventional stiff structures, since the simplifying assumption of non-deformable geometry clearly does not hold for structures in which large shape changes are allowed. Therefore, whilst modeling of conventional stiff structures results in a geometrically linear problem, which usually requires a single solution step, compliant structures shall be analyzed via geometrically non-linear formulations requiring multiple solution steps and yielding time-consuming analysis, design and optimization procedures. Computational costs are even a bigger issue for the prediction of multi-stability phenomena due to the strong non-linearities involved, for which advanced non-linear solution schemes with path-following capabilities are required to follow the unstable paths. A possible way to address these computational limitations is by reducing, whenever possible, the dimensionality of the problem from three-dimensional to two- or one-dimensional, allowing a great reduction of the mathematical problem in terms of the total number of unknown variables. This is typically done by introducing assumptions on the kinematic behavior, that are mainly based on geometric and material properties. Classical kinematic assumptions can well capture the global mechanical response of very slender and isotropic structures. Nevertheless, lower slenderness ratios or the use of composite materials yield an increased complexity in the kinematic behavior, due to peculiar behaviors such as cross-sectional warping and a greater influence of shear and normal stresses on the structural mechanics, which calls for refined structural models. In order to fill the existing gap in the literature, a novel computational framework for the mechanical analysis of bistable composite beam structures is proposed in this dissertation. An advanced modeling approach based on a Unified Formulation (UF) is adopted, allowing the relaxation of classical kinematic assumptions. Due to its one-dimensional nature and a generalized cross-sectional kinematics, this versatile mathematical framework ultimately allows refined predictions of force-displacement curves, snap-through loads and stress field evolution in bistability phenomena to be obtained at low computational costs. For these reasons, the proposed modeling approach represents a promising, more efficient alternative to state-of-the-art solutions as implemented in commercial software finite elements, to be further investigated and exploited for a correct and safe design of multi-stable composite structures.

1.1 Outline of the thesis

Before diving into the investigation of multi-stability phenomena via UF, some intermediate steps have been taken in order to assess the capability of the proposed approach. Therefore, the following preparatory research topics are also addressed in the linear regime:

- UF capabilities in challenging mechanical and thermo-elastic analysis of composites.
- UF capabilities in the mechanical analysis of curved beam-like structures.

The organization of the dissertation is herein discussed. The central core is divided into three main parts: a literature review part, including Chapters 2 and 3, a part describing the modeling methodology (Chapters 4, 5 and 6) and a numerical results part (Chapters 7 and 8). The main content of each chapter is provided below.

- In Chapter 2, a review of some important contributions concerning bistable structures is reported. Modeling approaches, design methodologies as well as application concepts, such as energy harvesters, actuators and morphing structures, are addressed.
- In Chapter 3, some of the existing literature on the mechanical modeling of composite multi-layered beam structures is briefly summarized with particular attention being paid to classical beam models (Euler-Bernoulli's and Timoshenko's theory), higher-order shear deformation theories and layer-wise models. The basic concepts of Unified Formulation are also introduced in this chapter, including the principle of virtual displacements, the unified form of the displacement field (based on Taylor, Lagrange or Legendre polynomials) and the variables description level, i.e. the equivalent single layer or layer-wise approach. Finally, some relevant works exploiting the enhanced capabilities of one-dimensional UF-based models are discussed.
- In Chapter 4, the mathematical formulation of UF-based one-dimensional finite elements for the mechanical and thermo-elastic analysis of composite structures in the geometrically linear regime is developed. The thermal problem is addressed by analytically solving Fourier's heat conduction equation, whereas the governing algebraic equations of the mechanical problem are derived via the principle of virtual displacements. Finally, the fundamental nuclei typical of the UF-approach are reported for the stiffness matrix, the mechanical load vector and the thermo-mechanical coupling vector.
- In Chapter 5, UF-methodology is extended to the study of curved beam structures. Also in this chapter, linear regime is considered. The governing differential equations are derived by writing the principle of virtual displacements in local

coordinates and both strong form Navier-type solution and weak form finite elements solution are developed. A strategy based on the Mixed Interpolation of Tensorial Components (MITC) for correcting detrimental shear and membrane locking phenomena typical of curved finite elements is implemented.

- In Chapter 6, the formulation of non-linear UF-based straight finite elements is provided, where the geometrical non-linearities in the Green-Lagrange sense are accounted for, in the framework of a total Lagrangian formulation. Linear, initial-displacement and initial-stress contributions to the fundamental nucleus of the tangent stiffness matrix are derived and the MITC-based locking correction technique is extended to the non-linear finite elements formulation. Finally, an overview of the non-linear solution procedures used in this work is given, including classical methods as well as an advanced path-following solver based on the Asymptotic Numerical Method (ANM).
- In Chapter 7, the potential of UF in the linear regime is assessed. Localized phenomena in very thick sandwich beams, thermal stresses in laminated and functionally graded structures and the mechanics of curved beams are addressed.
- In Chapter 8, the numerical results concerning large displacements analysis, post-buckling and bistability behavior provided by the geometrically non-linear UF-based finite elements are provided.
- Finally, in Chapter 9, the major outcomes and the original contributions of the present research work are discussed along with future perspectives.

Part I

Literature Review

Chapter 2

Multi-stability: Modeling, Design and Applications

2.1 Introduction

In the last few years, multi-stable structures have attracted considerable attention as a new class of multi-functional structures able to exploit a snap-through instability phenomenon to increase the efficiency and/or the capability of an engineering system.

After a preliminary theoretical framework described in Section 2.2, an overview of current research efforts in the field of multi-stability is provided. Section 2.3 presents a brief survey of contributions concerning modeling approaches for the purpose of understanding and predicting the mechanical behavior of multi-stable structures. Section 2.4 focuses on the methodologies for the design and optimization of functional multi-stable mechanisms and, finally, in Section 2.5, a review of promising fields of application is provided.

2.2 Brief theoretical background

2.2.1 Definition of multi-stable structure

From an energetic point of view, a structure is said multi-stable if it possesses two or more distinct minima of the total potential energy, i.e. two or more equilibrium states for which the second variation of the total potential is positive definite for any admissible displacement $\bar{\mathbf{u}}$:

$$\delta^2 E_T > 0 \quad \forall \bar{\mathbf{u}} \neq \mathbf{0} \quad (2.1)$$

The majority of the case studies and application concepts regarding multi-stability are bistable structures, i.e. structures possessing two distinct stable configurations without any external force applied. A classical load-displacement curve of a bistable structure

is provided in Figure 2.1. The bistability phenomenon relies on the snap-through buckling, which consists in the transition from a stable force-displacement region (curve A-B) to a second stable region (curve C-D) passing through an instability region (curve B-C). From a numerical point of view, stable regions are characterized by a positive definite tangent stiffness matrix, whereas for unstable conditions, at least one negative eigenvalue exists. Under force control, starting from the initial stable state (point A),

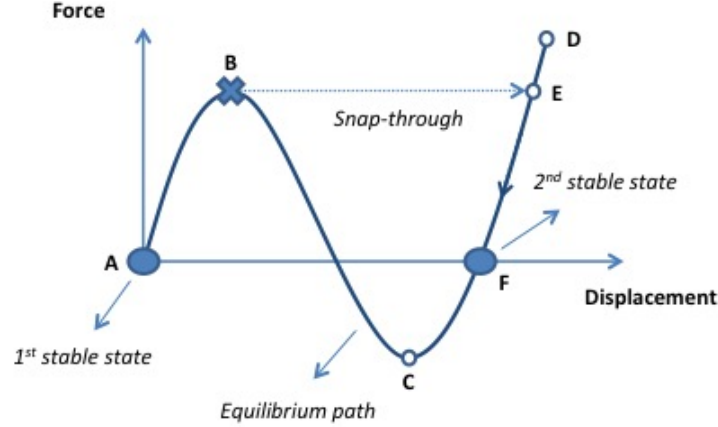


Figure 2.1: Typical equilibrium path of a bistable structure.

the force can be increased until the limit point B is reached. Then, the structure will suddenly snap to point E by means of a displacement jump and finally, when the external load is removed, it will rest in its second stable state (point F). A classical example of bistable structure, as already discussed in the Introduction, is a pre-buckled beam and this is the class of structures that will be thoroughly investigated in this dissertation. A proper choice of pre-compression parameter and external load is needed in order to achieve bistability in a pre-buckled beam. In fact, if the initial pre-compression is not sufficient, i.e. the pre-buckled configuration is too shallow, the structure will snap to a second configuration, but it will return to the first configuration after the external load is removed. Such behavior is said monostable and its typical unloading path is shown in Figure 2.2. On the other hand, if the external disturbance is too small, i.e. the limit point B in Figure 2.1 is not reached, the pre-buckled structure will simply remain in its first stable configuration without any snap-through phenomenon. Finally, if sufficient pre-compression and external disturbance are provided, the structure will show the typical unloading path provided in Figure 2.1, where two distinct stable configurations are obtained, corresponding to those equilibrium states with positive slope of the equilibrium path and external force equal to zero.

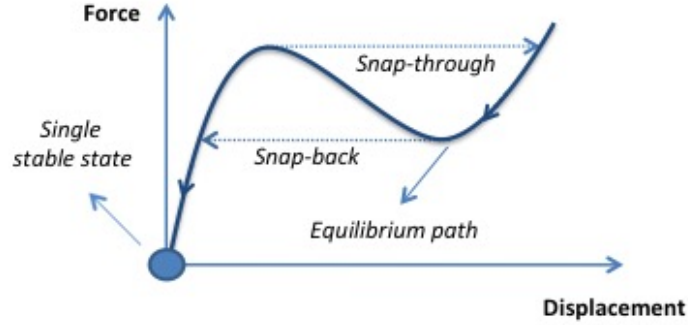


Figure 2.2: Unloading path for a pre-buckled beam with monostable behavior.

2.2.2 The role of composites in multi-stability

As it can be deduced from previous considerations, multi-stability is not a property associated to a specific material, but rather to a structural configuration, which includes material as well as geometry, boundary conditions and eventually pre-stress conditions. Nevertheless, a good amount of multi-stable structural applications studied in the literature are made of composite materials, as will be seen more in detail in Section 2.5. Composites are obtained by combining at least two distinct materials on a macroscopic scale to obtain a novel material exhibiting improved properties compared to its constituents [96]. Due to their enhanced performance, the use of composites has grown steadily over the last decades in many industries [11, 96] and the following potential benefits from exploitation of composites in multi-stable structural applications can be identified:

- Weight saving through optimal strength-to-weight and stiffness-to-weight ratios, particularly relevant for lightweight aerospace applications [5, 62].
- Increased durability, fatigue life and resistance to damage and environmental degradation [11].
- Versatile design of the structural performance parameters such as snap-through load and stable states through a proper material tailoring in terms of ply properties, fibers orientation and stacking sequence [158].
- Enabling of novel classes of multi-stable structures, such as thermally-induced multi-stable laminates [94] and smart multi-stable piezo-electric structures [135].

2.3 Modeling approaches

For exploitation of multi-stable structures in industrial applications, the capability to model multi-stability phenomena through accurate yet time-efficient approaches plays

a key role. Common approaches used for modeling the mechanics of bistable structures are mostly based on the classical beam and plate theories and the first-order shear deformation theory. In earlier studies, the adoption of Euler-Bernoulli's kinematic assumptions led to gain novel insights into the mechanics of bistable beam structures. Vangbo [160] investigated the influence of bending and compression energy on the snap-through of a doubly clamped beam as well as the effect of an additional central constraint along the beam axis to prevent twisting during the snap. Based on [160], a key parameter given by the ratio of initial deflection and beam thickness was identified by Qiu et al. [137] for the prediction of the force-displacement response in a stress-free bistable compliant mechanism. Timoshenko's beam model, accounting for a non-zero constant transverse shear deformation, was used by Santer and Pellegrino [144] for the design of a novel monolithic compliant multi-stable mechanism featuring bistable elements connected in series. On the other hand, when dealing with composite multi-layered structures, classical lamination theory represents the most commonly adopted mechanical model. By means of this approach, in the framework of a semi-analytical solution based on Rayleigh-Ritz method, Hufenbach and Gude [91] analyzed the multistability of unsymmetric GFRP and CFRP laminates generated by the out-of-plane deformation due to residual stresses induced by temperature, moisture and chemical shrinkage during manufacturing. Classical laminate theory was also used by Paknejad et al. [127] for the analysis of a energy harvesting device based on a multi-layered composite piezo-electric beam structure. A first-order shear deformation theory extended to composites is sometimes also considered, as shown in Cottone et al. [54]. Originally developed for metallic structures, these kinematic models can accurately describe the mechanical response of slender structures governed by global bending behavior, although a lack of generality could arise in the prediction of kinematic behaviors peculiar of composite materials, as further discussed in Chapter 3. Alternatively, albeit computationally more expensive, two-dimensional and three-dimensional finite element models represent high-fidelity models allowing refined and reliable mechanical predictions, as in [137, 23, 2].

Besides the structure kinematic model, a second important building block of a computational framework for the analysis of multi-stable structures is the solution method of the governing differential equations. In this respect, standard approaches are the mode superposition method, especially in the framework of bistable beams as in Xu et al. [168] and Cleary et al. [52], and the Rayleigh-Ritz method, as already mentioned for Hufenbach and Gude [91]. Much effort has been devoted to propose enhanced alternative solution procedures able to improve the snap-through behavior prediction. To this aim, Pirrera et al. [133] presented a higher-order Ritz approach for the investigation of thermally-induced bistability in laminated plate structures and Lamacchia et al. [106] adopted a differential quadrature method for the study of bistable laminated shells showing the enhanced capabilities of Legendre polynomials to model the transverse displacement variation in the shell reference plane compared to other polynomial approximations. Due to their reliability and versatility, finite elements also represents a

widely used solution approach, as in the works by Mattioni et al. [116] and Pontecorvo et al. [134]. To conclude, a more recent research area in the field of multi-stability modeling concerns the development of advanced non-linear solvers such as the generalized path-following technique, which has been recently exploited for the detection of complex multi-snap events in morphing composite laminates, as shown in Groh et al. [83].

2.4 Design methodologies

In addition to the formulation of efficient predictive models, an extremely relevant research area for the ultimate aim of delivering functional multi-stable applications, is the development of systematic design methods. Some relevant contributions in this respect are discussed in the present section. A simple but effective method to tailor the snap-through properties of post-buckled beam structures has been proposed and investigated by Gao et al. [70], both numerically and experimentally. By embedding local reinforcements within the beam structure, the design space can be extended to account for pre-compression as well as position of the local reinforcements, yielding a broader spectrum of achievable snap-through behaviors. Nevertheless, especially when dealing with large-sized finite elements analysis, the exploration of the design space through repeated structural simulations could represent a computationally expensive task to perform. To the aim of avoiding time-consuming parametric studies arising from the use of classical incremental-iterative non-linear solvers, a multi-parametric structural analysis has been addressed by Groh et al. [83] and Cox et al. [56] based on a generalized path-following technique and non-linear finite element models, allowing a computationally efficient design space exploration. A promising design methodology increasingly used in many industries and which could be also adopted for multi-stable applications is Topology Optimization (TO). Thanks to the increasing maturity of additive manufacturing techniques, which provide a large amount of design freedom in terms of manufacturable shapes, designers can fully exploit the potential of mathematical methods such as TO to obtain well-performing multi-stable structures featuring optimal material layout. TO techniques specific to multi-stability studies have been developed by Bruns et al. [24] via an enhanced arc-length method in combination with the Method of Moving Asymptotes and by Jensen et al. [95], who exploited a generalized reduced gradient method and a simulated annealing algorithm for the investigation of the design space of bistable micro-mechanisms with minimum footprint. A further challenge to be faced in multi-stability research concerns the robustness design. As in any buckling-related phenomenon, small imperfections in the geometry, load or material properties may significantly affect the mechanical behavior of multi-stable structures, making it difficult to design robust imperfection-insensitive multi-stable applications. To address this issue, bistable compliant mechanisms showing less sensitivity to imperfections have been investigated by Oh and Kota [123], who ultimately proposed a robust bistable mechanism exploiting the reverse-lateral deformation of a cantilever

beam. Finally, it is worth mentioning the work of Bessa and Pellegrino dealing with the design of deployable booms, which could be equally applied to any buckling-related as well as multi-stable application. In [20, 21], the authors presented the buckling and post-buckling analysis of shell structures for the optimal design of ultra-thin carbon fiber deployable booms via a data-driven computational framework. Numerical results provided by commercial software finite elements analyses for different properly chosen inputs were used to generate a large database of structural responses needed for the computation of the optimal design via a Bayesian method, showing the potential of machine learning processes as a design tool for buckling-induced engineering applications.

2.5 Application concepts

The sharp rise in interest in multi-stability is evidenced by the large number of applications across length-scales that has been recently proposed in the literature. The most thoroughly investigated concepts are in the field of energy harvesting devices and morphing aerospace technologies and a brief survey of research in these areas is reported in this section. A more extensive review can be also found in Harne and Wang [86], Emam and Inman [63] and Thill et al. [152].

2.5.1 Energy harvesters

Thanks to their large displacements capabilities and by embedding smart materials that convert deformations into power output, bistable beams have shown potential in energy harvesting applications. Unlike linear energy harvesters, that work efficiently only around the natural frequency, bistable beams can broaden the useful bandwidth for power output, which is especially useful in realistic random vibration environment. To this aim, Xu et al. [168] studied bistable buckled simply supported piezoelectric beams both analytically and experimentally for broadband energy harvesting in self-power MEMS, whereas Masana and Daqaq [114] had previously investigated the influence of the potential function shape in both mono-stable and bistable doubly-clamped piezoelectric beams subjected to harmonic vibrations. A very interesting study on the potential of harnessing the large strains occurring in composites to further enhance the harvesting efficiency of a bistable cantilever piezoelectric beam has been carried out by Arrieta et al. [4], whereas, still with regard to bistable composite energy harvesting, a novel efficient concept exploiting a *lever effect* in order to minimize the required snap-through energy has been presented by Scarselli et al. [146]. To conclude, electromagnetic energy harvesters have been also proposed, as in Chiacchiari et al. [50], who showed the advantages provided by the bistable behavior in terms of efficiency and total harvested energy.

2.5.2 Morphing structures

Conventional engineering adaptive systems are heavy multi-body mechanisms. They rely on components providing strength and stiffness, i.e. the rigid links, components that provide motion, i.e. the kinematic joints, and springs storing the elastic energy. They are usually optimized for a limited set of operating conditions, since shape adaptivity adds part count as well as design complexity. On the other hand, many structures in nature, such as bird wings as well as trees and plants are single-piece bodies that use compliance, i.e. elastic deformation, in order to adapt to changing environmental conditions [151, 108]. Therefore, inspired by nature, shape morphing can be obtained by integrating all the components in lightweight single-piece compliant elements. Furthermore, by exploiting multi-stability, stiffness and compliance can be properly balanced by design in order to meet the contradictory requirements of flexibility (to change shape) and load-carrying capabilities.

Due to the variety of different environments and loadings that structures experience during their lifetime as well as the complex functionalities, aerospace engineering is the primary field where adaptive structures could enable improved performance and environmental sustainability. Applications of thermally-induced bistability of laminated composites have been thoroughly investigated by Diaconu et al. [62] for morphing trailing-edge, camber and chord length of an aerofoil section and by Mattioni et al. [117] for shape-adaptable aircraft structures such as a variable sweep wing, a bistable winglet and a variable camber trailing edge. By further developing the concept of a monolithic mechanism featuring bistable elements as actuators of a compliant plate structure proposed by Santer and Pellegrino [144], Arrieta et al. [5] proposed the use of bistable laminates embedded within a compliant aerofoil for passive load alleviation, showing that decreased aerodynamic loads can be achieved by passively morphing the aerofoil camber via snap-through of the bistable laminate. A novel concepts about morphing aerofoils has been very recently proposed by Nicassio et al. [121], who conceived a lightweight and energy-efficient shape-adaptive surface based on the 'lever effect' of a bistable composite plate for passive morphing of an aircraft wing flaperon, see Figure 2.3. Another very promising application concept is the use of bistable elements as



Figure 2.3: Concept of a passively morphing wing flaperon by means of an embedded bistable composite plate proposed by Nicassio et al. [121].

unit cells of cellular structures, as proposed by Pontecorvo et al. [134], who studied bistable arch elements embedded in honeycomb structures for the morphing of a rotor blade. To conclude, by investigating the snap-through of a post-buckled beam-like member, the design and testing of a passively actuated shape-adaptive air duct for flow control and regulation has been carried out by Arena et al. [2, 3].

2.5.3 Other proposed applications

Besides energy harvesting and morphing technologies, multi-stable structures have been proposed for application in many other fields and a few examples are herein reported, for the sake of completeness.

Actuators. A theoretical as well as experimental analysis on the bistability of buckled micro-beam actuators for potential application in MEMS, such as mechanical memories, relays, valves and optical switches has been carried out by Park and Hah [128].

Deployable structures. By exploiting the enhanced capabilities of multi-material 3D printing, Chen et al. [49] designed and manufactured deployable hierarchical structures using a bistable von Mises truss as building block. A modified Dynamic Relaxation method was used to verify the design of two-dimensional and three-dimensional multi-state structures.

Metamaterials. A periodic cellular material with bistable unit cells based on a pre-shaped sinusoidal beam element has been presented by Restrepo et al. [143]. The constitutive behavior of such material was obtained both analytically and experimentally showing potential as fully recoverable energy absorbing material. A similar concept with a unit cell featuring tilted straight beams was studied by Shan et al. [147].

Nanotechnologies. Yamaletdinov et al. [169] studied buckled bistable graphene membranes for use in a memcapacitor, see Fig. 2.4. A molecular-dynamics simulation, an elasticity-based analytical model and the Density Functional Theory were compared in terms of threshold snap-through loads and corresponding voltages for different membrane dimensions.

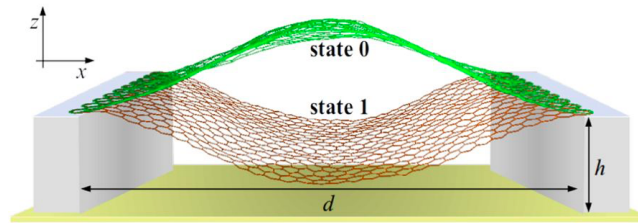


Figure 2.4: Bistable graphene membrane for application in memcapacitors proposed by Yamaletdinov et al. [169].

2.5.4 Bistability in nature: the Venus fly trap

The behavior of the Venus fly trap (see Figure 2.5) is a clear example of how nature is able to harness multi-stability in order to perform vital functions. Since Darwin [59],

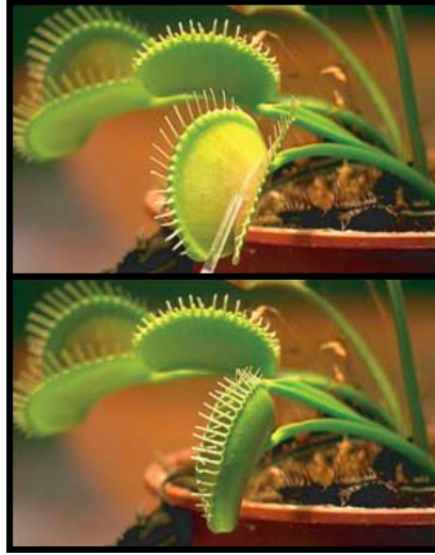


Figure 2.5: Closure mechanism of the Venus fly trap investigated by Forterre et al. [69].

the Venus fly trap has been subject of research due to its fast trap closure movement. Such sudden change of configuration of the leaf halves could not rely on cellular water pumps, since, for the typical values of flow rate involved in plants, water-driven actuation would only allow a much slower motion, such as in sunflowers for instance. As shown in Forterre et al. [69], the fast trap closure is made possible by harnessing the snap-through elastic instability of the doubly-curved leaves, whereas the trigger actuation only is driven by the differential turgor pressure in the hydraulic layers.

Chapter 3

Mechanics of Composite Multi-Layered Beam Structures: Classical Models and Recent Advances

3.1 Introduction

Over the last decades, the development of mathematical models able to accurately describe the behavior of multi-layered composites has become of extreme importance for full exploitation of their potential in industrial applications. Classical approaches consist in a mere extension of mechanical models previously conceived for metallic structures to account for variation of the material properties through space. Nevertheless, these models are based on kinematic assumptions that do not account for some peculiar features of multi-layered composite materials, such as transverse deformability and a greater influence of shear and normal stresses on the mechanical behavior. For this reason, ad-hoc theories able to account for these effects have been formulated over the years by many authors, yielding a better understanding of the mechanics of composites and improved predictions of their behavior.

A brief review of the most relevant one-dimensional mechanical models available in the literature is given in Section 3.2, with a special focus on equivalent single layer approaches, such as Euler-Bernoulli's, Timoshenko's and higher-order shear deformation theories, as well as layer-wise models. In Section 3.3, an advanced modeling approach based on a Unified Formulation of the displacement field is presented, in which the approximation order of the cross-sectional beam kinematics is generalized thanks to an elegant compact unified notation, allowing several refined one-dimensional models to be incorporated in a single mathematical framework. The nuts and bolts of UF are discussed, including the variational statements upon which it is built, the choice of the

base functions of the displacement field expansion and the variable description level, i.e. the use of either an equivalent single layer or a layer-wise approach. Finally, a brief survey about exploitation of UF methodology in a broad spectrum of mechanics-related fields of study is provided.

3.2 One-dimensional modeling literature review

A three-dimensional beam-like structure is a solid generated by the translation of a plane cross-section Ω along a line, i.e. the beam axis, the length of which is predominant with respect to the cross-section dimensions. The adopted Cartesian reference system is provided in Figure 3.1, being x the axis direction and (y, z) two orthogonal directions in the cross-section plane. The three-dimensional displacement field is:

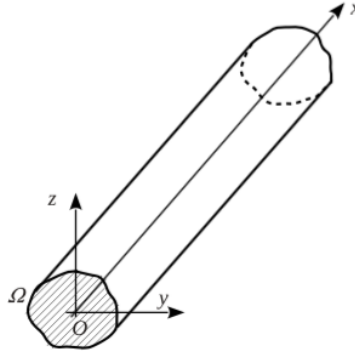


Figure 3.1: Coordinate reference system in a beam-like structure.

$$\mathbf{u}^T(x, y, z) = \{ u_x(x, y, z) \quad u_y(x, y, z) \quad u_z(x, y, z) \} \quad (3.1)$$

where u_x , u_y and u_z are the displacement components along the respective axis. Let ϵ and σ be, respectively, the three-dimensional strain and stress vectors:

$$\epsilon^T = \{ \epsilon_{xx} \quad \epsilon_{yy} \quad \epsilon_{zz} \quad \epsilon_{yz} \quad \epsilon_{xz} \quad \epsilon_{xy} \} \quad (3.2)$$

$$\sigma^T = \{ \sigma_{xx} \quad \sigma_{yy} \quad \sigma_{zz} \quad \sigma_{yz} \quad \sigma_{xz} \quad \sigma_{xy} \} \quad (3.3)$$

The main features of the classical approaches adopted for the study of composite multi-layered one-dimensional structures are briefly reported in this section.

3.2.1 Classical theories

Euler-Bernoulli's Theory (EBT)

Euler-Bernoulli's theory [65, 19] is based on the hypothesis that the cross-section remains plane and perpendicular to the axis after deformation. The assumed kinematic

field is:

$$\begin{aligned} u_x &= u_{x1} - \frac{\partial u_{y1}}{\partial x} y - \frac{\partial u_{z1}}{\partial x} z \\ u_y &= u_{y1} \\ u_z &= u_{z1} \end{aligned} \quad (3.4)$$

where u_{x1} , u_{y1} and u_{z1} are three unknown functions. Based on this kinematic behavior, in the framework of EBT, shear and transverse normal strains are neglected:

$$\varepsilon_{xy} = \varepsilon_{xz} = \varepsilon_{yy} = \varepsilon_{zz} = \varepsilon_{yz} = 0 \quad (3.5)$$

Timoshenko's Beam Theory (TBT)

According to Timoshenko's kinematics [154, 155], two additional unknown functions with respect to EBT, i.e. the section rotations ϕ_y and ϕ_z , are considered:

$$\begin{aligned} u_x &= u_{x1} + \phi_z y + \phi_y z \\ u_y &= u_{y1} \\ u_z &= u_{z1} \end{aligned} \quad (3.6)$$

Besides axial strain, constant transverse shear strains over the cross-sectional coordinates y and z are accounted for, whereas all other deformation components are neglected:

$$\begin{aligned} \varepsilon_{xy} \text{ and } \varepsilon_{xz} &= \text{constant} \\ \varepsilon_{yy} = \varepsilon_{zz} = \varepsilon_{yz} &= 0 \end{aligned} \quad (3.7)$$

Nevertheless, as it is well-known (see Reddy [140]), in order to accommodate stress-free conditions at the unloaded surfaces of the beam, a quadratic through-the-thickness variation of the transverse shear stresses, at least, should be imposed. For this reason, in order to improve the predictions provided by TBT, transverse shear stiffness is reduced via problem-dependent shear correction coefficients [154, 155, 55, 156].

3.2.2 Higher-Order Shear Deformation Theories (HSDT)

Higher-order expansions of the axial displacement component have been proposed in order to enhance the prediction of the transverse shear stress and avoid the use of shear correction factors. For a two-dimensional problem in the xz -plane, the kinematics of a second-order shear deformation theory [141] reads:

$$\begin{aligned} u_x &= u_{x1} + \phi z + \psi z^2 \\ u_z &= u_{z1} \end{aligned} \quad (3.8)$$

In a similar manner, the displacement field for a third-order theory [110, 22, 139, 87, 141] is given by:

$$\begin{aligned} u_x &= u_{x1} + \phi z - \frac{4z^3}{3h^2} \left(\phi + \frac{\partial u_{z1}}{\partial x} \right) \\ u_z &= u_{z1} \end{aligned} \quad (3.9)$$

where h is the beam thickness. The quadratic profile of transverse shear strain/stress as well as stress-free conditions at the unloaded edges of the beam can be accommodated through these kinematic assumptions. No additional unknowns are introduced with respect to the two-dimensional TBT. Since the transverse displacement does not vary along the thickness, normal inextensibility of the beam cross-section is assumed ($\epsilon_{zz} = 0$).

3.2.3 Layer-Wise (LW) models

The models described in the previous sections rely on an Equivalent Single Layer (ESL) approach, in which the number of unknowns is independent of the layer number and a unique continuous kinematic field is assumed over the whole cross-section. Therefore, within an ESL framework, a cross-section eventually composed by subdomains made of different materials is seen as an equivalent single domain cross-section with material properties that are the average of the different domains. An alternative method, known as layer-wise approach, consists in the assumption of a different kinematic field for each subdomain, where the structural integrity is assured by imposing the congruence of the displacements at the interfaces between subdomains. By means of a LW approach and mixed displacement-stress formulations, the C_z^0 requirement [25, 26] can be exactly satisfied, i.e. the continuity of the displacements as well as out-of-plane stresses at the interfaces between laminae can be imposed. Although a more refined local mechanical response at lamina level can be predicted via a LW approach, its use for practical applications with a large number of subdomains can be computationally heavy, since the number of unknowns of the model increases. A combination of the two approaches, in which some specific layers are modeled via LW and other stacks of lamina are modeled via ESL, is a commonly adopted modeling solution in order to achieve a good compromise between an accurate mechanical response and time-effective numerical simulations. In this framework, the use of a piece-wise continuous displacement field allows improved predictions of the typical zig-zag through-the-thickness distribution of the displacements, as shown for instance in Filippi and Carrera [66]. Zig-zag theories have been widely adopted in either the ESL or LW framework, within displacement-based or mixed formulations and an exhaustive review can be found in Carrera [27].

Some relevant works regarding the development of beam models using a LW approach will be reported hereafter. A layer-wise approximation of the displacement field under the hypothesis of non-deformable cross-section was adopted in Savoia et al. [145] and Krajcinovic [105] who investigated the static mechanical response of a sandwich beam-like structure by adopting Euler-Bernoulli's kinematics independently for each layer. Since classical ESL approaches are not adequate in the case of localized deformations caused by a pronounced transverse anisotropy, the use of refined layer-wise models for the mechanics of sandwich beams was investigated in several studies. Banerjee and Sobey [12] adopted Rayleigh's hypothesis for the skins and Timoshenko's beam theory for the core mechanics. Damanpack and Khalili [58] assumed cubic and quadratic

through-the-thickness variation of axial and transverse displacements, respectively, in the core, whereas Euler-Bernoulli's theory was adopted for the skins. A similar mechanical model was already used by Léotoing et al. [109] and by Hu et al. [89, 90] for the study of global and local instabilities.

An extension of higher-order sandwich beam theory by including transverse shear as well as core compressibility (non-zero axial strains) was provided by Phan et al. [130] and Wang and Wang [166]. Cho and Averill [51] proposed a novel one-dimensional finite elements formulation based on a layer-wise first-order zig-zag model for the study of thick and slender laminated beams. Averill and Yip [6] studied thick laminated and sandwich beams through a layer-wise higher-order zig-zag theory accounting for transverse deformation, in which the additional degrees of freedom coming from the layer-wise approximation with respect to an equivalent single layer approach are removed by imposing inter-laminar continuity of the transverse stresses. In Aitharaju and Averill [1] laminated composite beams were investigated by means of a quadratic layer-wise zig-zag theory under the assumption of a constant transverse normal stress in order to tackle Poisson's locking phenomenon. A novel beam theory based on a zig-zag third-order approximation of the in-plane displacement components and layer-wise quadratic approximation of the normal component was developed by Kapuria et al. [99] accounting for thermal stresses in laminated simply supported beams. Based on the same model, static, buckling and vibrations analyses were carried out in [100]

3.2.4 Other modeling approaches

In this section, other important contributions in the field of composite beam modeling are mentioned. A generalized form of different higher-order shear deformation theories was adopted by Aydogdu [7, 8] as well as Mahi et al. [112] for the vibration analysis of laminated and functionally graded beams, based on the work of Touratier [157] and Timarci and Soldatos [153] on the mechanics of multi-layered shells. Groh and Weaver [84] discussed the kinematic boundary inconsistencies of higher-order displacement based models enforcing a-priori vanishing of the shear strain at the top and bottom of clamped beams, plates and shells, leading to an over stiff representation of the structure. Soldatos and Elishakoff [150] provided a higher-order theory by taking into account both transverse shear and normal deformability. A refined shear deformation beam theory based on trigonometric functions ensuring inter-laminar continuity of the transverse shear within an equivalent single layer approach was developed by Vidal and Polit [163] for the thermo-mechanical investigation of laminated beams. Transverse normal stress was then included within the refined model by the same authors in [164] for the study of vibrations in multi-layered beams. In the context of asymptotic approaches, Hodges et al. [88] discussed a Variational Asymptotical Method (VAM) to predict the stiffness coefficients of composite beams in the geometrically non-linear regime via the derivation of an asymptotically exact strain energy. By means of VAM, Volovoi et al. [165] developed a generalization of Vlasov's theory for the study

of anisotropic thin-walled beam structures with open cross-sections. An advanced one-dimensional finite elements formulation adopting a Proper Generalized Decomposition has been proposed by Vidal et al. [162], in which a two-dimensional refined theory based on variable separation method within an ESL approach was developed for the study of multi-layered composite structures. Silvestre and Camotim [148, 149] investigated thin-walled orthotropic beam structures through the Generalized Beam Theory which relies on a piece-wise modeling of the beam cross-section. Such mathematical framework was, then, extended to the geometrically non-linear regime by Basaglia et al. [13] for post-buckling analyses.

3.3 One-dimensional hierarchical models based on Unified Formulation (UF)

Unified Formulation has been developed by Carrera [28] for plates and shells and it has been extended more recently to the modeling of beam-like structures by Carrera et al. [35] and Carrera and Giunta [34]. By means of this approach, classical and refined models, either in a ESL or LW approach, can be obtained within the same mathematical framework. The theoretical basis of UF is described in the following sections, including the variational statements, the polynomial expansion of the kinematic field written in a unified notation and the variables description level.

3.3.1 Variational statements

In order to obtain the governing equations, according to the choice of the main unknowns, the Principle of Virtual Displacements (PVD) and the Reissner's Mixed Variational Theorem (RMVT) can be applied for a displacement-based formulation and a mixed displacement-stress formulation, respectively.

Principle of Virtual Displacements

In a general dynamic case, PVD in matrix notation reads:

$$\int_V (\delta \epsilon^T \sigma) dV = \delta \mathcal{L}_e + \int_V \rho \delta \mathbf{u}^T \ddot{\mathbf{u}} dV \quad (3.10)$$

where the superscript T is the transposition operator, δ represents a virtual variation and ρ is the material density. The left-hand side of the latter equation is the virtual variation of the internal work, \mathcal{L}_e is the work done by the external loads and the second term on the right-hand side is the inertial work. The main unknown variable, in the case of PVD, is the displacement vector, whereas strains and stresses are derived via geometrical relations and Hooke's law, respectively.

Reissner's Mixed Variational Theorem (RMVT)

Within the framework of Reissner's Mixed Variational Theorem [142], a mixed unknown vector with displacement components and the components of the stress that are orthogonal to the lamination plane is considered:

$$\int_V \left[\delta \epsilon_{pG}^T \sigma_{pH} + \delta \epsilon_{nG}^T \sigma_{nM} + \delta \sigma_{nM}^T (\epsilon_{nG} - \epsilon_{nH}) \right] dV = \delta \mathcal{L}_e + \int_V \rho \delta \mathbf{u}_M^T \ddot{\mathbf{u}}_M dV \quad (3.11)$$

Subscript p refer to in-plane components and n to out-of-plane components; subscripts G and H stand for geometrical relations and Hooke's law, respectively, referring to the equations used in order to derive the respective quantity; subscript M stands for main variable unknown. By means of this approach, in the context of a layer-wise description, the continuity of the transverse stress components between laminae can be ensured [25, 26], therefore fulfilling the C_z^0 requirement described in Section 3.2.3.

3.3.2 Unified Formulation of the displacement field

In this thesis, displacement-based models developed via PVD are considered. In this context and by adopting Unified Formulation, the three-dimensional kinematic field is approximated via a generic polynomial expansion over the beam cross-section as follows:

$$\mathbf{u}(x, y, z) = F_\tau(y, z) \mathbf{u}_\tau(x) \quad \text{with } \tau = 1, 2, \dots, N_u \quad (3.12)$$

Relying on Einstein's notation, the repeated index τ represents a summation from 1 to N_u , which is the number of terms taken into account in the approximation. $F_\tau(y, z)$ is a generic expansion function over the cross-section coordinates. No assumption is made on the choice of $F_\tau(y, z)$ and N_u , therefore several displacement-based one-dimensional models with different levels of kinematic refinement can be straightforwardly derived within the same formulation. Through an appropriate choice of the expansion order, shear and torsional deformation as well as in-plane and out-of-plane cross-sectional warping can be implicitly accounted for. In the existing literature, three classes of expansion functions $F_\tau(y, z)$ have been studied more thoroughly: Taylor Expansion (TE), Lagrange Expansion (LE) and Hierarchical Legendre Expansions (HLE).

Taylor Expansion

The kinematic field approximated via N -order Taylor polynomials in explicit form reads:

$$\begin{aligned} u_x &= u_{x1} + u_{x2}y + u_{x3}z + \dots + u_{x \frac{(N^2+N+2)}{2}} y^N + \dots + u_{x \frac{(N+1)(N+2)}{2}} z^N \\ u_y &= u_{y1} + u_{y2}y + u_{y3}z + \dots + u_{y \frac{(N^2+N+2)}{2}} y^N + \dots + u_{y \frac{(N+1)(N+2)}{2}} z^N \\ u_z &= u_{z1} + u_{z2}y + u_{z3}z + \dots + u_{z \frac{(N^2+N+2)}{2}} y^N + \dots + u_{z \frac{(N+1)(N+2)}{2}} z^N \end{aligned} \quad (3.13)$$

In the context of UF notation given in Eq. (3.12), N_u and F_τ as functions of the polynomial order N are given in the Pascal's triangle in Table 3.1. It should be noticed that

N	N_u	F_τ
0	1	$F_1 = 1$
1	3	$F_2 = y \quad F_3 = z$
2	6	$F_4 = y^2 \quad F_5 = yz \quad F_6 = z^2$
3	10	$F_7 = y^3 \quad F_8 = y^2z \quad F_9 = yz^2 \quad F_{10} = z^3$
...
N	$\frac{(N+1)(N+2)}{2}$	$F_{\frac{(N^2+N+2)}{2}} = y^N \quad F_{\frac{(N^2+N+4)}{2}} = y^{N-1}z \quad \dots \quad F_{\frac{N(N+3)}{2}} = yz^{N-1} \quad F_{\frac{(N+1)(N+2)}{2}} = z^N$

Table 3.1: Terms of the Taylor's polynomial expansion via Pascal's triangle.

classical theories such as EBT and TBT can be derived as particular cases of Eq. (6.21) for $N = 1$ (complete linear displacement field), as discussed in Carrera et al. [35].

Lagrange Expansion

In the framework of higher-order Taylor-like expansions, the unknown vector features components with no physical meaning. If pure displacements components are preferred as unknown variables, Lagrange polynomial expansion can be adopted. The most commonly used Lagrange-like expansions in the literature are based on four and nine points of the beam cross-section and they are referred to as L4 and L9, respectively. The F_τ polynomials expressed in natural coordinates (ζ_1, ζ_2) for a L4 expansion are given by:

$$F_\tau = \frac{1}{4} (1 + \zeta_{1\tau}\zeta_1) (1 + \zeta_{2\tau}\zeta_2) \quad \text{with } \tau = 1, 2, 3, 4 \quad (3.14)$$

being $(\zeta_{1\tau}, \zeta_{2\tau})$ the coordinates of each point reported in Table 3.2.

Point	$\zeta_{1\tau}$	$\zeta_{2\tau}$
1	-1	-1
2	1	-1
3	1	1
4	-1	1

Table 3.2: Points of a L4 expansion in natural coordinates.

Polynomials F_τ for a L9 expansion are:

$$\begin{aligned}
 F_\tau &= \frac{1}{4} (\zeta_1^2 + \zeta_{1\tau}\zeta_1) (\zeta_2^2 + \zeta_{2\tau}\zeta_2) \quad \text{with } \tau = 1, 3, 5, 7 \\
 F_\tau &= \frac{1}{2} \zeta_{2\tau}^2 (\zeta_2^2 + \zeta_{2\tau}\zeta_2) (1 - \zeta_1^2) + \frac{1}{2} \zeta_{1\tau}^2 (\zeta_1^2 + \zeta_{1\tau}\zeta_1) (1 - \zeta_2^2) \quad \text{with } \tau = 2, 4, 6, 8 \\
 F_\tau &= (1 - \zeta_1^2) (1 - \zeta_2^2) \quad \text{with } \tau = 9
 \end{aligned} \quad (3.15)$$

being the coordinates of the nine points reported in Table 3.3.

Point	$\zeta_{1\tau}$	$\zeta_{2\tau}$
1	-1	-1
2	0	-1
3	1	-1
4	1	0
5	1	1
6	0	1
7	-1	1
8	-1	0
9	0	0

Table 3.3: Points of a L9 expansion in natural coordinates.

Hierarchical Legendre Expansion

The HLE-based expansion of the displacement field is obtained by defining vertex, edge and internal polynomials in the natural cross-section coordinates. The vertex polynomials F_τ with $\tau = 1, 2, 3, 4$ coincide with the L4 bi-linear polynomials introduced in Eq. (3.14) and Table 3.2. For a polynomial order $p \geq 2$, the following edge polynomials are introduced:

$$\begin{aligned}
 F_\tau(\zeta_1, \zeta_2) &= \frac{1}{2} (1 - \zeta_2) \phi_p(\zeta_1) \quad \text{with } \tau = 5, 9, 13, 18, \dots \\
 F_\tau(\zeta_1, \zeta_2) &= \frac{1}{2} (1 + \zeta_1) \phi_p(\zeta_2) \quad \text{with } \tau = 6, 10, 14, 19, \dots \\
 F_\tau(\zeta_1, \zeta_2) &= \frac{1}{2} (1 + \zeta_2) \phi_p(\zeta_1) \quad \text{with } \tau = 7, 11, 15, 20, \dots \\
 F_\tau(\zeta_1, \zeta_2) &= \frac{1}{2} (1 - \zeta_1) \phi_p(\zeta_2) \quad \text{with } \tau = 8, 12, 16, 21, \dots
 \end{aligned} \tag{3.16}$$

with:

$$\phi_p(\zeta_{1/2}) = \sqrt{\frac{2p-1}{p}} \int_{-1}^{\zeta_{1/2}} L_{p-1}(\chi) d\chi \tag{3.17}$$

being L_{p-1} a one-dimensional Legendre polynomial of order $p - 1$. Finally, for order $p \geq 4$, internal polynomials are added to the cross-sectional expansion. For instance, in the case of a sixth-order model ($p = 6$), referred to as HL6, the internal polynomials are the following:

$$\begin{aligned}
 F_{28}(\zeta_1, \zeta_2) &= \phi_4(\zeta_1) \phi_2(\zeta_2) \\
 F_{29}(\zeta_1, \zeta_2) &= \phi_3(\zeta_1) \phi_3(\zeta_2) \\
 F_{30}(\zeta_1, \zeta_2) &= \phi_2(\zeta_1) \phi_4(\zeta_2)
 \end{aligned} \tag{3.18}$$

More details about HLE-based beam models are discussed in Carrera et al. [41] and Pagani et al. [126].

3.3.3 Variables description level

Equivalent Single Layer (ESL) approach

Within the Equivalent Single Layer (ESL) approach, the variation of the model unknowns is assumed as in Eq. (3.12) over the whole laminate cross-section Ω . Therefore, ESL yields the definition of an equivalent lamina with material properties that are the average of the different layers. Within the literature related to UF, the most common way in to implement advanced one-dimensional models is by means of the Taylor-type expansions discussed in Section 3.3.2, since the enrichment of the cross-sectional kinematics can be straightforwardly obtained by adding higher-order terms to the polynomial basis.

Layer-Wise (LW) approach

In UF-based LW models, equation (3.12) holds independently for each layer k :

$$\mathbf{u}^k(x, y_k, z_k) = F_\tau(y_k, z_k) \mathbf{u}_\tau^k(x) \quad \text{with } \tau = 1, 2, \dots, N_u \quad (3.19)$$

where (y_k, z_k) are the natural coordinates at layer level such that $-1 \leq y_k, z_k \leq 1$ and $k = 1 \dots N_l$ with N_l the total layer number. Structural integrity is ensured by imposing the displacement congruency condition at each interface, which can be easily done if the interface values are used as unknown variables. In the existing literature related to UF, LW displacement-based models are developed by means of the Lagrange and Legendre expansions discussed in Section 3.3.2, since interface displacements can be chosen as main model unknowns and, therefore, compatibility conditions can be straightforwardly imposed. On the other hand, in order to derive LW models based on Taylor-type expansions (Section 3.3.2), additional constraint equations enforcing congruency conditions would be required. Within the category of Taylor-based theories, classical models (EBT, TBT) as well as HSDT are also included.

3.3.4 Recent applications of UF-based one-dimensional models

A short literature review based on Carrera et al. [46] and updated with the most recent contributions on UF-based one-dimensional modelling is given hereafter.

Vibration analysis. Higher vibration modes of laminated, sandwich and fiber-metal laminated simply supported beam-like structures have been studied by Giunta et al. [78, 79] and Hanten et al. [85] via refined Taylor-based models in the framework of an exact Navier-type analytical solution. Such approach was extended to the investigation of sandwich beams with generic boundary conditions by Hui et al. [92] in the framework

of a finite element solution.

Rotordynamics. The dynamics of rotors made of multi-layered composite material via Taylor-based higher-order models has been studied by Carrera et al. [30, 31] and Carrera and Filippi [29]. Mode aberration of rotating plates and shell-like structures via one-dimensional UF-based models has been explored by Filippi et al. [68] in the geometrically non-linear regime.

Thermal Analysis. Giunta et al. [76, 77, 73] investigated the thermo-elastic response of functionally graded and multi-layered beams via a Navier-type solution as well as radial basis collocation meshless solution. Static, transient and dynamic coupled thermoelastic analysis of nonhomogeneous anisotropic beams via Lagrange-type expansions has been performed by Entezari et al. [64] and Filippi et al. [67].

Smart Structures. Giunta et al. [74] and Koutsawa et al. [103, 102, 104] used both ESL-based refined finite elements and layer-wise approaches based on Lagrange expansion for the study of shear-actuated beam structures with piezo-electric layers or patches. Zappino and Carrera [171] adopted UF-based one-dimensional models to carry out a thermo-piezo-mechanical analysis of amplified piezoceramic actuators with complex geometry. The influence of the thermal field on the actuator performance was assessed. UF-based refined models with node-dependent kinematics was developed by Carrera et al. [44] and Zappino et al. [172] for a numerically efficient static and dynamic analysis of smart structures with piezo-patches.

Optimization. Montemurro et al. [120] exploited the enhanced capabilities of UF-based refined one-dimensional models to verify the design of composite reinforced panels previously optimized via a multi-scale two-level (mesoscopic and macroscopic) strategy.

Nano-structures. Taylor-based advanced atomistic theories were developed for the static, vibration and stability analysis of orthotropic nano-beams by Giunta et al. [81] by accounting for the surface free energy effect within the linear elastic constitutive law.

Component-Wise (CW) Approach. The investigation of multi-component structures via one-dimensional UF-based finite elements was proposed by Carrera et al. [45]. Based on this approach, aerospace structures [42], civil engineering structures [43] as well as micro-mechanics of composites [38, 39, 170] has been studied. Taylor, Lagrange and Legendre expansions have been considered within the CW approach.

Biomechanics. Varello and Carrera [161] used higher-order Taylor-based models to study the mechanical response of a nonhomogeneous atherosclerotic plaque. Based on this study, Carrera et al. [36] investigated the static and vibration response of atherosclerotic plaque and a dental prosthesis by exploiting the CW capabilities of Lagrange expansions.

Elastoplasticity. Higher-order Taylor- and Lagrange-based models with 3D-like accuracy were assessed by Carrera et al. [37] and Petrolo et al. [129] for the elastoplastic analysis of thin-walled structures through a global-local technique.

Post-buckling. The buckling and post-buckling of thin-walled metallic beams and laminated beams by means of Lagrange-based layer-wise approach was carried out by Paganini and Carrera [125, 124].

Failure and Damage Analysis. In de Miguel et al. [118], UF-based finite elements with Lagrange expansion of the kinematics have been adopted for a 3D-like prediction of failure indices in multi-layered composite structures for the first-ply failure prediction. UF models based on the Lagrange polynomial expansion within a CW approach have been used by Kaleel et al. [97, 98] for the progressive damage propagation analysis in fiber reinforced composites at the micro-scale. Viglietti et al. [118] and Cavallo et al. [47] investigated the free-vibration response of locally damaged aerospace structures, such as stringer reinforced panel and wing box structure, and civil engineering structures by means of Lagrange-based models in the framework of a CW approach.

Part II

Modeling Methodology

Chapter 4

Hierarchical 1D Finite Elements for Mechanical and Thermal Stress Analysis

4.1 Introduction

In this chapter, a family of refined one-dimensional finite elements based on the Unified Formulation has been derived for mechanical and thermo-mechanical problems, in the framework of an Equivalent Single Layer approach. The UF-based finite element approximation of the three-dimensional displacement field is described in Section 4.2. As discussed in Sections 4.3 and 4.4, linear geometrical and constitutive relations are considered and the temperature field, obtained by analytically solving Fourier's heat conduction equation, is accounted as an external load within the Hooke's law, according to a one-way staggered solution procedure. Finally, in Section 4.5, the governing algebraic equations are derived via the Principle of Virtual Displacements and, thanks to the UF compact notation, the element stiffness matrix, the mechanical load vector and the thermo-mechanical coupling vector are written in the form of fundamental nuclei, whose explicit expressions are also provided. This formulation should be regarded as an extension of the work done by Giunta et al. [77, 80, 72], where UF-based ESL models have been developed based on a strong form Navier-type solution accommodating simply supported boundary conditions. The novelty of the present work consists in the generalization of the applicable boundary conditions thanks to a weak form finite element solution of the governing differential equations. The formulation described in this chapter brings together contributions previously published in [61, 60, 75].

4.2 UF-based displacement field

A Cartesian reference system is used, where the x -axis is in the direction of the beam axis and y -axis and z -axis lay on the cross-section plane Ω , as shown in Fig. 3.1.

Cross-sectional kinematics

As discussed in Section 3.3.2, within the framework of Unified Formulation, the three-dimensional kinematic field is a priori assumed as follows:

$$\mathbf{u}(x, y, z) = F_\tau(y, z) \mathbf{u}_\tau(x) \quad \text{with } \tau = 1, 2, \dots, N_u \quad (4.1)$$

where $F_\tau(y, z)$ is a generic function of the cross-section coordinates. The repeated index τ implicitly stands for a summation over its variation range $[1, N_u]$, where N_u is the number of terms accounted for in the expansion.

Since the choice of the functions $F_\tau(y, z)$ and N_u is arbitrary, the cross-sectional kinematics can be freely enriched, yielding accurate predictions of shear mechanics, torsional effects, Poisson's effect, in- and out-of plane warping in a straightforward manner.

Axial approximation

Regarding the variation of the displacements along the beam axis, a one-dimensional finite elements approach is considered, therefore Eq. (4.1) reads:

$$\mathbf{u}(x, y, z) = F_\tau(y, z) N_i(x) \mathbf{q}_{\tau i} \quad \text{with } \tau = 1, 2, \dots, N_u \text{ and } i = 1, 2, \dots, N_n^e \quad (4.2)$$

being $N_i(x)$ standard one-dimensional Lagrangian shape functions and \mathbf{q}_i the element unknown vector. The number of nodes per element N_n^e is also a free input parameter. Two-node (linear), three-node (quadratic) and four-node (cubic) elements are used and they are referred to as “B2”, “B3” and “B4”, respectively.

4.3 Geometrical and constitutive equations

The total strain vector $\boldsymbol{\varepsilon}_t$ and the stress vector $\boldsymbol{\sigma}$ are both split into two vectors: $\boldsymbol{\varepsilon}_{tn}$ and $\boldsymbol{\sigma}_n$ with strain and stress components in the axial direction and $\boldsymbol{\varepsilon}_{tp}$ and $\boldsymbol{\sigma}_p$ with strain and stress components laying on the cross-section:

$$\boldsymbol{\varepsilon}_{tn}^T = \{ \varepsilon_{xx} \quad \varepsilon_{xy} \quad \varepsilon_{xz} \}, \quad \boldsymbol{\varepsilon}_{tp}^T = \{ \varepsilon_{yy} \quad \varepsilon_{zz} \quad \varepsilon_{yz} \}. \quad (4.3)$$

$$\boldsymbol{\sigma}_n^T = \{ \sigma_{xx} \quad \sigma_{xy} \quad \sigma_{xz} \}, \quad \boldsymbol{\sigma}_p^T = \{ \sigma_{yy} \quad \sigma_{zz} \quad \sigma_{yz} \}. \quad (4.4)$$

Strain-displacement relation

A linear strain-displacement relation is considered:

$$\begin{aligned}\epsilon_{tn}^T &= \left\{ u_{x,x} \quad u_{x,y} + u_{y,x} \quad u_{x,z} + u_{z,x} \right\}, \\ \epsilon_{tp}^T &= \left\{ u_{y,y} \quad u_{z,z} \quad u_{y,z} + u_{z,y} \right\}.\end{aligned}\quad (4.5)$$

where subscripts “, x”, “, y” and “, z” stand for derivation versus the respective direction. The matrix form of Eqs. (4.5) reads:

$$\begin{aligned}\epsilon_{tn} &= \mathbf{D}_{np} \mathbf{u} + \mathbf{D}_{nx} \mathbf{u}, \\ \epsilon_{tp} &= \mathbf{D}_p \mathbf{u}.\end{aligned}\quad (4.6)$$

being \mathbf{I} the identity matrix and \mathbf{D}_{np} , \mathbf{D}_{nx} , and \mathbf{D}_p the following differential operators:

$$\mathbf{D}_{np} = \begin{bmatrix} 0 & 0 & 0 \\ \frac{\partial}{\partial y} & 0 & 0 \\ \frac{\partial}{\partial z} & 0 & 0 \end{bmatrix}, \quad \mathbf{D}_{nx} = \mathbf{I} \frac{\partial}{\partial x}, \quad \mathbf{D}_p = \begin{bmatrix} 0 & \frac{\partial}{\partial y} & 0 \\ 0 & 0 & \frac{\partial}{\partial z} \\ 0 & \frac{\partial}{\partial z} & \frac{\partial}{\partial y} \end{bmatrix} \quad (4.7)$$

By using the UF-based displacement field in Eq.(4.2), the strain-displacement relation in Eqs. (4.6) is written in terms of the nodal unknowns vector:

$$\begin{aligned}\epsilon_{tn} &= \mathbf{D}_{np} F_\tau N_i \mathbf{q}_{ti} + \mathbf{D}_{nx} F_\tau N_i \mathbf{q}_{ti}, \\ \epsilon_{tp} &= \mathbf{D}_p F_\tau N_i \mathbf{q}_{ti}.\end{aligned}\quad (4.8)$$

Hooke's law

Under the assumption of linear elastic material behavior, Hooke's law is considered, which for a thermo-elastic analysis reads:

$$\boldsymbol{\sigma} = \mathbf{C}^k \boldsymbol{\epsilon}_e = \mathbf{C}^k (\boldsymbol{\epsilon}_t - \boldsymbol{\alpha}^k T) = \mathbf{C}^k \boldsymbol{\epsilon}_t - \lambda^k T, \quad (4.9)$$

where “k” stands for the k-th layer of a multi-layered structure, $\boldsymbol{\epsilon}_e$ is the elastic deformation, \mathbf{C}^k is the matrix of the material coefficients, $\boldsymbol{\alpha}^k$ is the vector of the thermal expansion coefficients, T is the over-temperature and λ^k is given by:

$$\lambda^k = \mathbf{C}^k \boldsymbol{\alpha}^k \quad (4.10)$$

By writing Eq. (4.9) in terms of $\boldsymbol{\sigma}_n$, ϵ_{tn} , $\boldsymbol{\sigma}_p$ and ϵ_{tp} :

$$\begin{aligned}\boldsymbol{\sigma}_n &= \mathbf{C}_{np}^k \epsilon_{tp} + \mathbf{C}_{nn}^k \epsilon_{tn} - \lambda_n^k T, \\ \boldsymbol{\sigma}_p &= \mathbf{C}_{pp}^k \epsilon_{tp} + \mathbf{C}_{pn}^k \epsilon_{tn} - \lambda_p^k T.\end{aligned}\quad (4.11)$$

In the case of isotropic materials, the matrices \mathbf{C}_{nn}^k , \mathbf{C}_{np}^k , \mathbf{C}_{pn}^k and \mathbf{C}_{pp}^k are:

$$\mathbf{C}_{nn}^k = \begin{bmatrix} C_{11}^k & 0 & 0 \\ 0 & C_{66}^k & 0 \\ 0 & 0 & C_{55}^k \end{bmatrix} \quad \mathbf{C}_{pn}^k = \mathbf{C}_{np}^{kT} = \begin{bmatrix} C_{12}^k & 0 & 0 \\ C_{13}^k & 0 & 0 \\ 0 & 0 & 0 \end{bmatrix} \quad \mathbf{C}_{pp}^k = \begin{bmatrix} C_{22}^k & C_{23}^k & 0 \\ C_{23}^k & C_{33}^k & 0 \\ 0 & 0 & C_{44}^k \end{bmatrix} \quad (4.12)$$

Coefficients C_{ij}^k are given by:

$$C_{11}^k = C_{22}^k = C_{33}^k = \frac{1 - \nu^k}{(1 + \nu^k)(1 - 2\nu^k)} E^k \quad C_{12}^k = C_{13}^k = C_{23}^k = \frac{\nu^k}{(1 + \nu^k)(1 - 2\nu^k)} E^k \\ C_{44}^k = C_{55}^k = C_{66}^k = \frac{1}{2(1 + \nu^k)} E^k \quad (4.13)$$

In the particular case of isotropic functionally graded material, elastic and thermal properties become function of the cross-section coordinates according to an assumed material gradation law. For orthotropic materials \mathbf{C}_{nn}^k , \mathbf{C}_{np}^k , \mathbf{C}_{pn}^k and \mathbf{C}_{pp}^k are given by:

$$\mathbf{C}_{nn}^k = \begin{bmatrix} C_{11}^k & C_{16}^k & 0 \\ C_{16}^k & C_{66}^k & 0 \\ 0 & 0 & C_{55}^k \end{bmatrix}, \quad \mathbf{C}_{pn}^k = \mathbf{C}_{np}^{kT} = \begin{bmatrix} C_{12}^k & C_{26}^k & 0 \\ C_{13}^k & C_{36}^k & 0 \\ 0 & 0 & C_{45}^k \end{bmatrix}, \quad (4.14) \\ \mathbf{C}_{pp}^k = \begin{bmatrix} C_{22}^k & C_{23}^k & 0 \\ C_{23}^k & C_{33}^k & 0 \\ 0 & 0 & C_{44}^k \end{bmatrix}.$$

The explicit expressions of the coefficients C_{ij}^k as function of the engineering material constants and the fibre angle are reported in Reddy [140].

Coefficients λ_n^k , λ_p^k , α_n^k and α_p^k are in the following form:

$$\lambda_n^{kT} = \{ \lambda_1^k \quad \lambda_6^k \quad 0 \}, \quad \lambda_p^{kT} = \{ \lambda_2^k \quad \lambda_3^k \quad 0 \} \quad (4.15)$$

$$\alpha_n^{kT} = \{ \alpha_1^k \quad 0 \quad 0 \}, \quad \alpha_p^{kT} = \{ \alpha_2^k \quad \alpha_3^k \quad 0 \}, \quad (4.16)$$

and they are related by means of the following equations:

$$\lambda_n = \mathbf{C}_{np}^k \alpha_p^k + \mathbf{C}_{nn}^k \alpha_n^k, \\ \lambda_p^k = \mathbf{C}_{pp}^k \alpha_p^k + \mathbf{C}_{pn}^k \alpha_n^k. \quad (4.17)$$

By substituting Eqs. (4.8) within Eqs. (4.11), stresses can be written in terms of the over-temperature T and of the unknown vector \mathbf{q}_i as follows:

$$\sigma_n = \mathbf{C}_{np}^k \mathbf{D}_p F_\tau N_i \mathbf{q}_{\tau i} + \mathbf{C}_{nn}^k (\mathbf{D}_{nx} + \mathbf{D}_{np}) F_\tau N_i \mathbf{q}_{\tau i} - \lambda_n^k T, \\ \sigma_p = \mathbf{C}_{pp}^k \mathbf{D}_p F_\tau N_i \mathbf{q}_{\tau i} + \mathbf{C}_{pn}^k (\mathbf{D}_{nx} + \mathbf{D}_{np}) F_\tau N_i \mathbf{q}_{\tau i} - \lambda_p^k T. \quad (4.18)$$

Poisson's locking

Classical models such as Euler-Bernoulli's Beam Theory and Timoshenko's Beam Theory can be derived, within the Unified Formulation framework, from a first-order model ($N = 1$), in which the following relation is used for the computation of the axial stress, instead of the relation given by Eqs. (4.11):

$$\sigma_{xx} = \bar{Q}_{11}\varepsilon_{xx} + \bar{Q}_{16}\varepsilon_{xy} \quad (4.19)$$

The reduced material stiffness coefficient \bar{Q}_{11} and \bar{Q}_{16} can be obtained by imposing σ_{yy} and σ_{zz} equal to zero in Hooke's law. A system of two linear equations in two unknowns ε_{yy} and ε_{zz} is obtained, which can, then, be substituted into Hooke's equation in σ_{xx} given by Eqs. (4.11). This is done in order to correct the kinematic incongruence known as Poisson's locking, due to the fact that classical beam models account for rigid cross-section ($\varepsilon_{yy} = \varepsilon_{zz} = 0$), which is in disagreement with the Poisson's effect.

4.4 Fourier's heat conduction equation

For the sake of completeness, the solution of the heat conduction problem is briefly reported hereafter. The over-temperature field is assumed to be in the following form:

$$T^k(x, z) = \Theta_n(x) \Theta_\Omega^k(z) = \left[\bar{T}_1^k e^{s_1^k z} + \bar{T}_2^k e^{s_2^k z} \right] \sin(\alpha x) \quad (4.20)$$

where $\bar{T}_{1,2}^k$ are unknown amplitudes and $s_{1,2}^k$ are constant values depending on the material properties. For more details, readers are referred to Giunta et al. [75] and De Pietro et al. [131]. By means of Eq. (4.20), a Navier-type closed form solution of Fourier's heat conduction equation can be obtained.

4.5 Governing equations and fundamental nuclei

4.5.1 Principle of virtual displacements

For a thermo-mechanical analysis, the Principle of Virtual Displacements reads:

$$\delta \mathcal{L}_{\text{int}} = \delta \mathcal{L}_{\text{ext}}, \quad (4.21)$$

where \mathcal{L}_{int} is the strain energy and \mathcal{L}_{ext} represents the work done by the external mechanical loads. The virtual variation of the strain energy is written in terms of stress and strain components:

$$\delta \mathcal{L}_{\text{int}} = \int_{l_e} \int_{\Omega} (\delta \epsilon_{tn}^T \sigma_n + \delta \epsilon_{tp}^T \sigma_p) d\Omega dx. \quad (4.22)$$

being l_e the length of a one-dimensional finite element. In the case of a multi-layered structure, Ω is split into N_{Ω^k} layers:

$$\Omega = \bigcup_{k=1}^{N_{\Omega^k}} \Omega^k, \quad (4.23)$$

By substituting the geometrical relations in Eqs. (4.8), the constitutive law in Eqs. (4.18) and the assumed temperature field in Eq. (4.20) into Eq. (4.22):

$$\begin{aligned} \delta \mathcal{L}_{\text{int}} = & \delta \mathbf{q}_{\tau i}^T \int_{l_e} \int_{\Omega^k} \left\{ (\mathbf{D}_{nx} N_i)^T F_{\tau} [\mathbf{C}_{np}^k (\mathbf{D}_p F_s) N_j + \mathbf{C}_{nn}^k (\mathbf{D}_{np} F_s) N_j + \mathbf{C}_{nn}^k F_s (\mathbf{D}_{nx} N_j)] \right. \\ & + (\mathbf{D}_{np} F_{\tau})^T N_i [\mathbf{C}_{np}^k (\mathbf{D}_p F_s) N_j + \mathbf{C}_{nn}^k (\mathbf{D}_{np} F_s) N_j + \mathbf{C}_{nn}^k F_s (\mathbf{D}_{nx} N_j)] \\ & + (\mathbf{D}_p F_{\tau})^T N_i [\mathbf{C}_{pp}^k (\mathbf{D}_p F_s) N_j + \mathbf{C}_{pn}^k (\mathbf{D}_{np} F_s) N_j + \mathbf{C}_{pn}^k F_s (\mathbf{D}_{nx} N_j)] \left. \right\} d\Omega dx \mathbf{q}_{sj} \\ & - \delta \mathbf{q}_{\tau i}^T \int_{l_e} \int_{\Omega^k} [\mathbf{D}_p^T F_{\tau} N_i \lambda_{\mathbf{p}}^k + (\mathbf{D}_{nx}^T + \mathbf{D}_{np}^T) F_{\tau} N_i \lambda_{\mathbf{n}}^k] \Theta_{\Omega}^k \Theta_n d\Omega dx \end{aligned}$$

The latter equation can be written in a compact form as:

$$\delta \mathcal{L}_{\text{int}} = \delta \mathbf{q}_{\tau i}^T \mathbf{K}_{uu}^{\tau sij} \mathbf{q}_{sj} - \delta \mathbf{q}_{\tau i}^T \mathbf{K}_{u\theta}^{\tau i} \quad (4.24)$$

where $\mathbf{K}_{uu}^{\tau sij} \in \mathbb{R}^{3 \times 3}$ is the stiffness matrix fundamental nucleus and $\mathbf{K}_{u\theta}^{\tau i} \in \mathbb{R}^3$ is the thermo-mechanical coupling vector.

4.5.2 Element stiffness matrix

The components of the stiffness matrix fundamental nucleus are:

$$\begin{aligned} K_{uuxx}^{\tau sij} &= I_{i,xj,x} J_{\tau s}^{11} + I_{i,xj} J_{\tau s,y}^{16} + I_{ij,x} J_{\tau,y s}^{16} + I_{ij} \left(J_{\tau,z s,z}^{55} + J_{\tau,y s,y}^{66} \right) \\ K_{uuxy}^{\tau sij} &= I_{ij,x} J_{\tau,y s}^{12} + I_{i,xj,x} J_{\tau s}^{16} + I_{ij} \left(J_{\tau,y s,y}^{26} + J_{\tau,z s,z}^{45} \right) + I_{i,xj} J_{\tau s,y}^{66} \\ K_{uuxz}^{\tau sij} &= I_{ij,x} J_{\tau,z s}^{13} + I_{ij} \left(J_{\tau,z s,y}^{36} + J_{\tau,y s,z}^{45} \right) + I_{i,xj} J_{\tau s,z}^{55} \\ K_{uuyx}^{\tau sij} &= I_{i,xj} J_{\tau s,y}^{12} + I_{i,xj,x} J_{\tau s}^{16} + I_{ij} \left(J_{\tau,y s,y}^{26} + J_{\tau,z s,z}^{45} \right) + I_{ij,x} J_{\tau,y s}^{66} \\ K_{uuyy}^{\tau sij} &= I_{ij} \left(J_{\tau,y s,y}^{22} + J_{\tau,z s,z}^{44} \right) + I_{ij,x} J_{\tau,y s}^{26} + I_{i,xj} J_{\tau s,y}^{26} + I_{i,xj,x} J_{\tau s}^{66} \\ K_{uuyz}^{\tau sij} &= I_{ij} \left(J_{\tau,z s,y}^{23} + J_{\tau,y s,z}^{44} \right) + I_{ij,x} J_{\tau,z s}^{36} + I_{i,xj} J_{\tau s,z}^{45} \\ K_{uuzx}^{\tau sij} &= I_{i,xj} J_{\tau s,z}^{13} + I_{ij} \left(J_{\tau,y s,z}^{36} + J_{\tau,z s,y}^{45} \right) + I_{ij,x} J_{\tau,z s}^{55} \\ K_{uuzy}^{\tau sij} &= I_{ij} \left(J_{\tau,y s,z}^{23} + J_{\tau,z s,y}^{44} \right) + I_{i,xj} J_{\tau s,z}^{36} + I_{ij,x} J_{\tau,z s}^{45} \\ K_{uuzz}^{\tau sij} &= I_{ij} \left(J_{\tau,z s,z}^{33} + J_{\tau,y s,y}^{44} \right) + I_{ij,x} J_{\tau,y s}^{45} + I_{i,xj} J_{\tau s,y}^{45} + I_{i,xj,x} J_{\tau s}^{55} \end{aligned} \quad (4.25)$$

$I_{i(x)j(x)}$ is an integral along element axis direction of the product of the shape functions or their derivatives:

$$I_{i(x)j(x)} = \int_{l_e} N_{i(x)} N_{j(x)} dx \quad (4.26)$$

$J_{\tau(\phi)S(\xi)}^{gh}$ is a cross-section moment given by:

$$J_{\tau(\phi)S(\xi)}^{gh} = \int_{\Omega^k} C_{gh}^k F_{\tau(\phi)} F_{S(\xi)} d\Omega \quad (4.27)$$

Gauss' quadrature method is used to compute these integrals. The term I_{ij} in $K_{uuuxx}^{\tau sij}$, which is related to shear deformations ε_{xy} and ε_{xz} , is under-integrated (i.e. one Gauss' point less is used) in order to tackle the shear locking phenomenon, according to a classical selective integration technique, see Bathe [14]. Finally, it should be noticed that, due to the compact notation of the displacement field in Eq. (4.2), the form of the stiffness matrix fundamental nucleus given in Eqs. (4.25) is unique regardless the cross-sectional expansion order N and the number of nodes per element N_n^e .

4.5.3 Thermo-mechanical coupling vector

The explicit form of the thermo-mechanical coupling vector $\mathbf{K}_{u\theta}^{\tau i}$ is:

$$\begin{aligned} K_{u\theta x}^{\tau i} &= I_{\theta_n i, x} J_{\theta_{\Omega} \tau}^1 + I_{\theta_n i} J_{\theta_{\Omega} \tau, y}^6 \\ K_{u\theta y}^{\tau i} &= I_{\theta_n i} J_{\theta_{\Omega} \tau, y}^2 + I_{\theta_n i, x} J_{\theta_{\Omega} \tau}^6 \\ K_{u\theta z}^{\tau i} &= I_{\theta_n i} J_{\theta_{\Omega} \tau, z}^3 \end{aligned} \quad (4.28)$$

where $J_{\theta_{\Omega} \tau(\phi)}^g$ is given by:

$$J_{\theta_{\Omega} \tau(\phi)}^g = \int_{\Omega^k} F_{\tau(\phi)} \lambda_g^k (\bar{T}_1^k e^{s_1 z} + \bar{T}_2^k e^{s_2 z}) d\Omega \quad (4.29)$$

and $I_{\theta_n j(x)}$ is:

$$I_{\theta_n j(x)} = \int_{l_e} N_{i(x)} \sin(\alpha x) dx \quad (4.30)$$

The over-temperature field obtained by exactly solving Fourier's equation is integrated separately over the cross-section and along the axis in order to derive a thermal load vector which is variationally consistent with the proposed formulation. After a convergence analysis, the integral in Eq. (4.30) is computed via five Gauss' quadrature points.

4.5.4 Mechanical load vector

The virtual variation of the work \mathcal{L}_{ext} done by a line loading l_{ij} and a surface loading p_{ij} is given by:

$$\delta \mathcal{L}_{\text{ext}} = \delta \mathcal{L}_{\text{ext}}^{p_{ij}} + \delta \mathcal{L}_{\text{ext}}^{l_{ij}} \quad (4.31)$$

The different contributions to a line load $\delta \mathcal{L}_{\text{ext}}^{l_{ij}}$ applied along the beam axis at the cross-section coordinates (\hat{y}, \hat{z}) are:

$$\delta \mathcal{L}_{\text{ext}}^{l_{ij}} = \delta \mathcal{L}_{\text{ext}}^{l_{zz}} + \delta \mathcal{L}_{\text{ext}}^{l_{zx}} + \delta \mathcal{L}_{\text{ext}}^{l_{zy}} + \delta \mathcal{L}_{\text{ext}}^{l_{yy}} + \delta \mathcal{L}_{\text{ext}}^{l_{yx}} + \delta \mathcal{L}_{\text{ext}}^{l_{yz}}, \quad (4.32)$$

being:

$$\begin{aligned} \delta \mathcal{L}_{\text{ext}}^{l_{zx}} &= \delta q_{xi\tau} I_i^{l_{zx}} F_\tau(\hat{y}, \hat{z}), & \delta \mathcal{L}_{\text{ext}}^{l_{yx}} &= \delta q_{xi\tau} I_i^{l_{yx}} F_\tau(\hat{y}, \hat{z}), \\ \delta \mathcal{L}_{\text{ext}}^{l_{yy}} &= \delta q_{yi\tau} I_i^{l_{yy}} F_\tau(\hat{y}, \hat{z}), & \delta \mathcal{L}_{\text{ext}}^{l_{zy}} &= \delta q_{yi\tau} I_i^{l_{zy}} F_\tau(\hat{y}, \hat{z}), \end{aligned} \quad (4.33)$$

$$\begin{aligned} \delta \mathcal{L}_{\text{ext}}^{l_{zz}} &= \delta q_{zi\tau} I_i^{l_{zz}} F_\tau(\hat{y}, \hat{z}), & \delta \mathcal{L}_{\text{ext}}^{l_{yz}} &= \delta q_{zi\tau} I_i^{l_{yz}} F_\tau(\hat{y}, \hat{z}) \\ I_i^{l_{ij}} &= \int_{l_e} N_i l_{ij} dx. \end{aligned} \quad (4.34)$$

As far as the surface load $\delta \mathcal{L}_{\text{ext}}^{p_{ij}}$ is concerned, the following contributions are considered:

$$\delta \mathcal{L}_{\text{ext}}^{p_{ij}} = \delta \mathcal{L}_{\text{ext}}^{p_{zz}} + \delta \mathcal{L}_{\text{ext}}^{p_{zx}} + \delta \mathcal{L}_{\text{ext}}^{p_{zy}} + \delta \mathcal{L}_{\text{ext}}^{p_{yy}} + \delta \mathcal{L}_{\text{ext}}^{p_{yx}} + \delta \mathcal{L}_{\text{ext}}^{p_{yz}}, \quad (4.35)$$

being:

$$\begin{aligned} \delta \mathcal{L}_{\text{ext}}^{p_{zx}} &= \delta q_{xi\tau} I_i^{p_{zx}} E_\tau^{\bar{z}}, & \delta \mathcal{L}_{\text{ext}}^{p_{yx}} &= \delta q_{xi\tau} I_i^{p_{yx}} E_\tau^{\bar{y}}, \\ \delta \mathcal{L}_{\text{ext}}^{p_{yy}} &= \delta q_{yi\tau} I_i^{p_{yy}} E_\tau^{\bar{y}}, & \delta \mathcal{L}_{\text{ext}}^{p_{zy}} &= \delta q_{yi\tau} I_i^{p_{zy}} E_\tau^{\bar{z}}, \\ \delta \mathcal{L}_{\text{ext}}^{p_{zz}} &= \delta q_{zi\tau} I_i^{p_{zz}} E_\tau^{\bar{z}}, & \delta \mathcal{L}_{\text{ext}}^{p_{yz}} &= \delta q_{zi\tau} I_i^{p_{yz}} E_\tau^{\bar{y}} \end{aligned} \quad (4.36)$$

and:

$$I_i^{p_{ij}} = \int_{l_e} N_i p_{ij} dx \quad (4.37)$$

$$\begin{aligned} E_\tau^{\bar{z}} &= \int_{\bar{y}_1}^{\bar{y}_2} F_\tau(y, \bar{z}) dy, \\ E_\tau^{\bar{y}} &= \int_{\bar{z}_1}^{\bar{z}_2} F_\tau(\bar{y}, z) dz. \end{aligned} \quad (4.38)$$

where the over-lined cross-sectional coordinates \bar{y} and \bar{z} are the limits of the load area. Once the number of nodes per element N_n^e and the approximation order N are fixed, the global element stiffness matrix, thermal and mechanical load vector can be obtained straightforwardly by assembling the respective fundamental nuclei given in Eq. (4.25), Eq. (4.28), (4.33) and (4.36). The assembly procedure is a basic concept of Unified Formulation and it can be found in several textbooks discussing the UF-based modeling approach, such as [35].

Chapter 5

Extension of UF-based Approach to Curved Beam Structures

5.1 Introduction

The formulation presented in the previous chapter is limited to the study of initially straight beams. By means of straight finite elements, structures with a curved longitudinal axis could be also accurately modeled, as long as a very refined discretization able to minimize the geometrical approximation error is considered. Moreover, this modeling strategy is commonly adopted in the majority of commercial software finite elements dealing with curved geometries. Clearly, additional computational costs deriving from a refined discretization can be easily avoided if curvature is inherently accounted for within the geometrical relations of the finite element formulation. In order to preserve the computational advantages provided by the UF approach even when dealing with curved beam structures, the extension of UF-based one-dimensional models to account for curvature of the beam reference axis is discussed in this chapter. The adopted local Frenet-Serret coordinate system is introduced in Section 5.2. Displacement field, strain-displacement relations and Hooke's law are reported in Section 5.3. In Section 5.4, by writing the Principle of Virtual Displacements in the local reference system, the governing differential equations are derived and a strong form Navier-type analytical solution based on a harmonic displacement field is obtained. A weak form finite element solution is also derived by approximating the axial variation of the displacement field via classical one-dimensional Lagrangian shape functions. The fundamental nuclei of the stiffness matrix and load vector, featuring additional curvature-dependent terms with respect to the straight beam formulation, are provided and, finally, a technique based on MITC for tackling locking phenomena typical of curved elements is discussed. The research presented in this chapter has been previously published in [132, 119].

5.2 Preliminaries

In order to study a generic curved beam-like structure, the Frenet-Serret coordinate system shown in Figure 5.1 is introduced. It is defined by the orthonormal vector basis $\{\mathbf{t}, \mathbf{n}, \mathbf{b}\}$, being \mathbf{t} the tangent, \mathbf{n} the principal normal and \mathbf{b} the principal bi-normal vectors, respectively:

$$\mathbf{t}(s) = \frac{d\mathbf{r}(s)}{ds} \quad \mathbf{n}(s) = \frac{\frac{d^2\mathbf{r}(s)}{ds^2}}{\left\| \frac{d^2\mathbf{r}(s)}{ds^2} \right\|} \quad \mathbf{b}(s) = \mathbf{t}(s) \times \mathbf{n}(s) \quad (5.1)$$

$\mathbf{r}(s) \in \mathbb{R}^3$ is the vector defining a generic unit-speed curve, i.e. $\|\mathbf{t}(s)\| = 1$, being s the independent arc-length variable. The Frenet-Serret formulae provide the derivatives of

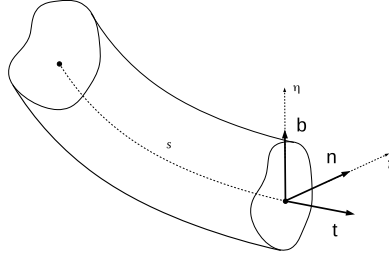


Figure 5.1: Three-dimensional curved beam-like structure and Frenet-Serret reference system.

$\{\mathbf{t}, \mathbf{n}, \mathbf{b}\}$ with respect to the arc-length coordinate s :

$$\frac{d}{ds} \begin{Bmatrix} \mathbf{t} \\ \mathbf{n} \\ \mathbf{b} \end{Bmatrix} = \begin{bmatrix} 0 & \kappa & 0 \\ -\kappa & 0 & \tau \\ 0 & -\tau & 0 \end{bmatrix} \begin{Bmatrix} \mathbf{t} \\ \mathbf{n} \\ \mathbf{b} \end{Bmatrix} \quad (5.2)$$

where κ is the beam axis curvature, defined as:

$$\kappa(s) = \left\| \frac{d^2\mathbf{r}(s)}{ds^2} \right\| \quad (5.3)$$

and τ is the geometric torsion of the curve, given by:

$$\tau(s) = \frac{d\mathbf{n}(s)}{ds} \cdot \mathbf{b}(s) \quad (5.4)$$

In some cases, the reference system $\{\mathbf{e}_1, \mathbf{e}_2, \mathbf{e}_3\}$ could be needed, being $\mathbf{e}_1 \equiv \mathbf{t}$ and $\mathbf{e}_2, \mathbf{e}_3$ the unit vectors in the direction of the cross-section's principal axes, which are rotated

with respect to \mathbf{n} and \mathbf{b} by an angle θ :

$$\begin{Bmatrix} \mathbf{e}_1 \\ \mathbf{e}_2 \\ \mathbf{e}_3 \end{Bmatrix} = \begin{bmatrix} 1 & 0 & 0 \\ 0 & \cos \theta & \sin \theta \\ 0 & -\sin \theta & \cos \theta \end{bmatrix} \begin{Bmatrix} \mathbf{t} \\ \mathbf{n} \\ \mathbf{b} \end{Bmatrix} \quad (5.5)$$

The Frenet-Serret formulae in Eq. (5.2) applied to the reference system defined in Eq. (5.5) read:

$$\frac{d}{ds} \begin{Bmatrix} \mathbf{e}_1 \\ \mathbf{e}_2 \\ \mathbf{e}_3 \end{Bmatrix} = \begin{bmatrix} 0 & \kappa_2 & -\kappa_1 \\ -\kappa_2 & 0 & \kappa_3 \\ \kappa_1 & -\kappa_3 & 0 \end{bmatrix} \begin{Bmatrix} \mathbf{e}_1 \\ \mathbf{e}_2 \\ \mathbf{e}_3 \end{Bmatrix} \quad (5.6)$$

being $\kappa_1 = \kappa \sin \theta$, $\kappa_2 = \kappa \cos \theta$ and $\kappa_3 = \tau + \frac{d\theta}{ds}$.

Finally, a generic point P within the beam volume can be defined by the following position vector:

$$\mathbf{r}_P = \mathbf{r}(s) + \xi \mathbf{e}_2 + \eta \mathbf{e}_3 \quad (5.7)$$

where $\{s, \xi, \eta\}$ are the coordinates associated to the coordinate system $\{\mathbf{e}_1, \mathbf{e}_2, \mathbf{e}_3\}$. The determinant of the metric tensor g and the infinitesimal volume dV can be derived from Eq. (5.7), as shown in Washizu [167]:

$$g = (1 - \xi \kappa_2 + \eta \kappa_1)^2 \quad (5.8)$$

$$dV = H ds d\xi d\eta \quad (5.9)$$

where $H = \sqrt{g}$.

The cross-section's principal axes defined by \mathbf{e}_2 and \mathbf{e}_3 are assumed to be aligned with the principal normal and bi-normal vectors \mathbf{n} and \mathbf{b} , i.e. $\theta = 0^\circ$ and, therefore, $\kappa_1 = 0$, $\kappa_2 = \kappa$ and $\kappa_3 = \tau$. Furthermore, the following assumptions are made: $\kappa = 1/R$ and $\tau = 0$, i.e. a beam axis with a constant radius of curvature R and no twist is considered.

5.3 Geometrical and constitutive relations in local coordinates

The vectors of displacements \mathbf{u} , strains $\boldsymbol{\varepsilon}$ and stresses $\boldsymbol{\sigma}$ are expressed in the local coordinate system $\{s, \xi, \eta\}$ and they are grouped as follows:

$$\mathbf{u}^T(s, \xi, \eta) = \{ u_s(s, \xi, \eta) \quad u_\xi(s, \xi, \eta) \quad u_\eta(s, \xi, \eta) \} \quad (5.10)$$

$$\boldsymbol{\varepsilon}^T = \{ \varepsilon_{ss} \quad \varepsilon_{\xi\xi} \quad \varepsilon_{\eta\eta} \quad \varepsilon_{\xi\eta} \quad \varepsilon_{s\eta} \quad \varepsilon_{s\xi} \} \quad (5.11)$$

$$\boldsymbol{\sigma}^T = \{ \sigma_{ss} \quad \sigma_{\xi\xi} \quad \sigma_{\eta\eta} \quad \sigma_{\xi\eta} \quad \sigma_{s\eta} \quad \sigma_{s\xi} \} \quad (5.12)$$

Strain-displacement equations

The linear strain-displacement relations for a curved beam-like structure are given by:

$$\begin{aligned}
 \varepsilon_{ss} &= \frac{1}{H} \left(\frac{\partial u_s}{\partial s} - \kappa u_\xi \right) \\
 \varepsilon_{\xi\xi} &= \frac{\partial u_\xi}{\partial \xi} \\
 \varepsilon_{\eta\eta} &= \frac{\partial u_\eta}{\partial \eta} \\
 \varepsilon_{\xi\eta} &= \frac{\partial u_\xi}{\partial \eta} + \frac{\partial u_\eta}{\partial \xi} \\
 \varepsilon_{s\eta} &= \frac{1}{H} \left(\frac{\partial u_\eta}{\partial s} \right) + \frac{\partial u_s}{\partial \eta} \\
 \varepsilon_{s\xi} &= \frac{1}{H} \left(\frac{\partial u_\xi}{\partial s} + \kappa u_s \right) + \frac{\partial u_s}{\partial \xi}
 \end{aligned} \tag{5.13}$$

These latter equations, in a matrix form, read:

$$\boldsymbol{\varepsilon} = (\mathbf{D}_s + \mathbf{D}_\Omega + \mathbf{D}_\kappa) \mathbf{u} \tag{5.14}$$

where \mathbf{D}_s and \mathbf{D}_Ω are differential operators with respect to the longitudinal coordinate s and cross-sectional coordinates $\{\xi, \eta\}$, respectively, and \mathbf{D}_κ accounts for the terms depending on the axis curvature κ :

$$\mathbf{D}_s = \begin{bmatrix} \frac{1}{H} \frac{\partial}{\partial s} & 0 & 0 \\ 0 & 0 & 0 \\ 0 & 0 & 0 \\ 0 & 0 & 0 \\ 0 & 0 & \frac{1}{H} \frac{\partial}{\partial s} \\ 0 & \frac{1}{H} \frac{\partial}{\partial s} & 0 \end{bmatrix} \quad \mathbf{D}_\Omega = \begin{bmatrix} 0 & 0 & 0 \\ 0 & \frac{\partial}{\partial \xi} & 0 \\ 0 & 0 & \frac{\partial}{\partial \eta} \\ 0 & \frac{\partial}{\partial \eta} & \frac{\partial}{\partial \xi} \\ \frac{\partial}{\partial \eta} & 0 & 0 \\ \frac{\partial}{\partial \xi} & 0 & 0 \end{bmatrix} \quad \mathbf{D}_\kappa = \begin{bmatrix} 0 & -\frac{\kappa}{H} & 0 \\ 0 & 0 & 0 \\ 0 & 0 & 0 \\ 0 & 0 & 0 \\ 0 & 0 & 0 \\ \frac{\kappa}{H} & 0 & 0 \end{bmatrix} \tag{5.15}$$

UF-based displacement field

The a-priori approximation of the three-dimensional displacement field based on Unified Formulation in local coordinates (s, ξ, η) reads:

$$\mathbf{u}(s, \xi, \eta) = F_\tau(\xi, \eta) \mathbf{u}_\tau(s) \quad \text{with } \tau = 1, 2, \dots, N_u \tag{5.16}$$

being $\mathbf{u}_\tau = \{u_{s\tau} \ u_{\xi\tau} \ u_{\eta\tau}\}^T$.

By replacing Eq. (5.16) into Eq. (5.13), the following expressions are obtained:

$$\begin{aligned} \varepsilon_{ss} &= \frac{F_\tau}{H} (u_{s\tau,s} - \kappa u_{\xi\tau}) \\ \varepsilon_{\xi\xi} &= F_{\tau,\xi} u_{\xi\tau} \\ \varepsilon_{\eta\eta} &= F_{\tau,\eta} u_{\eta\tau} \\ \varepsilon_{\xi\eta} &= F_{\tau,\eta} u_{\xi\tau} + F_{\tau,\xi} u_{\eta\tau} \\ \varepsilon_{s\eta} &= \frac{1}{H} F_\tau u_{\eta\tau,s} + F_{\tau,\eta} u_{s\tau} \\ \varepsilon_{s\xi} &= \frac{F_\tau}{H} (u_{\xi\tau,s} + \kappa u_{s\tau}) + F_{\tau,\xi} u_{s\tau} \end{aligned} \quad (5.17)$$

where the subscripts ‘, s’ ‘, ξ ’ and ‘, η ’ stand for derivation versus the respective coordinate.

Hooke’s law

The constitutive relation for a generic k-th layer made of an orthotropic linear elastic material reads:

$$\boldsymbol{\sigma} = \mathbf{C}^k \boldsymbol{\varepsilon} \quad (5.18)$$

where \mathbf{C}^k is the material elastic stiffness matrix:

$$\mathbf{C}^k = \begin{bmatrix} C_{11}^k & C_{12}^k & C_{13}^k & 0 & 0 & C_{16}^k \\ C_{12}^k & C_{22}^k & C_{23}^k & 0 & 0 & C_{26}^k \\ C_{13}^k & C_{23}^k & C_{33}^k & 0 & 0 & C_{36}^k \\ 0 & 0 & 0 & C_{44}^k & C_{45}^k & 0 \\ 0 & 0 & 0 & C_{45}^k & C_{55}^k & 0 \\ C_{16}^k & C_{26}^k & C_{36}^k & 0 & 0 & C_{66}^k \end{bmatrix} \quad (5.19)$$

and the expressions of the material coefficients C_{ij}^k has been already discussed in Section 4.3.

5.4 Governing equations and fundamental nuclei

The PVD is used in order to derive the governing equations for the case of a static mechanical analysis:

$$\delta \mathcal{L}_{\text{int}} = \delta \mathcal{L}_{\text{ext}} \quad (5.20)$$

5.4.1 Strong form Navier-type solution

In the presented analytical solution, by means of the PVD, governing differential equations and boundary conditions are obtained. The virtual variation of the internal work is defined as:

$$\delta \mathcal{L}_{\text{int}} = \int_l \int_{\Omega} \delta \epsilon^T \sigma H(\xi) ds d\xi d\eta \quad (5.21)$$

By substituting the strains-displacements relations in Eqs. (5.14), the constitutive law in Eqs. (5.18) and the displacements field in Eq. (5.16), the following compact form of the virtual variation of the internal work in terms of displacements can be obtained:

$$\delta \mathcal{L}_{\text{int}} = \int_l \delta \mathbf{u}_t^T \bar{\mathbf{K}}^{\tau t} \mathbf{u}_\tau ds + \delta \mathbf{u}_t^T \bar{\mathbf{\Pi}}^{\tau t} \mathbf{u}_\tau \Big|_{s=0}^{s=l} \quad (5.22)$$

$\bar{\mathbf{K}}^{\tau t}$ and $\bar{\mathbf{\Pi}}^{\tau t}$ are the fundamental nuclei of the differential stiffness matrix and boundary conditions, respectively.

As far as the virtual variation of the external work is concerned, only the contribution given by a transverse surface load components p_ξ applied at $\xi = \bar{\xi}$ over an area $A_\xi : [0, l] \times [\bar{\eta}_1, \bar{\eta}_2]$ and p_η applied at $\eta = \bar{\eta}$ over the domain $A_\eta : [0, l] \times [\bar{\xi}_1, \bar{\xi}_2]$ are reported below, for the sake of brevity:

$$\delta \mathcal{L}_{\text{ext}} = \int_l \left(p_\xi E_t^{\bar{\xi}} \delta u_{\xi t} + p_\eta E_t^{\bar{\eta}} \delta u_{\eta t} \right) ds \quad (5.23)$$

being:

$$\begin{aligned} E_t^{\bar{\xi}} &= H(\bar{\xi}) \int_{\bar{\eta}_1}^{\bar{\eta}_2} F_t(\bar{\xi}, \eta) d\eta \\ E_t^{\bar{\eta}} &= \int_{\bar{\xi}_1}^{\bar{\xi}_2} H(\xi) F_t(\bar{\eta}, \xi) d\xi \end{aligned} \quad (5.24)$$

The variation of the external work done by other surface load components can be derived in a similar manner. In the framework of a Navier-type closed form analytical solution, in order to solve the differential governing equations and satisfy simply-supported boundary conditions, the following harmonic kinematic field is assumed along the longitudinal direction s :

$$\begin{aligned} u_{s\tau} &= U_{s\tau} \cos(\alpha s) \\ u_{\xi\tau} &= U_{\xi\tau} \sin(\alpha s) \\ u_{\eta\tau} &= U_{\eta\tau} \sin(\alpha s) \end{aligned} \quad (5.25)$$

being $\alpha = \frac{m\pi}{l}$, m the number of half-waves along the curved beam axis and $\{U_{s\tau}, U_{\xi\tau}, U_{\eta\tau}\}$ the unknown vector. A harmonic variation along the axis is also

assumed for the external loads p_ξ and p_η :

$$\begin{aligned} p_\xi &= P_\xi \sin(\alpha s) \\ p_\eta &= P_\eta \sin(\alpha s) \end{aligned} \quad (5.26)$$

Under the assumption of a linear load-displacement relation, by means of Fourier's series expansion, any loading profile can be obtained from Eq. (5.26), as shown in Carrera and Giunta [32, 33]). The explicit form of the differential stiffness matrix $\bar{\mathbf{K}}^{tt}$ defined in Eq. (5.22) is given by:

$$\begin{aligned} \bar{K}_{ss}^{tt} &= -J_{\tau t \frac{1}{H}}^{11} \frac{\partial^2}{\partial s^2} + J_{\tau, \eta^t, \eta}^{55} + J_{\tau, \xi^t, \xi}^{66} + \kappa \left(J_{\tau t, \xi}^{66} + J_{\tau, \xi^t}^{66} \right) + \kappa^2 J_{\tau t \frac{1}{H}}^{66} \\ \bar{K}_{s\xi}^{tt} &= \left[-J_{\tau, \xi^t}^{12} + J_{\tau t, \xi}^{66} + \kappa \left(J_{\tau t \frac{1}{H}}^{66} + J_{\tau t \frac{1}{H}}^{11} \right) \right] \frac{\partial}{\partial s} \\ \bar{K}_{s\eta}^{tt} &= \left(-J_{\tau, \eta^t}^{13} + J_{\tau t, \eta}^{55} \right) \frac{\partial}{\partial s} \\ \bar{K}_{\xi s}^{tt} &= \left[J_{\tau t, \xi}^{12} - J_{\tau, \xi^t}^{66} - \kappa \left(J_{\tau t \frac{1}{H}}^{66} + J_{\tau t \frac{1}{H}}^{11} \right) \right] \frac{\partial}{\partial s} \\ \bar{K}_{\xi\xi}^{tt} &= J_{\tau, \xi^t, \xi}^{22} + J_{\tau, \eta^t, \eta}^{44} - J_{\tau t \frac{1}{H}}^{66} \frac{\partial^2}{\partial s^2} - \kappa \left(J_{\tau t, \xi}^{12} + J_{\tau, \xi^t}^{12} \right) + \kappa^2 J_{\tau t \frac{1}{H}}^{11} \\ \bar{K}_{\xi\eta}^{tt} &= J_{\tau, \eta^t, \xi}^{23} + J_{\tau, \xi^t, \eta}^{44} - \kappa J_{\tau, \eta^t}^{13} \\ \bar{K}_{\eta s}^{tt} &= \left(J_{\tau t, \eta}^{13} - J_{\tau, \eta^t}^{55} \right) \frac{\partial}{\partial s} \\ \bar{K}_{\eta\xi}^{tt} &= J_{\tau, \xi^t, \eta}^{23} + J_{\tau, \eta^t, \xi}^{44} - \kappa J_{\tau t, \eta}^{13} \\ \bar{K}_{\eta\eta}^{tt} &= J_{\tau, \eta^t, \eta}^{33} + J_{\tau, \xi^t, \xi}^{44} - J_{\tau t \frac{1}{H}}^{55} \frac{\partial^2}{\partial s^2} \end{aligned} \quad (5.27)$$

where $J_{\tau(\phi)^t(\psi)}^{gh}$, $J_{\tau(\phi)^t(\psi)H}^{gh}$ and $J_{\tau(\phi)^t(\psi)\frac{1}{H}}^{gh}$ are the following cross-section integrals:

$$\begin{aligned} J_{\tau(\phi)^t(\psi)}^{gh} &= \int_{\Omega} C_{gh}^k F_{\tau(\phi)} F_{t(\psi)} d\xi d\eta \\ J_{\tau(\phi)^t(\psi)H}^{gh} &= \int_{\Omega} C_{gh}^k F_{\tau(\phi)} F_{t(\psi)} H d\xi d\eta \\ J_{\tau(\phi)^t(\psi)\frac{1}{H}}^{gh} &= \int_{\Omega} C_{gh}^k F_{\tau(\phi)} F_{t(\psi)} \frac{1}{H} d\xi d\eta \end{aligned} \quad (5.28)$$

The components of the differential matrix related to the boundary conditions $\bar{\mathbf{\Pi}}^{\tau t}$ are:

$$\begin{aligned}
 \bar{\Pi}_{ss}^{\tau t} &= J_{\tau t \frac{1}{H}}^{11} \frac{\partial}{\partial s} & \bar{\Pi}_{s\xi}^{\tau t} &= J_{\tau, \xi t}^{12} - \kappa J_{\tau t \frac{1}{H}}^{11} & \bar{\Pi}_{s\eta}^{\tau t} &= J_{\tau, \eta t}^{13} \\
 \bar{\Pi}_{\xi s}^{\tau t} &= J_{\tau, \xi t}^{66} + \kappa J_{\tau t \frac{1}{H}}^{66} & \bar{\Pi}_{\xi\xi}^{\tau t} &= J_{\tau t \frac{1}{H}}^{66} \frac{\partial}{\partial s} & \bar{\Pi}_{\xi\eta}^{\tau t} &= 0 \\
 \bar{\Pi}_{\eta s}^{\tau t} &= J_{\tau, \eta t}^{55} & \bar{\Pi}_{\eta\xi}^{\tau t} &= 0 & \bar{\Pi}_{\eta\eta}^{\tau t} &= J_{\tau t \frac{1}{H}}^{55} \frac{\partial}{\partial s}
 \end{aligned} \tag{5.29}$$

Therefore, the explicit expression for the boundary conditions $\delta \mathbf{u}_t^T \bar{\mathbf{\Pi}}^{\tau t} \mathbf{u}_\tau \big|_{s=0}^{s=l}$ is given by:

$$\begin{aligned}
 \delta u_{st} \left[J_{\tau t \frac{1}{H}}^{11} u_{s\tau, s} + \left(J_{\tau, \xi t}^{12} - \kappa J_{\tau t \frac{1}{H}}^{11} \right) u_{\xi\tau} + J_{\tau, \eta t}^{13} u_{\eta\tau} \right] \bigg|_{s=0}^{s=l} &= 0 \\
 \delta u_{\xi t} \left[\left(J_{\tau, \xi t}^{66} + \kappa J_{\tau t \frac{1}{H}}^{66} \right) u_{s\tau} + J_{\tau t \frac{1}{H}}^{66} u_{\xi\tau, s} \right] \bigg|_{s=0}^{s=l} &= 0 \\
 \delta u_{\eta t} \left[J_{\tau, \eta t}^{55} u_{s\tau} + J_{\tau t \frac{1}{H}}^{55} u_{\eta\tau, s} \right] \bigg|_{s=0}^{s=l} &= 0
 \end{aligned} \tag{5.30}$$

Eqs. (5.30) are identically satisfied by the assumed displacement profile, Eqs. (5.25), for simply supported beams, since:

$$\begin{aligned}
 u_{s\tau, s}(0) &= u_{s\tau, s}(l) = 0 \\
 u_{\xi\tau}(0) &= u_{\xi\tau}(l) = 0 \\
 u_{\eta\tau}(0) &= u_{\eta\tau}(l) = 0
 \end{aligned} \tag{5.31}$$

$$\begin{aligned}
 \delta u_{st, s}(0) &= \delta u_{st, s}(l) = 0 \\
 \delta u_{\xi t}(0) &= \delta u_{\xi t}(l) = 0 \\
 \delta u_{\eta t}(0) &= \delta u_{\eta t}(l) = 0
 \end{aligned} \tag{5.32}$$

The fundamental nuclei of the algebraic stiffness matrix $\mathbf{K}^{\tau t}$ and of the load vector \mathbf{P}^t are obtained by substituting Eq. (5.25) and (5.26) into the governing differential equations.

The components of the algebraic stiffness matrix fundamental nucleus $\mathbf{K}^{\tau t}$ are:

$$\begin{aligned}
 K_{ss}^{\tau t} &= \alpha^2 J_{\tau t \frac{1}{H}}^{11} + J_{\tau, \eta^t, \eta}^{55} H + J_{\tau, \xi^t, \xi}^{66} H + \kappa \left(J_{\tau t, \xi}^{66} + J_{\tau, \xi^t}^{66} \right) + \kappa^2 J_{\tau t \frac{1}{H}}^{66} \\
 K_{s\xi}^{\tau t} &= \alpha \left[-J_{\tau, \xi^t}^{12} + J_{\tau t, \xi}^{66} + \kappa \left(J_{\tau t \frac{1}{H}}^{66} + J_{\tau t \frac{1}{H}}^{11} \right) \right] \\
 K_{s\eta}^{\tau t} &= \alpha \left(-J_{\tau, \eta^t}^{13} + J_{\tau t, \eta}^{55} \right) \\
 K_{\xi s}^{\tau t} &= \alpha \left[-J_{\tau t, \xi}^{12} + J_{\tau, \xi^t}^{66} + \kappa \left(J_{\tau t \frac{1}{H}}^{66} + J_{\tau t \frac{1}{H}}^{11} \right) \right] \\
 K_{\xi\xi}^{\tau t} &= J_{\tau, \xi^t, \xi}^{22} H + J_{\tau, \eta^t, \eta}^{44} H + \alpha^2 J_{\tau t \frac{1}{H}}^{66} - \kappa \left(J_{\tau t, \xi}^{12} + J_{\tau, \xi^t}^{12} \right) + \kappa^2 J_{\tau t \frac{1}{H}}^{11} \\
 K_{\xi\eta}^{\tau t} &= J_{\tau, \eta^t, \xi}^{23} H + J_{\tau, \xi^t, \eta}^{44} H - \kappa J_{\tau, \eta^t}^{13} \\
 K_{\eta s}^{\tau t} &= \alpha \left(-J_{\tau t, \eta}^{13} + J_{\tau, \eta^t}^{55} \right) \\
 K_{\eta\xi}^{\tau t} &= J_{\tau, \xi^t, \eta}^{23} H + J_{\tau, \eta^t, \xi}^{44} H - \kappa J_{\tau t, \eta}^{13} \\
 K_{\eta\eta}^{\tau t} &= J_{\tau, \eta^t, \eta}^{33} H + J_{\tau, \xi^t, \xi}^{44} H + \alpha^2 J_{\tau t \frac{1}{H}}^{55}
 \end{aligned} \tag{5.33}$$

Once the expansion order N of the UF-based displacement field has been chosen, by assembling the fundamental nucleus of Eqs. (5.33) for each term τ and t , the global stiffness matrix can be obtained.

Finally, according to Eq. (5.23), the non-zero components of the load vector fundamental nucleus \mathbf{P}^t are:

$$\begin{aligned}
 P_{\xi}^t &= p_{\xi} E_t^{\bar{\xi}} \\
 P_{\eta}^t &= p_{\eta} E_t^{\bar{\eta}}
 \end{aligned} \tag{5.34}$$

5.4.2 Weak form finite elements solution

In the framework of finite element method, the vector $\mathbf{u}_{\tau}(s)$ defined in Eq. (5.16) is interpolated along the curved axis by means of standard one-dimensional Lagrangian shape functions N_i :

$$\mathbf{u}_{\tau}(s) = N_i(s) \mathbf{q}_{\tau i} \quad \text{with } \tau = 1, 2, \dots, N_u \text{ and } i = 1, \dots, N_n^e \tag{5.35}$$

The subscript i stands for an implicit summation from 1 to the number of nodes per element N_n^e and $\mathbf{q}_{\tau i}$ is the unknown vector. The virtual variation of the internal virtual work within the element is given by:

$$\delta \mathcal{L}_{\text{int}} = \int_{l^e} \int_{\Omega} \delta \epsilon^T \boldsymbol{\sigma} H(\xi) ds d\xi d\eta \tag{5.36}$$

Upon substitution of the finite elements discretization given by Eq. (5.35), together with geometrical relations (5.14), constitutive equation (5.18) and UF-based displacement field (5.16) within Eq. (5.36), the virtual variation of the internal work can be written as:

$$\delta \mathcal{L}_{\text{int}} = \delta \mathbf{q}_{ij}^T \mathbf{K}_e^{\tau tij} \mathbf{q}_{\tau i} \quad (5.37)$$

$\mathbf{K}_e^{\tau tij} \in \mathbb{R}^{3 \times 3}$ is the fundamental nucleus of the element stiffness matrix, whose components are:

$$\begin{aligned} K_{ess}^{\tau tij} &= I_{i,sj,s} J_{\tau t \frac{1}{H}}^{11} + I_{ij} \left(J_{\tau, \eta^t, \eta H}^{55} + J_{\tau, \xi^t, \xi H}^{66} \right) + \kappa I_{ij} \left(J_{\tau t, \xi}^{66} + J_{\tau, \xi^t}^{66} \right) + \kappa^2 I_{ij} J_{\tau t \frac{1}{H}}^{66} \\ K_{e\xi\xi}^{\tau tij} &= I_{ij,s} J_{\tau, \xi^t}^{12} + I_{i,sj} J_{\tau t, \xi}^{66} + \kappa \left(I_{i,sj} J_{\tau t \frac{1}{H}}^{66} - I_{ij,s} J_{\tau t \frac{1}{H}}^{11} \right) \\ K_{e\eta\eta}^{\tau tij} &= I_{ij,s} J_{\tau, \eta^t}^{13} + I_{i,sj} J_{\tau t, \eta}^{55} \\ K_{e\xi s}^{\tau tij} &= I_{i,sj} J_{\tau t, \xi}^{12} + I_{ij,s} J_{\tau, \xi^t}^{66} + \kappa \left(I_{ij,s} J_{\tau t \frac{1}{H}}^{66} - I_{i,sj} J_{\tau t \frac{1}{H}}^{11} \right) \\ K_{e\xi\xi}^{\tau tij} &= I_{ij} \left(J_{\tau, \xi^t, \xi H}^{22} + J_{\tau, \eta^t, \eta H}^{44} \right) + I_{i,sj,s} J_{\tau t \frac{1}{H}}^{66} - \kappa I_{ij} \left(J_{\tau t, \xi}^{12} + J_{\tau, \xi^t}^{12} \right) + \kappa^2 I_{ij} J_{\tau t \frac{1}{H}}^{11} \\ K_{e\xi\eta}^{\tau tij} &= I_{ij} \left(J_{\tau, \eta^t, \xi H}^{23} + J_{\tau, \xi^t, \eta H}^{44} \right) - \kappa I_{ij} J_{\tau, \eta^t}^{13} \\ K_{e\eta s}^{\tau tij} &= I_{i,sj} J_{\tau t, \eta}^{13} + I_{ij,s} J_{\tau, \eta^t}^{55} \\ K_{e\eta\xi}^{\tau tij} &= I_{ij} \left(J_{\tau, \xi^t, \eta H}^{23} + J_{\tau, \eta^t, \xi H}^{44} \right) - \kappa I_{ij} J_{\tau t, \eta}^{13} \\ K_{e\eta\eta}^{\tau tij} &= I_{ij} \left(J_{\tau, \eta^t, \eta H}^{33} + J_{\tau, \xi^t, \xi H}^{44} \right) + I_{i,sj,s} J_{\tau t \frac{1}{H}}^{55} \end{aligned} \quad (5.38)$$

being $I_{i(s)j(s)}$ the following integral along the beam longitudinal direction s :

$$I_{i(s)j(s)} = \int_{l_e} N_{i(s)} N_{j(s)} ds \quad (5.39)$$

Similarly to the procedure for the closed-form solution, in order to derive the element stiffness matrix of a N th-order curved beam element, $\mathbf{K}_e^{\tau tij}$ has to be assembled over the indexes τ, t, i and j , according to the procedure explained in Carrera et al. [35].

Finally, the virtual variation of the external work within the element is defined as the summation of the following contributions:

$$\delta \mathcal{L}_{\text{ext}} = \delta \mathcal{L}_{\text{ext}}^F + \delta \mathcal{L}_{\text{ext}}^{l_\xi} + \delta \mathcal{L}_{\text{ext}}^{l_\eta} + \delta \mathcal{L}_{\text{ext}}^{p_\xi} + \delta \mathcal{L}_{\text{ext}}^{p_\eta} \quad (5.40)$$

where:

$$\delta \mathcal{L}_{\text{ext}}^F = F_t (\xi_F, \eta_F) N_j (s_F) \delta \mathbf{q}_{ij}^T \mathbf{F} \quad (5.41)$$

is the contribution of a load \mathbf{F} concentrated at the location (s_F, ξ_F, η_F) ,

$$\delta \mathcal{L}_{\text{ext}}^{l_\xi} = \delta q_{\xi t j} l_\xi I_j F_t(\xi_l, \eta_l) H(\xi_l), \quad \delta \mathcal{L}_{\text{ext}}^{l_\eta} = \delta q_{\eta t j} l_\eta I_j F_t(\xi_l, \eta_l) H(\xi_l) \quad (5.42)$$

are the contributions given by the line loads l_ξ and l_η acting at (ξ_l, η_l) and

$$\delta \mathcal{L}_{\text{ext}}^{p_\xi} = \delta q_{\xi t j} p_\xi I_j E_t^\xi, \quad \delta \mathcal{L}_{\text{ext}}^{p_\eta} = \delta q_{\eta t j} p_\eta I_j E_t^\eta \quad (5.43)$$

being the contributions given by the transverse pressure loadings p_ξ and p_η , where:

$$I_j = \int_{I_e} N_j(s) ds \quad (5.44)$$

MITC-based locking correction

When dealing with curved beam elements, locking phenomena are a major issue that needs to be tackled to avoid detrimental effects on the accuracy and performance of the results, especially for slender structures. A correction technique based on Mixed Interpolation of Tensorial Components (MITC), see Bathe and Dvorkin [16, 15], is used. The interpolation of axial and shear strains along the curved beam axis reads:

$$\begin{aligned} \bar{\epsilon}_{ss} &= \bar{N}_m \epsilon_{ss}^m \\ \bar{\epsilon}_{s\eta} &= \bar{N}_m \epsilon_{s\eta}^m \\ \bar{\epsilon}_{s\xi} &= \bar{N}_m \epsilon_{s\xi}^m \end{aligned} \quad (5.45)$$

Subscript m implicitly means summation from 1 to $N_n^e - 1$, \bar{N}_m are the assumed interpolating functions and ϵ_{ss}^m , $\epsilon_{s\eta}^m$ and $\epsilon_{s\xi}^m$ are the axial and shear strains computed at the m -th tying point. The explicit expressions for the assumed functions \bar{N}_m and tying points location used in the proposed framework can be found in [119] for two-nodes, three-nodes and four-nodes elements. After taking into account the strains interpolation given by Eq. (5.45) within the constitutive equation (5.18) and within the definition of the element strain energy (5.36), the stiffness matrix fundamental nucleus of the

MITC one-dimensional element reads:

$$\begin{aligned}
 K_{ess}^{\tau ij} &= I_{\bar{i},s\bar{j},s} J_{\tau t \frac{1}{H}}^{11} + I_{ij} \left(J_{\tau,\eta^t,\eta H}^{55} + J_{\tau,\xi^t,\xi H}^{66} \right) + \kappa I_{ij} \left(J_{\tau t,\xi}^{66} + J_{\tau,\xi^t}^{66} \right) + \kappa^2 I_{ij} J_{\tau t \frac{1}{H}}^{66} \\
 K_{es\xi}^{\tau ij} &= I_{\bar{i},s} J_{\tau,\xi^t}^{12} + I_{\bar{i},s\bar{j}} J_{\tau t,\xi}^{66} + \kappa \left(I_{\bar{i},s\bar{j}} J_{\tau t \frac{1}{H}}^{66} - I_{\bar{i},s} J_{\tau t \frac{1}{H}}^{11} \right) \\
 K_{es\eta}^{\tau ij} &= I_{\bar{i},s} J_{\tau,\eta^t}^{13} + I_{\bar{i},s\bar{j}} J_{\tau t,\eta}^{55} \\
 K_{e\xi s}^{\tau ij} &= I_{\bar{i},s\bar{j}} J_{\tau t,\xi}^{12} + I_{\bar{i},s} J_{\tau,\xi^t}^{66} + \kappa \left(I_{\bar{i},s} J_{\tau t \frac{1}{H}}^{66} - I_{\bar{i},s\bar{j}} J_{\tau t \frac{1}{H}}^{11} \right) \\
 K_{e\xi\xi}^{\tau ij} &= I_{ij} \left(J_{\tau,\xi^t,\xi H}^{22} + J_{\tau,\eta^t,\eta H}^{44} \right) + I_{\bar{i},s\bar{j},s} J_{\tau t \frac{1}{H}}^{66} - \kappa I_{ij} J_{\tau t,\xi}^{12} - \kappa I_{\bar{i}} J_{\tau,\xi^t}^{12} + \kappa^2 I_{ij} J_{\tau t \frac{1}{H}}^{11} \\
 K_{e\xi\eta}^{\tau ij} &= I_{ij} \left(J_{\tau,\eta^t,\xi H}^{23} + J_{\tau,\xi^t,\eta H}^{44} \right) - \kappa I_{ij} J_{\tau,\eta^t}^{13} \\
 K_{e\eta s}^{\tau ij} &= I_{\bar{i},s\bar{j}} J_{\tau t,\eta}^{13} + I_{\bar{i},s} J_{\tau,\eta^t}^{55} \\
 K_{e\eta\xi}^{\tau ij} &= I_{ij} \left(J_{\tau,\xi^t,\eta H}^{23} + J_{\tau,\eta^t,\xi H}^{44} \right) - \kappa I_{ij} J_{\tau t,\eta}^{13} \\
 K_{e\eta\eta}^{\tau ij} &= I_{ij} \left(J_{\tau,\eta^t,\eta H}^{33} + J_{\tau,\xi^t,\xi H}^{44} \right) + I_{\bar{i},s\bar{j},s} J_{\tau t \frac{1}{H}}^{55}
 \end{aligned} \tag{5.46}$$

where:

$$\begin{aligned}
 I_{i(s)j(s)} &= \int_{l_e} \bar{N}_m N_{i(s)}^m N_{j(s)} ds \\
 I_{i(s)\bar{j}(s)} &= \int_{l_e} N_{i(s)} \bar{N}_n N_{j(s)}^n ds \\
 I_{\bar{i}(s)\bar{j}(s)} &= \int_{l_e} \bar{N}_m N_{i(s)}^m \bar{N}_n N_{j(s)}^n ds
 \end{aligned} \tag{5.47}$$

and $N_{i(s)}^m$ stands for the i -th shape function (or its derivative) computed at the m -th tying point location s_m :

$$N_{i(s)}^m = N_{i(s)}(s_m) \tag{5.48}$$

Chapter 6

Geometrically Non-Linear Hierarchical Structural Modeling

6.1 Introduction

By accounting for linear geometrical relations as in the previous chapters, coincidence of the initial undeformed geometry and geometry after loading is assumed. Nevertheless, to the aim of investigating multi-stable structures, large shape changes have to be taken into account and, therefore, the simplifying assumption of geometrical linearity has to be relaxed. When the geometry of a structure varies to a great extent in response to external loads, its stiffness will not remain constant during deformation, but it will change as function of the displacement and stress fields, resulting in a non-linear structural problem.

This chapter is devoted to the derivation of UF-based one-dimensional finite elements in the framework of geometrically non-linear analysis to the aim of providing a high-fidelity one-dimensional modeling framework with enhanced kinematic and stress prediction capabilities. Preliminaries about geometrical non-linearities in a Green-Lagrange sense are provided in Section 6.2, whereas the notation for second Piola-Kirchoff and Cauchy stresses, their relation under the hypothesis of small strains as well as the constitutive equation based on Hooke's law are introduced in Section 6.3. Plane stress hypothesis are assumed. The principle of virtual displacements in the framework of a total Lagrangian formulation is discussed in Section 6.4. In Section 6.5, due to plane stress hypothesis, a two-dimensional displacement field is considered and it is approximated via a UF-based through-the-thickness expansion and a one-dimensional finite elements discretization yielding the derivation of the gradient vector as function of the nodal unknown vector. Fundamental nuclei of linear, initial-displacement and initial-stress contributions to the tangent stiffness matrix are reported in Section 6.6. Due to the coupling of the displacement components deriving from the non-linear geometrical relations, a locking correction strategy needs to be implemented in order to avoid detrimental numerical phenomena. To this aim, a MITC-based method extended to the

UF-based non-linear one-dimensional formulation is proposed in Section 6.7. Finally, the algorithms for the solution of the resulting non-linear algebraic system, including classical methods such as Newton-Raphson and arc-length method as well as an advanced ANM-based path-following technique, are discussed in Section 6.8. The formulation presented in this chapter has been previously published in [93].

6.2 Non-linear strains-displacements relation

A fixed Cartesian coordinate system $\{x, z\}$ in the framework of a two-dimensional approach is adopted, being x the beam axis coordinate and z the through-the-thickness coordinate. The generic displacement vector is:

$$\mathbf{u}^T(x, z) = \{ u(x, z) \quad w(x, z) \} \quad (6.1)$$

being u and w the displacement components in the x - and z -direction, respectively. The gradient vector of the displacements $\boldsymbol{\theta}$ is given by:

$$\boldsymbol{\theta} = \{ u_{,x} \quad u_{,z} \quad w_{,x} \quad w_{,z} \} \quad (6.2)$$

The Green-Lagrange strain vector \mathbf{E} is considered:

$$\mathbf{E}^T = \{ E_{xx} \quad E_{zz} \quad E_{xz} \} \quad (6.3)$$

with:

$$\begin{aligned} E_{xx} &= u_{,x} + \frac{1}{2} (u_{,x}^2 + w_{,x}^2) \\ E_{zz} &= w_{,z} + \frac{1}{2} (u_{,z}^2 + w_{,z}^2) \\ E_{xz} &= u_{,z} + w_{,x} + u_{,x}u_{,z} + w_{,x}w_{,z} \end{aligned} \quad (6.4)$$

Therefore, large displacements and rotations are accounted for. The matrix form of Eq. (6.4) is given by:

$$\mathbf{E} = \left[\mathbf{H} + \frac{1}{2} \mathbf{A}(\boldsymbol{\theta}) \right] \boldsymbol{\theta} \quad (6.5)$$

being:

$$\mathbf{H} = \begin{bmatrix} 1 & 0 & 0 & 0 \\ 0 & 0 & 0 & 1 \\ 0 & 1 & 1 & 0 \end{bmatrix} \quad (6.6)$$

and

$$\mathbf{A}(\boldsymbol{\theta}) = \begin{bmatrix} u_{,x} & 0 & w_{,x} & 0 \\ 0 & u_{,z} & 0 & w_{,z} \\ u_{,z} & u_{,x} & w_{,z} & w_{,x} \end{bmatrix} \quad (6.7)$$

6.3 Stress notation and constitutive relation

Second Piola-Kirchhoff's stress \mathbf{S} is considered, since it is energetically-conjugate to the Green-Lagrange strains introduced in Eq. (6.4):

$$\mathbf{S}^T = \{ S_{xx} \quad S_{zz} \quad S_{xz} \} \quad (6.8)$$

Under the assumption of small strains, Hooke's law is considered:

$$\mathbf{S} = \mathbf{Q}^k \mathbf{E} \quad (6.9)$$

where the components of the reduced material stiffness matrix \mathbf{Q}^k for a generic k-th layer made of an anisotropic material are given by:

$$\mathbf{Q}^k = \begin{bmatrix} Q_{11}^k & Q_{13}^k & Q_{15}^k \\ Q_{13}^k & Q_{33}^k & Q_{35}^k \\ Q_{15}^k & Q_{35}^k & Q_{55}^k \end{bmatrix} \quad (6.10)$$

Plane stress conditions are assumed and the explicit expression for the coefficients Q_{ij}^k is reported in Reddy [140]. The Cauchy stress tensor $\boldsymbol{\sigma}^g$ expressed in the global reference system is related to the second Piola-Kirchhoff stress tensor by means of the following equation:

$$\boldsymbol{\sigma}^g = \frac{1}{J} \mathbf{F} \begin{bmatrix} S_{xx} & S_{xz} \\ S_{xz} & S_{zz} \end{bmatrix} \mathbf{F}^T \quad (6.11)$$

where \mathbf{F} is the deformation tensor:

$$\mathbf{F} = \begin{bmatrix} 1 + u_{,x} & u_{,z} \\ w_{,x} & 1 + w_{,z} \end{bmatrix} \quad (6.12)$$

and J is its determinant: $J = \det(\mathbf{F})$. Finally, as shown in Crisfield [57], under the small strains hypothesis, the Cauchy stress in the local reference system $\boldsymbol{\sigma}$, which represents the physical stress, is equivalent to the second Piola-Kirchhoff's stress \mathbf{S} expressed in the global coordinate.

6.4 Principle of virtual displacements

Weak-form governing equations are derived via the Principle of Virtual Displacements:

$$\delta \mathcal{L} = \delta \mathcal{L}_{int} - \delta \mathcal{L}_{ext} = 0 \quad (6.13)$$

In the framework of a total Lagrangian formulation, the virtual variation of the internal work $\delta \mathcal{L}_{int}$ is computed over the undeformed volume V_0 :

$$\delta \mathcal{L}_{int} = \int_{V_0} \delta \mathbf{E}^T \mathbf{S} dV \quad (6.14)$$

Let $\delta \mathcal{L}_{int}$ be an infinitesimal variation of the internal virtual work:

$$d(\delta \mathcal{L}_{int}) = \int_{V_0} [\delta \mathbf{E}^T d\mathbf{S} + d(\delta \mathbf{E}^T) \mathbf{S}] dV \quad (6.15)$$

This latter expression can be rearranged as follows, see Crisfield [57]:

$$d(\delta \mathcal{L}_{int}) = \int_{V_0} [\delta \mathbf{E}^T \mathbf{Q}^k d\mathbf{E} + \delta \boldsymbol{\theta}^T \hat{\mathbf{S}} d\boldsymbol{\theta}] dV \quad (6.16)$$

being $\hat{\mathbf{S}} \in \mathbb{R}^{4 \times 4}$:

$$\hat{\mathbf{S}} = \begin{bmatrix} S_{xx} & S_{xz} & 0 & 0 \\ S_{xz} & S_{zz} & 0 & 0 \\ 0 & 0 & S_{xx} & S_{xz} \\ 0 & 0 & S_{xz} & S_{zz} \end{bmatrix} \quad (6.17)$$

Finally, by considering that the virtual variation of the strain vector $\delta \mathbf{E}$ is:

$$\delta \mathbf{E} = \delta \left\{ \left[\mathbf{H} + \frac{1}{2} \mathbf{A}(\boldsymbol{\theta}) \right] \boldsymbol{\theta} \right\} = [\mathbf{H} + \mathbf{A}(\boldsymbol{\theta})] \delta \boldsymbol{\theta} \quad (6.18)$$

the final form of the variation of the internal virtual work in terms of the actual and virtual variation of the gradient vector is given by:

$$d(\delta \mathcal{L}_{int}) = \int_{V_0} \delta \boldsymbol{\theta}^T \{ [\mathbf{H}^T + \mathbf{A}^T(\boldsymbol{\theta})] \mathbf{Q}^k [\mathbf{H} + \mathbf{A}(\boldsymbol{\theta})] + \hat{\mathbf{S}} \} d\boldsymbol{\theta} dV \quad (6.19)$$

6.5 UF-based one-dimensional finite element formulation

By considering a through-the-thickness displacement field based on UF and a one-dimensional finite elements approximation along the beam axis, the two-dimensional displacement field reads:

$$\begin{aligned} u_x(x, z) &= F_\tau(z) N_i(x) q_{\tau i}^u & \text{with } \tau = 1, 2, \dots, N_u \\ u_z(x, z) &= F_\tau(z) N_i(x) q_{\tau i}^w & \text{and } i = 1, \dots, N_n^e \end{aligned} \quad (6.20)$$

being $q_{\tau i}^n : n = u, w$ the nodal unknowns. In analogy with the three-dimensional UF-based displacement field presented in Section 3.3.2, a N-order through-the-thickness Taylor expansion of the displacement field reads:

$$\begin{aligned} u_x &= u_{x1} + u_{x2}z + u_{x3}z^2 + \dots + u_{x(N+1)}z^N \\ u_z &= u_{z1} + u_{z2}z + u_{z3}z^2 + \dots + u_{z(N+1)}z^N \end{aligned} \quad (6.21)$$

Upon substitution of Eq. (6.20) within Eq. (6.2), the expression for the gradient vector in terms of the nodal unknowns is obtained:

$$\boldsymbol{\theta} = \left\{ F_{\tau} N_{i,x} q_{\tau i}^u \quad F_{\tau,z} N_i q_{\tau i}^u \quad F_{\tau} N_{i,x} q_{\tau i}^w \quad F_{\tau,z} N_i q_{\tau i}^w \right\} = \mathbf{G}_{\tau i} \mathbf{q}_{\tau i} \quad (6.22)$$

being $\mathbf{G}_{\tau i} \in \mathbb{R}^{4 \times 2}$ and $\mathbf{q}_{\tau i} \in \mathbb{R}^{2 \times 1}$:

$$\mathbf{G}_{\tau i} = \begin{bmatrix} F_{\tau} N_{i,x} & 0 \\ F_{\tau,z} N_i & 0 \\ 0 & F_{\tau} N_{i,x} \\ 0 & F_{\tau,z} N_i \end{bmatrix} \quad (6.23)$$

and:

$$\mathbf{q}_{\tau i}^T = \left\{ q_{\tau i}^u \quad q_{\tau i}^w \right\} \quad (6.24)$$

6.6 Tangent stiffness matrix fundamental nucleus

By replacing Eq. (6.22) within Eq. (6.19), the variation of the internal virtual work reads:

$$\begin{aligned} d(\delta \mathcal{L}_{int}^e) = & \delta \mathbf{q}_{\tau i}^T \int_{V_0^e} \mathbf{G}_{\tau i}^T \left\{ [\mathbf{H}^T + \mathbf{A}^T(\boldsymbol{\theta})] \mathbf{Q}^k [\mathbf{H} + \mathbf{A}(\boldsymbol{\theta})] + \hat{\mathbf{S}} \right\} \mathbf{G}_{\sigma j} dV d\mathbf{q}_{\sigma j} = \\ & \delta \mathbf{q}_{\tau i}^T \left(\mathbf{K}_{\tau \sigma ij}^{el} + \mathbf{K}_{\tau \sigma ij}^{et1} + \mathbf{K}_{\tau \sigma ij}^{et2} \right) d\mathbf{q}_{\sigma j} \end{aligned} \quad (6.25)$$

where V_0^e is the element undeformed volume and $\mathbf{K}_{\tau \sigma ij}^{el}$, $\mathbf{K}_{\tau \sigma ij}^{et1}$, $\mathbf{K}_{\tau \sigma ij}^{et2} \in \mathbb{R}^{2 \times 2}$ are the fundamental nuclei of the linear, initial-displacement and initial-stress contributions to the element tangent stiffness matrix:

$$\begin{aligned} \mathbf{K}_{\tau \sigma ij}^{el} &= \int_{V_0^e} \mathbf{G}_{\tau i}^T \mathbf{H}^T \mathbf{Q}^k \mathbf{H} \mathbf{G}_{\sigma j} dV \\ \mathbf{K}_{\tau \sigma ij}^{et1} &= \int_{V_0^e} \mathbf{G}_{\tau i}^T \left[\mathbf{H}^T \mathbf{Q}^k \mathbf{A} + \mathbf{A}^T \mathbf{Q}^k (\mathbf{H} + \mathbf{A}) \right] \mathbf{G}_{\sigma j} dV \\ \mathbf{K}_{\tau \sigma ij}^{et2} &= \int_{V_0^e} \mathbf{G}_{\tau i}^T \hat{\mathbf{S}} \mathbf{G}_{\sigma j} dV \end{aligned} \quad (6.26)$$

In analogy with the stiffness matrix fundamental nucleus for linear analyses derived in the previous chapters, also the fundamental nuclei of the tangent stiffness matrix are expressed in a unified form that does not depend on the approximation order of the displacement field N , the class of expansion functions F_{τ} and the number of nodes per element N_n^e . Once these terms are fixed, the element tangent stiffness matrix is obtained by assembling the fundamental nuclei corresponding to each term of the expansion τ , σ , i and j , following the same procedure as in classical linear UF-approach [35].

6.6.1 Linear contribution

The explicit expression for the components of the linear stiffness matrix $\mathbf{K}_{\tau\sigma ij}^{el}$ is:

$$\begin{aligned} K_{\tau\sigma ij}^{elxx} &= J_{\tau\sigma}^{11} I_{i,xj,x} + J_{\tau,z\sigma,z}^{55} I_{ij} + J_{\tau,z\sigma}^{15} I_{ij,x} + J_{\tau\sigma,z}^{15} I_{i,xj} \\ K_{\tau\sigma ij}^{elxz} &= J_{\tau\sigma,z}^{13} I_{i,xj} + J_{\tau\sigma}^{15} I_{i,xj,x} + J_{\tau,z\sigma,z}^{35} I_{ij} + J_{\tau,z\sigma}^{55} I_{ij,x} \\ K_{\tau\sigma ij}^{elzx} &= J_{\tau,z\sigma}^{13} I_{ij,x} + J_{\tau\sigma}^{15} I_{i,xj,x} + J_{\tau,z\sigma,z}^{35} I_{ij} + J_{\tau\sigma,z}^{55} I_{i,xj} \\ K_{\tau\sigma ij}^{elzz} &= J_{\tau,z\sigma,z}^{33} I_{ij} + J_{\tau\sigma}^{55} I_{i,xj,x} + J_{\tau\sigma,z}^{35} I_{i,xj} + J_{\tau,z\sigma}^{35} I_{ij,x} \end{aligned} \quad (6.27)$$

where $J_{\tau(z)\sigma(z)}^{gh}$ is the following cross-section moment:

$$J_{\tau(z)\sigma(z)}^{gh} = \int_{\Omega_e=h_e \times b_e} Q_{gh}^k F_{\tau(z)} F_{\sigma(z)} d\Omega \quad (6.28)$$

$I_{i(x)j(x)}$ is the integral of the product of the shape functions or their derivatives along the axis of the one-dimensional element:

$$I_{i(x)j(x)} = \int_{l_e} N_{i(x)} N_{j(x)} dx \quad (6.29)$$

6.6.2 Initial-displacement contribution

The components of the initial displacement (or initial-slope) contribution $\mathbf{K}_{\tau\sigma ij}^{et1}$ are:

$$\begin{aligned} K_{\tau\sigma ij}^{et1xx} &= q_{tl}^u \left(2J_{\tau\sigma t}^{11} I_{i,xj,x}^{l,x} + J_{\tau\sigma,zt}^{13} I_{i,xj,l} + J_{\tau,z\sigma t,z}^{13} I_{ij,x}^{l,x} + 2J_{\tau\sigma t,z}^{15} I_{i,xj,x}^{l,x} + \right. \\ &\quad \left. 2J_{\tau\sigma,zt}^{15} I_{i,xj,l,x} + 2J_{\tau,z\sigma t}^{15} I_{ij,x}^{l,x} + 2J_{\tau,z\sigma,zt}^{35} I_{ij,l} + 2J_{\tau,z\sigma,zt}^{55} I_{ij,l,x} \right) + \\ &\quad \left. J_{\tau,z\sigma t,z}^{55} I_{ij,x}^{l,x} + J_{\tau\sigma,zt,z}^{55} I_{i,xj,l} \right) + \\ &\quad q_{tl}^u q_{sm}^u \left(J_{\tau\sigma ts}^{11} I_{i,xj,x}^{l,xm,x} + J_{\tau\sigma,zts}^{13} I_{i,xj,l,x}^m + J_{\tau,z\sigma t,zs}^{13} I_{ij,x}^{lm,x} + \right. \\ &\quad \left. J_{\tau\sigma ts,z}^{15} I_{i,xj,x}^{l,xm,x} + J_{\tau\sigma,zts}^{15} I_{i,xj,l,x}^m + J_{\tau\sigma t,zs}^{15} I_{i,xj,x}^{lm,x} + J_{\tau,z\sigma ts}^{15} I_{ij,x}^{l,xm,x} + \right. \\ &\quad \left. J_{\tau\sigma,zts}^{35} I_{i,xj,l,x}^m + J_{\tau,z\sigma t,zs}^{35} I_{ij,x}^{lm,x} + J_{\tau,z\sigma,zts}^{35} I_{ij,l,x}^m + J_{\tau,z\sigma,zts}^{35} I_{ij,l,x}^m + \right. \\ &\quad \left. J_{\tau,z\sigma,zts}^{33} I_{ij,l,x}^m + J_{\tau\sigma t,zs}^{55} I_{i,xj,x}^{lm,x} + J_{\tau\sigma,zts}^{55} I_{i,xj,l,x}^m + J_{\tau,z\sigma t,zs}^{55} I_{i,xj,l,x}^m + J_{\tau,z\sigma ts}^{55} I_{ij,x}^{l,xm,x} + \right. \\ &\quad \left. J_{\tau,z\sigma,zts}^{55} I_{ij,l,x}^m \right) \end{aligned}$$

$$\begin{aligned}
 K_{\tau\sigma ij}^{et1xz} = & q_{tl}^u \left(J_{\tau\sigma,zt}^{13} I_{i,xj,l,x} + J_{\tau\sigma t}^{15} I_{i,xj,x,l,x} + J_{\tau\sigma,z,t,z}^{35} I_{i,xj,l} + J_{\tau\sigma t,z}^{55} I_{i,xj,x,l} + \right. \\
 & \left. J_{\tau,z\sigma,z,t,z}^{33} I_{ij,l} + J_{\tau,z\sigma t,z}^{35} I_{ij,x,l} + J_{\tau,z\sigma,z,t}^{35} I_{ij,l,x} + J_{\tau,z\sigma t}^{55} I_{ij,x,l,x} \right) + \\
 & q_{tl}^w \left(J_{\tau\sigma t}^{11} I_{i,xj,x,l,x} + J_{\tau\sigma,zt}^{13} I_{i,xj,l} + J_{\tau\sigma t,z}^{15} I_{i,xj,x,l} + J_{\tau\sigma,z,t,z}^{15} I_{i,xj,l,x} + \right. \\
 & \left. J_{\tau,z\sigma t}^{15} I_{ij,x,l,x} + J_{\tau,z\sigma,z,t,z}^{35} I_{ij,l} + J_{\tau,z\sigma t,z}^{55} I_{ij,x,l} + J_{\tau,z\sigma,z,t}^{55} I_{ij,l,x} \right) + \\
 & q_{tl}^u q_{sm}^w \left(J_{\tau\sigma ts}^{11} I_{i,xj,x,l,x,m,x} + J_{\tau\sigma,z,ts,z}^{13} I_{i,xj,l,x,m} + J_{\tau\sigma ts,z}^{15} I_{i,xj,x,l,x,m} + \right. \\
 & J_{\tau\sigma,z,ts}^{15} I_{i,xj,l,x,m,x} + J_{\tau\sigma t,z,s}^{15} I_{i,xj,x,l,m,x} + J_{\tau\sigma,z,t,z,s,z}^{35} I_{i,xj,l,m} + J_{\tau\sigma t,z,s,z}^{55} I_{i,xj,x,l,m} + \\
 & J_{\tau\sigma,z,t,z,s}^{55} I_{i,xj,l,m,x} + J_{\tau,z\sigma t,z,s}^{13} I_{ij,x,l,m,x} + J_{\tau,z\sigma,z,t,z,s,z}^{33} I_{ij,l,m} + J_{\tau,z\sigma t,z,s,z}^{35} I_{ij,x,l,m} + \\
 & J_{\tau,z\sigma,z,t,z,s}^{35} I_{ij,l,m,x} + J_{\tau,z\sigma ts}^{15} I_{ij,x,l,x,m,x} + J_{\tau,z\sigma,z,ts,z}^{35} I_{ij,l,x,m} + J_{\tau,z\sigma ts,z}^{55} I_{ij,x,l,x,m} + \\
 & \left. J_{\tau,z\sigma,z,ts}^{55} I_{ij,l,x,m,x} \right) \\
 K_{\tau\sigma ij}^{et1zx} = & q_{tl}^u \left(J_{\tau\sigma t}^{15} I_{i,xj,x,l,x} + J_{\tau\sigma,z,t,z}^{35} I_{i,xj,l} + J_{\tau\sigma t,z}^{55} I_{i,xj,x,l} + J_{\tau\sigma,z,t}^{55} I_{i,xj,l,x} + \right. \\
 & \left. J_{\tau,z\sigma t}^{13} I_{ij,x,l,x} + J_{\tau,z\sigma,z,t,z}^{33} I_{ij,l} + J_{\tau,z\sigma t,z}^{35} I_{ij,x,l} + J_{\tau,z\sigma,z,t}^{35} I_{ij,l,x} \right) + \\
 & q_{tl}^w \left(J_{\tau\sigma t}^{11} I_{i,xj,x,l,x} + J_{\tau\sigma,zt}^{15} I_{i,xj,l,x} + J_{\tau\sigma t,z}^{15} I_{i,xj,x,l} + J_{\tau\sigma,z,t,z}^{15} I_{i,xj,l} + \right. \\
 & \left. J_{\tau,z\sigma t,z}^{13} I_{ij,x,l} + J_{\tau,z\sigma,z,t,z}^{35} I_{ij,l} + J_{\tau,z\sigma t}^{15} I_{ij,x,l,x} + J_{\tau,z\sigma,z,t}^{55} I_{ij,l,x} \right) + \\
 & q_{tl}^w q_{sm}^u \left(J_{\tau\sigma ts}^{11} I_{i,xj,x,l,x,m,x} + J_{\tau\sigma,z,ts,z}^{13} I_{i,xj,l,x,m} + J_{\tau\sigma ts,z}^{15} I_{i,xj,x,l,x,m} + \right. \\
 & J_{\tau\sigma,z,ts}^{15} I_{i,xj,l,x,m,x} + J_{\tau\sigma t,z,s}^{15} I_{i,xj,x,l,m,x} + J_{\tau\sigma,z,t,z,s,z}^{35} I_{i,xj,l,m} + J_{\tau\sigma t,z,s,z}^{55} I_{i,xj,x,l,m} + \\
 & J_{\tau\sigma,z,t,z,s}^{55} I_{i,xj,l,m,x} + J_{\tau,z\sigma t,z,s}^{13} I_{ij,x,l,m,x} + J_{\tau,z\sigma,z,t,z,s,z}^{33} I_{ij,l,m} + J_{\tau,z\sigma t,z,s,z}^{35} I_{ij,x,l,m} + \\
 & J_{\tau,z\sigma,z,t,z,s}^{35} I_{ij,l,m,x} + J_{\tau,z\sigma ts}^{15} I_{ij,x,l,x,m,x} + J_{\tau,z\sigma,z,ts,z}^{35} I_{ij,l,x,m} + J_{\tau,z\sigma ts,z}^{55} I_{ij,x,l,x,m} + \\
 & \left. J_{\tau,z\sigma,z,ts}^{55} I_{ij,l,x,m,x} \right)
 \end{aligned}
 \tag{6.30}$$

$$\begin{aligned}
 K_{\tau\sigma ij}^{et1zz} = & q_{tl}^w \left(J_{\tau\sigma,zt}^{13} I_{i,xjl,x} + J_{\tau,z\sigma t}^{13} I_{ij,xl,x} + 2J_{\tau\sigma t}^{15} I_{i,xj,xl,x} + 2J_{\tau\sigma,zt}^{35} I_{i,xjl,x} + \right. \\
 & 2J_{\tau,z\sigma t}^{35} I_{i,xjl,x} + 2J_{\tau,z\sigma,zt}^{35} I_{ijl,x} + 2J_{\tau\sigma t,z}^{55} I_{i,xj,xl,x} + J_{\tau\sigma,zt}^{55} I_{i,xjl,x} \left. \right) + \\
 & J_{\tau,z\sigma t}^{55} I_{ij,xl,x} + 2J_{\tau,z\sigma,zt}^{33} I_{ijl} \left. \right) + \\
 & q_{tl}^w q_{sm}^w \left(J_{\tau\sigma ts}^{11} I_{i,xj,xl,xm,x} + J_{\tau,z\sigma,zt,zs}^{33} I_{ijlm} + J_{\tau\sigma t,zs}^{55} I_{i,xj,xl,xm} + \right. \\
 & J_{\tau,zt,zs}^{55} I_{i,xjlm,x} + J_{\tau,z\sigma ts,z}^{55} I_{ij,xl,xm} + J_{\tau,z\sigma,zts}^{55} I_{ijl,xm,x} + J_{\tau\sigma,zts,z}^{13} I_{i,xjl,xm} + \\
 & J_{\tau,z\sigma t,zs}^{13} I_{ij,xlm,x} + J_{\tau\sigma ts,z}^{15} I_{i,xj,xl,xm} + J_{\tau\sigma,zts}^{15} I_{i,xjl,xm,x} + J_{\tau\sigma t,zs}^{15} I_{i,xj,xlm,x} + \\
 & J_{\tau,z\sigma ts}^{15} I_{ij,xl,xm,x} + J_{\tau\sigma,zt,zs}^{35} I_{i,xjlm} + J_{\tau,z\sigma t,zs}^{35} I_{ij,xlm} + J_{\tau,z\sigma,zt,zs}^{35} I_{ijlm,x} + \\
 & \left. J_{\tau,z\sigma,zts,z}^{35} I_{ijl,xm} \right)
 \end{aligned}$$

6.6.3 Initial-stress contribution

The components of the the initial stress (or geometric) contribution $\mathbf{K}_{\tau\sigma ij}^{et2}$ are:

$$\begin{aligned}
 K_{\tau\sigma ij}^{et2xx} = K_{\tau\sigma ij}^{et2zz} = & q_{tl}^u \left(J_{\tau\sigma t}^{11} I_{i,xj,xl,x} + J_{\tau\sigma t,z}^{15} I_{i,xj,xl,x} + J_{\tau\sigma,zt}^{15} I_{i,xjl,x} + J_{\tau\sigma,zt}^{55} I_{i,xjl,x} + \right. \\
 & J_{\tau,z\sigma t}^{15} I_{ij,xl,x} + J_{\tau,z\sigma t,z}^{55} I_{ij,xl,x} + J_{\tau,z\sigma,zt}^{13} I_{ijl,x} + J_{\tau,z\sigma,zt}^{35} I_{ijl} \left. \right) \\
 & q_{tl}^w \left(J_{\tau\sigma t,z}^{13} I_{i,xj,xl,x} + J_{\tau\sigma t,z}^{15} I_{i,xj,xl,x} + J_{\tau\sigma,zt,z}^{35} I_{i,xjl,x} + J_{\tau\sigma,zt}^{55} I_{i,xjl,x} + \right. \\
 & J_{\tau,z\sigma t,z}^{35} I_{ij,xl,x} + J_{\tau,z\sigma t,z}^{55} I_{ij,xl,x} + J_{\tau,z\sigma,zt,z}^{33} I_{ijl} + J_{\tau,z\sigma,zt}^{35} I_{ijl,x} \left. \right) \\
 & \frac{1}{2} \left(q_{tl}^u q_{sm}^u + q_{tl}^w q_{sm}^w \right) \left(J_{\tau\sigma ts}^{11} I_{i,xj,xl,xm,x} + J_{\tau\sigma t,zs}^{13} I_{i,xj,xl,xm} + \right. \\
 & J_{\tau\sigma t,zs}^{15} I_{i,xj,xl,xm,x} + J_{\tau\sigma ts,z}^{15} I_{i,xj,xl,xm} + J_{\tau\sigma,zts}^{15} I_{i,xjl,xm,x} + \\
 & J_{\tau\sigma,zt,zs}^{35} I_{i,xjlm} + J_{\tau\sigma,zt,zs}^{55} I_{i,xjlm,x} + J_{\tau\sigma,zts,z}^{55} I_{i,xjl,xm} + \\
 & J_{\tau,z\sigma ts}^{15} I_{ij,xl,xm,x} + J_{\tau,z\sigma t,zs}^{35} I_{ij,xlm} + J_{\tau,z\sigma,t,zs}^{55} I_{ij,xlm,x} + \\
 & J_{\tau,z\sigma ts,z}^{55} I_{ij,xl,xm} + J_{\tau,z\sigma,zts}^{13} I_{ijl,xm,x} + J_{\tau,z\sigma,zt,zs}^{33} I_{ijlm} + \\
 & \left. J_{\tau,z\sigma,zt,zs}^{35} I_{ijlm,x} + J_{\tau,z\sigma,zts,z}^{35} I_{ijl,xm} \right) \\
 K_{\tau\sigma ij}^{et2xz} = K_{\tau\sigma ij}^{et2zx} = & 0
 \end{aligned} \tag{6.31}$$

The integrals $J_{\tau(z)\sigma(z)t(z)}^{gh}$, $I_{i(x)j(x)l(x)}$, $J_{\tau(z)\sigma(z)t(z)s(z)}^{gh}$ and $I_{i(x)j(x)l(x)m(x)}$ are defined as:

$$J_{\tau(z)\sigma(z)t(z)}^{gh} = \int_{\Omega_e=h_e \times b_e} Q_{gh}^k F_{\tau(z)} F_{\sigma(z)} F_{t(z)} d\Omega \tag{6.32}$$

$$I_{i(x)j(x)l(x)} = \int_{l_e} N_{i(x)} N_{j(x)} N_{l(x)} dx \quad (6.33)$$

$$J_{\tau(z)\sigma(z)t(z)s(z)}^{gh} = \int_{\Omega_e=h_e \times b_e} Q_{gh}^k F_{\tau(z)} F_{\sigma(z)} F_{t(z)} F_{s(z)} d\Omega \quad (6.34)$$

$$I_{i(x)j(x)l(x)m(x)} = \int_{l_e} N_{i(x)} N_{j(x)} N_{l(x)} N_{m(x)} dx \quad (6.35)$$

All the I - and J -integrals in Eqs. (6.27), (6.30) and (6.31) are numerically evaluated via Gaussian quadrature.

6.7 Locking-free higher-order elements based on MITC

In order to tackle the detrimental effects of locking phenomena due to the coupling of the displacement components in the non-linear geometric relations, see Eq. (6.4), a correction strategy based on MITC, see Bathe et al. [15, 17, 18], is proposed. Axial strain \bar{E}_{xx} , transverse normal strain \bar{E}_{zz} as well as shear strain \bar{E}_{xz} are interpolated along the axis as follows:

$$\begin{aligned} \bar{E}_{xx} &= \bar{N}_p E_{xx}^p \\ \bar{E}_{zz} &= \bar{N}_p E_{zz}^p \\ \bar{E}_{xz} &= \bar{N}_p E_{xz}^p \end{aligned} \quad (6.36)$$

p implicitly stands for a summation from 1 to $N_n^e - 1$, \bar{N}_p are the assumed interpolating functions of the natural beam element coordinate $r \in [-1, 1]$ and E_{xx}^p , E_{zz}^p and E_{xz}^p are the strains computed at the p -th tying point coordinate r_{Tp} . The explicit expression for the interpolating functions \bar{N}_p can be found in Carrera et al. [40] and it is reported below, for the sake of completeness:

- For linear elements ($N_n^e = 2$):

$$\begin{aligned} \bar{N}_1 &= 1 \\ r_{T1} &= 0 \end{aligned} \quad (6.37)$$

- For quadratic elements ($N_n^e = 3$):

$$\begin{aligned} \bar{N}_1 &= -\frac{1}{2}\sqrt{3}\left(r - \frac{1}{\sqrt{3}}\right) & \bar{N}_2 &= \frac{1}{2}\sqrt{3}\left(r + \frac{1}{\sqrt{3}}\right) \\ r_{T1} &= -\frac{1}{\sqrt{3}} & r_{T2} &= \frac{1}{\sqrt{3}} \end{aligned} \quad (6.38)$$

- And, finally, for cubic elements ($N_n^e = 4$):

$$\begin{aligned} \bar{N}_1 &= \frac{5}{6}r \left(r - \sqrt{\frac{3}{5}} \right) & \bar{N}_2 &= -\frac{5}{3} \left(r - \sqrt{\frac{3}{5}} \right) \left(r + \sqrt{\frac{3}{5}} \right) & \bar{N}_3 &= \frac{5}{6}r \left(r + \sqrt{\frac{3}{5}} \right) \\ r_{T1} &= -\sqrt{\frac{3}{5}} & r_{T2} &= 0 & r_{T3} &= \sqrt{\frac{3}{5}} \end{aligned} \quad (6.39)$$

In order to account for the MITC-based locking correction within the element tangent stiffness matrix derived in Section 6.6, the only modification is the definition of the I -integrals in Eqs. (6.29), (6.33), (6.35) which are replaced, respectively, by the following expressions:

$$\bar{I}_{i(x)j(x)} = \int_{l_e} \bar{N}_p N_{i(x)}^p \bar{N}_q N_{j(x)}^q dx \quad (6.40)$$

$$\bar{I}_{i(x)j(x)l(x)} = \int_{l_e} \bar{N}_p N_{i(x)}^p \bar{N}_q N_{j(x)}^q N_{l(x)}^q dx \quad (6.41)$$

$$\bar{I}_{i(x)j(x)l(x)m(x)} = \int_{l_e} \bar{N}_p N_{i(x)}^p N_{j(x)}^p \bar{N}_q N_{l(x)}^q N_{m(x)}^q dx \quad (6.42)$$

6.8 Solution of non-linear algebraic systems

The finite element formulation of structural problems results in a system of non-linear algebraic equations in the following form:

$$\mathbf{K}(\mathbf{q}) \mathbf{q} = \lambda \mathbf{F} \quad (6.43)$$

where \mathbf{K} is the so-called secant stiffness matrix, \mathbf{q} is the unknown vector to be solved for and $\lambda \mathbf{F}$ is the external load applied. Let \mathbf{R} be the residual vector:

$$\mathbf{R}(\mathbf{q}, \lambda) = \mathbf{K}(\mathbf{q}) \mathbf{q} - \lambda \mathbf{F} = 0 \quad (6.44)$$

Three different solution procedures are considered and their main features are described in the following.

6.8.1 Newton-Raphson procedure

Newton-Raphson technique is one of the most simple and used non-linear solution procedures. As also discussed in [138], in order to compute the solution of Eq. (6.43) at

the n -th load step and k -th iteration \mathbf{q}_n^k , the residual vector $\mathbf{R}(\mathbf{q}_n^k)$, for a fixed load, is approximated via a first-order Taylor's series in the following manner:

$$\mathbf{R}(\mathbf{q}_n^k) = \mathbf{R}(\mathbf{q}_n^{k-1}) + \left. \frac{\partial \mathbf{R}}{\partial \mathbf{q}} \right|_{\mathbf{q}_n^{k-1}} \cdot \delta \mathbf{q}_n^k = 0 \quad (6.45)$$

where $\delta \mathbf{q}_n^k = \mathbf{q}_n^k - \mathbf{q}_n^{k-1}$ and:

$$\mathbf{K}^t(\mathbf{q}_n^{k-1}) = \left. \frac{\partial \mathbf{R}}{\partial \mathbf{q}} \right|_{\mathbf{q}_n^{k-1}} \quad (6.46)$$

is the tangent stiffness matrix at the iteration $k-1$. It is worth clarifying that the symbol δ in this section stands for increment between two consecutive iterations, in contrast to its previous use as a virtual variation symbol. From Eqs. (6.44), (6.45) and (6.46):

$$\delta \mathbf{q}_n^k = -[\mathbf{K}^t(\mathbf{q}_n^{k-1})]^{-1} \cdot \mathbf{R}(\mathbf{q}_n^{k-1}) = [\mathbf{K}^t(\mathbf{q}_n^{k-1})]^{-1} \cdot [\lambda \mathbf{F} - \mathbf{K}(\mathbf{q}_n^{k-1}) \cdot \mathbf{q}_n^{k-1}] \quad (6.47)$$

and, finally:

$$\mathbf{q}_n^k = \mathbf{q}_n^{k-1} + \delta \mathbf{q}_n^k \quad (6.48)$$

Such iterative procedure is continued until convergence is obtained. A common primary convergence criterion is based on the norm of the residual vector \mathbf{R} . Auxiliary criteria based on the relative difference between two consecutive iterations can be also adopted, such as:

$$\sqrt{\frac{\|(\mathbf{q}_n^k - \mathbf{q}_n^{k-1})^T \cdot (\mathbf{q}_n^k - \mathbf{q}_n^{k-1})\|}{\|(\mathbf{q}_n^k)^T \cdot \mathbf{q}_n^k\|}} < \epsilon \quad (6.49)$$

being ϵ the margin of tolerance. For a fixed load, according to Eq. (6.47), the tangent stiffness matrix should be assembled and inverted at each iteration, which could represent, in some cases, a computationally expensive task. An alternative scheme, known as modified Newton-Raphson procedure, is commonly used, consisting in updating the tangent stiffness matrix at the beginning of each load step only or for a limited number of iterations. In this way, despite a larger number of iterations for each load step, a less time-consuming procedure can be obtained for problems involving a high number of degrees of freedom.

6.8.2 Arc-length method

Newton-Raphson procedures may fail to predict the complete equilibrium path if singular points exist, such as in snap-through buckling problems, in which convergence after the limit point can not be obtained under force control. A more robust non-linear solution scheme for these cases is given by the arc-length methods. In this work, the

procedure developed by Crisfield [57] is considered. In analogy with Eq. (6.45), but considering that both \mathbf{q} and λ are unknown, a first-order Taylor series of the residual vector reads:

$$\mathbf{R}(\mathbf{q}_n^k, \lambda_n^k) = \mathbf{R}(\mathbf{q}_n^{k-1}, \lambda_n^{k-1}) - \mathbf{F} \delta \lambda_n^k + \mathbf{K}^t(\mathbf{q}_n^{k-1}, \lambda_n^{k-1}) \cdot \delta \mathbf{q}_n^k = 0 \quad (6.50)$$

and solving for the increment of the displacement vector $\delta \mathbf{q}_n^k$:

$$\delta \mathbf{q}_n^k = - [\mathbf{K}^t(\mathbf{q}_n^{k-1}, \lambda_n^{k-1})]^{-1} \cdot [\mathbf{R}(\mathbf{q}_n^{k-1}, \lambda_n^{k-1}) - \mathbf{F} \delta \lambda_n^k] \quad (6.51)$$

This latter equation can be written in a compact form as:

$$\delta \mathbf{q}_n^k = \delta \bar{\mathbf{q}}_n^k + \delta \lambda_n^k \delta \hat{\mathbf{q}}_n^k \quad (6.52)$$

where the following definitions have been introduced:

$$\delta \bar{\mathbf{q}}_n^k = - [\mathbf{K}^t(\mathbf{q}_n^{k-1}, \lambda_n^{k-1})]^{-1} \cdot \mathbf{R}(\mathbf{q}_n^{k-1}, \lambda_n^{k-1}) \quad (6.53)$$

$$\delta \hat{\mathbf{q}}_n^k = [\mathbf{K}^t(\mathbf{q}_n^{k-1}, \lambda_n^{k-1})]^{-1} \cdot \mathbf{F} \quad (6.54)$$

In analogy with modified Newton-Raphson procedure, as suggested in Crisfield [57], the tangent stiffness matrix in Eqs (6.51), (6.53) and (6.54) could be computed at the last converged equilibrium point $(\mathbf{q}_n^0, \lambda_n^0)$ rather than at each iteration, such that better computational performances can be achieved. In this case, also the terms in Eq. (6.54) could be evaluated at the beginning of each load step only. By defining the cumulative incremental nodal unknowns vector $\Delta \mathbf{q}_n^k$ at k-th iteration within the current step, the total nodal unknowns vector \mathbf{q}_n and the load parameter λ_n^k :

$$\Delta \mathbf{q}_n^k = \Delta \mathbf{q}_n^{k-1} + \delta \mathbf{q}_n^k \quad (6.55)$$

$$\mathbf{q}_n = \mathbf{q}_{n-1} + \Delta \mathbf{q}_n^k \quad (6.56)$$

$$\lambda_n^k = \lambda_n^{k-1} + \delta \lambda_n^k \quad (6.57)$$

A parameter Δs representing the radius of a circular arc with center in the current equilibrium point can be introduced:

$$\Delta s = \sqrt{(\Delta \mathbf{q}_n^k)^T \cdot \Delta \mathbf{q}_n^k} \quad (6.58)$$

From Eqs. (6.52) and (6.58), it is possible to derive the following scalar quadratic relation, see also Reddy [138]:

$$a (\delta \lambda_n^k)^2 + b (\delta \lambda_n^k) + c = 0 \quad (6.59)$$

being:

$$\begin{aligned} a &= (\delta \hat{\mathbf{q}}_n^k)^T \cdot \delta \hat{\mathbf{q}}_n^k \\ b &= 2 (\Delta \mathbf{q}_n^{k-1} + \delta \bar{\mathbf{q}}_n^k)^T \cdot \delta \hat{\mathbf{q}}_n^k \\ c &= (\Delta \mathbf{q}_n^{k-1} + \delta \bar{\mathbf{q}}_n^k)^T \cdot (\Delta \mathbf{q}_n^{k-1} + \delta \bar{\mathbf{q}}_n^k) - (\Delta s)^2 \end{aligned} \quad (6.60)$$

The solution of the quadratic equation (6.59) provides two values $\delta\lambda_{n1}^k$ and $\delta\lambda_{n2}^k$ corresponding to two different values $\Delta\mathbf{q}_{n1}^k$ and $\Delta\mathbf{q}_{n2}^k$. The root λ_n^k is chosen according to the desired sign, positive or negative, of the angle between the incremental displacement vectors at two consecutive iterations, i.e. according to the sign of the product $\Delta\mathbf{q}_n^{k-1} \cdot \Delta\mathbf{q}_n^k$. In the case both roots are positive, the one closest to the linear solution $\delta\lambda_n^k = -c/b$ should be selected. For the first iteration within the first step, an initial load increment $\delta\lambda_1^0$ needs to be assumed and, by means of the definition in Eq. (6.58), the starting arc-length increment can be obtained:

$$\Delta s_1 = \delta\lambda_1^0 \cdot \sqrt{(\delta\hat{\mathbf{q}}_1^0)^T \cdot \delta\hat{\mathbf{q}}_1^0} \quad (6.61)$$

For all subsequent steps, in order to enhance the performance of the algorithm, the arc-length within the current step Δs_n could be automatically adjusted it by scaling it with respect to the value at the previous step Δs_{n-1} according to a desired number of iterations I_d and the number of iterations needed for convergence in the previous step I_{n-1} :

$$\Delta s_n = \Delta s_{n-1} \cdot \sqrt{\left(\frac{I_d}{I_{n-1}}\right)} \quad (6.62)$$

Finally, the value of the incremental load parameter at the first iteration for all steps, except the first one, is given by:

$$\delta\lambda_n^0 = \pm \frac{\Delta s_n}{\sqrt{(\delta\hat{\mathbf{q}}_n^0)^T \cdot \delta\hat{\mathbf{q}}_n^0}} \quad (6.63)$$

where the sign is chosen positive when the tangent stiffness matrix \mathbf{K}^t is positive definite and negative when \mathbf{K}^t has at least one negative eigenvalue. This occurs, for instance, when the equilibrium path has overcome a limit point.

6.8.3 Path-following solver based on the Asymptotic Numerical Method

In this section, a path-following method via the Asymptotic Numerical Method (ANM) perturbation technique based on Cochelin [53] is described. The displacement and the stress vectors \mathbf{u} , \mathbf{S} as well as the load parameter λ are expanded via a n -order power series with respect to a real scalar parameter a :

$$\begin{aligned} \mathbf{u} &= \mathbf{u}^j + a^p \mathbf{u}_p = \mathbf{u}^j + a\mathbf{u}_1 + a^2\mathbf{u}_2 + \dots + a^n \mathbf{u}_n \\ \mathbf{S} &= \mathbf{S}^j + a^p \mathbf{S}_p = \mathbf{S}^j + a\mathbf{S}_1 + a^2\mathbf{S}_2 + \dots + a^n \mathbf{S}_n \\ \lambda &= \lambda^j + a^p \lambda_p = \lambda^j + a\lambda_1 + a^2\lambda_2 + \dots + a^n \lambda_n \end{aligned} \quad (6.64)$$

where p stands for a summation from 1 to n and the subscript j refers to the last converged solution. The path parameter a is an arc-length measure defined in the following manner:

$$a = \mathbf{u}_1(\mathbf{u} - \mathbf{u}^j) + \lambda_1(\lambda - \lambda^j) \quad (6.65)$$

being $(\mathbf{u}_1, \lambda_1)$ the tangent vector to the equilibrium path. The sign of a defines the direction of the solution path and it is taken as positive when the tangent stiffness matrix is positive definite and negative otherwise. Finally, as shown in Cochelin [53], by transforming the non-linear problem in Eq. (6.43), which is cubic with respect to the displacements, into a quadratic problem with respect to a temporary mixed displacement-stress unknown vector, a solution algorithm consisting in a set of linear systems for each expansion order p can be obtained and it is reported below.

Solution algorithm for the first order ($p=1$)

The set of three linear systems that needs to be solved in order to compute the 1-st order unknowns \mathbf{u}_1 , \mathbf{S}_1 and λ_1 are given by:

$$\mathbf{K}^t(\theta(\mathbf{u}^j)) \mathbf{u}_1 = \lambda_1 \mathbf{F} \quad (6.66)$$

$$\mathbf{S}_1 = \mathbf{Q}^k [\mathbf{H} + \mathbf{A}(\theta(\mathbf{u}^j))] \theta(\mathbf{u}_1) \quad (6.67)$$

$$\mathbf{u}_1^T \mathbf{u}_1 + \lambda_1^2 = 1 \quad (6.68)$$

where Eqs. (6.5), Eqs. (6.9), (6.20) and Eqs. (6.64) have been accounted for.

Solution algorithm for an order $2 \leq p \leq n$

For each subsequent order p , the following linear systems need to be solved for the unknowns \mathbf{u}_p , \mathbf{S}_p and λ_p :

$$\mathbf{K}^t(\theta(\mathbf{u}^j)) \mathbf{u}_p = \lambda_p \mathbf{F} + \mathbf{F}_p^{nl} \quad (6.69)$$

$$\mathbf{S}_p = \mathbf{Q}^k [\mathbf{H} + \mathbf{A}(\theta(\mathbf{u}^j))] \theta(\mathbf{u}_p) + \mathbf{S}_p^{nl} \quad (6.70)$$

$$\mathbf{u}_1^T \mathbf{u}_p + \lambda_1 \lambda_p = 0 \quad (6.71)$$

where \mathbf{S}_p^{nl} and \mathbf{F}_p^{nl} can be computed at each order p in terms of displacement and stress unknowns at previous orders. Their complete expressions are not reported here, for the sake of brevity, and can be found in Baguet [9].

Convergence criterion

Finally, the length of each step a_{max} is computed a posteriori, according to the following convergence criterion on the displacements:

$$a_{max} = \left(\epsilon \frac{\|\mathbf{u}_1\|}{\|\mathbf{u}_n\|} \right)^{\frac{1}{n-1}} \quad (6.72)$$

where ϵ is the tolerance parameter. The latter relation in addition to the Eqs. (6.66) to (6.71) represent $3n+1$ linear systems allowing to compute the $3n+1$ unknowns in Eq. (6.64). Due to the higher-order analytical representation, see Eq. (6.64), a larger non-linear branch can be predicted within a single solution step in an efficient manner, since the tangent stiffness matrix needs to be computed only at the beginning of the solution step, as shown in the solution algorithm. These features differentiate the ANM-based solver from the predictor-corrector methods seen in Sections 6.8.1 and 6.8.2, in which the non-linear path is piece-wise linearly approximated and therefore a higher number of steps is needed for strongly non-linear problems. Moreover, unless a modified Newton-Raphson scheme is used, the assembly and inversion of the tangent stiffness matrix is required at each iteration within the step. For these reasons, significant computational time saving can be obtained via ANM-based path following, especially when dealing with instability problems and complex equilibrium paths. A further advantage of the present method is that, due to the automatic a posteriori computation of the arc-length in Eq. (6.72), no initial guess for the step length or first increment is needed. As far as the robustness of the ANM approach in bifurcation problems is concerned, readers are referred to Baguet and Cochelin [10].

Part III

Numerical Results

Chapter 7

Mechanical and Thermo-Mechanical Analysis

7.1 Introduction

For some simple structural problems, such as the global bending of slender isotropic beams, the mechanical response can be accurately yet efficiently predicted by means of classical one-dimensional models discussed in Chapter 3. Nevertheless, structural components in advanced engineering applications can often have anisotropic material properties (such as in laminated or sandwich structures) and be subjected to a different variety of external loads (multi-field environment) yielding much more complex kinematic behaviors. For instance, several aerospace structures, such as engine components or re-entry vehicles, are often multi-layered structures subjected to harsh thermal loads that, due to their isotropic nature, generate complex three-dimensional stress fields. For these kind of problems, a three-dimensional finite elements analysis, although computationally expensive, is certainly more reliable than a classical one-dimensional modeling approach.

With the aim of providing an efficient alternative to three-dimensional modeling, this chapter is devoted to the assessment of a refined one-dimensional approach for the elastic response of beam structures subjected to mechanical and thermal loadings. A geometrically linear behavior is assumed. By means of the formulation developed in Chapter 4, the mechanical response of sandwich beams subjected to localized loads is investigated in Section 7.2, whereas in Section 7.3 the thermal stress analysis of laminated and functionally graded beam structures is carried out. A complex 3D-like kinematic response, accounting for cross-sectional warping and torsional effects, as well as an accurate three-dimensional stress field can be predicted by hierarchically increasing the approximation order of the UF-based one-dimensional models, with remarkable computational savings. The limitation of straight beam axis is relaxed in Section 7.4, where the mechanics of curved three-dimensional beam structures subjected to in-plane and out-of-plane mechanical loads is studied by means of UF-based curved beam models

formulated in Chapter 5. Locking phenomena typical of curved finite elements are assessed towards an exact Navier-type analytical solution showing the effectiveness of the proposed MITC-based correction strategy. Numerical results presented in this chapter have been previously published in [60, 61, 75, 132].

7.2 Mechanical analysis of sandwich beams

Sandwich structures exhibit high stiffness-to-weight and strength-to-weight ratios and, for this reason, they are ideal candidates for several lightweight industrial applications. Due to the large difference in stiffness between the skins and the core layer, such structures can show localized deformations in the soft core. Such mechanical behavior can not be predicted by classical structural theories, since these are based on the hypothesis of rigid cross-section. Therefore, higher-order models are required for an accurate prediction of the three-dimensional displacement and stress field. In this section, three-dimensional sandwich beam structures are investigated via one-dimensional hierarchical finite elements. The beam domain is $[0, l] \times [-b/2, b/2] \times [-h/2, h/2]$ being l the beam length, h the thickness and b the width. The thickness of the faces is referred to as h_f . Fig. 7.1 shows the beam geometry as well as the reference coordinate system. A square

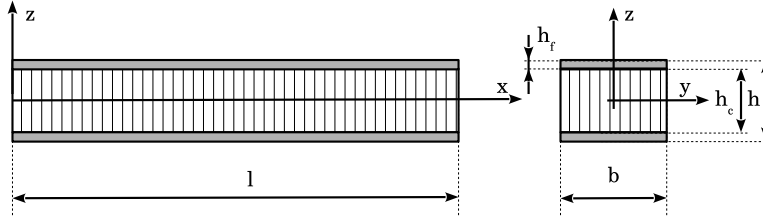


Figure 7.1: Adopted notation and cartesian coordinate system for sandwich beam-like structures.

cross-section ($h = b = 0.01$ m) is considered, being the ratio between the thickness of the faces and the total thickness h equal to 0.1. Both skins and the hexagonal honeycomb core are made of aluminium. Young's modulus and the Poisson's ratio for the face sheets are $E_f = 69$ GPa and $\nu_f = 0.33$, respectively, whereas the equivalent mechanical properties of the core are: $E_{c1} = E_{c2} = 1.62$ MPa, $E_{c3} = 2.3$ GPa, $\nu_{c12} = 0.99$, $\nu_{c13} = \nu_{c23} = 2.32 \cdot 10^{-4}$, $G_{c12} = 0.97$ MPa, $G_{c13} = 499$ MPa and $G_{c23} = 324$ MPa, where G is the shear modulus. Such material coefficients are obtained via the analytical relations given by Gibson and Ashby [71] and Grediac [82], starting from the geometry of the core cell, i.e. the nominal size $\phi = 6.4 \cdot 10^{-3}$ m and the thickness $t = 80 \cdot 10^{-6}$ m. The three-dimensional displacement and stress fields obtained via the presented one-dimensional formulation are assessed towards three-dimensional tri-quadratic 20-node elements "Solid186" implemented in the commercial software Ansys. A coarse and a

refined mesh, ‘FEM 3D-C’ and ‘FEM 3D-R’, respectively, are adopted for the three-dimensional finite elements solution. About the computational costs, the number of degrees of freedom (N_{DOFs}) of the UF-based one-dimensional finite elements approach depends on both the expansion order N and the total number of nodes N_n according to the following relation:

$$N_{DOFs} = 3 \cdot \frac{(N+1)(N+2)}{2} \cdot N_n \quad (7.1)$$

As shown in the full paper [60], one extra order of magnitude in terms of N_{DOFs} is needed for the refined three-dimensional solution with respect to the most refined one-dimensional model used in this study, which is a 19th-order theory ($N=19$).

7.2.1 Strain energy convergence analysis

As a first assessment, the convergence of the proposed one-dimensional finite elements solution is assessed by analyzing the relative strain energy error Δ_E versus the number of nodes. An exact Navier-type closed form solution, see Carrera and Giunta [34], is used as reference.

$$\Delta_E = \frac{\mathcal{L}_{int}^{Nav} - \mathcal{L}_{int}^{FEM}}{\mathcal{L}_{int}^{Nav}} \quad (7.2)$$

The relative strain energy error Δ_E versus the dimensionless distance between two consecutive nodes δ_{ii+1}/l is shown in Fig. 7.2 for linear (B2), quadratic (B3) and cubic (B4) elements. These results have been derived via an expansion order $N = 2$ for a

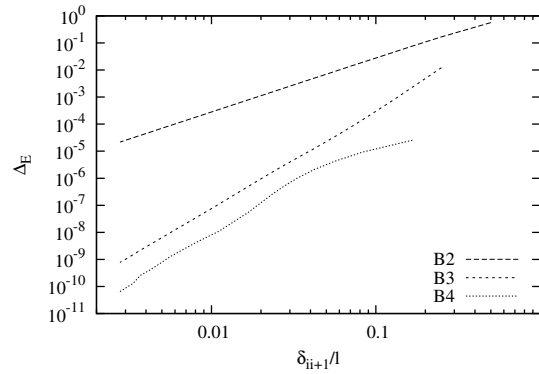


Figure 7.2: Strain energy error as function of the distance between two consecutive nodes.

simply supported beam ($l/h = 10$) loaded by a uniform unitary pressure $p_{zz} = 1$ Pa acting at the top surface of the beam. Different UF orders N and slenderness ratios l/h provide a similar behavior. In order to have a good compromise between accuracy and computational efficiency, a total number of nodes N_n equal to 121 (corresponding to $\delta_{ii+1}/l = 0.008\bar{3}$) is chosen for the following analyses, unless otherwise stated.

7.2.2 Shear locking correction

In order to tackle the shear locking phenomenon, a selective integration strategy is used. Fig. 7.3 presents the variation of \hat{u}_z computed at $(x/l, y/b, z/h) = (1/2, 0, 0)$ via linear (B2) one-dimensional elements versus l/h , being \hat{u}_z the transverse displacement normalized with respect to the exact Navier-type solution:

$$\hat{u}_z = \frac{u_z^{\text{FEM}}}{u_z^{\text{Nav}}} \quad (7.3)$$

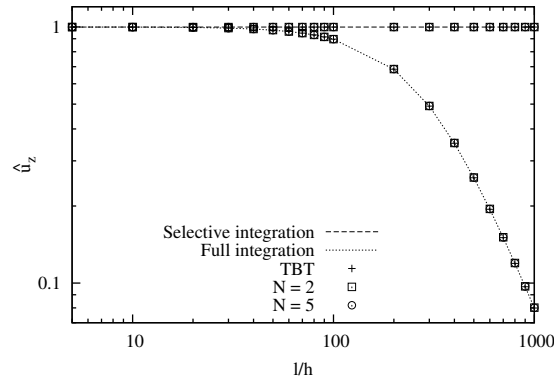


Figure 7.3: Locking mitigation by means of selective integration. Simply supported sandwich beam subjected to pressure. B2 elements.

Results show that the locking phenomenon exists if a full integration scheme is adopted, whereas a selective integration is an effective correction strategy, regardless the choice of the expansion order N .

7.2.3 Flexural-torsional response

In order to assess the capability of the proposed approach, a very short sandwich beam ($l/h = 5$) subjected to bending, torsion as well as localized deformations provided by a uniform off-centric unitary line load $l_{zz} = -1 \text{ N/m}$ applied at $(y, z) = (-b/2, h/2)$ is studied. Table 7.1 shows the displacement components for a clamped-clamped beam, whereas the stress components are given in Table 7.2. The following evaluation points are considered:

$$\begin{aligned} \tilde{u}_x &= u_x \left(\frac{l}{4}, \frac{b}{2}, \frac{h}{2} \right) & \tilde{u}_y &= u_y \left(\frac{l}{2}, \frac{b}{2}, \frac{h}{2} \right) & \tilde{u}_z &= u_z \left(\frac{l}{2}, 0, \frac{h}{2} \right) \\ \tilde{\sigma}_{xx} &= \sigma_{xx} \left(\frac{l}{2}, \frac{b}{2}, \frac{h}{2} \right) & \tilde{\sigma}_{xz} &= \sigma_{xz} \left(\frac{l}{4}, \frac{b}{4}, \frac{h}{4} \right) & \tilde{\sigma}_{xy} &= \sigma_{xy} \left(\frac{l}{4}, \frac{b}{4}, -\frac{h}{2} \right) \end{aligned} \quad (7.4)$$

	$10^{10} \times \tilde{u}_x$			$-10^9 \times \tilde{u}_y$			$-10^9 \times \tilde{u}_z$		
FEM 3D-R ^a	5.3473			1.6120			5.8759		
FEM 3D-C ^b	5.3456			1.6111			5.8727		
	B2	B3	B4	B2	B3	B4	B2	B3	B4
$N = 19$	5.2398	5.2865	5.2419	1.5873	1.5878	1.5880	5.6305	5.6325	5.6331
$N = 16$	5.2307	5.2776	5.2327	1.5884	1.5889	1.5891	5.5794	5.5809	5.5818
$N = 14$	5.1921	5.2386	5.1941	1.5790	1.5796	1.5797	5.4800	5.4815	5.4824
$N = 10$	5.1232	5.1690	5.1250	1.5624	1.5629	1.5630	5.3079	5.3093	5.3101
$N = 7$	4.9961	5.0409	4.9978	1.5241	1.5245	1.5246	5.2360	5.2373	5.2380
$N = 5$	4.7642	4.8069	4.7655	1.4459	1.4462	1.4462	4.9144	4.9152	4.9154
$N = 2$	2.1132	2.1290	2.1137	0.5410	0.5410	0.5410	1.1148	1.1151	1.1151
TBT	1.7401	1.7508	1.7401	0.0000	0.0000	0.0000	1.1393	1.1393	1.1393
EBT	1.7401	1.7508	1.7401	0.0000	0.0000	0.0000	0.5805	0.5806	0.5806

a: Mesh $96 \times 48 \times 48$. b: Mesh $48 \times 24 \times 24$.

Table 7.1: Displacements [m] for a very thick doubly-clamped sandwich beam subjected to an off-centric line load.

	$-10^{-3} \times \tilde{\sigma}_{xx}$			$-10^{-1} \times \tilde{\sigma}_{xz}$			$10^{-2} \times \tilde{\sigma}_{xy}$		
FEM 3D-R ^a	3.7175			9.9206			10.126		
FEM 3D-C ^b	3.7192			9.9214			10.132		
	B2	B3	B4	B2	B3	B4	B2	B3	B4
$N = 19$	3.5135	3.5129	3.5083	10.086	10.445	10.154	9.8592	10.1940	9.9967
$N = 16$	3.6194	3.6210	3.6208	8.8559	9.1464	8.9525	9.8497	10.182	9.9808
$N = 14$	3.5605	3.5621	3.5619	9.8799	10.191	9.9743	9.8181	10.149	9.9487
$N = 10$	3.6506	3.6523	3.6519	11.169	11.507	11.260	9.6825	10.010	9.8122
$N = 7$	3.6239	3.6255	3.6251	10.656	10.978	10.747	9.4915	9.8162	9.6192
$N = 5$	3.4314	3.4330	3.4324	8.2948	8.5636	8.3791	9.3204	9.6422	9.4456
$N = 2$	1.4695	1.4703	1.4700	0.3778	0.3994	0.3894	3.6036	3.7375	3.6562
TBT	1.2806	1.2810	1.2807	1.0994	1.1387	1.1164	0.0000	0.0000	0.0000
EBT	1.2806	1.2810	1.2807	— ^c	—	—	—	—	—

a: Mesh $96 \times 48 \times 48$. b: Mesh $48 \times 24 \times 24$.

c: Result not provided by the theory.

Table 7.2: Stresses $\tilde{\sigma}_{xx}$, $\tilde{\sigma}_{xz}$ and $\tilde{\sigma}_{xy}$ [Pa] for a very thick doubly-clamped sandwich beam subjected to an off-centric line load.

Despite the limitations of an ESL approach in modeling sandwich structures, relative differences on the displacements of about 4%, at worst, with respect to the three-dimensional finite elements solution, can be obtained via a theory with $N = 19$, whereas stress predictions differ by 5.6%, at worst. The comparison of the cross-sectional distribution of the displacement components provided by a 19th-order theory

and the 3D FEM is given in Figs. 7.4 to 7.6, whereas the axial and shear stress distributions σ_{xx} and σ_{xy} are presented in Figs. 7.7 and 7.8, showing that a fairly accurate mechanical description can be obtained. Shear deformation, cross-sectional warping

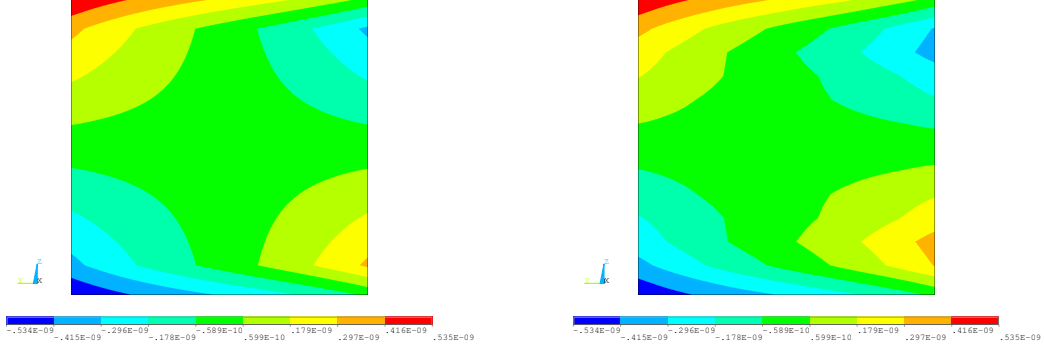


Figure 7.4: Cross-sectional distribution of the axial displacement u_x [m] at $x = l/4$ via three-dimensional finite elements (left) and 19th-order B4 one-dimensional elements (right). Doubly-clamped sandwich beam ($l/h = 5$) subjected to an off-centric line load.

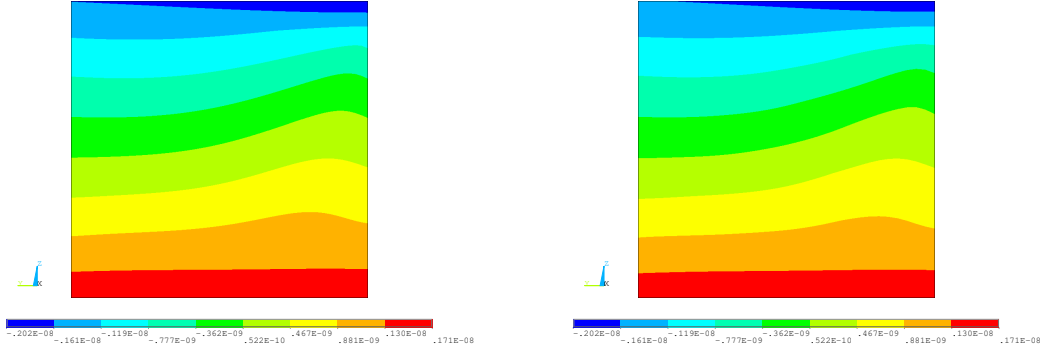


Figure 7.5: Cross-sectional distribution of the through-the-width displacement u_y [m] at $x = l/2$ via three-dimensional finite elements (left) and 19th-order B4 one-dimensional elements (right). Doubly-clamped sandwich beam ($l/h = 5$) subjected to an off-centric line load.

and localized deformations are all accounted for in the higher-order model. Due to the great difference in stiffness between face-sheets and core, sandwich beams present a complex stress state that calls for highly refined beam models.

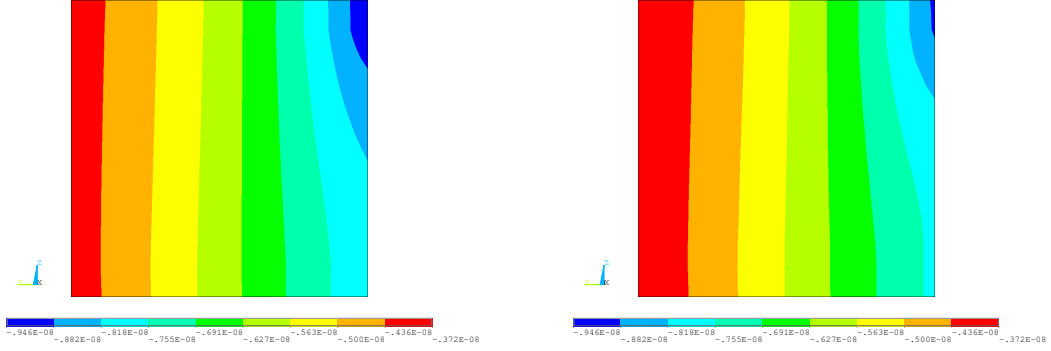


Figure 7.6: Cross-sectional distribution of the through-the-thickness displacement u_z [m] at $x = l/2$ via three-dimensional finite elements (left) and 19th-order B4 one-dimensional elements (right). Doubly-clamped sandwich beam ($l/h = 5$) subjected to an off-centric line load.

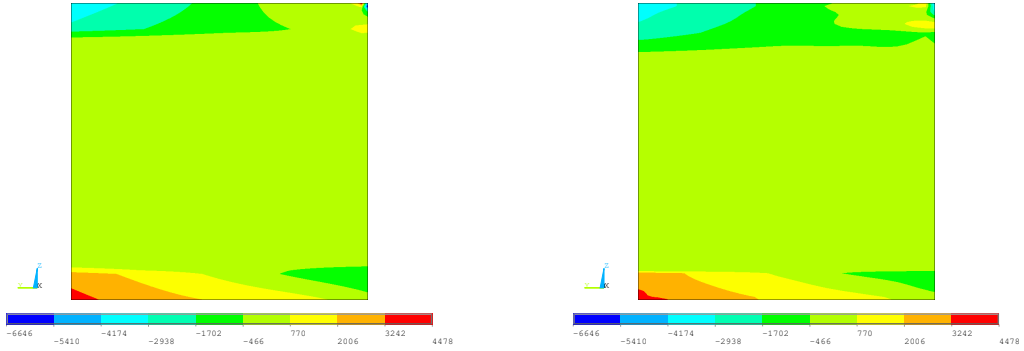


Figure 7.7: Cross-sectional distribution of the axial stress σ_{xx} [Pa] at $x = l/2$ via three-dimensional finite elements (left) and 19th-order B4 one-dimensional elements (right). Doubly-clamped sandwich beam ($l/h = 5$) subjected to an off-centric line load.

7.2.4 Comparison with experiments

The linear load-displacement relation provided by the proposed approach for a three point bending test of a sandwich beam is compared with experimental results carried out by Kim and Swanson [101]. The skins are made of carbon/epoxy composite and the core is made of polyurethane foam, with the following material properties: $E_f = 68300$ MPa, $\nu_f = 0.05$, $E_c = 72$ MPa, $\nu_c = 0.3$ and $G_c = 23.2$ MPa. The foam panel and the face sheets are bonded together by means of Hysol EA 9309NA adhesive. The beam length is $l = 152.4$ mm, the core thickness is $h_c = 6.35$ mm, the thickness of the faces is

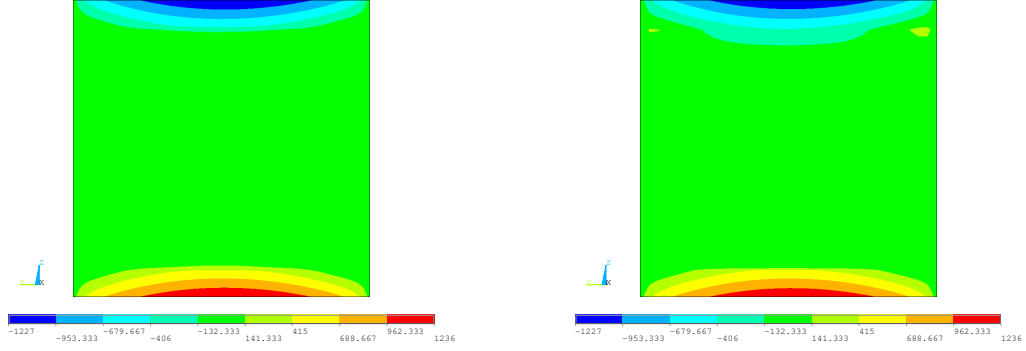


Figure 7.8: Cross-sectional distribution of the shear stress σ_{xy} [Pa] at $x = l/4$ via three-dimensional finite elements (left) and 19th-order B4 one-dimensional elements (right). Doubly-clamped sandwich beam ($l/h = 5$) subjected to an off-centric line load.

$h_f = 0.526$ mm and the width is $b = 25.4$ mm. The applied load versus the displacement evaluated at the center of the cross-section is shown in Fig. 7.9 for a 19th-order theory (B4, 121 nodes), a three-dimensional FEM solution ($40 \times 40 \times 24$ mesh), a Timoshenko's model and experiments. In the linear regime, a fairly accurate match between UF-based

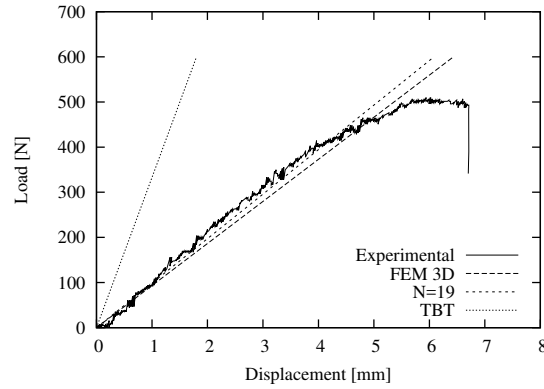


Figure 7.9: Load-displacement response for a sandwich beam with carbon/epoxy composite faces and core layer made of polyurethane foam. Three-point bending test.

refined one-dimensional model and the experimental results is found.

7.3 Thermal stress analysis

The thermo-elastic behavior of three-dimensional composite laminated and functionally graded beam-like structures is studied via UF-based one-dimensional finite elements. The temperature field is obtained by exactly solving the Fourier's heat conduction equation via a Navier-type closed form solution and it is accounted as an external load within the mechanical analysis, as it is done in classical one-way staggered solution procedures [122]). A three-dimensional finite element solution provided by the commercial software Ansys is used for comparison for both the thermal and mechanical analysis, by using the tri-quadratic elements “Solid90” and “Solid186”, respectively. The thermal load leads to a three-dimensional stress state and numerical investigations show that the proposed hierarchical one-dimensional approach yield accurate yet computationally efficient predictions.

7.3.1 Orthotropic laminated beams

A two-layer composite beam is considered, in which the laminae are parallel to the Oxy plane, the fibers in the top layer are aligned to the beam axis and in the bottom layer they are orthogonal to it. Such configuration is referred to as $[0/90]$ lamination stacking sequence. The elastic and thermal material properties are the following: $E_L = 172.72$ GPa, $E_T = 6.91$ GPa, $G_{LT} = 3.45$ GPa, $G_{TT} = 1.38$ GPa, $\nu_{LT} = \nu_{TT} = 0.25$, $K_L = 36.42$ W/mK, $K_T = 0.96$ W/mK, $\alpha_L = 0.57 \cdot 10^{-6} \text{ K}^{-1}$ and $\alpha_T = 35.60 \cdot 10^{-6} \text{ K}^{-1}$, where the subscripts “L” and “T” refer to the longitudinal and transverse direction, respectively, with respect to the fibers. The domain of the beam structure is $[0, l] \times [-a/2, a/2] \times [-b/2, b/2]$ being l the length, b the thickness and a the width, as shown in Figure 7.10. A very short

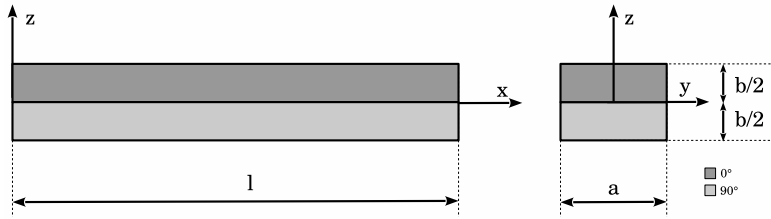


Figure 7.10: Reference system and cross-section of the laminated two-layer beam.

beam is considered, being the slenderness ratio $l/b = 3$, with a square cross-section ($a = b = 1$ m). The applied over-temperature profile varies sinusoidally along the axis direction, with amplitudes $T_{\top} = 400$ K and $T_{\perp} = 300$ K at the top and bottom surfaces of the beam, respectively. The through-the-width variation of the over-temperature is considered to be constant. As far as the computational costs are concerned, the DOFs' number (N_{DOFs}) for the most refined three-dimensional finite elements solution is

about $2.7 \cdot 10^6$, corresponding to a mesh of $60 \times 60 \times 60$ elements used for an accurate description of the thermal stress state, whereas for the most computationally expensive one-dimensional model used in this analysis, which is a 14th-order theory and 121 nodes, N_{DOFs} is about $4.4 \cdot 10^4$. In Fig. 7.11, the through-the-thickness temperature profile $T(z)$ at the mid-span of the beam is shown for different slenderness ratios l/b , showing that the numerical results provided by 3D FEM solution match the Navier-type analytical solution of Fourier's heat conduction equation. By reducing the beam slenderness ($l/b \leq 25$), a non-linear through-the-thickness temperature variation can be observed. The following displacements and stresses are shown in Tables 7.3, 7.4

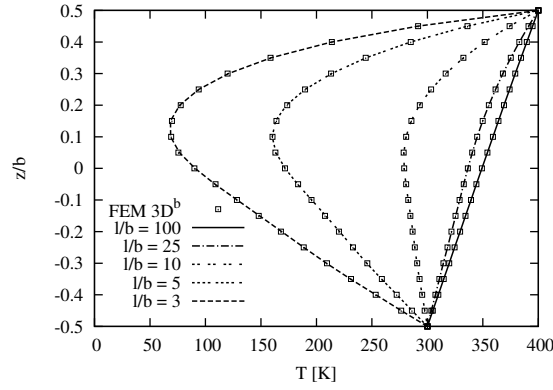


Figure 7.11: Through-the-thickness variation of the over-temperature $T(z)$ [K] at $x = l/2$ for different slenderness ratios l/b .

and 7.5 for a very thick cantilever beam.

$$\begin{aligned}
 \tilde{u}_x &= u_x \left(l, 0, -\frac{b}{2} \right) & \tilde{u}_y &= u_y \left(\frac{l}{2}, \frac{a}{2}, \frac{b}{2} \right) & \tilde{u}_z &= u_z \left(l, 0, \frac{b}{2} \right) \\
 \tilde{\sigma}_{xx} &= \sigma_{xx} \left(\frac{l}{2}, 0, \frac{b}{2} \right) & \tilde{\sigma}_{xz} &= \sigma_{xz} \left(\frac{l}{2}, -\frac{a}{2}, \frac{b}{4} \right) & \tilde{\sigma}_{xy} &= \sigma_{xy} \left(\frac{l}{2}, \frac{a}{4}, \frac{b}{2} \right) \\
 \tilde{\sigma}_{zz} &= \sigma_{zz} \left(\frac{l}{2}, 0, \frac{b}{4} \right) & \tilde{\sigma}_{yy} &= \sigma_{yy} \left(\frac{l}{2}, 0, \frac{b}{2} \right) & \tilde{\sigma}_{yz} &= \sigma_{yz} \left(\frac{l}{2}, -\frac{a}{4}, \frac{b}{4} \right)
 \end{aligned} \tag{7.5}$$

Results that are very close to the three-dimensional solution can be obtained via the proposed family of one-dimensional elements. The relative difference for the displacements obtained via a $N = 9$ B4 is about 0.4%, at worst, with respect to the refined three-dimensional solution, whereas, for the stress components, a relative error of about 1.9% for B3 and B4, at worst, can be achieved. The errors on the shear stresses $\tilde{\sigma}_{xz}$ and $\tilde{\sigma}_{yz}$ obtained via the B2 elements are due to the fact that the one-dimensional finite elements solution has not converged yet for linear elements and $N_n = 121$. Figs. 7.12 to 7.15 present the cross-sectional distribution for the through-the-thickness displacement u_z , axial stress σ_{xx} , and transverse normal stresses σ_{zz} and σ_{yy} obtained via 14th-order

	$10^2 \times \tilde{u}_x$			$10^3 \times \tilde{u}_y$		$10^2 \times \tilde{u}_z$		
FEM 3D-R ^a	1.0544			5.3013		1.2740		
FEM 3D-C ^b	1.0545			5.3012		1.2742		
	B2	B3	B4	B2	B3,B4	B2	B3	B4
$N = 14$	1.0543	1.0542	1.0542	5.3017	5.3014	1.2770	1.2770	1.2770
$N = 11$	1.0540	1.0539	1.0540	5.2874	5.2871	1.2777	1.2777	1.2776
$N = 9$	1.0525	1.0524	1.0524	5.2891	5.2888	1.2789	1.2790	1.2790
$N = 7$	1.0528	1.0527	1.0528	5.1668	5.1665	1.2774	1.2773	1.2773
$N = 4$	1.0424	1.0423	1.0423	5.1206	5.1203	1.2834	1.2835	1.2835
$N = 3$	1.0041	1.0041	1.0041	4.3826	4.3823	1.2085	1.2084	1.2084
$N = 2$	1.0443	1.0443	1.0443	1.3259	1.3259	1.1748	1.1747	1.1747

a: Mesh $40 \times 40 \times 40$. *b*: Mesh $20 \times 20 \times 20$.

Table 7.3: Displacements [m] for a very thick ($l/b = 3$) cantilever two-layer laminated beam. [0/90] stacking sequence.

	$-10^{-8} \times \tilde{\sigma}_{xx}$			$10^{-5} \times \tilde{\sigma}_{xy}$			$10^{-6} \times \tilde{\sigma}_{xz}$		
FEM 3D-R ^a	1.1976			4.6410			2.3747		
FEM 3D-C ^b	1.1942			4.6604			2.3947		
	B2	B3	B4	B2	B3	B4	B2	B3	B4
$N = 14$	1.2013	1.2038	1.2037	3.5669	4.6279	4.6292	2.6051	2.3536	2.3535
$N = 11$	1.1971	1.1996	1.1994	3.5804	4.6404	4.6417	2.5549	2.3022	2.3022
$N = 9$	1.2104	1.2128	1.2127	3.6198	4.6779	4.6792	2.6416	2.3882	2.3882
$N = 7$	1.1768	1.1792	1.1791	3.4760	4.5540	4.5553	2.7151	2.4626	2.4626
$N = 4$	1.2895	1.2920	1.2918	3.7074	4.9019	4.9029	2.2309	1.9837	1.9836
$N = 3$	1.1263	1.1303	1.1303	2.3786	3.4114	3.4127	0.8488	0.6219	0.6219
$N = 2$	1.0907	1.0946	1.0946	0.1218	0.4345	0.4349	0.9138	0.7354	0.7354

a: Mesh $60 \times 60 \times 60$. *b*: Mesh $20 \times 20 \times 20$.

Table 7.4: Axial stress $\tilde{\sigma}_{xx}$ and shear stresses $\tilde{\sigma}_{xy}$ and $\tilde{\sigma}_{xz}$ [Pa] for a very thick ($l/b = 3$) cantilever two-layer laminated beam. [0/90] stacking sequence.

model and cubic elements (B4). Although a fairly accurate description of the displacement field can be obtained with lower-order theories, such a refined model is required for the prediction of the three-dimensional thermal stress state.

7.3.2 Functionally graded beams

Functionally Graded Materials (FGMs) made of metal and ceramic constituents are characterized by high thermal resistance and smooth stress distributions, due to the

	$-10^{-7} \times \tilde{\sigma}_{yy}$			$10^{-6} \times \tilde{\sigma}_{zz}$			$-10^{-6} \times \tilde{\sigma}_{yz}$	
FEM 3D-R ^a	4.0689			4.8927			3.0258	
FEM 3D-C ^b	3.9995			4.9166			3.0501	
	B2	B3	B4	B2	B3	B4	B2	B3, B4
$N = 14$	4.0824	4.0832	4.0832	4.9833	4.9831	4.9832	3.0698	3.0696
$N = 11$	4.0635	4.0643	4.0643	5.0429	5.0427	5.0427	2.8530	2.8528
$N = 9$	4.2319	4.2327	4.2327	4.4578	4.4577	4.4577	3.1068	3.1067
$N = 7$	3.9861	3.9869	3.9869	4.5607	4.5607	4.5607	3.3787	3.3785
$N = 4$	3.0560	3.0569	3.0569	9.7645	9.7645	9.7646	1.9877	1.9876
$N = 3$	4.6257	4.6267	4.6267	18.790	18.789	18.790	1.6755	1.6754
$N = 2$	10.214	10.214	10.214	19.781	19.781	19.781	0.1973	0.0197

a: Mesh $60 \times 60 \times 60$. *b*: Mesh $20 \times 20 \times 20$.

Table 7.5: Normal stresses $\tilde{\sigma}_{yy}$, $\tilde{\sigma}_{zz}$ and shear stress $\tilde{\sigma}_{yz}$ [Pa] for a very thick ($l/b = 3$) cantilever two-layer laminated beam. [0/90] stacking sequence.

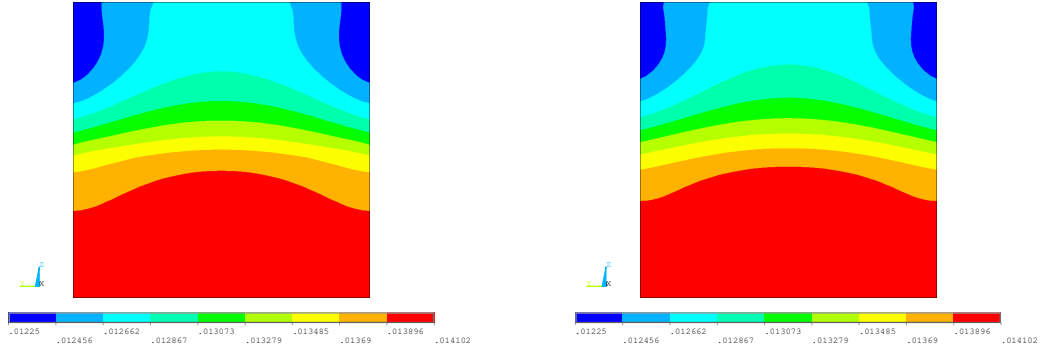


Figure 7.12: Cross-sectional distribution of the through-the-thickness displacement u_z [m] at $x = l/2$ via three-dimensional finite elements (left) and 14th-order B4 one-dimensional elements (right). Very thick ($l/b = 3$) laminated cantilever beam.

gradual variation of the material properties. These features make them good candidates for structural applications in a high temperature environment. In this study, the thermo-elastic response of beam-like structures made of FGM are investigated considering a power law variation of the material properties (both elastic and thermal coefficients) along the thickness direction. As shown in Fig. 7.16, the beam domain is $[0, l] \times [0, a] \times [0, b]$. As in the previous case studies, a square cross-section is considered ($a = b = 1$ m). A ceramic-metal material is considered, being Zirconia (ZrO_2) the ceramic constituent and Monel (70Ni-30Cu) the metallic one, whose materials properties

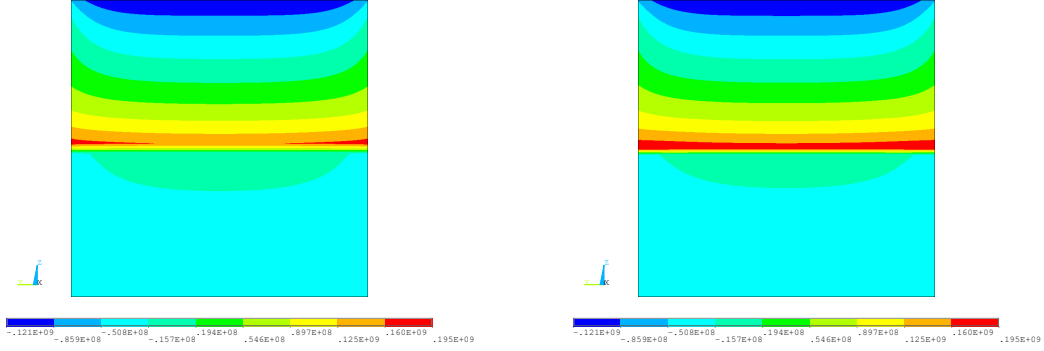


Figure 7.13: Cross-sectional distribution of the axial stress σ_{xx} [Pa] at $x = l/2$ via three-dimensional finite elements (left) and 14th-order B4 one-dimensional elements (right). Very thick ($l/b = 3$) laminated cantilever beam.

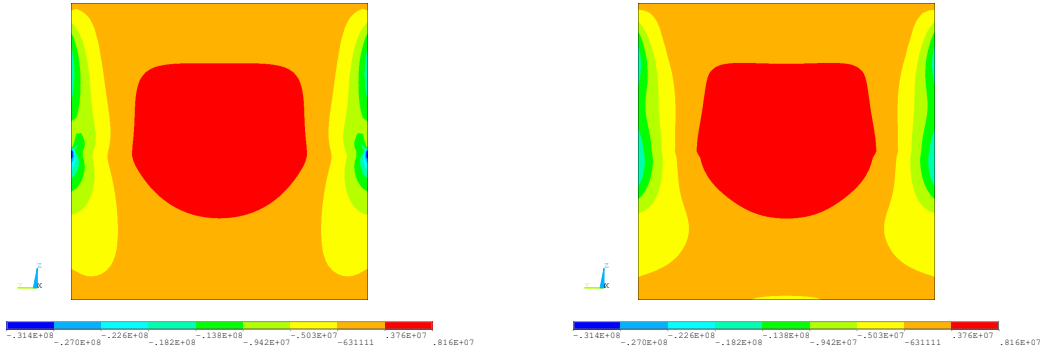


Figure 7.14: Cross-sectional distribution of the through-the-thickness normal stress σ_{zz} [Pa] at $x = l/2$ via three-dimensional finite elements (left) and 14th-order B4 one-dimensional elements (right). Very thick ($l/b = 3$) laminated cantilever beam.

are given in Table. 7.6. By assuming a power law for the volume fraction gradation of the constituent materials and applying the mixture rule, see Praveen and Reddy [136] and Chakraborty et al. [48], the generic material property f will also vary along the thickness coordinate z according to a power law with order n_z :

$$f = (f_1 - f_2) (\alpha_z z + \beta_z)^{n_z} + f_2 \quad (7.6)$$

where f_i is the generic property of each constituent material. Due to the choice of the reference system, $\alpha_z = 1/b$ and $\beta_z = 0$. In the following analyses, different values for the gradation law order n_z are considered. As far as the boundary conditions of the thermal problem are concerned, a sinusoidal variation of the applied over-temperature

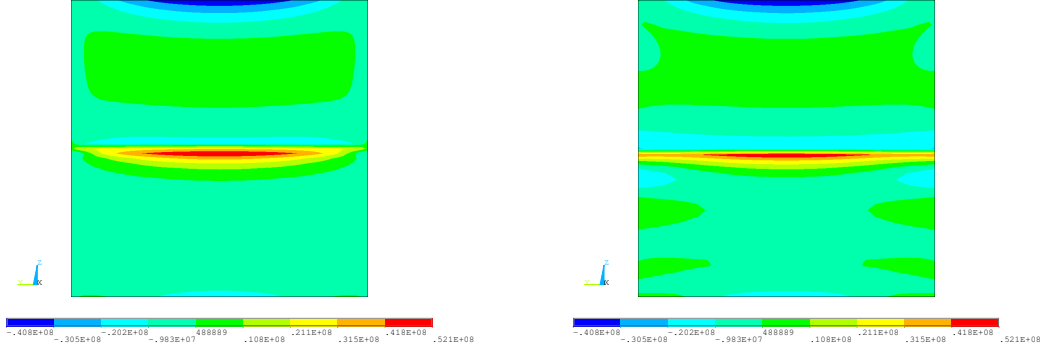


Figure 7.15: Cross-sectional distribution of the through-the-width normal stress σ_{yy} [Pa] at $x = l/2$ via three-dimensional finite elements (left) and 14th-order B4 one-dimensional elements (right). Very thick ($l/b = 3$) laminated cantilever beam.

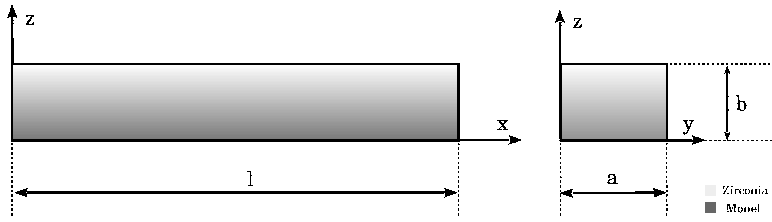


Figure 7.16: Adopted reference system and geometry of the FGM beam.

along the axis direction is considered, being $T_t = 150$ K and $T_b = 50$ K the amplitudes at the beam top surface ($z = b$) and bottom surface ($z = 0$). Within the three-dimensional FEM solution that is used for validation purposes, the FGM is modeled by assigning to each finite element the material properties computed at its central point according to the Eq. (7.6). Therefore, a refined finite elements discretization is needed for both an accurate approximation of the material variation law as well as an accurate mechanical response prediction. About the computational costs, a 13th-order theory and 121 nodes is the highest-order one-dimensional model used in this study, corresponding to about $3.8 \cdot 10^4$ N_{DOFs} , whereas N_{DOFs} are about $2.7 \cdot 10^6$ for a refined three-dimensional mesh with $60 \times 60 \times 60$ elements and about $1.1 \cdot 10^5$ for a coarse 3D FEM solution with $20 \times 20 \times 20$ elements. The through-the-thickness distribution of the temperature field at the mid-span of the beam ($x = l/2$) is given in Fig. 7.17 for a slender ($l/b = 100$) and for a thick beam ($l/b = 5$). The analytical solution of the Fourier's heat conduction equation, which is thoroughly described in De Pietro et al. [61], is in good agreement with the temperature field provided by the refined 3D FEM solution. Concerning the mechanical response of the structure to the applied thermal load, the displacements for a very thick beam ($l/b = 5$) with a linear material gradation ($n_z = 1$) are shown in

	E [GPa]	ν	K [W/mK]	α [10^{-6} K $^{-1}$]
Zirconia	151.01	0.300	2.09	10.
Monel	179.40	0.368	25.00	15.

Table 7.6: Elastic and thermal properties of the FGM constituents materials.

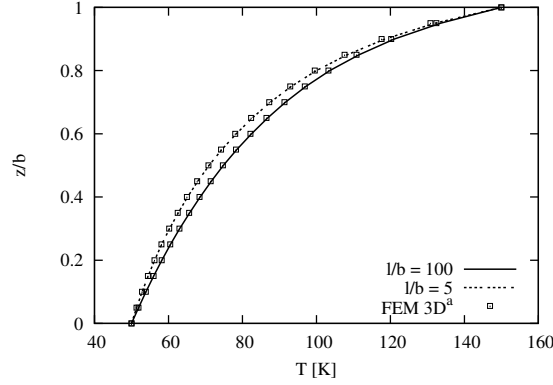

 Figure 7.17: Through-the-thickness profile of the over-temperature $T(z)$ [K] at $x = l/2$ for slender and thick FGM beam-like structures. $n_z = 1$.

Table 7.7. The relative error provided by one-dimensional models with expansion order N as low as 4 with respect to the benchmark results is about 1.6%, whereas for the stress components a 13th-order model and cubic shape functions are required in order to achieve a relative error of 3.3%, as shown in Tables 7.8 and 7.9. Previous tabular results refer to the following evaluation points for displacements and stresses:

$$\begin{aligned}
 \bar{u}_x &= u_x \left(l, \frac{a}{2}, b \right) & \bar{u}_y &= u_y \left(\frac{l}{2}, a, b \right) & \bar{u}_z &= u_z \left(l, \frac{a}{2}, \frac{b}{2} \right) \\
 \bar{\sigma}_{xx} &= \sigma_{xx} \left(\frac{l}{2}, \frac{a}{2}, \frac{b}{4} \right) & \bar{\sigma}_{xy} &= \sigma_{xy} \left(\frac{l}{4}, \frac{a}{4}, b \right) & \bar{\sigma}_{xz} &= \sigma_{xz} \left(\frac{l}{4}, \frac{a}{2}, \frac{b}{2} \right) \\
 \bar{\sigma}_{yy} &= \sigma_{yy} \left(\frac{l}{2}, \frac{a}{2}, \frac{b}{2} \right) & \bar{\sigma}_{zz} &= \sigma_{zz} \left(\frac{l}{2}, \frac{a}{2}, \frac{b}{2} \right) & \bar{\sigma}_{yz} &= \sigma_{yz} \left(\frac{l}{2}, \frac{a}{4}, \frac{3}{4}b \right)
 \end{aligned} \tag{7.7}$$

The cross-sectional variation of the shear stresses σ_{xy} and σ_{yz} are presented in Figs. 7.18 and 7.19 for different types of material gradation law ($n_z = 0.5$, $n_z = 1$ and $n_z = 2$), showing that higher-order theories such as $N = 13$ yield accurate yet computationally efficient results.

7.4 Mechanical analysis of curved beams

In this section, closed-form and weak-form finite element solutions based on Unified Formulation are shown for the prediction of the mechanical behavior of three-dimensional curved beams. Straight finite elements with a very refined discretization

	$-10^3 \times \bar{u}_z$			$10^3 \times \bar{u}_x$			$10^4 \times \bar{u}_y$		
FEM 3D-R ^a	4.6144			3.9723			6.9765		
FEM 3D-C ^b	4.6669			3.9899			7.0240		
	B2	B3	B4	B2	B3	B4	B2	B3	B4
$N = 13$	4.6893	4.6895	4.6896	3.9986	3.9985	3.9984	7.0261	7.0255	7.0256
$N = 11$	4.6893	4.6895	4.6896	3.9986	3.9984	3.9984	7.0229	7.0223	7.0224
$N = 8$	4.6894	4.6896	4.6897	3.9988	3.9986	3.9986	7.0124	7.0119	7.0119
$N = 4$	4.6867	4.6868	4.6869	3.9953	3.9952	3.9952	6.8768	6.8763	6.8763
$N = 2$	4.5242	4.5243	4.5243	3.9814	3.9814	3.9814	6.1463	6.1458	6.1458

a: Mesh $60 \times 60 \times 60$. b: Mesh $20 \times 20 \times 20$.

Table 7.7: Displacements [m] \bar{u}_z , \bar{u}_x and \bar{u}_y . Very thick ($l/b = 5$) metal-ceramic FGM ($n_z = 1$) cantilever beam.

	$10^{-6} \times \bar{\sigma}_{xx}$			$-10^{-6} \times \bar{\sigma}_{xy}$			$10^{-6} \times \bar{\sigma}_{xz}$		
FEM 3D-R ^a	8.5121			2.3812			1.4490		
FEM 3D-C ^b	8.7014			2.4166			1.4815		
	B2	B3	B4	B2	B3	B4	B2	B3	B4
$N = 13$	8.7749	8.8410	8.7890	2.2846	2.4063	2.4050	0.9233	1.4857	1.4767
$N = 11$	8.8734	8.9397	8.8875	2.3079	2.4295	2.4282	0.9185	1.4810	1.4719
$N = 9$	8.8864	8.9524	8.9005	2.3342	2.4558	2.4545	0.9242	1.4867	1.4775
$N = 7$	8.8520	8.9185	8.8661	2.4193	2.5414	2.5398	0.9178	1.4803	1.4712
$N = 4$	6.3049	6.3715	6.3191	1.2997	1.4227	1.4217	0.7969	1.3593	1.3502
$N = 2$	22.250	22.315	22.264	1.9555	2.0653	2.0634	-0.5945	-0.0544	-0.0632

a: Mesh $60 \times 60 \times 60$. b: Mesh $20 \times 20 \times 20$.

Table 7.8: Stresses [Pa] $\bar{\sigma}_{xx}$, $\bar{\sigma}_{xy}$ and $\bar{\sigma}_{xz}$. Very thick ($l/b = 5$) metal-ceramic FGM ($n_z = 1$) cantilever beam.

are often used in order to approximate curved geometries and model curved structural components. Computationally more efficient solutions can be obtained by developing models accounting for the curvature of the structure. Nevertheless, curved beam elements exhibit locking phenomena that can compromise the accuracy of the results and the convergence performance of the element. In this study, locking is tackled via a correction strategy based on the Mixed Interpolation of Tensorial Components (MITC). For validation purposes, displacement and stress components are assessed through comparison with benchmark results from the literature, elasticity solutions and commercial software finite elements showing that a correct mechanical response of curved beams can be efficiently obtained via UF-based one-dimensional models. The domain of the beam structure in curvilinear coordinate is $[0, l] \times [-h/2, h/2] \times [-b/2, b/2]$, as shown in Figure 7.20. Homogeneous isotropic beams are considered with material properties $E = 30$ GPa and $\nu = 0.17$.

	$10^{-6} \times \bar{\sigma}_{yy}$			$10^{-6} \times \bar{\sigma}_{zz}$			$-10^{-6} \times \bar{\sigma}_{yz}$		
FEM 3D-R ^a	4.7895			6.3625			4.0032		
FEM 3D-C ^b	4.8667			6.4935			4.1018		
	B2	B3	B4	B2	B3	B4	B2	B3	B4
$N = 13$	4.9357	4.9494	4.9233	6.4854	6.4990	6.4729	4.0826	4.0824	4.0824
$N = 11$	5.0384	5.0522	5.0260	6.6774	6.6911	6.6649	4.0817	4.0815	4.0815
$N = 9$	5.0554	5.0688	5.0430	6.6990	6.7124	6.6865	4.0295	4.0293	4.0293
$N = 7$	4.9819	4.9961	4.9695	6.6645	6.6787	6.6521	3.9214	3.9212	3.9212
$N = 4$	1.9724	1.9868	1.9602	1.9703	1.9847	1.9581	1.7367	1.7366	1.7366
$N = 2$	26.398	26.411	26.385	26.845	26.857	26.832	0.0552	0.0552	0.0055

a: Mesh $60 \times 60 \times 60$. b: Mesh $20 \times 20 \times 20$.

Table 7.9: Stresses [Pa] $\bar{\sigma}_{yy}$, $\bar{\sigma}_{zz}$ and $\bar{\sigma}_{yz}$. Very thick ($l/b = 5$) metal-ceramic FGM ($n_z = 1$) cantilever beam.

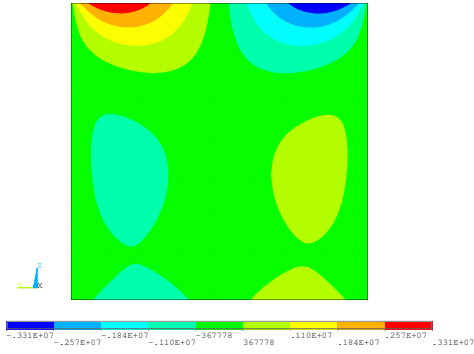
7.4.1 Convergence performance

Under the assumption of a plane stress state, simply supported circular arches are herein investigated, in order to evaluate the convergence performance of the proposed formulation. The beam thickness and width are $h = 0.6$ m and $b = 0.4$ m, respectively, whereas an opening angle $\Phi = \frac{2}{3}\pi$ is considered. Tables 7.10 and 7.11 show the transverse displacement evaluated at ($s = l/2, \xi = 0$) for a very thick ($l/h = 5$) and a very slender beam ($l/h = 1000$) subjected to a uniform pressure $p_\xi = 1$ Pa at the top surface ($\xi = h/2$). The reference solution is an exact Navier-type closed form solution, also

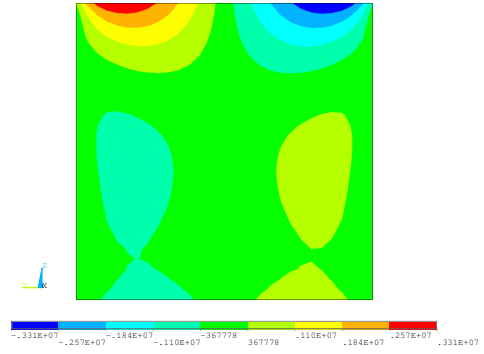
	$10^9 \times u_\xi$	
Navier	8.0640	
N_e	B4	MITC4
60	8.0640	8.0640
40	8.0640	8.0640
20	8.0640	8.0640
10	8.0640	8.0640
8	8.0640	8.0640
6	8.0639	8.0640
4	8.0627	8.0640
2	7.9893	8.0619

Table 7.10: Transverse displacement u_ξ [m] versus number of elements N_e . Very thick simply supported circular beam. 2nd-order UF-based model (TE2).

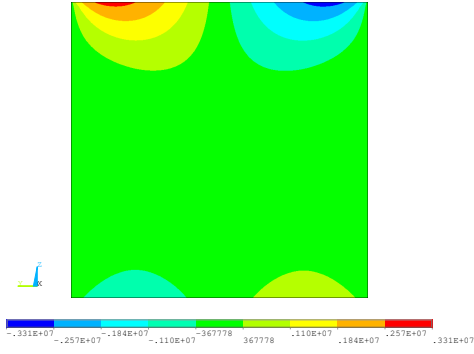
developed in the framework of Unified Formulation. Classical cubic elements (B4) and



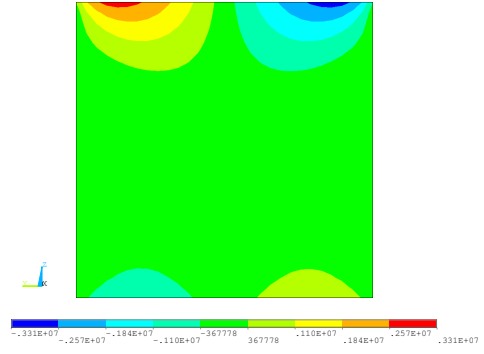
FEM 3D-R, $n_z = 0.5$



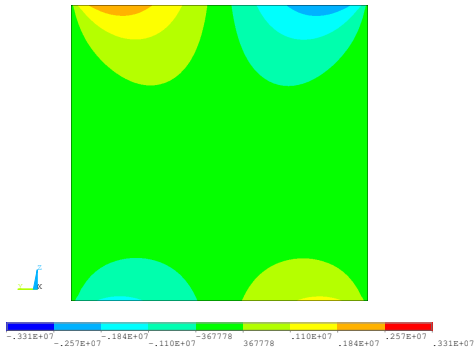
N=13, $n_z = 0.5$



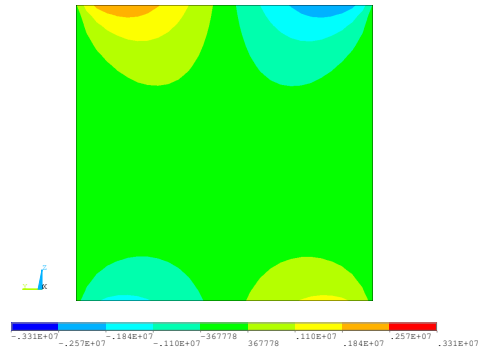
FEM 3D-R, $n_z = 1$



N=13, $n_z = 1$

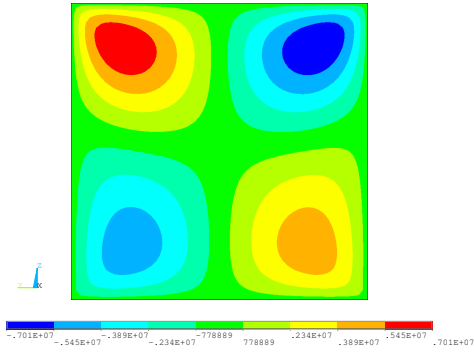


FEM 3D-R, $n_z = 2$

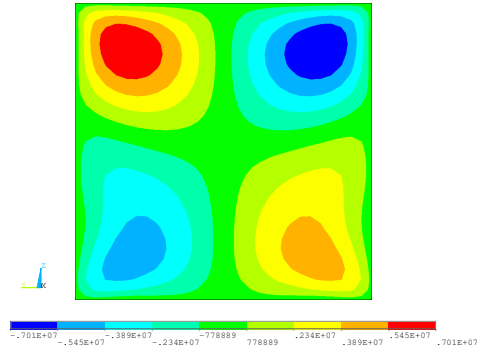


N=13, $n_z = 2$

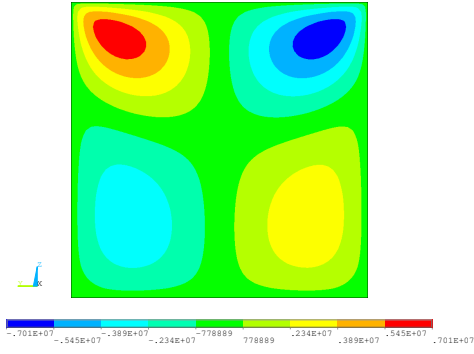
Figure 7.18: Shear stress σ_{xy} [Pa] at $x = l/4$. Very thick ($l/b = 5$) metal-ceramic FGM cantilever beam.



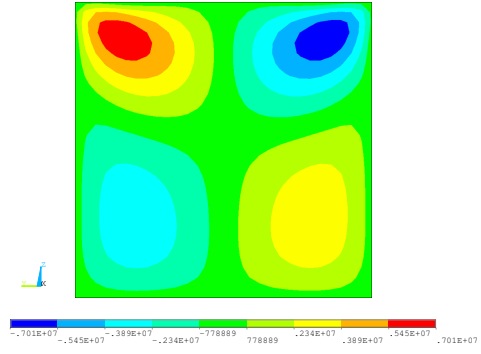
FEM 3D-R, $n_z = 0.5$



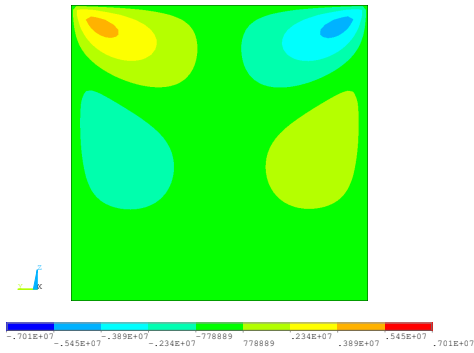
N=13, $n_z = 0.5$



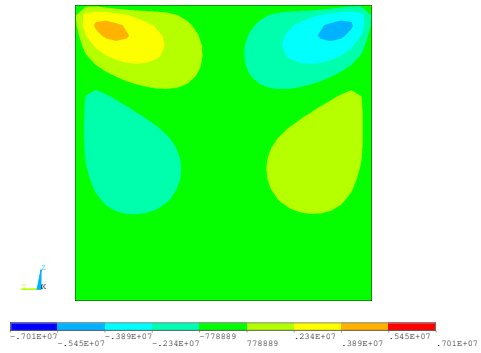
FEM 3D-R, $n_z = 1$



N=13, $n_z = 1$



FEM 3D-R, $n_z = 2$



N=13, $n_z = 2$

Figure 7.19: Shear stress σ_{yz} [Pa] at $x = l/2$. Very thick ($l/b = 5$) metal-ceramic FGM cantilever beam.

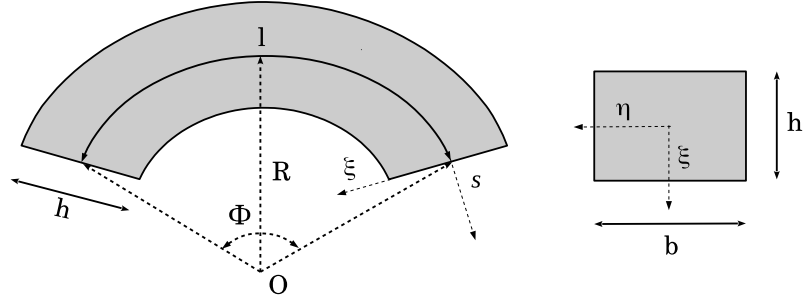


Figure 7.20: Adopted reference system, geometry and cross-section of a thick arch structure.

u_ξ		
Navier	10.1613	
N_e	B4	MITC4
60	10.1613	10.1613
40	10.1613	10.1613
20	10.1587	10.1613
10	10.0565	10.1613
8	9.9082	10.1613
6	9.5641	10.1613
4	8.7190	10.1613
2	5.8122	10.1587

Table 7.11: Transverse displacement u_ξ [m] versus number of elements N_e . Very thick simply supported circular beam. 2nd-order UF-based model (TE2).

MITC-based cubic elements (MITC4) are compared, being N_e the number of elements. A significant improvement on the convergence rate of the beam element can be observed due to the MITC-based locking correction technique. In fact, the radial component of the displacement can be exactly predicted with only 4 curved cubic MITC-corrected elements instead of 40 elements required if standard cubic beam elements were considered. The presented results are obtained for a 2nd-order beam theory based on Taylor expansion (TE2), nevertheless similar behavior is obtained for different order of the theory and different expansion base functions.

7.4.2 Circular thick arch

The validation of the displacement and stress field prediction obtained via UF-based modeling approach towards literature results and elasticity solutions is provided here. Plane stress hypothesis is assumed and, therefore, bi-quadratic 8-node two-dimensional Ansys elements “Plane183” are used for further comparison. The most computationally expensive UF-based model used in this study is a 5th-order theory and 121 nodes, either within a Hierarchical Legendre expansion (HL5) or Taylor expansion (TE5), for which N_{DOFs} is equal to 1452. For the two-dimensional finite elements solution used for validation (120×24 elements), $N_{DOFs} = 70274$.

Validation towards literature

A doubly-clamped beam with rectangular cross-section ($h = 0.6$ m and $b = 0.4$ m), constant radius of curvature $R = 4$ m and opening angle $\Phi = 2/3\pi$ is studied. Two different loading conditions are considered: a concentrated force $F = 1000$ N applied at the mid-span central point of the beam ($s = l/2$, $\xi = 0$) and a uniform transverse load per unit length along the beam axis $p_\xi b = 1000$ N/m applied at $\xi = 0$. Table 7.12 presents the dimensionless displacement components $\tilde{u} = u/l$ evaluated at the mid-span bottom point ($s = l/2$, $\xi = -h/2$) provided by the proposed UF-based finite elements as well as literature results provided by Tupecki and Arpaci [159], Litewka and Rakowski [111] and Ansys two-dimensional plane stress finite elements. Through UF-

	Radial force F_ξ $10^6 \times \tilde{u}_\xi$	Axial force F_s $10^6 \times \tilde{u}_s$	Uniform pressure $p_\xi b$ $10^5 \times \tilde{u}_\xi$
PLANE183	0.2456	0.1488	0.1183
Tufekci and Arpaci [159]	0.2205 ^a 0.2488 ^b	0.1412 ^a 0.1537 ^b	- -
Litewka and Rakowski [111]	0.2205 ^a 0.2488 ^b	0.1412 ^a 0.1537 ^b	0.1190 ^a 0.1180 ^b
TE5	0.2458	0.1493	0.1183
TE4	0.2457	0.1492	0.1183
TE3	0.2448	0.1478	0.1183
TE2	0.2410	0.1457	0.1185

a: Axial deformation only. *b*: Axial and shear deformation.

Table 7.12: Dimensionless axial and radial displacements \tilde{u}_s and \tilde{u}_ξ . Thick doubly-clamped circular beam subjected to different in-plane loading conditions.

based higher-order theories, shear and localized deformations can be accounted for, allowing to obtain displacement predictions with errors being lower than 0.1% for the

concentrated radial load and as high as 0.3% for the concentrated axial load, with respect to the two-dimensional reference solution.

Validation towards elasticity solution

An elasticity solution provided by Timoshenko and Goodier [156] is used as a reference for the stress analysis of a cantilever circular beam with radius of curvature $R = 1$ m, opening angle $\Phi = \pi/2$ and square cross-section ($h = b = l/10$). A concentrated radial load $F_\xi = 1$ N is applied at the beam free end ($s = l, \xi = 0$). The distribution of the dimensionless stresses $\tilde{\sigma} = \sigma bh/(F_\xi \sqrt{2})$ at $s = l/2$ versus the dimensionless thickness coordinate $\tilde{\xi} = \xi/h$ is given in Figure 7.21, showing that, unlike classical beam models, higher-order theories, such as TE5, lead to the exact prediction of the through-the-thickness distribution of all the stresses, including axial, shear and radial components.

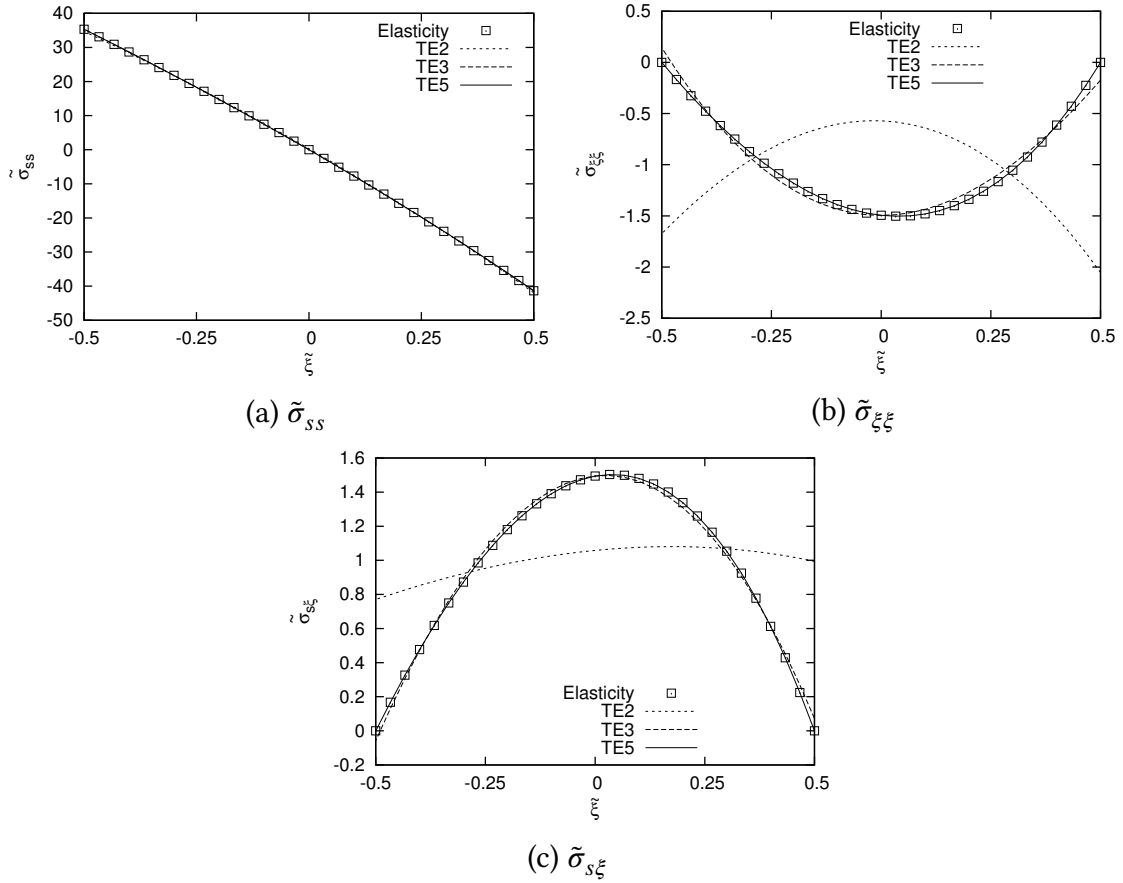


Figure 7.21: Dimensionless axial, radial and shear stress components at $s = l/2$. Thick cantilever circular arch.

7.4.3 Three-dimensional balcony structure

As a last case study, a semi-circular balcony is studied, in order to assess the capability of the proposed approach to predict the mechanical behavior of curved structural components subjected to out-of-plane loadings in a more general three-dimensional case. Radius of curvature $R = 3$ m, opening angle $\Phi = \pi$ and square cross section ($h = b = 0.3$ m) are chosen. Clamped-clamped boundary conditions and a uniform line load $l_\eta = 5$ kN/m are applied, see Figure 7.22. Within the framework of the Unified

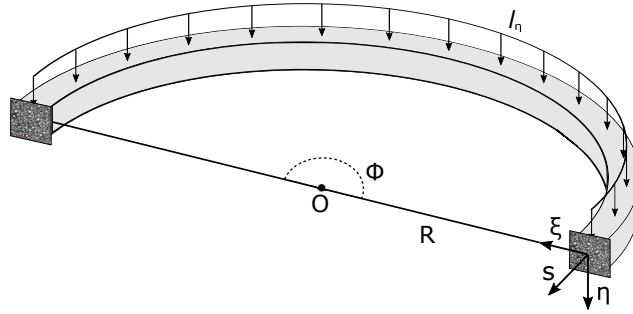


Figure 7.22: Semi-circular three-dimensional balcony structure subjected to a uniform out-of-plane line load.

Formulation, a Hierarchical Legendre (HL) expansion for the cross-sectional kinematics is used and results are validated towards Abaqus “C3D8” linear three-dimensional elements. N_{DOFs} is about 4.2×10^2 for the HL5 beam model and 61 nodes, which is the most refined UF-based one-dimensional model used in this analysis, whereas N_{DOFs} is about 2.8×10^5 for the three-dimensional solution used as a reference, with a mesh of $200 \times 10 \times 10$ elements. The variation of the transverse displacement along the arch axis is shown in Figure 7.23 for the Abaqus brick elements, for the proposed hierarchical one-dimensional finite elements based on Legendre expansions as well as for a reference literature result provided by Zhang et al. [173]. Finally, the three-dimensional distribution of the axial stress σ_{ss} and transverse shear stresses $\sigma_{s\eta}$ and $\sigma_{s\xi}$ obtained via a fifth-order HL5 model is shown in Figure 7.24. By enriching the beam cross-sectional kinematics in the framework of the Unified Formulation, the mechanical response of thick curved beam-like structures in terms of both displacements and stresses can be predicted with a solid-like accuracy, at reduced computational costs with respect to three-dimensional commercial software finite elements. Full details about the extension of UF-based one-dimensional models to the study of curved beam-like structures can be found in [132], whereas the application of such formulation to the stress analysis

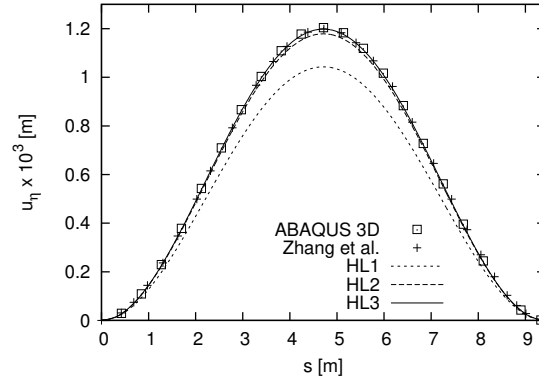


Figure 7.23: Longitudinal variation of the transverse displacement u_{η} . Out-of-plane line load. Three-dimensional semi-circular balcony structure.

in curved laminates and 3D micro-mechanics analysis of fiber-reinforced composites is reported in the companion paper by de Miguel et al. [119].

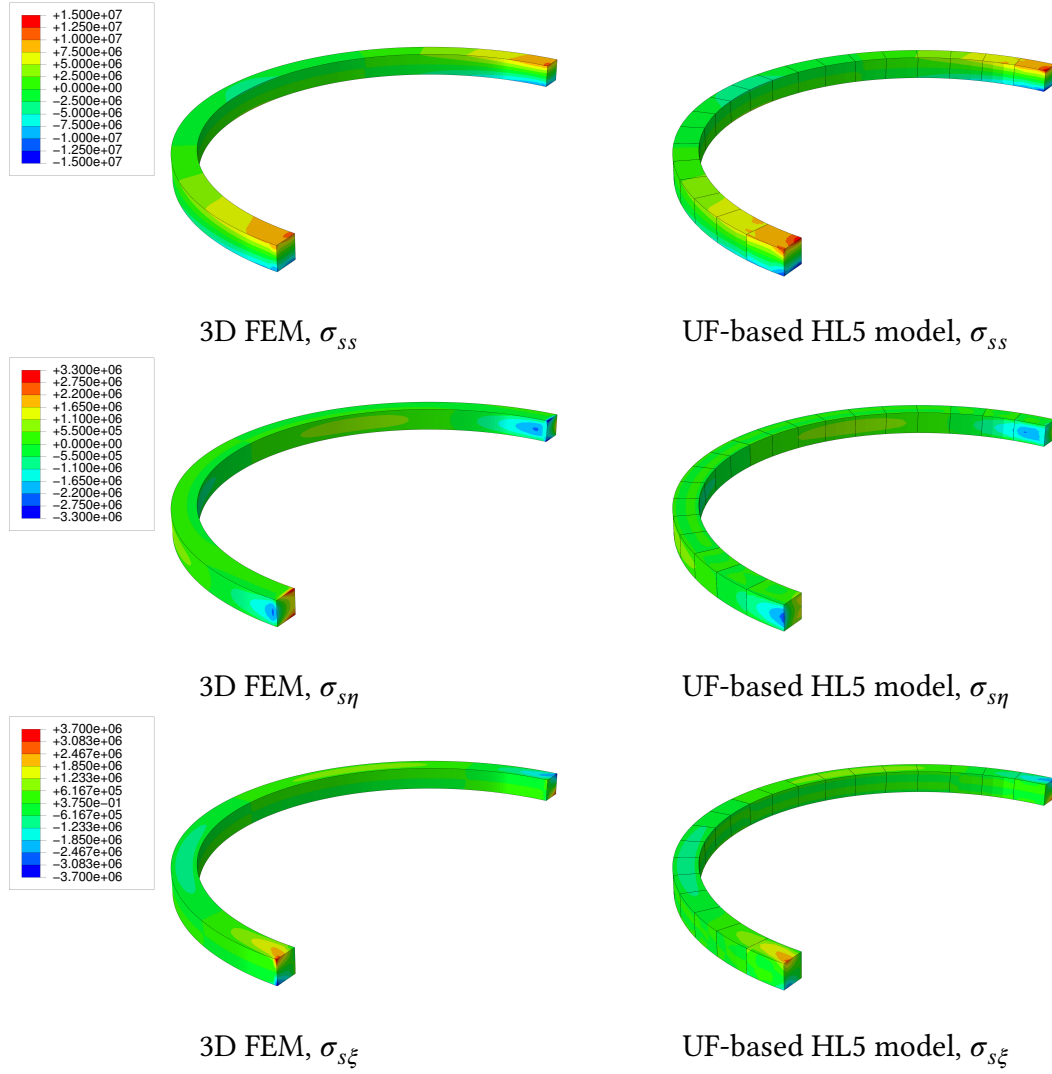


Figure 7.24: Axial and transverse shear stress distributions. Out-of-plane line load. Three-dimensional semi-circular balcony structure.

Chapter 8

Large Deflection and Bistability Analysis

8.1 Introduction

By means of the UF-based advanced one-dimensional finite elements formulation developed in Chapter 6 within the framework of a total Lagrangian formulation and under small strains hypothesis, geometrically non-linear structural problems are investigated in this chapter. Large deflection of metallic and multi-layered beams is addressed in Section 8.2, whereas Section 8.3 focuses on the study of pre-buckled bistable beams with different material properties, slenderness ratios and boundary conditions. Thanks to the UF-approach, several advanced one-dimensional models featuring an enriched kinematic field can be straightforwardly formulated within the same mathematical framework. Validation of the proposed modeling approach towards reference solutions and commercial software finite elements is provided. Refined non-linear equilibrium paths can be achieved by hierarchically enriching the cross-sectional displacement field with no need to resort to computationally expensive two- or three-dimensional finite elements. Furthermore, the stress prediction capabilities (including axial, transverse shear and normal stresses) in strongly non-linear regime such as post-buckling and snap-through analyses are demonstrated, showing that the presented UF-based hierarchical framework can represent a viable alternative to state-of-the-art modeling solutions as implemented in commercial software finite elements for a safe yet efficient design of multi-stable composite structures. Some of the work described hereafter has been previously published in [93].

8.2 Beam-like structures under large deflection

In the following results, N -order Taylor's polynomials are used as expansion functions through the thickness in the framework of an Equivalent Single Layer approach, unless stated otherwise. A locking correction strategy based on the Mixed Interpolation of Tensorial Components has been implemented. The weak form of the non-linear governing equations is derived by means of the PVD and they are solved via a classical Newton-Raphson procedure, see Subsection 6.8.1. Besides the polynomial order N , the number of nodes per element N_n^e is also a free input parameter within the present formulation. Linear (B2), quadratic (B3) and cubic (B4) elements are considered hereafter. The support of the beam is $[0, l] \times [-h/2, h/2] \times [-b/2, b/2]$. Both displacements and stresses are computed in the fixed global coordinate system, see Figure 3.1.

8.2.1 Metallic structures

Slender ($l/h = 100$) as well as thick beams ($l/h = 10$) made of aluminium ($E = 75$ GPa and $\nu = 0.33$) with square cross-sections ($h = b = 1$ m) are first studied. Cantilever, doubly-clamped and simply supported boundary conditions are considered. The external load is a concentrated force P_z applied at ($x/l = 1$, $z/h = 0$) for cantilever beams and ($x/l = 1/2$, $z/h = 0$) for doubly-clamped and simply supported cases. A dimensionless form of the external load is adopted:

$$\lambda = \frac{P_z l^2}{EI} \quad (8.1)$$

where I is the moment of inertia of the cross-section.

The results provided by the presented UF-based advanced one-dimensional finite elements formulation are compared with two-dimensional small-strain finite elements solution developed within a total Lagrangian formulation, see Hu et al. [89], and referred to as "FEM 2D TL". Classical one-dimensional solutions from the literature as well as Ansys one-dimensional co-rotational finite elements "Beam3" based on both Euler-Bernoulli's (EBT) and Timoshenko's beam theory (TBT) are used for comparison. Finally, results provided by large-strain Ansys two-dimensional finite elements "Plane183" are also reported, for the sake of completeness. As far as the computational costs of the proposed approach are concerned, a fifth-order theory ($N = 5$) with 121 nodes, which represents the most refined UF-based model used in this numerical investigation, corresponds to $1.5 \cdot 10^3$ degrees of freedom (N_{DOFs}). On the other hand, a mesh of 240×24 two-dimensional finite elements, used for an accurate stress field prediction in both thick and slender structures, corresponds to N_{DOFs} equal to about $3.6 \cdot 10^4$. Since a full Newton-Raphson solution procedure is used, the tangent stiffness matrix needs to be assembled and inverted at each iteration within a single load step, therefore such computational advantage can be achieved at each iteration.

Locking and convergence assessment

Due to membrane and shear locking phenomena, the performance of non-linear one-dimensional finite elements could be strongly degraded, unless proper correction strategies are implemented. Such numerical phenomena are even more evident in the analysis of very slender structures by means of finite elements with low-order shape functions [113, 138]. A locking correction technique based on Mixed Interpolation of Tensorial Components (MITC) has been developed in this work. The locking phenomenon in linear finite elements (B2) for increasing slenderness ratios l/h and the effectiveness of MITC-based mitigation technique is shown in Fig. 8.1, where $\hat{u}_z = u_z/u_z^{\text{Cubic}}$ is the normalized transverse displacement with respect to the converged solution u_z^{Cubic} obtained with 40 cubic (B4) elements. By looking at the results for $N = 2$ and $N = 5$,

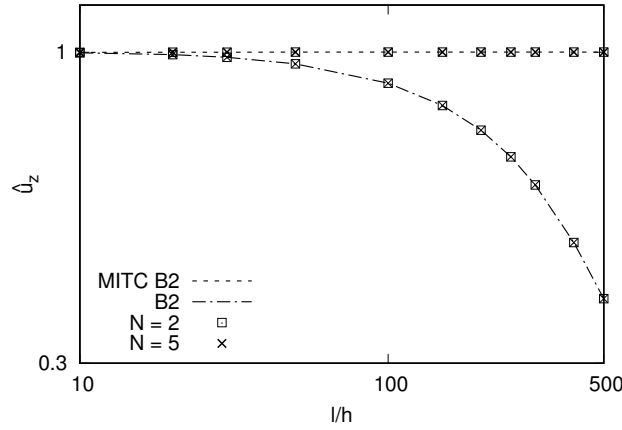


Figure 8.1: Locking phenomenon in linear elements for increasing slenderness ratios and effectiveness of the MITC-based correction method. Doubly-clamped boundary conditions. $\lambda = 2$. \hat{u}_z computed at $(l/2, -h/2)$.

it is worth mentioning that the enrichment of the cross-sectional kinematics via UF neither influence the locking phenomenon nor the effectiveness of its correction. Results for different boundary conditions are qualitatively similar to Fig. 8.1 and they are not reported, for the sake of brevity. In Figure 8.2 it is shown that the locking correction via MITC also leads to a significant improvement of convergence rate in slender beams. \hat{u}_z is the normalized transverse displacement as defined before and N_n is the total number of nodes. Reference solution u_z^{Cubic} for normalization of \hat{u}_z is here obtained with 140 cubic (B4) one-dimensional finite elements. Convergence improvement is even more evident for beam elements with lower-order shape functions, such as linear (B2) or quadratic (B3) elements. As it can be noticed from Fig. 8.2, a classical monotonic convergence “from below” is no longer ensured when finite elements adopting MITC are considered [107]. From the convergence study, a total number of nodes $N_n = 121$ will be used for the following numerical results.

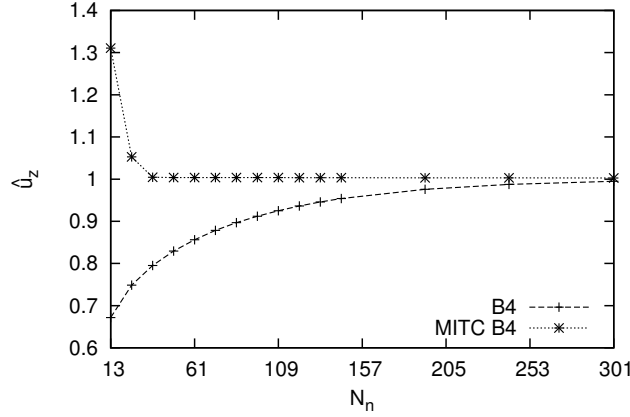


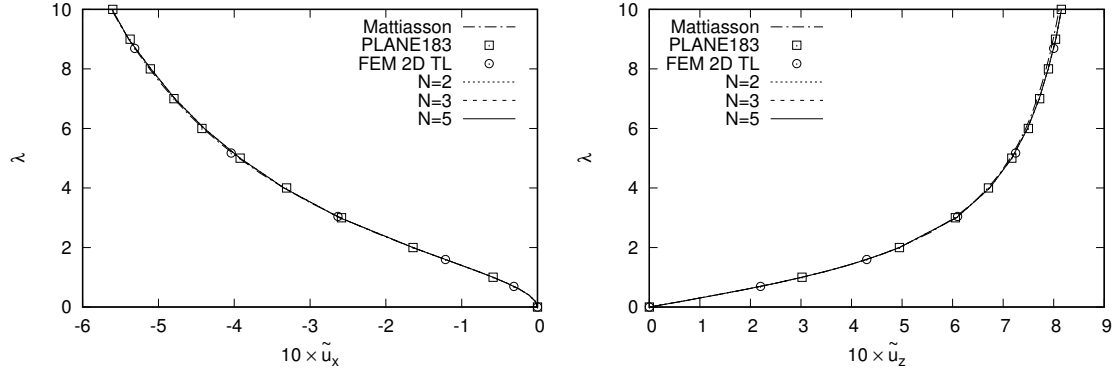
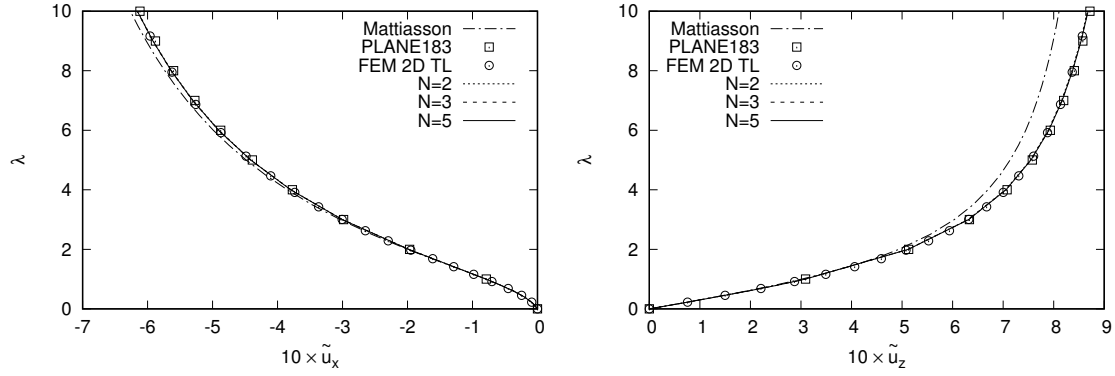
Figure 8.2: Convergence analysis for classical and MITC-based cubic one-dimensional finite elements. Simply supported beam ($l/h = 100$). $\lambda = 3$. \hat{u}_z evaluated at $(l/2, h/2)$.

Cantilever beam

In order to validate the proposed approach with respect to classical beam models, a slender beam structure ($l/h = 100$) has been considered. Cantilever boundary conditions are applied. Displacements and Cauchy stresses expressed in the fixed global reference system are given in a dimensionless form:

$$\begin{aligned} \tilde{u}_i &= u_i/l \\ \tilde{\sigma}_{ij}^g &= \sigma_{ij}^g \frac{2I}{P_z l h} \end{aligned} \quad (8.2)$$

Dimensionless thickness coordinate $\tilde{z} = z/h$ is also considered. Cubic beam elements (B4) have been used for the plots, whereas linear (B2), quadratic (B3) and cubic (B4) elements have been compared in the tables. In Figure 8.3 the evolution of the axial and transverse displacements with the load factor is shown. \tilde{u}_x and \tilde{u}_z components have been computed at the locations $(l, h/2)$ and $(l, -h/2)$, respectively. As expected, the reference solution provided by Mattiasson [115] based on Euler-Bernoulli's beam theory yields a good prediction of the non-linear load-displacement response for slender homogeneous beams. Higher-order UF-based models as well as two-dimensional FEM solutions perfectly match the reference solution. On the other hand, higher-order effects become more significant for smaller slenderness ratios, as shown in Fig. 8.4. At least a second-order expansion ($N = 2$) should be adopted in order to match the two-dimensional finite elements solutions. Table 8.1 provides a more detailed numerical assessment, showing that a Timoshenko's beam model yields errors of about 5.5% with respect to two-dimensional finite element solution, whereas higher-order models ($N \geq 2$) lead to differences in the displacement predictions as high as 0.7%. In Figure 8.5 the through-the-thickness variation of the stresses for the thick beam case is provided.

Figure 8.3: Geometrically non-linear response of a slender cantilever beam ($l/h = 100$).Figure 8.4: Geometrically non-linear response of a thick cantilever beam ($l/h = 10$).

Stresses are expressed in the global fixed reference system. Small differences in the stress prediction provided by the large-strain two-dimensional formulation “Plane183” and the small-strain elements “FEM 2D TL” can be noticed. Furthermore, as shown in Table 8.2, the UF-based one-dimensional theories yield accurate stress results, being the relative errors with respect to the two-dimensional small-strain solution as high as 0.6% for $N \geq 3$ and B4 elements. Finally, Figure 8.6 shows the mechanical response in terms of axial and shear stress components over the whole beam domain. Unlike classical beam models, global accurate predictions of thick structures in the geometrically non-linear regime can be provided by the present UF-based higher-order models, including localized concentrations of axial, shear and normal stresses in the proximity of boundary conditions, as shown in Figure 8.6.

Doubly-clamped beam

Doubly-clamped beams are now considered. In Figure 8.7 the non-linear relations between load and displacements for a slender beam are provided, whereas a thick beam

	$10 \times -\tilde{u}_x$			$10 \times \tilde{u}_z$		
Plane183	6.1163			8.7165		
Beam3 TBT	6.4377			8.2409		
Beam3 EBT	6.3579			8.1661		
Mattiasson [115]	6.2652			8.1061		
N	B2	B3	B4	B2	B3	B4
5	6.1579	6.1585	6.1585	8.6817	8.6820	8.6820
4	6.1575	6.1580	6.1581	8.6809	8.6812	8.6812
3	6.1596	6.1601	6.1601	8.6760	8.6764	8.6764
2	6.1521	6.1527	6.1527	8.6671	8.6674	8.6674

Table 8.1: Displacement components prediction provided by UF-based models and several reference solutions. Thick cantilever beam. $\lambda = 10$.

	$10 \times \tilde{\sigma}_{xx}^g$			$10 \times \tilde{\sigma}_{zz}^g$			$10 \times \tilde{\sigma}_{xz}^g$		
Plane183	2.4166			1.3372			1.7978		
FEM 2D TL	2.7403			1.5302			2.0480		
N	B2	B3	B4	B2	B3	B4	B2	B3	B4
5	2.5622	2.7426	2.7414	1.6556	1.5336	1.5291	2.0730	2.0496	2.0474
4	2.5632	2.7435	2.7424	1.6552	1.5332	1.5287	2.0730	2.0494	2.0472
3	2.5554	2.7355	2.7344	1.6468	1.5248	1.5203	2.0779	2.0546	2.0522
2	2.4216	2.5995	2.5984	1.7133	1.5896	1.5851	2.1354	2.1114	2.1090

Table 8.2: Global Cauchy stresses computed at $(l/4, -h/2)$. Thick cantilever beam. $\lambda = 5.20$.

is considered in Figure 8.8. \tilde{u}_x and \tilde{u}_z are evaluated at $(l/4, h/2)$ and $(l/2, -h/2)$, respectively. In analogy with the previous case, an error reduction from 4.6% (TBT) to 0.3% ($N \geq 3$) with respect to the small-strain 2D FEM can be achieved through enrichment of the cross-sectional kinematics, as shown in Table 8.3. The importance of higher-order models for stress prediction in a thick doubly-clamped beam is highlighted in Figure 8.9 as well as in Table 8.4. This latter shows that a relative error of 27.8% provided by a second-order model may be reduced to 0.8%, at worse, for models with $N \geq 3$.

Simply supported beam

To conclude, a simply-supported thick beam structure ($l/h = 10$) is investigated. Fig. 8.10 provides the load-displacement non-linear responses, whereas in Fig. 8.11 the through-the-thickness distribution of the Cauchy stress components expressed in global reference system is shown. \tilde{u}_x and \tilde{u}_z are evaluated at $(0, -h/2)$ and $(l/2, h/2)$, respectively. Similarly to the previous cases, by increasing the order of the approximating

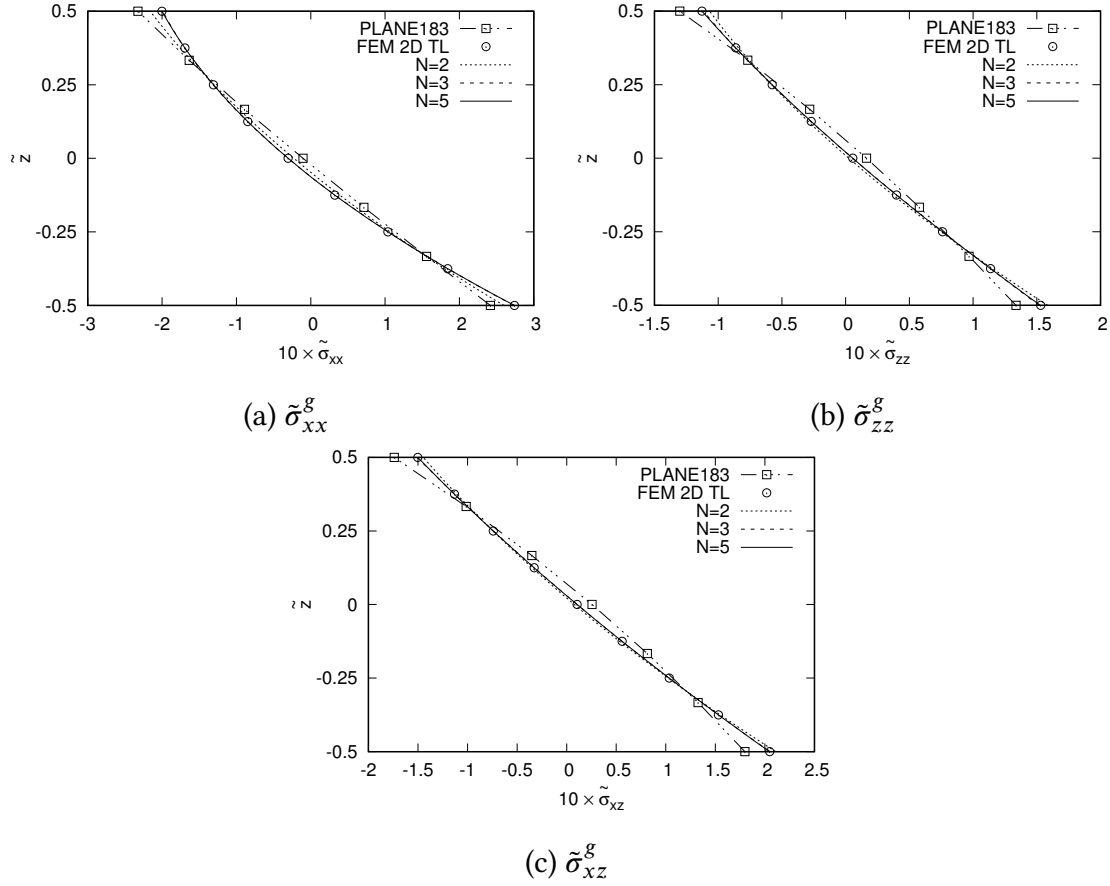


Figure 8.5: Through-the-thickness distribution of global Cauchy stresses at $x = l/4$. $\lambda = 5.20$. Thick cantilever beam.

polynomial N , the relative error on the displacement prediction can be enhanced from about 3.7% for a second-order model to 0.8% for $N = 5$, as can be seen from the results in Table 8.5. Table 8.6 shows that enhancement in the stress prediction can be achieved as well. A second-order theory ($N = 2$) and cubic (B4) elements yield relative errors of about 2.3% for $\tilde{\sigma}_{xx}$, 60.5% for $\tilde{\sigma}_{zz}$ and 35.2% for $\tilde{\sigma}_{xz}$, whereas for a fifth-order model ($N = 5$) and cubic (B4) finite elements, the errors reduce to about 0.3% with respect to “FEM 2D TL”. Finally, Fig. 8.12 provides the stress distributions at $x = l/4$ obtained via a fifth-order model ($N = 5$) and reference two-dimensional solution at increasing load factors λ , showing that the stress capabilities of the proposed formulation are preserved throughout the whole non-linear deformation path.

8.2.2 Asymmetric laminate

The enhanced capabilities of the proposed UF-based one-dimensional finite elements demonstrated in the previous section for the analysis of thick metallic structures are

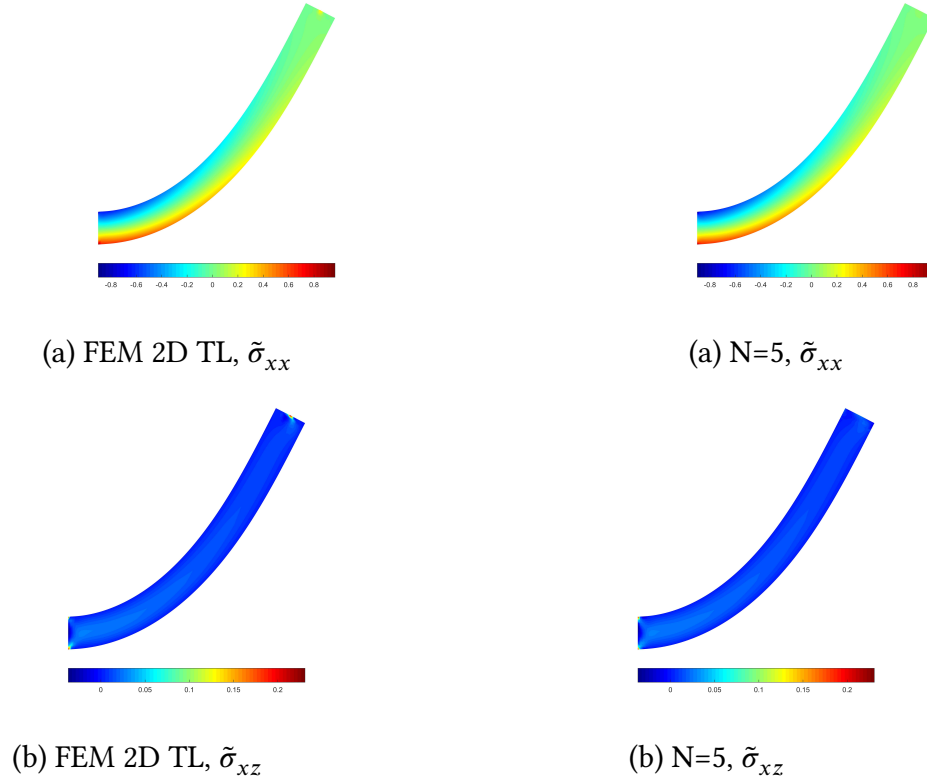


Figure 8.6: (a) Axial and (b) shear stress components two-dimensional distribution. Thick cantilever beam. $\lambda = 3.79$.

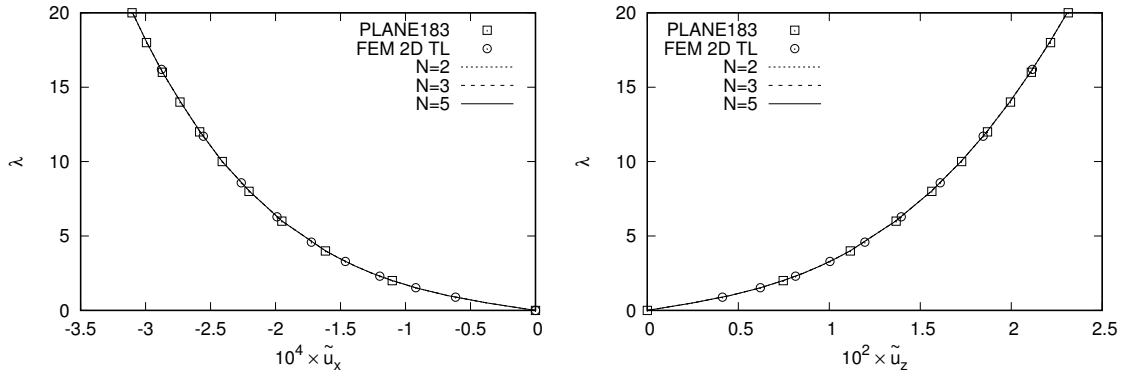


Figure 8.7: Geometrically non-linear response of a slender doubly-clamped beam ($l/h = 100$).

herein assessed for the study of laminated beam structures. The study provided by Paganini and Carrera [124] is taken as reference. In [124], the authors demonstrated the

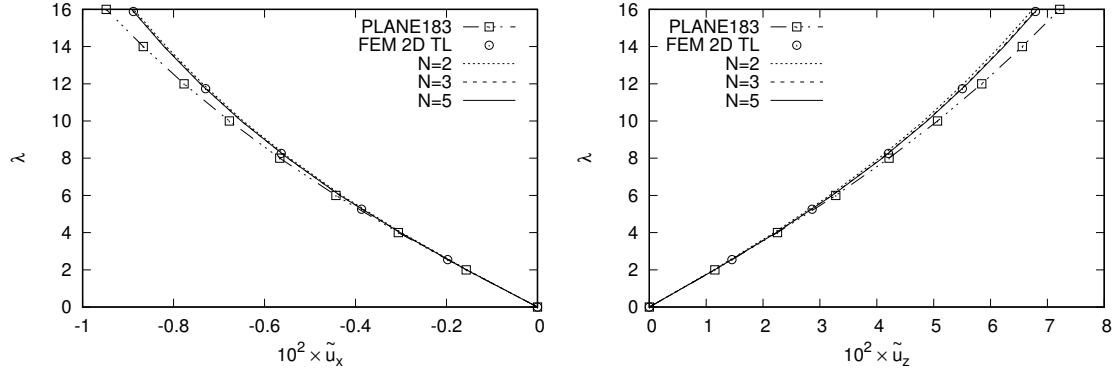


Figure 8.8: Geometrically non-linear response of a thick doubly-clamped beam ($l/h = 10$).

	$10^3 \times -\tilde{u}_x$			$10^2 \times \tilde{u}_z$		
Plane183	9.4375			7.1822		
FEM 2D TL	8.8841			6.7892		
Beam3 TBT	9.2102			7.1003		
Beam3 EBT	9.5180			6.4598		
N	B2	B3	B4	B2	B3	B4
5	8.8863	8.8848	8.8848	6.7911	6.7918	6.7918
4	8.8857	8.8841	8.8841	6.7879	6.7887	6.7887
3	8.8829	8.8814	8.8814	6.7725	6.7733	6.7733
2	8.8476	8.8461	8.8460	6.7109	6.7117	6.7117

Table 8.3: Displacement components prediction provided by UF-based models and several reference solutions. Thick doubly-clamped beam. $\lambda = 15.89$.

advantages of UF-based layer-wise approach for the geometrically non-linear analysis of composites. The aim of this work, instead, is to assess the accuracy and efficiency of an equivalent single layer approach for the same kind of problem. As discussed in Chapter 6, a two-dimensional plane stress approach is considered for the geometrically non-linear formulation. A cross-ply two-layer laminate with laminae parallel to the Oxy plane and stacking sequence $[90/0]$ is investigated. Therefore, the fibers in the top layer are in a direction orthogonal to the beam axis, whereas, in the bottom layer, they are aligned to the longitudinal axis. The beam structure is made of AS4/3501-6 graphite/epoxy composite material with the following equivalent orthotropic properties: $E_L = 144.8$ GPa, $E_T = 9.65$ GPa, $G_{LT} = 4.14$ GPa, $G_{TT} = 3.45$ GPa and $\nu_{LT} = \nu_{TT} = 0.3$. The geometric properties of the beam structure are $l = 9$ m, $h = 0.6$

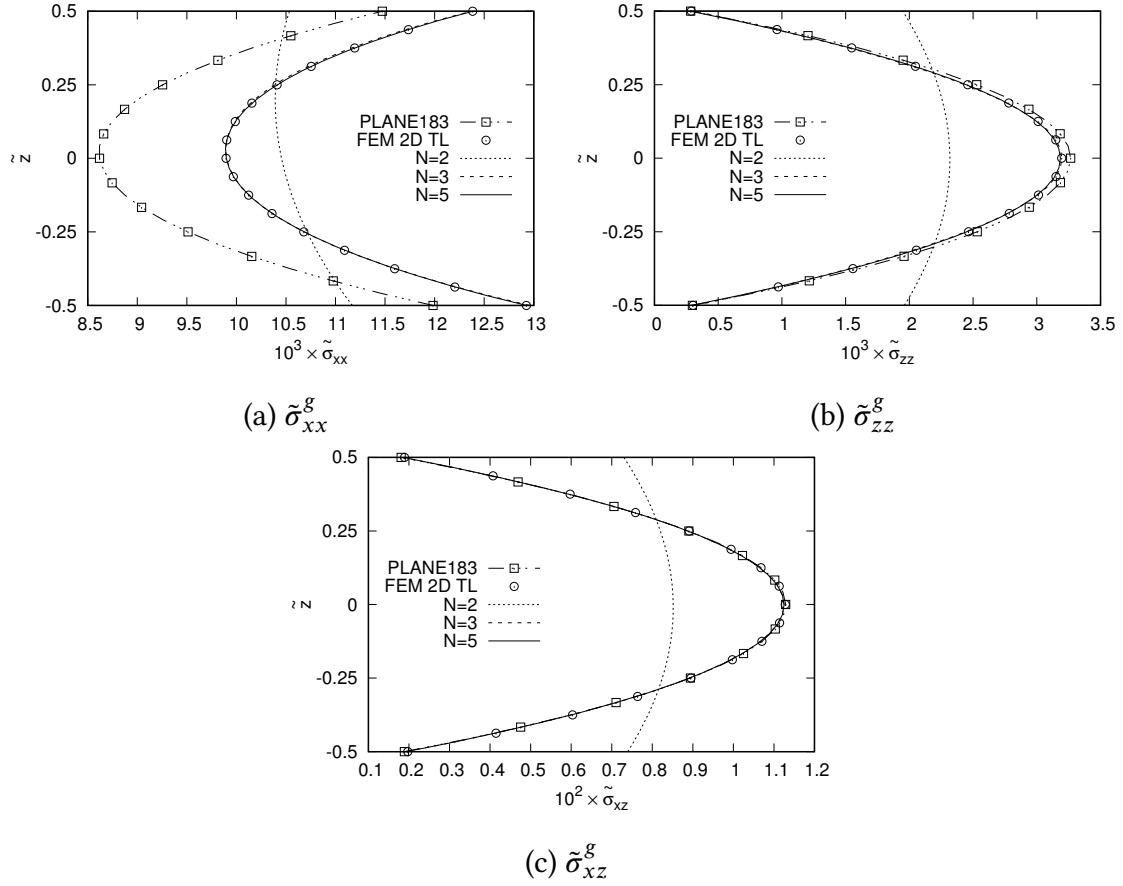


Figure 8.9: Through-the-thickness distribution of global Cauchy stresses at $x = l/4$. $\lambda = 5.20$. Thick doubly-clamped beam.

	$10^3 \times \tilde{\sigma}_{xx}^g$			$10^3 \times \tilde{\sigma}_{zz}^g$			$10^2 \times \tilde{\sigma}_{xz}^g$		
Plane183	8.6194			3.2658			1.1290		
FEM 2D TL	9.8958			3.1957			1.1281		
N	B2	B3	B4	B2	B3	B4	B2	B3	B4
5	9.9050	9.8829	9.8987	3.1738	3.2083	3.1858	1.1210	1.1315	1.1250
4	9.9077	9.8858	9.9014	3.1859	3.2205	3.1979	1.1208	1.1312	1.1248
3	9.9050	9.8830	9.8987	3.1858	3.2200	3.1976	1.1210	1.1314	1.1249
2	10.4620	10.4390	10.4550	2.3066	2.3405	2.3182	0.8477	0.8581	0.8516

Table 8.4: Global Cauchy stresses computed at $(l/4, 0)$. Thick doubly-clamped beam. $\lambda = 11.04$.

m and $b = 1$ m. The two layers possess the same thickness $t = h/2 = 0.3$ m. Cantilever boundary conditions are considered and a uniform non-follower surface load

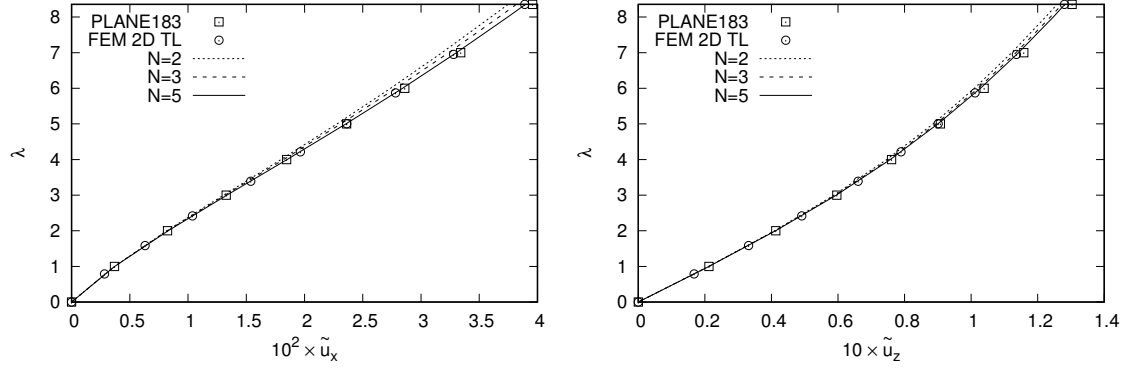


Figure 8.10: Geometrically non-linear response of a thick simply supported beam ($l/h = 10$).

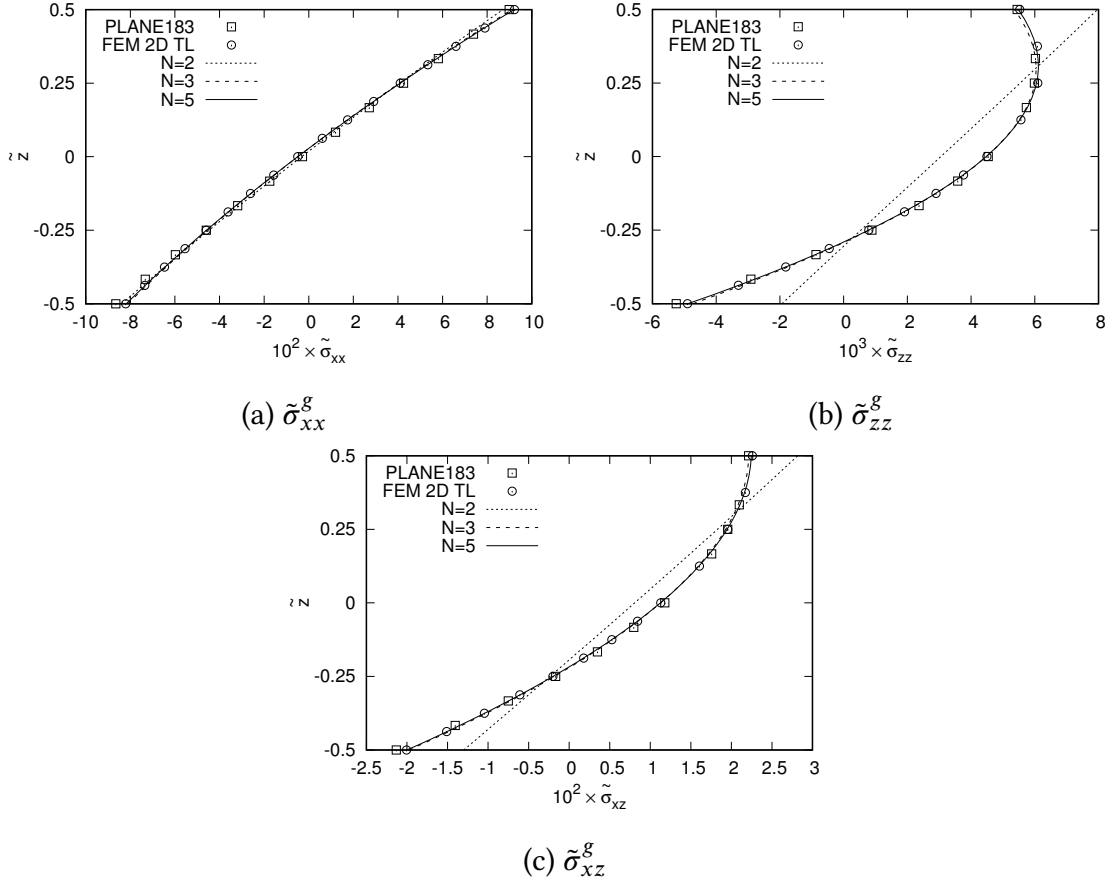


Figure 8.11: Through-the-thickness distribution of global Cauchy stresses at $x = l/4$. $\lambda = 6.03$. Thick simply supported beam-like structure.

		$10^2 \times \tilde{u}_x$			$10 \times \tilde{u}_z$		
Plane183		3.9585			1.3032		
FEM 2D TL		3.8909			1.2805		
N		B2	B3	B4	B2	B3	B4
5		3.9239	3.9239	3.9192	1.2843	1.2843	1.2839
4		3.9011	3.9000	3.8960	1.2820	1.2819	1.2814
3		3.8267	3.8251	3.8232	1.2739	1.2738	1.2735
2		3.7501	3.7482	3.7474	1.2583	1.2580	1.2579

Table 8.5: Displacement components prediction provided by UF-based models and two-dimensional finite elements solutions. Thick simply supported beam. $\lambda = 8.36$.

		$10^2 \times -\tilde{\sigma}_{xx}^g$			$10^3 \times -\tilde{\sigma}_{zz}^g$			$10^2 \times -\tilde{\sigma}_{xz}^g$		
Plane183		8.6470			5.2555			2.1314		
FEM 2D TL		8.2064			4.8990			2.0056		
N		B2	B3	B4	B2	B3	B4	B2	B3	B4
5		8.2878	8.2030	8.2002	6.9946	4.8699	4.9120	2.2776	2.0010	2.0067
4		8.2696	8.1840	8.1811	6.9402	4.8190	4.8614	2.2707	1.9942	2.0002
3		8.2018	8.1142	8.1125	6.7966	4.6917	4.7352	2.2464	1.9717	1.9779
2		8.4861	8.3928	8.3917	4.0106	1.8893	1.9344	1.5683	1.2941	1.3006

Table 8.6: Global Cauchy stresses computed at $(l/4, -h/2)$. Thick simply supported beam. $\lambda = 6.03$.

$p_0 = 3$ MPa is applied at the top surface of the beam. In Tables 8.7 and 8.8 displacement, axial and shear stress values provided by the proposed UF-based plane stress ESL models (referred to as “ESL PS”) are given. Numerical results are assessed towards a three-dimensional ABAQUS solution given in [124], two-dimensional plane stress Ansys finite elements “Plane183”, bi-linear, quadratic and cubic layer-wise models developed in the UF framework [124] and a plane stress UF-based layer-wise cubic model, referred to as “LW PS cubic”. Axial and transverse displacements have been evaluated at $(l, 0)$, whereas axial and shear stresses are computed at $(l/2, -h/2)$ and $(l/2, -h/4)$, respectively. Forty cubic one-dimensional elements are used for the finite element discretization along the axis. The equivalent single layer theories starting from the second-order provide all a fairly accurate estimation of axial, transverse displacements as well as axial stress with respect to two-dimensional and three-dimensional reference solutions, whereas a further refinement of the cross-sectional kinematics is required for the shear stress prediction in order to reach the accuracy level provided by the refined layer-wise models. Figure 8.13 presents the through-the-thickness distribution of

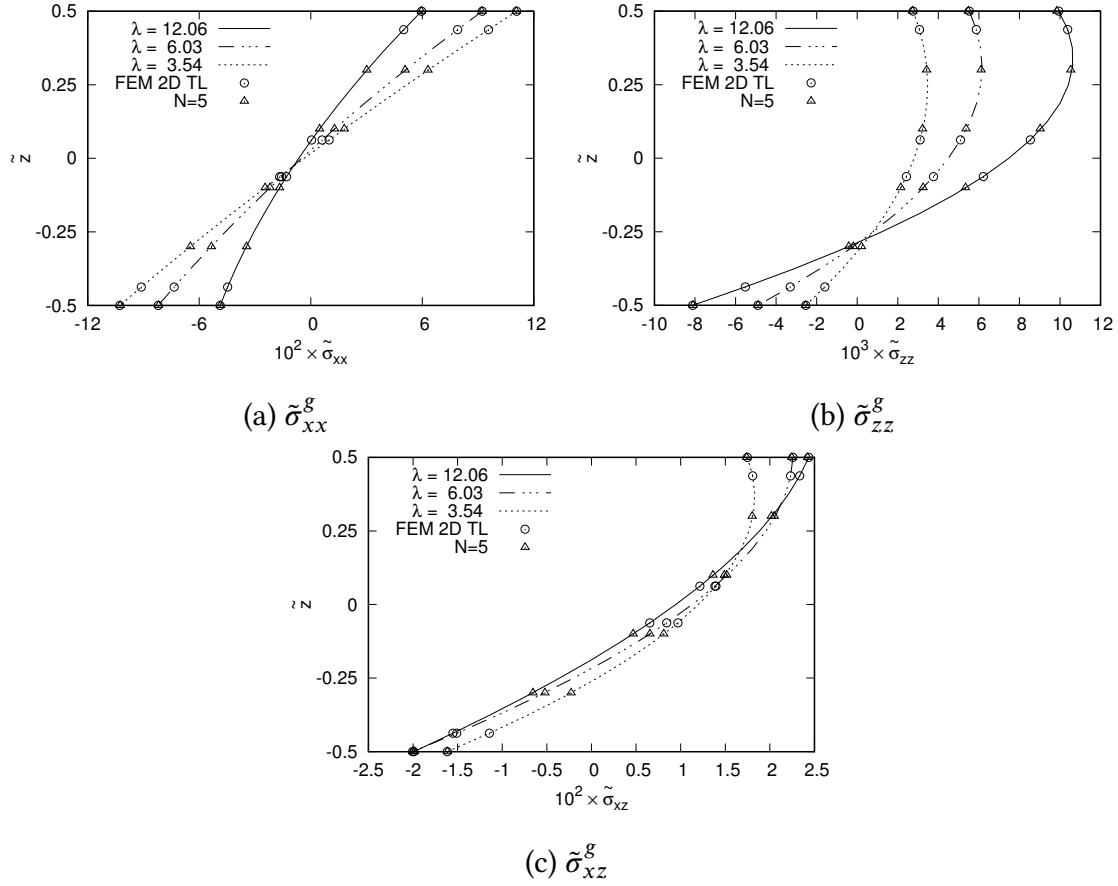


Figure 8.12: Through-the-thickness distribution of global Cauchy stresses at increasing load factors λ . Thick simply-supported beam. $x = l/4$.

axial, transverse shear and normal stresses at the mid-span of the beam ($x = l/2$) provided by a second-order ESL model, a fifth-order ESL model and a LW cubic model. In those figures, the following dimensionless quantities have been plotted: $\tilde{\sigma} = \sigma/p_0$ and $\tilde{z} = z/h$. As it is well-known, since pure displacement-based theories are considered in this work, the inter-laminar continuity of the transverse stresses is not ensured. It is clear that by enriching the Taylor's polynomial expansion of the kinematic field via higher-order terms, ESL models ($N=5$, in this particular case) yield stress predictions as accurate as refined LW models. For the sake of completeness, Figure 8.14 shows the global two-dimensional distribution of axial, shear and normal stresses over the beam domain. Unlike classical beam theories, UF-based refined models allow the prediction of localized axial, shear and normal stress concentrations (in the bottom layer and at the clamped edge). Table 8.8 reports the computational costs in terms of number of degrees of freedom (N_{DOFs}) for the different models considered in the analysis. It is clear that a considerable reduction in degrees of freedom is possible by means of the UF-approach, either LW or ESL, with respect to three-dimensional commercial software

	$-u_x$ [m]	u_z [m]
FEM 3D [124]	0.85	3.43
PLANE183	0.84	3.43
LW cubic [124]	0.99	3.51
LW quadratic [124]	0.88	3.51
LW bi-linear [124]	0.88	3.50
LW PS cubic	0.89	3.52
ESL PS $N = 8$	0.89	3.52
ESL PS $N = 5$	0.89	3.52
ESL PS $N = 2$	0.89	3.51

Table 8.7: Displacements in a cantilever laminated beam-like structure under large deflection via LW and ESL refined models.

	σ_{xx} [MPa]	σ_{xz} [MPa]	N_{DOFs}
FEM 3D [124]	959.4	41.0	573675
LW cubic [124]	1007.7	40.3	5124
LW quadratic [124]	1003.8	29.4	2745
LW bi-linear [124]	1019.3	29.8	1098
LW PS cubic	1000.5	40.2	1936
ESL PS $N = 8$	1000.8	40.9	2178
ESL PS $N = 5$	1001.0	39.1	1452
ESL PS $N = 2$	1010.0	27.2	726

Table 8.8: Axial and shear stresses in a cantilever laminated beam-like structure under large deflection via LW and ESL refined models.

finite elements. As far as the comparison between ESL or LW approach is concerned, for this particular case the choice of a higher-order ESL model such as $N=5$ yields the best compromise between results accuracy and computational costs. Nevertheless, laminates with a higher number of layers and extremely complex stress profiles would call for very high-order ESL models, which means that their computational benefits, in these cases, could be not so evident. The mechanical behavior of composites in linear as well as non-linear regime is strongly problem-dependent. An a priori choice of the best kinematic model is often not possible and this is why the capability to handle different kinematic descriptions as well as different approximation orders via UF proves to be very useful.

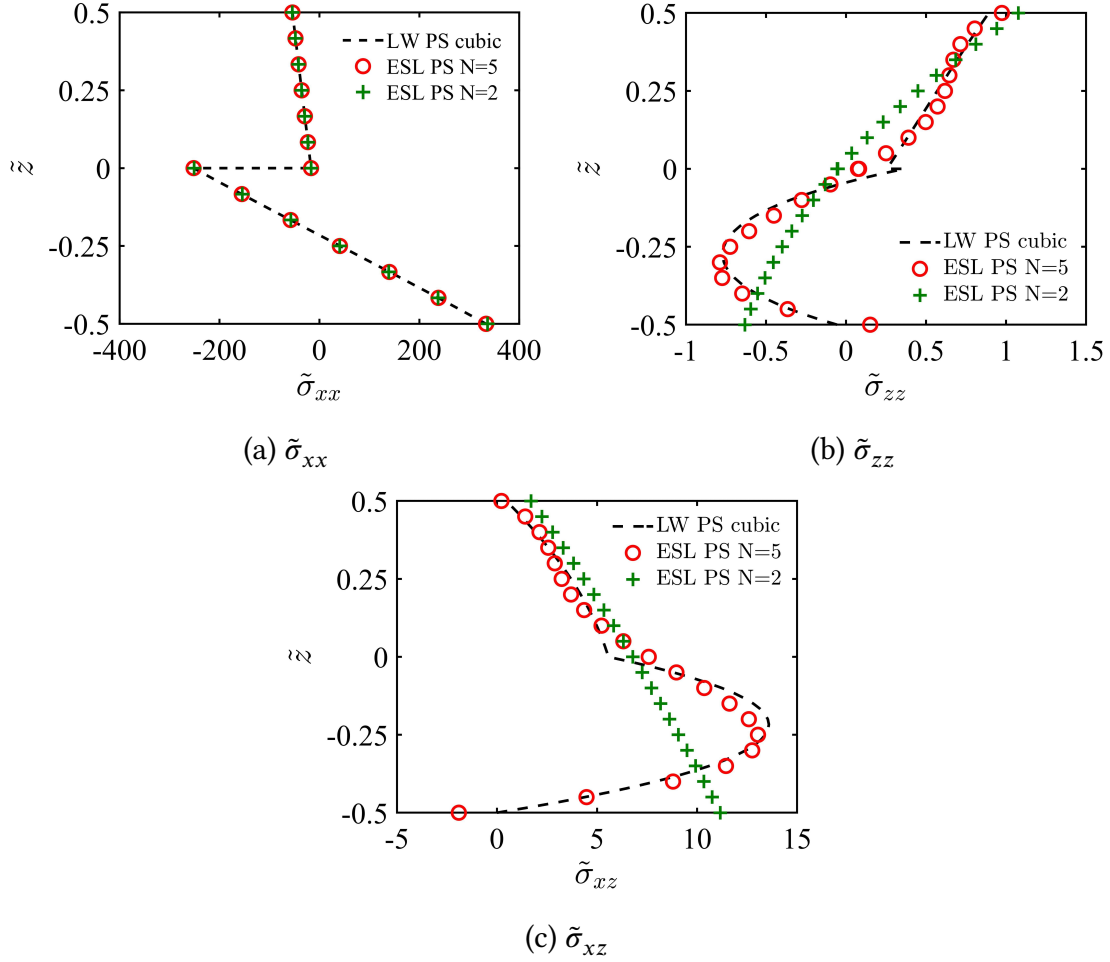
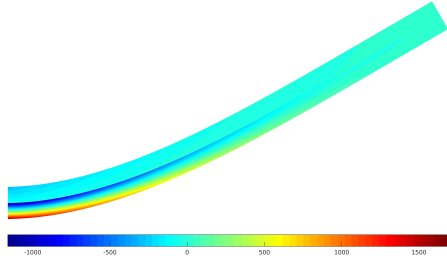


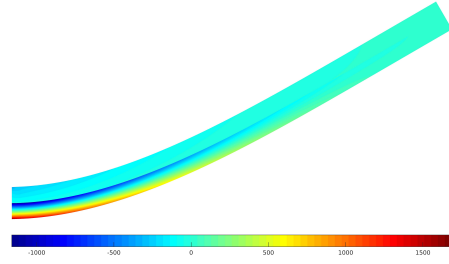
Figure 8.13: Through-the-thickness profile of (a) axial, (b) normal through-the-thickness and (c) transverse shear stress components via ESL and LW refined models. Two-layer [90/0] laminated beam under large deflection. $x = l/2$.

8.2.3 Three-layer beam

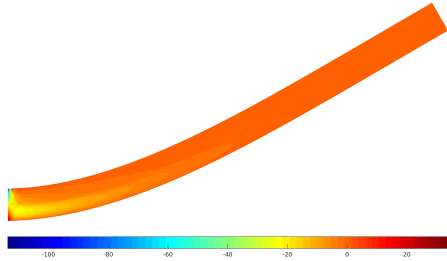
As already mentioned, models based on an equivalent single layer description suffer in terms of accuracy when dealing with either a high number of different layers or very different mechanical properties from layer to layer. In these circumstances, the use of a layer-wise approach is recommended. In this subsection, the capabilities of a UF-based cubic layer-wise model for the analysis of a three-layer beam structure in the geometrically non-linear regime are assessed. A full Newton-Raphson scheme is adopted in order to solve the non-linear governing equations. Results are compared with a two-dimensional small-strain quadratic finite elements solution based on a total Lagrangian approach within the framework of a ANM-based solution scheme [89] and referred to as “FEM 2D TL”. The following geometric properties are considered: $l = 20$ m, square



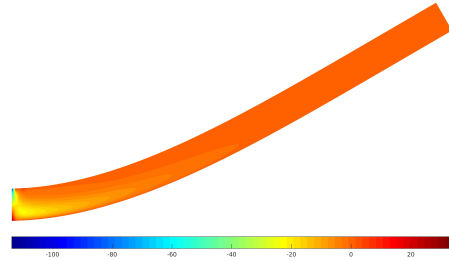
(a) LW PS cubic, $\tilde{\sigma}_{xx}$



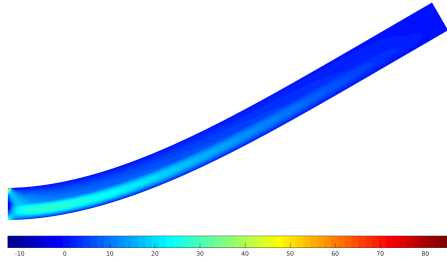
(a) N=5, $\tilde{\sigma}_{xx}$



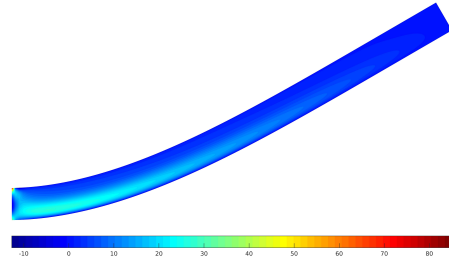
(b) LW PS cubic, $\tilde{\sigma}_{zz}$



(b) N=5, $\tilde{\sigma}_{zz}$



(c) LW PS cubic, $\tilde{\sigma}_{xz}$



(c) N=5, $\tilde{\sigma}_{xz}$

Figure 8.14: Two-dimensional distribution of dimensionless (a) axial, (b) normal through-the-thickness and (c) transverse shear stress components. Two-layer [90/0] laminated beam under large deflection. $\tilde{\sigma}_{ij} = \sigma_{ij}/p_0$.

cross-section ($h = b = 1$ m) and layers of equal thickness $t = h/3$. Isotropic materials are considered. The mechanical properties of top and bottom layers are the following: $E_{top} = E_{bot} = 75$ GPa, $\nu_{top} = \nu_{bot} = 0.33$, whereas the mechanical properties of the middle layer are: $E_{mid} = 0.75$ GPa, $\nu_{mid} = 0.33$. A cantilever beam with a transverse concentrated force $P_z = \lambda_z P_{ref}$ applied at the free end ($x = l, z = -h/2$) is considered, being λ_z the load factor, $P_{ref} = \frac{E_{bot} I}{l^2}$ and I the cross-section moment of inertia. Figure 8.15 shows the through-the-thickness profile of axial and transverse displacements, respectively, at the free end of the beam ($x = l$) for a load factor $\lambda_z = 1$. The following dimensionless form of displacements and thickness coordinate is considered: $\tilde{u} = u/l$ and $\tilde{z} = z/h$. Due to the strong discontinuity in the mechanical properties through the thickness direction, localized cross-sectional deformations occur in the softer middle layer, which can be fairly well predicted by the cubic LW models. Figure 8.16 presents the

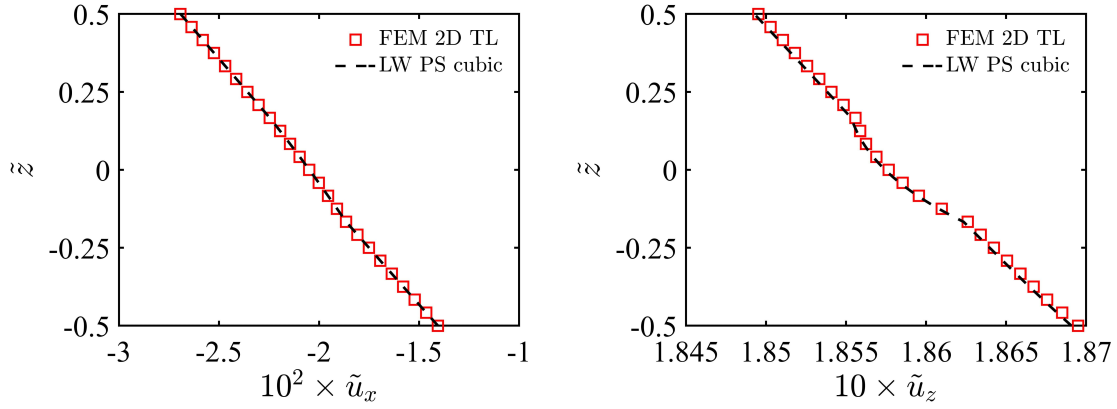


Figure 8.15: Through-the-thickness profile of axial and through-the-thickness displacement components in a three-layer beam under large deflection. $\lambda_z = 1$. $x = l$.

through-the-thickness distribution of axial, shear and normal stresses at $x = l/4$ at increasing load factors λ_z , showing the capabilities of the presented refined LW model in accurately predicting the evolution of the full in-plane stress state throughout the large deflection analysis. Dimensionless stress $\tilde{\sigma} = \frac{2I\sigma}{\lambda_z^{fin} P_{ref} l h}$ is considered, being $\lambda_z^{fin} = 2$

the final load factor. Finally, Figure 8.17 shows the global two-dimensional distribution of the shear stress component at the final load factor $\lambda_z = 2$. The accurate prediction of an extremely complex shear stress distribution in the vicinity of the boundary conditions with localized concentrations in the middle layer as well as in the proximity of the external load application point should be noticed. Concerning the computational costs of the considered models, the number of degrees of freedom for the refined LW-based one-dimensional model is about $2.7 \cdot 10^3$ (4-node Lagrange expansion for each layer and 121-node discretization along the beam axis), whereas a mesh of 120×12 elements was used for the two-dimensional 8-node quadratic finite elements solution, corresponding

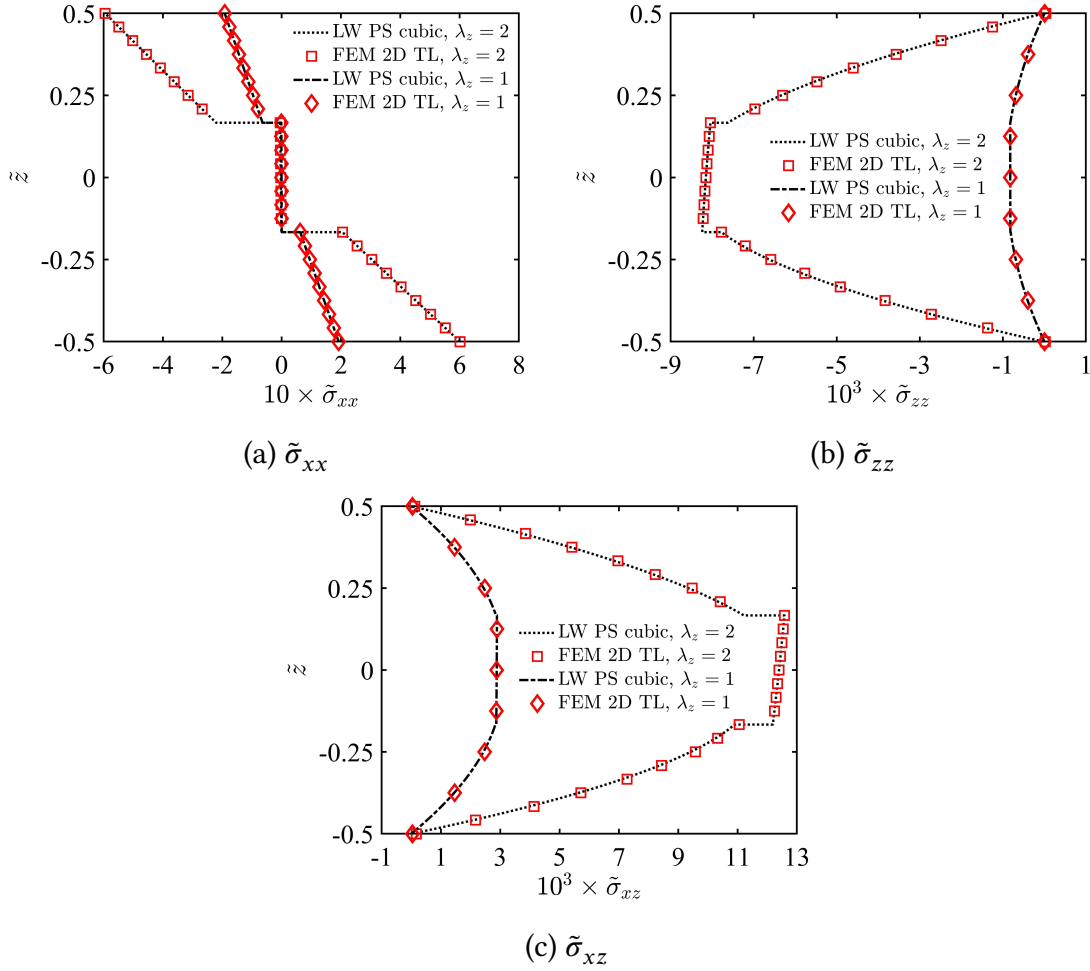


Figure 8.16: Evolution of (a) axial, (b) normal through-the-thickness and (c) transverse shear stress profiles from $\lambda_z = 1$ to $\lambda_z = 2$ in a three-layer beam under large deflection. $x = l/4$.

to $9.2 \cdot 10^3$ DOFs. Therefore, if the same non-linear solver is adopted, about 70% saving in terms of DOFs could be exploited every time the tangent stiffness matrix is assembled and inverted within the adopted non-linear solution scheme.

8.3 Bistability analysis of pre-buckled beams

After assessing the proposed geometrically non-linear UF-based one-dimensional finite elements for the large deflection analysis of composite beam structures, post-buckling and snap-through analyses need to be addressed in order to model the mechanical response of pre-buckled bistable beam structures. Such elastic instability phenomena involve highly non-linear equilibrium paths that calls for robust non-linear solution

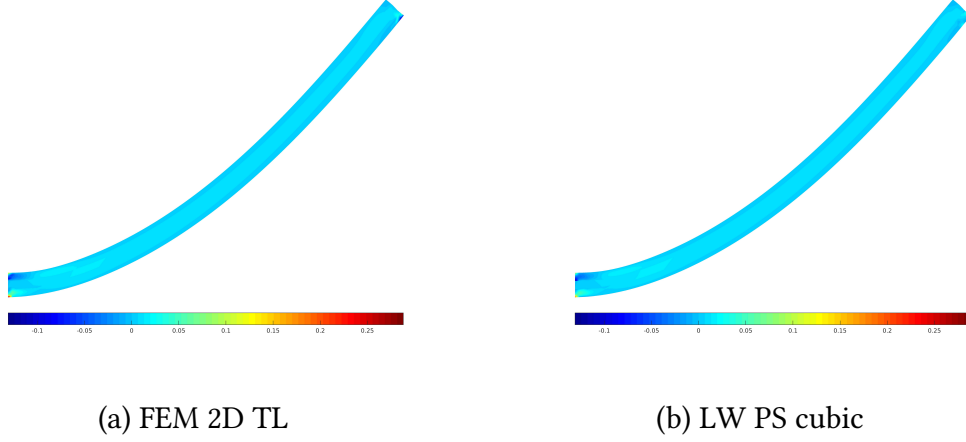


Figure 8.17: Transverse shear stress $\tilde{\sigma}_{xz}$. Three-layer beam under large deflection. $\lambda_z = 2$.

schemes. For this reason, the ANM-based path-following technique described in Section 6.8.3 has been used in obtaining the following numerical results.

8.3.1 Influence of ANM parameters

A first preliminary analysis on the post-buckling behavior of a slender simply supported metallic beam is carried out in order to show the influence on the final solution of the parameters peculiar of the ANM procedure, i.e. the expansion order n and the tolerance parameter ϵ . The following geometric and material properties have been considered: $l = 100$ m, $h = b = 1$ m, $E = 75$ GPa and $\nu = 0.33$. Simply supported boundary conditions are assumed ($u_z = 0$ at $x = 0, x = l$ and $u_x = 0$ at $x = l/2$). Two opposite compressive loads $P_x = \lambda_x \frac{\pi^2 EI}{l^2}$ are applied at the beam ends $(0,0)$ and $(l,0)$ together with a perturbation transverse load $q_z = 10^{-3} \cdot P_x$ acting at $(l/2, 0)$. A second-order ESL UF-based model ($N = 2$) is used as beam model. The influence of the tolerance parameter ϵ on the load-displacement responses for a fixed expansion order is shown in Figure 8.18. It is clear that the tolerance parameter ϵ drives the solution accuracy and that convergence is obtained for $\epsilon < 10^{-6}$. Moreover, Figure 8.19 shows the influence of the ANM expansion order on the solution for a fixed tolerance parameter. Each line marker symbol (circle- or plus-symbol) corresponds to the beginning of a new solution step, therefore the total number of markers correspond to the number of times that the tangent stiffness matrix needs to be assembled and inverted. It can be noticed that by increasing the order n of the asymptotic expansion, larger non-linear branches and, therefore, a lower number of steps can be obtained with a negligible accuracy loss. A very robust solution is obtained for sufficiently small tolerance values, even in the presence of very localized non-linearities, as shown in Fig. 8.19 (a). Since this work

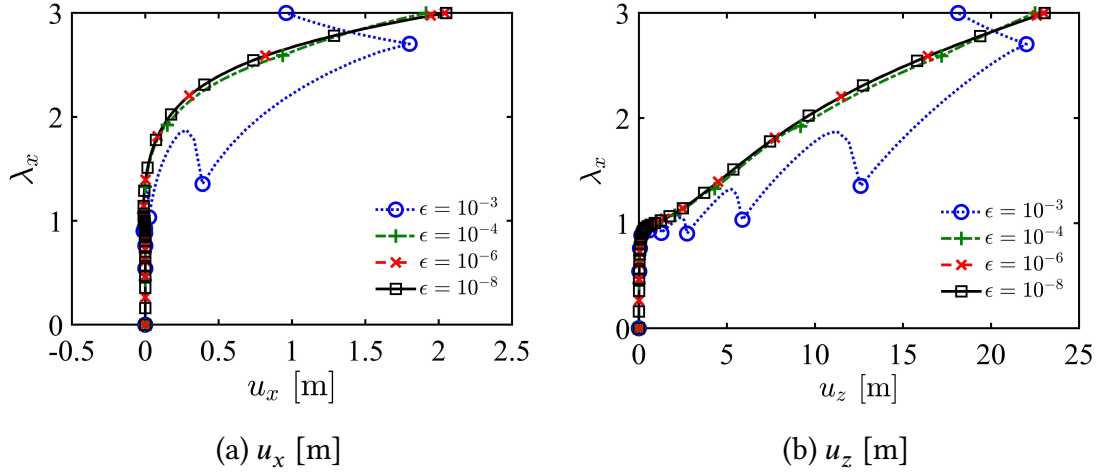


Figure 8.18: Influence of the ANM tolerance parameter in the post-buckling of a simply supported beam. ANM order $n = 10$. $N = 2$ beam model.

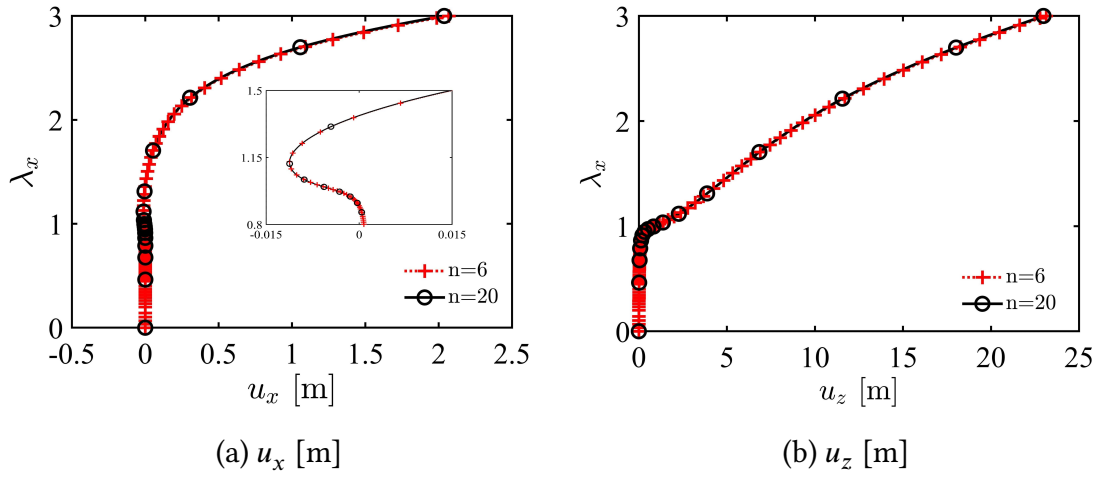


Figure 8.19: Influence of the ANM order parameter in the post-buckling of a simply supported beam. ANM tolerance $\epsilon = 10^{-8}$. Beam model $N = 2$.

focuses on advanced mechanical modeling approaches rather than non-linear solution procedures, quite conservative values of the ANM parameters have been chosen for the following analyses ($n = 10$ and $\epsilon = 10^{-8}$) in order to avoid the introduction of errors that, although small, could have made the assessment of the proposed UF-based refined models more difficult.

8.3.2 Validation towards literature: bistable air inlet

A first assessment to validate the proposed methodology in bistability analysis is presented in this section. The study carried out by Arena et al. [2] is taken as reference. A pre-buckled, doubly-clamped beam-like structure was investigated in order to design mono- and bi-stable shape-adaptive air inlets providing flow regulation and control. In response to the external aerodynamic forces, the inlet can passively snap between the closed and open configuration, with no need of joints, linkages and classical actuation mechanisms. If the behavior of the beam component is designed to be mono-stable, the structure will snap-back to the closed configuration after load removal, whereas if it is bistable, an external transverse force F_z will be required in order to trigger the snap-back phenomenon. The axial dimension of the beam is 150 mm, the width is 11.2 mm and the thickness 1.04 mm. The initial buckled configuration is obtained by a vertical deflection $u_{z0} = 15$ mm and, in a second step, a horizontal deflection $u_{x0} = 1.5$ mm at the end of the beam ($x/l = 1$). A graphical sketch of the shape-adaptive air inlet concept is shown in Figure 8.20. The structure is made of unidirectional glass fibre-

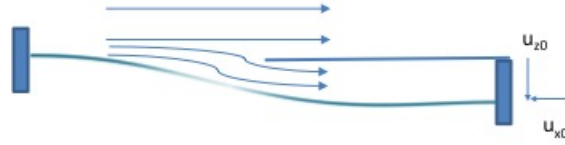


Figure 8.20: Graphical sketch of a pre-buckled beam component embedded in a passively actuated shape-adaptive air inlet (Arena et al. [2]).

epoxy resin composite (Glass/913) with the following elastic properties: $E_L = 43.7$ GPa, $E_T = 7.5$ GPa, $G_{LT} = 4.3$ GPa and $\nu_{LT} = 0.3$. Numerical results in [2] were obtained via 8-node linear brick elements. Abaqus solution and arc-length Riks method was used as non-linear solver, since a classical Newton-Raphson force controlled solution procedure would not be able to follow the negative stiffness branches of the equilibrium path. An external transverse mechanical force F_z is considered to be applied at the mid-span of the beam ($l/2, 0$) and the resulting deflection is evaluated at the same point. Fig. 8.21 shows the snap-through phenomenon and the existence of two different stable mechanical configurations corresponding to those equilibrium points where the external applied force is zero and the tangent stiffness matrix is positive definite (positive slope of the force-displacement curve). Triggered by the central concentrated force, the shape-adaptive air inlet can suddenly snap from the open configuration to the closed one by harnessing the snap-through instability phenomenon. As expected, due to the high slenderness of the structure and the homogeneity of the material, no influence of the higher-order theories is found on the load-displacement behavior. As shown in Fig. 8.21, both a second- and a third-order theory ($N = 2$ and $N = 3$) match the 3D finite elements solution provided by Arena et al. [2]. For the sake of completeness, the pre-buckled beam shape (for $F_z = 0$ N) and the snapped deformed shape (for

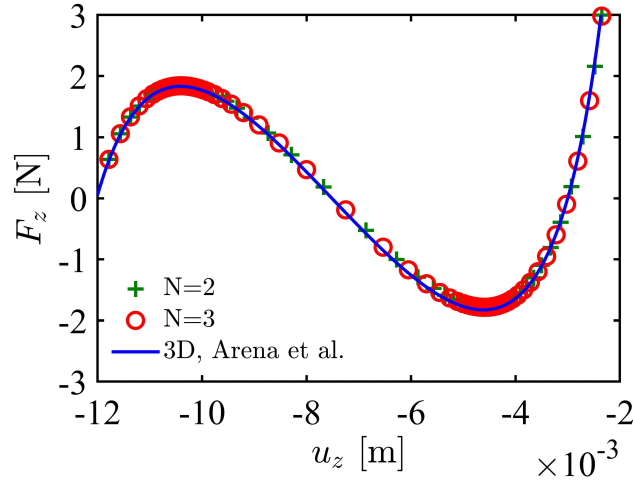


Figure 8.21: Equilibrium path of a bistable beam-like air inlet. Uni-directional glass fibre-epoxy resin composite laminate.

$F_z = 3$ N) are given in Figs. 8.22.



(a) Open configuration

(b) Closed configuration

Figure 8.22: Open-closed configurations of a bistable air inlet. Resultant displacement u_{res} [m]. $N = 3$ beam model.

8.3.3 Refined post-buckling and snap-through equilibrium paths

As already seen in the previous section, a possible way to obtain mechanically bi-stable structures is to pre-buckle an initially straight beam by generating an initial transverse deflection and an initial stress field inside the beam and then, in a second phase, apply a

transverse load in order to trigger a snap-through buckling and force the curved beam to flip to a second stable position. In this study case, in order to demonstrate the influence of higher-order theories on the mechanics of bistable beams, a lower slenderness ratio ($l/h = 20$) has been chosen with respect to the typical values found in literature and a two-phase analysis, consisting of a non-linear buckling and a snap-through phase, has been carried out on a beam structure made of an homogeneous material ($E = 75$ GPa and $\nu = 0.33$) and square cross-section ($h = b = 1$ m). Several boundary conditions are investigated. The following dimensionless parameters have been used: $\tilde{u}_x = u_x/l$,

$$\tilde{u}_z = u_z/l, \lambda_x = -\frac{P_x l^2}{\pi^2 EI}, \lambda_z = -P_z/P_x, \tilde{\sigma}_{xx} = \frac{\sigma_{xx} 2I}{P_x l h} \text{ and } \tilde{\sigma}_{xz} = \frac{\sigma_{xz} 2I}{P_x l h}.$$

Results obtained via the present refined one-dimensional finite elements under the hypothesis of a plane stress state, large displacements, large rotations and small strains are assessed towards two-dimensional finite elements (“FEM 2D TL”) based on small strains assumption and developed using a Total Lagrangian formulation, see Hu et al. [89]. 121 nodes and MITC B4 elements are used for the one-dimensional finite elements discretization. As far as computational costs are concerned, the number of degrees of freedom for the most refined UF-based one-dimensional model adopted in the following numerical results is $1.5 \cdot 10^3$, corresponding to a mesh of 121 nodes (N_n) and beam theory $N = 5$. The generic relation among N_{DOFs} , N and N_n is given by:

$$N_{DOFs} = 2 \cdot (N + 1) \cdot N_n \quad (8.3)$$

A mesh of 120×12 elements was used for the 8-node quadratic 2D FEM solutions, corresponding to $9.2 \cdot 10^3$ DOFs.

Doubly-clamped beam

The first case study deals with a pre-buckled simply-supported beam, which is then fully constrained and the beam ends in order to obtain a doubly-clamped bistable structure. Fig. 8.23 shows the load-displacement curves for the non-linear buckling of a simply supported beam ($\tilde{u}_z = 0$ at $x/l = 0, x/l = 1$ and $\tilde{u}_x = 0$ at $x/l = 1/2$) loaded by two opposite axial forces at the ends of the beam, whereas numerical values at specific evaluation points for displacements as well as axial and shear stresses at the end of the load step ($\lambda_x = 2.1835$) can be found in Table 8.9. For the sake of clarity, a qualitative color plot distribution of each displacement component is also shown within the line plots. The following evaluation points have been chosen for both line plots and tables: $u_x(l, h/2)$, $u_z(l/2, -h/2)$, $\sigma_{xx}(l/2, -h/2)$ and $\sigma_{xz}(l/4, 0)$. The small *kink* of the equilibrium path in Fig. 8.23 (a) can be explained by an initial compression phase (small negative axial displacements), followed by the onset of buckling which allows the right beam end to rotate (top point of the cross-section experiences positive values of the axial displacements) and finally, when the buckling is fully triggered, the right support can slide towards negative values of the axial displacement component again. It should be noticed that a second-order theory ($N=2$) is not refined enough to accurately

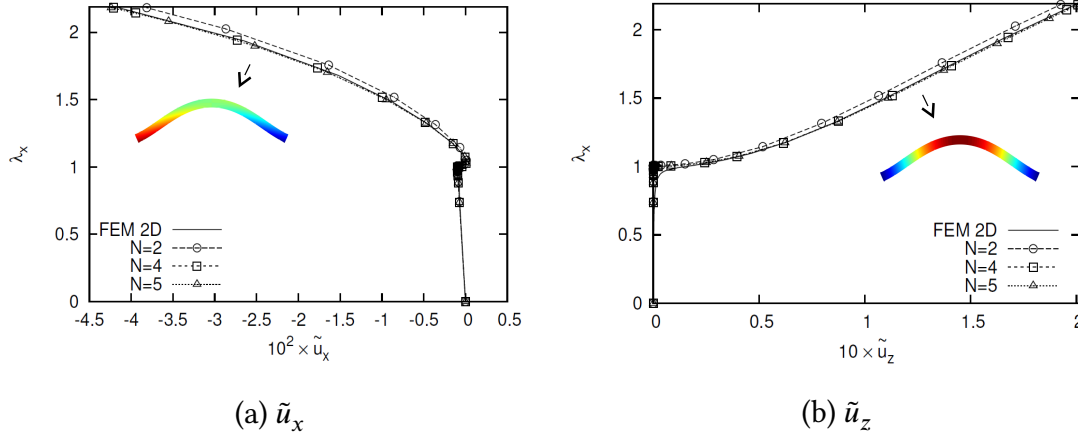


Figure 8.23: Pre-compression load vs. axial and transverse displacements. Post-buckling response. Simply supported beam. $l/h = 20$.

	$-10^2 \times \tilde{u}_x$	$10 \times \tilde{u}_z$	$-10 \times \tilde{\sigma}_{xx}$	$10^3 \times \tilde{\sigma}_{xz}$
FEM 2D	4.1517	1.9954	1.3065	6.3942
$N = 5$	4.2403	2.0149	1.3098	6.3428
$N = 4$	4.2099	2.0074	1.3050	6.3202
$N = 3$	4.0510	1.9789	1.2867	6.2333
$N = 2$	3.8134	1.9255	1.2556	4.2963

Table 8.9: Displacement and stress components in a post-buckled simply supported beam. $l/h = 20$. $\lambda_x = 2.1835$.

predict the post-buckling response. Based on Table 8.9, Fig. 8.24 shows that the relative difference between reference results provided by 2D FEM and those provided by higher-order 1D theories goes from a maximum difference of 8.2% for displacements obtained via a second-order theory to a maximum 2.1% obtained with fifth-order theory; the shear stress prediction improvement is even more meaningful, going from 32.8% error given by second-order theory to 0.8% when computed using $N=5$. Starting from the previous buckled configuration and applying doubly-clamped boundary conditions with an additional central constraint ($\tilde{u}_x, \tilde{u}_z = 0$ at $x/l = 0, x/l = 1/2$ and $x/l = 1$), as already done in previous works presented in the literature [160], a bistable structure can be obtained. Fig. 8.25 provides the load-displacement evolution due to a transverse vertical force λ_z applied at the center of the beam. The axial and transverse displacements are evaluated at $(l/4, -h/2)$ and $(l/2, -h/2)$, respectively. The highly non-linear snap-through buckling is well-described by higher-order theories such as $N=4$. In addition to the right choice of a refined structural theory, the importance of the asymptotic

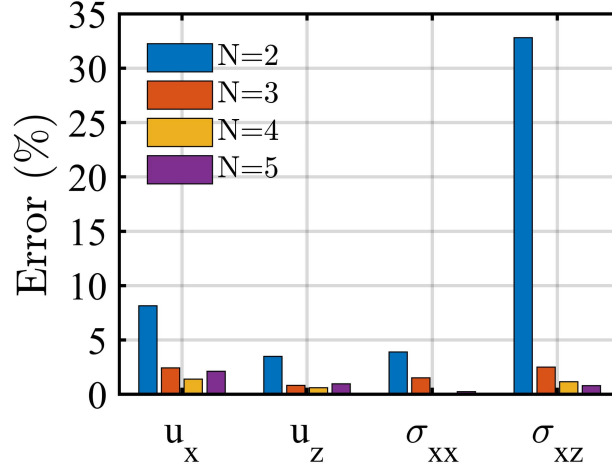


Figure 8.24: Error trends on displacements, axial and shear stress components via refined UF-based one-dimensional models. Post-buckled simply supported beam. $l/h = 20$. $\lambda_x = 2.1835$.

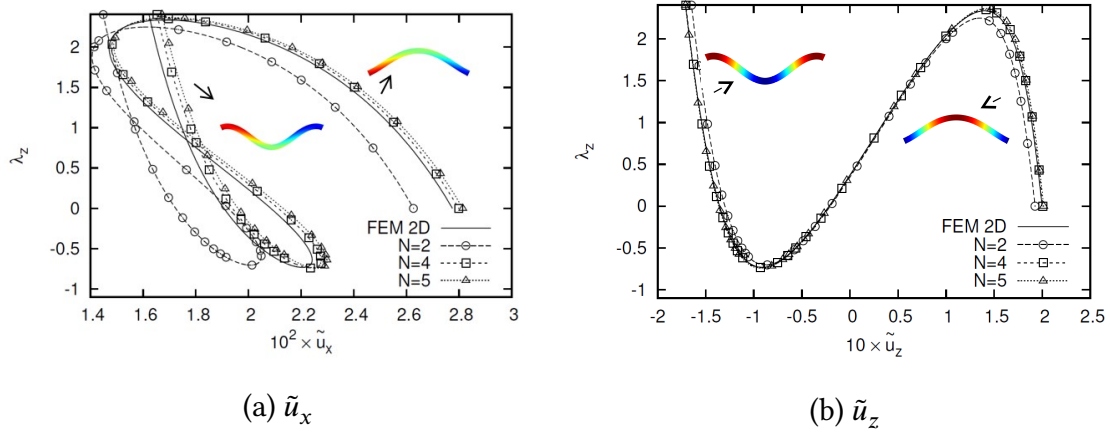


Figure 8.25: Transverse actuation load vs. axial and transverse displacements. Snap-through behavior of a pre-buckled doubly-clamped beam. $l/h = 20$.

numerical method as non-linear solver should be pointed out, due to its total automation and computational efficiency in following complex non-linear paths. Unlike classical predictor-corrector schemes, no choice of the step length or first increment (for those algorithms with auto-stepping) is required, therefore avoiding time-consuming and case-dependent trial and error before a computationally efficient solution can be performed. For the sake of clarity, the steps accumulation in the vicinity of limit points provided by the ANM-based solution technique is not shown in Fig. 8.25. Therefore, marker symbols do not correspond to the steps of the non-linear solution procedure. The resultant displacement field in the buckled configuration ($\lambda_x = 2.1835$) and in the

snapped configuration ($\lambda_z = 2.6135$) are shown in Fig. 8.26. A good prediction of the

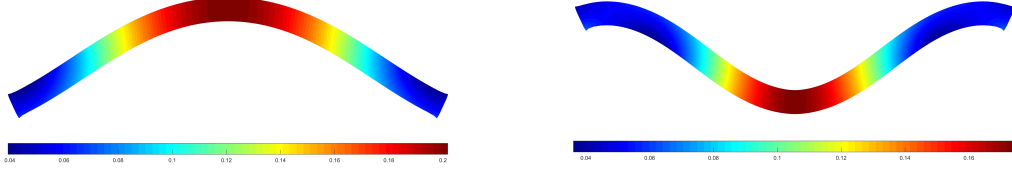


Figure 8.26: Dimensionless resultant displacement \tilde{u}_{res} . Post-buckled and snapped configurations. $l/h = 20$. UF-based one-dimensional model $N = 5$.

snap-through load can be obtained by all higher-order theories of the proposed family, as shown in Table 8.10, being the error provided by $N=2$ about 3.8%, which can be furtherly reduced to 1.2%, if a fifth-order displacement approximation is used. By looking at

	λ_z
FEM 2D	2.3355
$N = 5$	2.3637
$N = 4$	2.3521
$N = 3$	2.3082
$N = 2$	2.2480

Table 8.10: Snap-through load for a pre-buckled doubly-clamped beam structure via UF-based refined one-dimensional models. $l/h = 20$. Pre-compression load $\lambda_x = 2.1835$.

the load-deflection curves in Fig. 8.25, the phenomenon consists in the transition from a stable force-displacement region to another stable region (increasing external force) passing through an instability region (decreasing external force). From a mathematical point of view, stability regions are assessed by checking the positive definiteness of the tangent stiffness matrix, whereas instability condition is given by the existence of at least one negative eigenvalue. In the end, the two stable shapes of the bistable structure are those equilibrium states corresponding to the external load equal to zero. Due to the rotations of the beam ends given by the previous non-linear buckling phase, the energy to snap the structure from the first configuration to the second one is higher than the one required to snap from the second to the first one, resulting in an asymmetric force-displacement curve, see Fig. 8.25 (b). Figs. from 8.27 to 8.29 present the distribution of axial, normal through-the-thickness and transverse shear stress fields over the whole 2D beam domain for the post-buckled ($\lambda_x = 2.1835$) and snapped configurations ($\lambda_z = 2.6135$). An accurate and complete mechanical description can be

efficiently obtained by UF-based higher-order one-dimensional theories throughout a highly non-linear deformation path. Unlike classical structural theories, that are limited by Saint-Venant's principle, accurate predictions even in the vicinity of boundary constraints and load application points can be achieved (see Figs. 8.27 and 8.29). Nev-

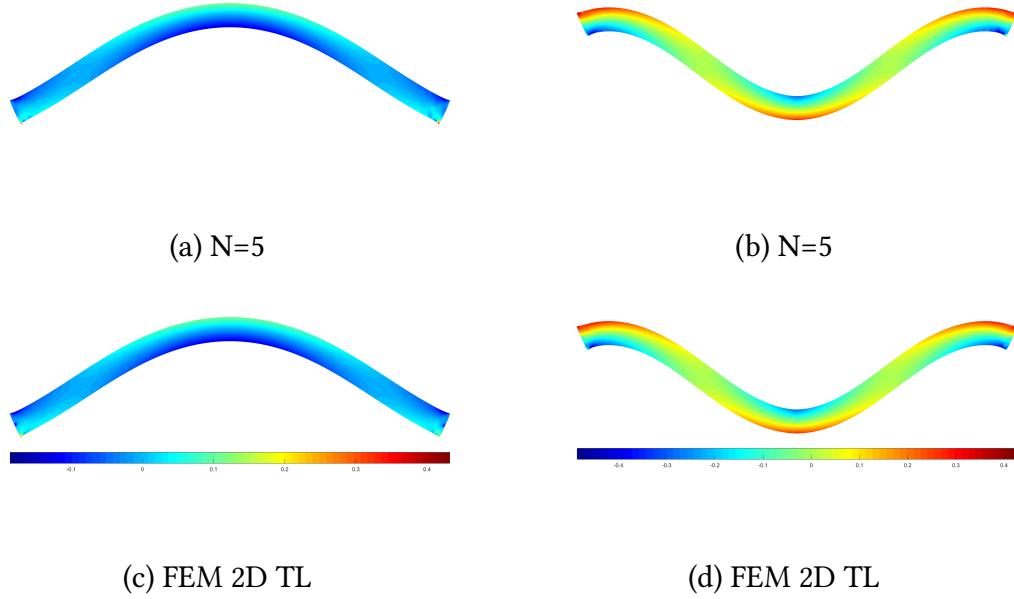


Figure 8.27: Dimensionless axial stress $\tilde{\sigma}_{xx}$ distribution in the post-buckled (a,c) and snapped configurations (b,d). $l/h = 20$.

ertheless, in some cases, especially when dealing with strongly non-linear analyses, the increase of the order of the approximating polynomials can yield numerical instability phenomena as it can be seen from Fig. 8.28, where some non-physical normal stress peaks start to arise at the edges in the vicinity of the beam ends. These numerical problems need to be treated with care and a possible solution could be the use of an appropriate pre-conditioner matrix within the numerical solution procedure or, more simply, the use of a bias one-dimensional mesh with higher refinement in proximity of discontinuities.

Clamped-simply supported beam

Similarly to the case shown in the previous section, the second study case is a clamped-simply supported beam ($\tilde{u}_x, \tilde{u}_z = 0$ at $x/l = 0$ and $\tilde{u}_z = 0$ at $x/l = 1$) which is initially buckled due to an axial load λ_x at $x/l = 1$. Starting from the deformed shape and full pre-stress field generated by the buckling step, the beam is pushed towards a reversed

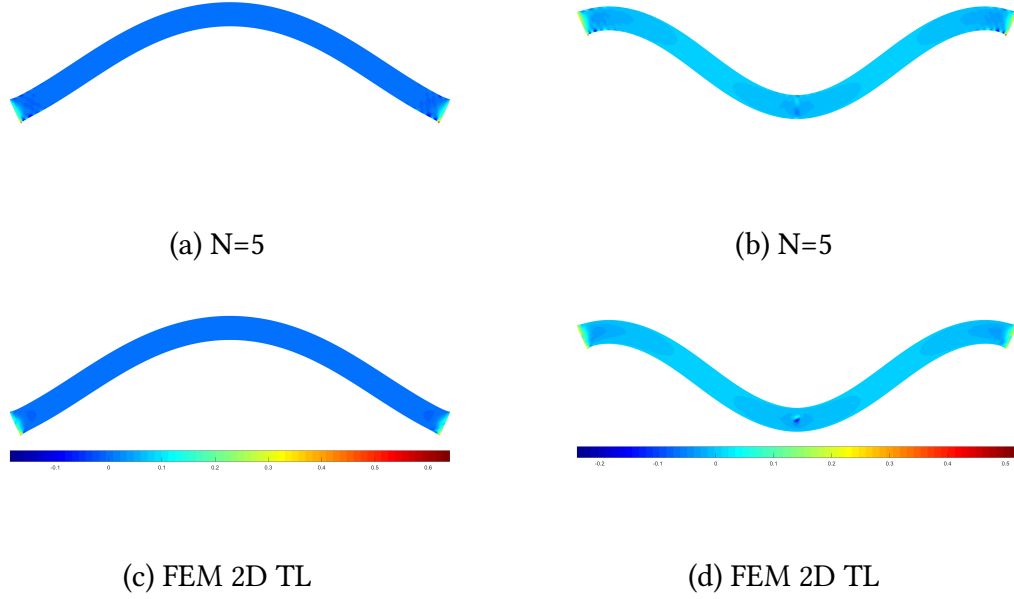


Figure 8.28: Dimensionless normal through-the-thickness stress $\tilde{\sigma}_{zz}$ distribution in the post-buckled (a,c) and snapped configurations (b,d). $l/h = 20$.

curvature configuration by means of a transverse load λ_z applied at $x/l = 1/2$. The geometric properties, material properties as well as the evaluation points for plots and tables are the same as in the previous case. Figs. 8.30 and 8.31 show the load-displacement evolution for both buckling and snap-through steps. The resultant displacement field in the buckled state and in the snapped state are shown in Fig. 8.32. As in the previous case, higher-order theories such as $N=4$ and $N=5$ lead to errors on the displacement prediction as high as 2.6% and 0.9%, at worse, on the axial and shear stresses, whereas a lower-order theory such as $N=2$ yields much poorer results, being 9.4% for the displacements, 4.4% for the axial stress and 33.0% for the shear stress, as it is shown in Table 8.11 and Fig. 8.33. As shown in Table 8.12, improvements on the accuracy of the snap-through load prediction are also obtained, being the error for $N=2$ as high as 7.8%, 4.2% for $N=3$ and being as high as 0.7% for $N=4$ and $N=5$. The stiffer structural behaviour (i.e. higher snap-through load) provided by higher-order models (such as $N=5$) with respect to less refined models (such as $N=2$) is affected by the prediction of the pre-buckling phase, which provides a more shallow initial shape for lower-order theories and, therefore, lower values of the snap-through load λ_z . In Figs. 8.34 to 8.36, the distribution of axial, shear and normal stresses for both buckled and snapped configurations are provided. Again, it is clear how, unlike classical structural models such as Euler-Bernoulli's and Timoshenko's theory, refined one-dimensional lead to an accurate yet efficient prediction of localized stresses over the whole domain of the structure.

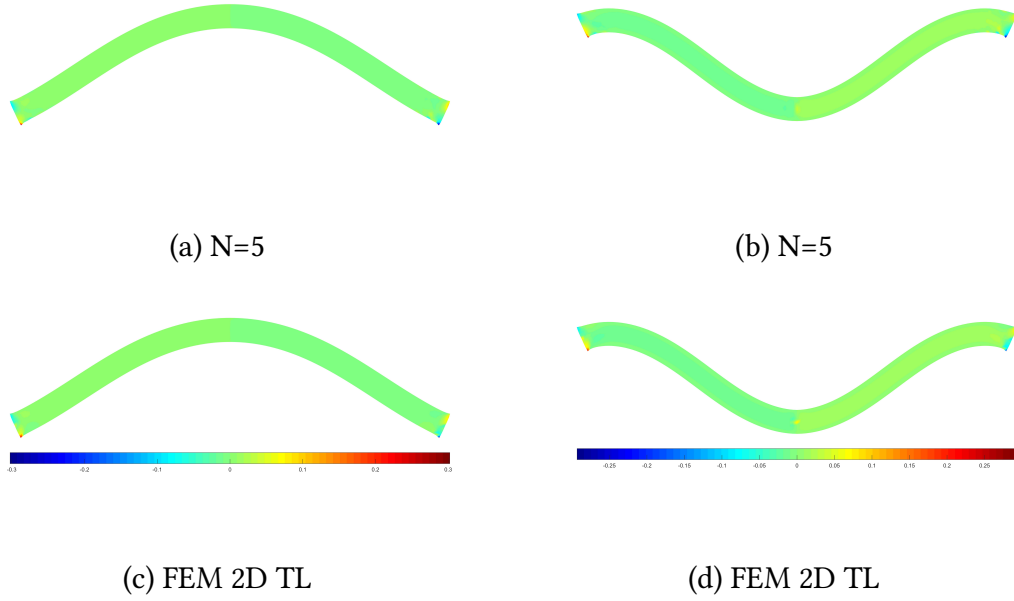


Figure 8.29: Dimensionless transverse shear stress $\tilde{\sigma}_{xz}$ distribution in the post-buckled (a,c) and snapped configurations (b,d). $l/h = 20$.

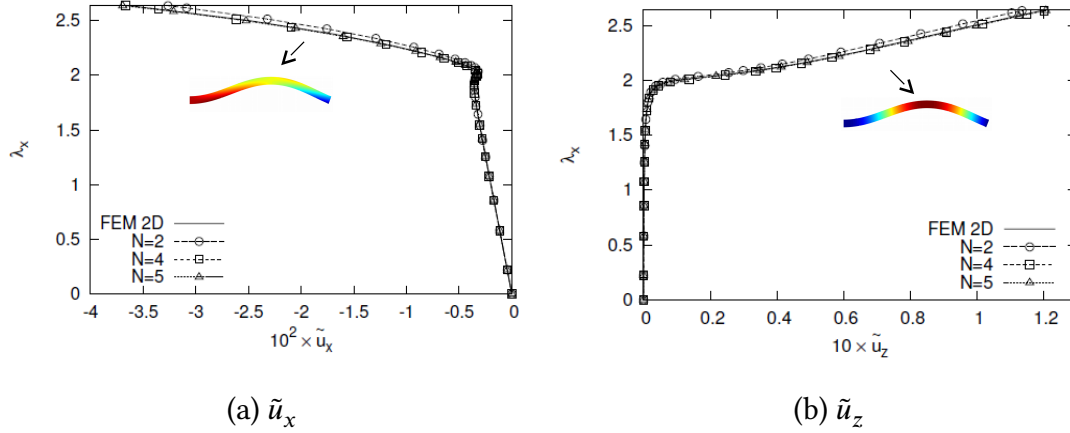


Figure 8.30: Pre-compression load vs. axial and transverse displacements. Post-buckling response. Clamped-simply supported beam. $l/h = 20$.

8.3.4 Stress prediction in bistable composites

In this section, slender composite beam structures ($l/h = 100$) with pinned-roller boundary conditions ($\tilde{u}_x = \tilde{u}_z = 0$ at $(0,0)$ and $\tilde{u}_z = 0$ at $(l,0)$) are investigated in order to assess the stress capabilities of the UF-based refined ESL models when dealing with bistable composites. Beam cross-section is square with $h = b = 1$ m. The material

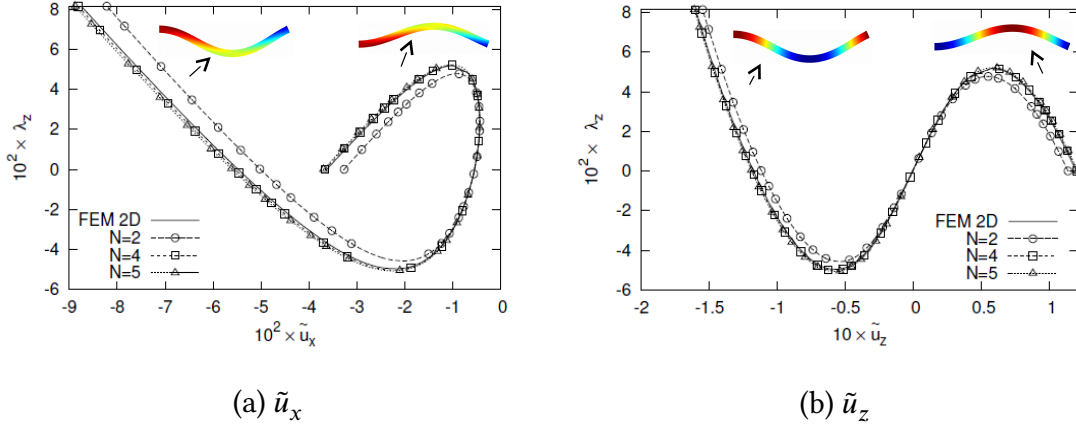


Figure 8.31: Transverse actuation load vs. axial and transverse displacements. Snap-through behavior of a pre-buckled clamped-simply supported beam. $l/h = 20$.

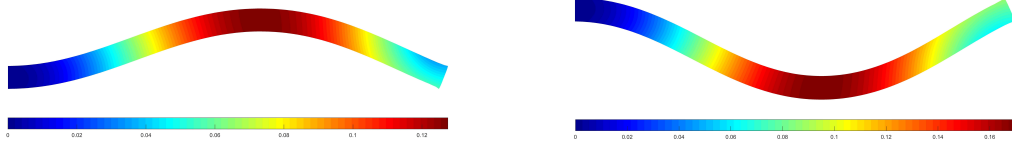


Figure 8.32: Dimensionless resultant displacement \tilde{u}_{res} . Post-buckled and snapped configurations. Clamped-simply supported beam. $l/h = 20$. UF-based one-dimensional model $N = 5$.

is glass fibre-epoxy resin composite (Glass/913) with equivalent orthotropic properties given in Section 8.3.2. Uni-directional and three-layer symmetric cross-ply stacking sequence $[0/90/0]$ are considered. An axial pre-compression load $P_x = \lambda_x \pi^2 E_L I / l^2$ with $\lambda_x = 1.1$ is applied at $(l, 0)$ in the first buckling phase (transverse disturbance $q = 0.001 \pi^2 E_L I / l^2$) and a transverse load λ_z is applied at the mid-span of the beam $(l/2, 0)$ in the subsequent snap-through phase. Stress components are expressed in the global fixed reference system, unless stated otherwise. Reference solution is obtained via two-dimensional quadratic Ansys finite elements “Plane183” (120×12 elements mesh) based on an updated Lagrangian formulation. Plane stress hypothesis are assumed for both the UF-based one-dimensional models and the two-dimensional finite elements solution. The computational costs in terms of degrees of freedom are the same as in Section 8.3.3.

	$10^2 \times -\tilde{u}_x$	$10 \times \tilde{u}_z$	$10^2 \times -\tilde{\sigma}_{xx}$	$10^3 \times \tilde{\sigma}_{xz}$
FEM 2D	3.6025	1.1951	7.4363	4.6339
$N = 5$	3.6956	1.2071	7.5044	4.6517
$N = 4$	3.6653	1.2015	7.4731	4.6313
$N = 3$	3.4891	1.1755	7.3307	4.5319
$N = 2$	3.2647	1.1356	7.1131	3.1055

Table 8.11: Displacement and stress components in a post-buckled clamped-simply supported beam. $l/h = 20$ $\lambda_x = 2.6347$.

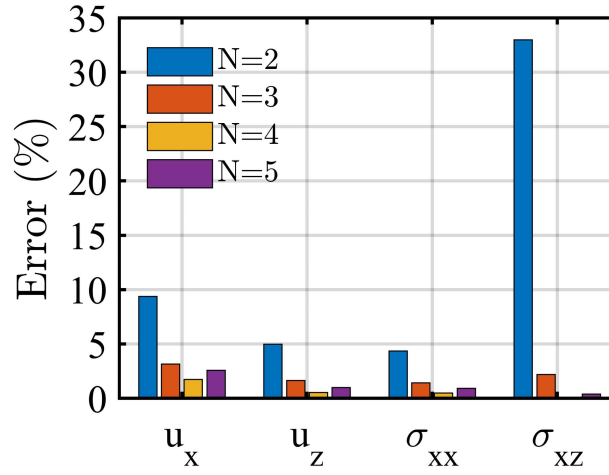


Figure 8.33: Error trends on displacements, axial and shear stress components via refined UF-based one-dimensional models. Post-buckled clamped-simply supported beam. $l/h = 20$. $\lambda_x = 2.6347$.

Uni-directional laminate

The evolution of axial and transverse displacement components response in the snap-through phase evaluated at $(l, h/2)$ and $(l/2, -h/2)$, respectively, is given in Fig. 8.37. Figure 8.38 shows the through-the-thickness distribution of stress components at the initial and final configuration throughout the snap-through phenomenon: the first configuration corresponds to the post-buckled state ($\lambda_z = 0$) and it is referred to as “C1”, whereas the second configuration, referred to as “C2”, corresponds to the snapped configuration at the final load $\lambda_z = 0.1265$. The capability of UF-based models to predict the evolution of the full in-plane stress field throughout the snapping phenomenon is shown. At least a third-order model is required in order to predict the peak of normal through-the-thickness stress at the central point of the cross-section, as shown in Fig. 8.38 (b).

	$10^2 \times \lambda_z$
FEM 2D	5.1738
$N = 5$	5.2111
$N = 4$	5.1915
$N = 3$	4.9553
$N = 2$	4.7726

Table 8.12: Snap-through load for a pre-buckled clamped-simply supported beam structure via UF-based refined one-dimensional models. $l/h = 20$. Pre-compression load $\lambda_x = 2.6347$.

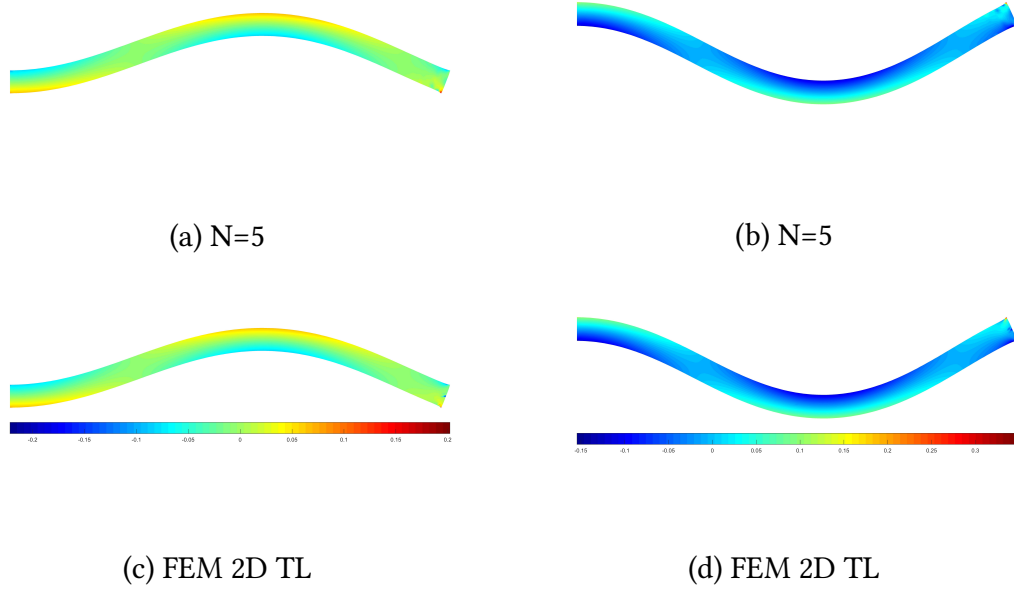


Figure 8.34: Dimensionless axial stress $\tilde{\sigma}_{xx}$ distribution in the post-buckled (a,c) and snapped configurations (b,d). Clamped-simply supported beam. $l/h = 20$.

Three-layer cross-ply symmetric laminate

The three-layer stacking sequence $[0/90/0]$ is addressed hereafter. A configuration in close proximity to buckling given by a pre-compression parameter $\lambda_x = 0.8$ is analyzed in Fig. 8.39. The through-the-thickness distribution of the stresses in the buckled and in the snapped configurations is provided in Figure 8.40.

A fairly accurate prediction of the axial stress via either a second- or third-order model in both pre-buckled and snapped configuration can be achieved. As shown in Fig. 8.40 (a), tension and compression states are inverted at top and bottom layers due to the

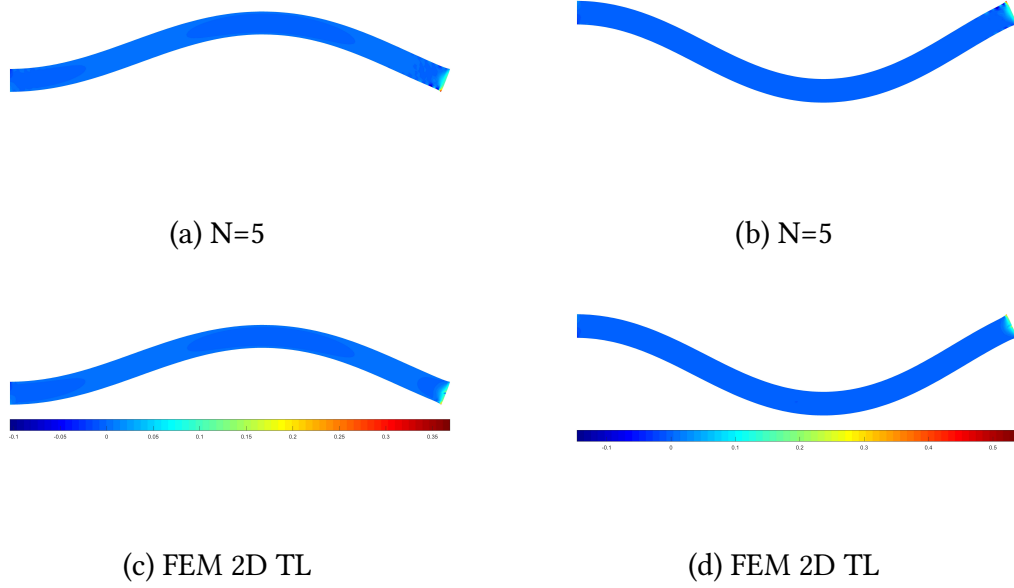


Figure 8.35: Dimensionless normal through-the-thickness stress $\tilde{\sigma}_{zz}$ distribution in the post-buckled (a,c) and snapped configurations (b,d). Clamped-simply supported beam. $l/h = 20$.

reversed curvature in the buckled and snapped configurations. Similarly to the uni-directional lay-up case, at least a third-order theory should be adopted in order to improve the description of the normal stress through-the-thickness profile.

To conclude, through UF-based modeling approach, a unified higher-order description of the cross-sectional kinematics can be obtained within the same mathematical framework yielding a refined description of the kinematics of pre-buckled bistable beams. Accurate load-displacement responses, snap-through loads and stable geometries can be derived by properly choosing the approximation order of the theory as well as an accurate evolution of the full in-plane stress field throughout strongly non-linear post-buckling and snap-through instability phenomena. Due to the one-dimensional modeling approach, the mathematical model developed via UF is characterized by a lower number of unknown variables, when compared to two-dimensional or three-dimensional finite elements solution. For the numerical results presented in this last section, a two-dimensional solution with 120×12 elements was used as reference, corresponding to about 9.2×10^3 number of degrees of freedom, whereas the most refined UF-based model was a fourth-order model ($N = 4$) with 121-node one-dimensional finite elements discretization, corresponding to 1.2×10^3 number of degrees of freedom (-86.8%). For these reasons, the presented hierarchical framework represents a reliable yet efficient modeling approach for the analysis of multi-stable composite structures.

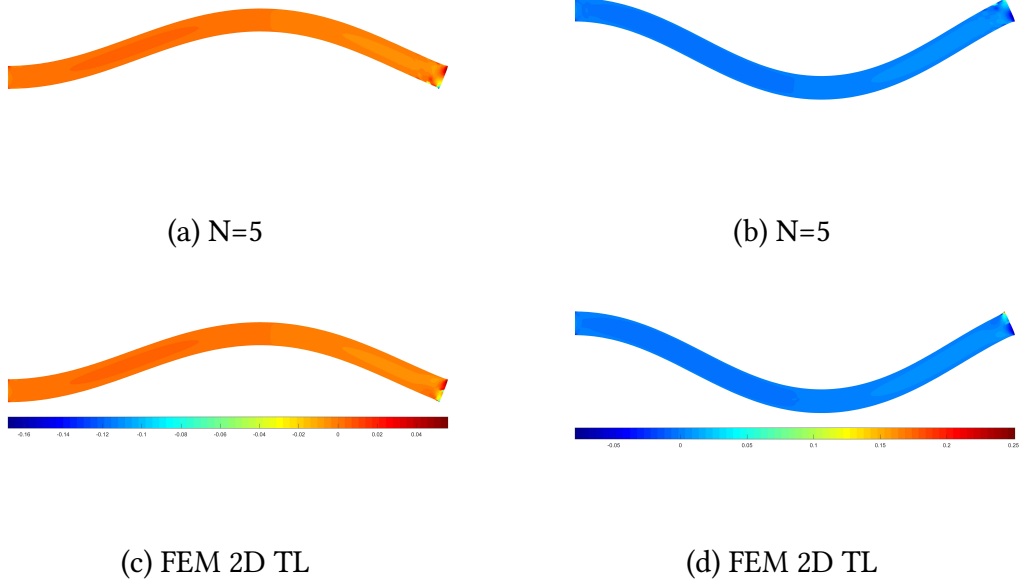


Figure 8.36: Dimensionless transverse shear stress $\tilde{\sigma}_{xz}$ distribution in the post-buckled (a,c) and snapped configurations (b,d). Clamped-simply supported beam. $l/h = 20$.

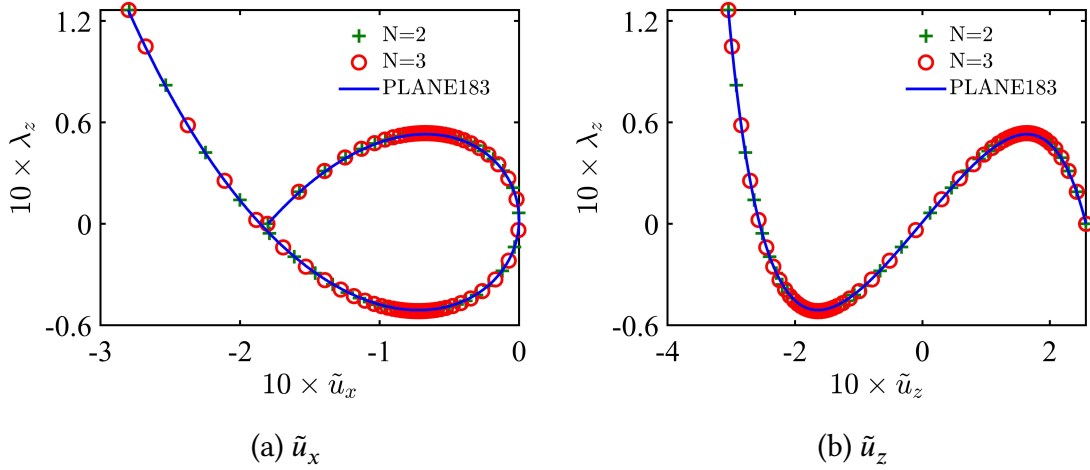


Figure 8.37: Transverse actuation load vs. (a) axial and (b) transverse displacements. Snap-through behavior of a pre-buckled pinned-roller composite beam. $l/h = 100$. Unidirectional lay-up.

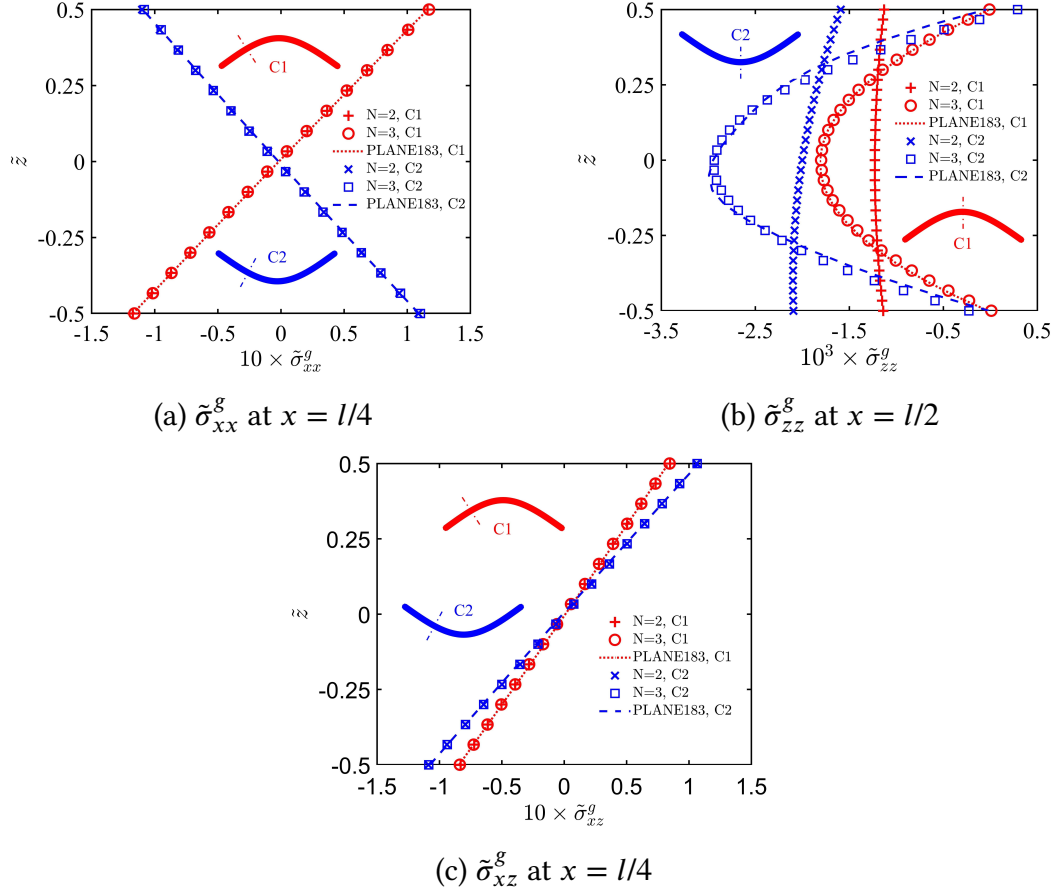


Figure 8.38: Through-the-thickness profile of global Cauchy stresses in the pre-buckled and snapped configurations. Pinned-roller composite beam. $l/h = 100$. Uni-directional lay-up.

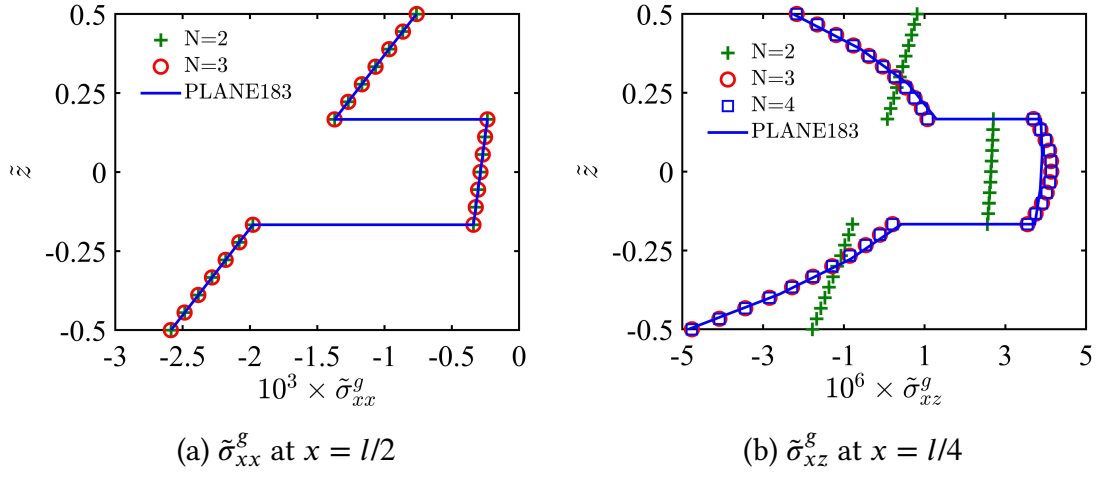


Figure 8.39: Through-the-thickness profile of global Cauchy stresses prior to buckling. $\lambda_x = 0.8$. Pinned-roller composite beam. $l/h = 100$. Three-layer cross-ply lay-up.

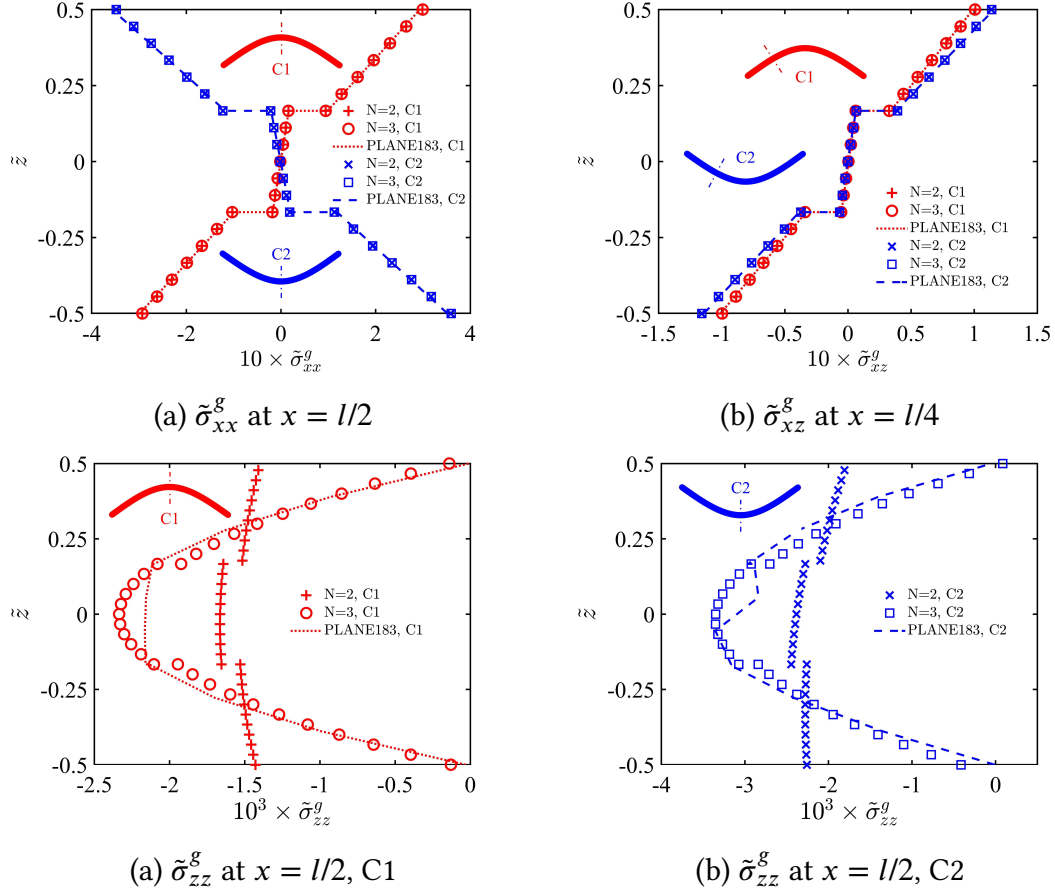


Figure 8.40: Through-the-thickness profile of global Cauchy stresses in the pre-buckled and snapped configurations. Pinned-roller composite beam. $l/h = 100$. Three-layer cross-ply lay-up.

Chapter 9

Conclusions and Outlooks

9.1 Concluding remarks

Multi-stable structures have recently received great attention thanks to their potential to increase the efficiency and extend the functionalities of conventional engineering systems. This can be achieved by properly harnessing the high-rate release of energy and motion deriving from a snap-through elastic instability phenomenon. The enhancement of the existing computational tools for the analysis of multi-stable structures in terms of accuracy and efficiency is needed for their full exploitation in industrial applications. To this aim, a novel computational framework based on an advanced structural modeling approach, i.e. the Unified Formulation, has been proposed in this dissertation. Thanks to an elegant compact notation of the displacement field, UF allows several refined one-dimensional models and different variable description approaches to be incorporated into a single mathematical framework. In order to address post-buckling and snap-through behaviors involved in multi-stability phenomena via UF approach, the extension of the formulation to account for geometric non-linearities was required. Therefore, UF-based refined finite elements accounting for Green-Lagrange strain-displacement relations have been developed in the framework of a total Lagrangian formulation. Based on linear elasticity, plane stress state and small strains assumptions, the explicit form of the fundamental nuclei of the linear, initial-displacement and initial-stress contributions to the tangent stiffness matrix has been obtained. By means of geometrically non-linear UF methodology and a path-following non-linear solver based on the Asymptotic Numerical Method, a hierarchical computational framework for a refined higher-order description of the kinematics of pre-buckled bistable beam structures has been developed. The proposed formulation has been validated towards literature results obtained by Arena et al. [2] via three-dimensional commercial software finite elements and arc-length solution procedure for the analysis of a bistable shape-adaptive air inlet, showing that, due to the high slenderness ratio and material homogeneity, a second-order UF-based model is sufficient for an accurate prediction of the load-displacement response in this case. Nevertheless, pre-buckled bistable beams

with a reduced slenderness ratio ($l/h = 20$) yield a more complex kinematic behavior that calls for higher-order one-dimensional models. Both symmetric and asymmetric bistability phenomena have been investigated, i.e. featuring symmetric or asymmetric non-linear equilibrium paths. The assumption of a second-order model for the non-linear response in the post-buckling phase yields maximum errors close to ten percent on the displacement prediction with respect to a two-dimensional small-strain finite elements formulation, which can be reduced to a few percent if a fifth-order model is considered. The enrichment of the model kinematics is even more significant for stress prediction, since a second-order model yields maximum errors greater than thirty percent (on the shear stress component), which can be reduced to less than one percent for a fifth-order expansion. The peculiar capability of UF-based refined models to predict localized stresses, even in the vicinity of boundary conditions and load application points, has been shown. Inaccuracies in the post-buckling phase provided by low-order models have also an influence on the subsequent bistability analysis, in which the snap-through load prediction can be refined up to maximum errors of a few percent. Ultimately, by properly choosing the approximation order of the theory, accurate load-displacement responses, snap-through loads and stable geometries can be derived. Moreover, the enhanced stress capabilities of the presented UF-based modeling approach in composite bistable beams have been shown. For the considered cases, the evolution of the through-the-thickness profile of a full in-plane stress field (including axial, transverse shear and transverse normal stress components) could be accurately predicted throughout the whole snap-instability phenomenon by means of either a second- or third-order theory. Finally, due to the one-dimensional nature of the UF-based modeling strategy, the size of the resulting governing algebraic system to be solved is significantly lower than in two-dimensional finite elements formulation (reductions between eighty and ninety percent for the considered cases), yielding a computational gain every time that the tangent stiffness matrix has to be assembled and inverted within the adopted non-linear solution scheme.

9.2 Original contributions

The present research represents the first known attempt to investigate multi-stability phenomena via higher-order structural models and wants to contribute to fill the gap between classical structural models and computationally expensive two- and three-dimensional commercial software finite elements for the analysis of multi-stable structures. The main novel contributions of the present research are summarized below:

- Geometrically non-linear UF-based models adopting an Equivalent Single Layer modeling strategy have been developed and assessed for the first time for large deflection analysis of metallic and multi-layered composite beam structures.
- The formulation resulting from the developed geometrically non-linear UF-based

models combined with an advanced path-following non-linear solver based on the Asymptotic Numerical Method has been implemented in a novel powerful computational tool for the analysis of non-linear and multi-stable composite beam structures.

- The significance of enriching the cross-sectional beam kinematics via higher-order terms in bistability analysis has been demonstrated for the first time, yielding refined post-buckling and snap-through equilibrium paths as well as improved predictions of snap-through loads and stable geometries in pre-buckled bistable beam structures.
- The capabilities of UF-based models to accurately predict the stress field evolution in strongly non-linear bistable composite structures via a computationally efficient one-dimensional approach has been demonstrated.

Additional original contributions provided within the present dissertation are herein reported:

- A weak form finite elements solution of the governing differential equations for the mechanical and thermo-mechanical analysis of composite beam structures via UF-based models adopting an Equivalent Single Layer approach has been developed, allowing to relax the limitations in terms of boundary conditions provided by strong form solutions previously developed by Giunta et al. [77, 80, 72].
- UF methodology has been extended to curved beam models for the first time. By expressing the principle of virtual displacements in local coordinates and accounting for curvature-dependent terms in the strain-displacement relations, the governing differential equations have been derived and solved via both strong form Navier-type solution and weak form finite elements solution. Finally, the fundamental nucleus of the stiffness matrix, typical of UF approach, has been obtained for both curved beam analytical models and curved beam elements.
- The Mixed Interpolation of Tensorial Components approach has been extended to UF-based curved beam elements in the linear regime and UF-based straight beam elements in the geometrically non-linear regime, allowing a mitigation of detrimental locking phenomena and improved convergence rate of the finite elements solution.

9.3 Scope for future research

This work laid the foundations for future research on the potential of advanced one-dimensional models in the framework of a Unified Formulation for multi-stable composite structures. In future studies, the versatility and efficiency of the developed mathematical tool for accurate modeling of homogeneous as well as multi-layered structures

could be exploited for material tailoring of bistable beam structures with no need to resort to two-dimensional or three-dimensional finite elements. By changing the composite material properties, the number of layers and the stacking sequence, the snap-through equilibrium path of the bistable structure can be tailored to fit the desired behavior depending on the application. Due to the enhanced capabilities of higher-order models to provide a good estimation of inter-laminar and intra-laminar stresses in composite structures by means of a one-dimensional approach, the developed computational framework also shows a great potential for efficient failure analysis in safe design of multi-stable composite applications. The prediction of first-ply failure indices, dominating failure modes and onset of delamination in pre-buckled bistable composite beam structures by means of the proposed UF-based one-dimensional finite elements is therefore an interesting and straightforward follow-up of the present research. As far as the further development of the modeling framework is concerned, several possible advancements can be identified stemming from this dissertation. By relaxing the plane stress hypothesis considered in Chapter 6, three-dimensional multi-stable structures, such as beams as well as plates and shells, may be investigated via a UF-based one-dimensional approach, with potentially dramatic computational savings with respect to three-dimensional non-linear finite elements solution. Furthermore, the extension of the UF-based curved beam formulation developed in Chapter 5 to the geometrically non-linear regime could open up new modeling possibilities for the design of initially curved stress-free multi-stable structures. Finally, by accounting for thermo-mechanical coupling, see Chapter 4, within the geometrically non-linear framework of Chapter 6, the three-dimensional stress capabilities of the developed UF-based models could be extremely effective to investigate challenging thermally-induced multi-stability phenomena. Besides the thermo-mechanical coupled problem, piezo-mechanical coupling could be also considered for the study of piezo-actuated multi-stable structures.

Curriculum Vitae

Name: Gabriele
Last name: De Pietro
Date of birth: 27 February 1990
Place of birth: Foggia, Italy
E-mail: gabriele.depietro@polito.it

Education

- ◊ **October 2015 - March 2019:** PhD candidate in Mechanical Engineering at Polytechnic of Turin. Dissertation: “Modeling and Design of Multi-Stable Composite Structures”.
- ◊ **3-7 April 2017:** Summer school on “Computational Methods for the Analysis, Design and Failure of Composites”, International Centre for Mechanical Sciences (CISM), Udine, Italy.
- ◊ **July 2015:** Master of Science in Aerospace Engineering from Polytechnic of Turin, Italy. Dissertation: “Wave propagation and damage analysis in metallic and composite aerospace structures via refined structural models”.
- ◊ **September 2013 - March 2014:** Visiting student at Institut Polytechnique des Science Avancées (IPSA), Paris, France.
- ◊ **October 2012:** Bachelor of Science in Aerospace Engineering from Polytechnic of Turin, Italy. Dissertation: “Methods of reduction of pollutant emissions for gas turbine combustors”.

Working Experience

- ◊ **October 2015 - October 2018:** Marie Curie research fellow at Luxembourg Institute of Science and Technology (LIST), Materials Research and Technology Department.
- ◊ **July - August 2018:** Visiting research fellow at University of Bristol, Bristol Composite Institute.
- ◊ **March - June 2018:** Visiting research fellow at Thales Alenia Space Belgium (Mont-sur-Marchienne), Technology Department.
- ◊ **January - May 2015:** Visiting research fellow at Royal Melbourne Institute of

Technology (RMIT), Aerospace Engineering Department.

Publications

International journal articles

- Y. Hui, G. De Pietro, G. Giunta, S. Belouettar, H. Hu, E. Carrera, A. Pagani, “*Geometrically non-linear analysis of beam structures via hierarchical one-dimensional finite elements*”, Mathematical Problems in Engineering, 2018.
- G. De Pietro, A. G. de Miguel, E. Carrera, G. Giunta, S. Belouettar, A. Pagani, “*Strong and weak form solutions of curved beams via Carrera’s Unified Formulation*”, Mechanics of Advanced Materials and Structures, 2018.
- M. Petrolo, I. Kaleel, G. De Pietro, E. Carrera, “*Wave propagation in compact, thin-walled and layered beams using variable kinematic beam theories*”, International Journal for Computational Methods in Engineering Science & Mechanics, 2018.
- A. G. de Miguel, G. De Pietro, E. Carrera, G. Giunta, A. Pagani, “*Locking-free curved elements with refined kinematics for the analysis of composite structures*”, Computer Methods in Applied Mechanics and Engineering, 337: 481-500, 2018.
- G. De Pietro, G. Giunta, S. Belouettar, E. Carrera, “*A static analysis of three-dimensional sandwich beam structures by hierarchical finite elements modelling*”, Journal of Sandwich Structures and Materials, 2016.
- G. De Pietro, Y. Hui, G. Giunta, S. Belouettar, E. Carrera, H. Hu, “*Hierarchical one-dimensional finite elements for the thermal stress analysis of three-dimensional functionally graded beams*”, Composite Structures, 153: 514-528, 2016.
- G. Giunta, G. De Pietro, H. Nasser, S. Belouettar, E. Carrera, M. Petrolo, “*A thermal stress finite element analysis of beam structures by hierarchical modelling*”, Composites Part B: Engineering, 95: 179-195, 2016.

Book chapters

- G. De Pietro, G. Giunta, S. Belouettar, E. Carrera, “*Bistable buckled beam-like structures by one-dimensional hierarchical modelling*”, Advances in predictive models and methodologies for numerically efficient linear and nonlinear analysis of composites, Springer. To be published.

Conference proceedings

- G. De Pietro, G. Giunta, Y. Hui, E. Carrera, S. Belouettar, H. Hu, “*One-dimensional hierarchical modelling of bistable composite beams*”, IX International Conference on the Design, Modelling and Experiments of Advanced Structures and Systems (DeMEASS), Sesimbra, Portugal, 2018.
- Y. Hui, G. Giunta, G. De Pietro, R. Xu, S. Belouettar, H. Hu, E. Carrera, “*Multi-scale CUF-FE2 nonlinear analysis of beam structures*”, IX International Conference on the

Design, Modelling and Experiments of Advanced Structures and Systems (DeMEASS), Sesimbra, Portugal, 2018.

- G. De Pietro, G. Giunta, Y. Hui, S. Belouettar, H. Hu, E. Carrera, "*Geometrically non-linear hierarchical finite elements for the analysis of bi-stable beam structures*", International Conference on Mechanics of Advanced Materials and Structures (ICMAMS), Turin, Italy, 2018.

- G. Giunta, G. De Pietro, Y. Hui, S. Belouettar, "*Newton's series expansion based theories in the framework of Carrera's Unified Formulation for the analysis of plates*", International Conference on Mechanics of Advanced Materials and Structures (ICMAMS), Turin, Italy, 2018.

- Y. Hui, G. Giunta, G. De Pietro, S. Belouettar, H. Hu, E. Carrera, "*Hierarchical beam finite elements for multi-scale geometrically nonlinear analysis of beam structures via multi-scale asymptotic numerical method*", International Conference on Mechanics of Advanced Materials and Structures (ICMAMS), Turin, Italy, 2018.

- I. Liemans, J. Garnier, J. Polome, Garraay D., Vermeir S., De Pietro G., "*Topology optimization of a PCB supporting frame*", European Conference on Spacecraft Structures, Materials and Environmental Testing (ECSSMET), Noordwijk, Netherlands, 2018.

- G. De Pietro, G. Giunta, S. Belouettar, A. Pagani, E. Carrera, "*Geometrically nonlinear hierarchical finite elements via a unified formulation*", XX International Conference on Composite Structures (ICCS), Paris, France, 2017.

- G. De Pietro, G. Giunta, S. Belouettar, E. Carrera, "*A thermal stress analysis of functionally graded beam structures by hierarchical finite elements*", II International Conference on Mechanics of Composites (MechComp), Porto, Portugal, 2016.

- G. Giunta, S. Belouettar, G. De Pietro, "*A thermal stress finite element analysis of isotropic and laminated beams via unified formulation*", XXIII Conference of the Italian Association of Aeronautics and Astronautics (AIDAA), Turin, Italy, 2015.

- M. Petrolo, E. Carrera, G. De Pietro, A. Rosati, "*Evaluation of damage effects on metallic and composite aerospace structures via refined models*", XXIII National Conference of the Italian Association of Aeronautics and Astronautics (AIDAA), Turin, Italy, 2015.

- M. Petrolo, E. Carrera, G. De Pietro, "*Dynamic response analysis of structures through component-wise models*", XXIII National Conference of the Italian Association of Aeronautics and Astronautics (AIDAA), Turin, Italy, 2015.

Bibliography

- [1] V. R. Aitharaju and R. C. Averill. “ C^0 zig-zag finite element for analysis of laminated composite beams”. In: *Journal of Engineering mechanics* 125.3 (1999), pp. 323–330.
- [2] G. Arena et al. “Adaptive compliant structures for flow regulation”. In: *Proc. R. Soc. A* 473.2204 (2017), p. 20170334.
- [3] G. Arena et al. “Design and testing of a passively adaptive inlet”. In: *Smart Materials and Structures* 27.8 (2018), p. 085019.
- [4] A. F. Arrieta et al. “Broadband vibration energy harvesting based on cantilevered piezoelectric bi-stable composites”. In: *Applied Physics Letters* 102.17 (2013), p. 173904.
- [5] A. F. Arrieta et al. “Passive load alleviation aerofoil concept with variable stiffness multi-stable composites”. In: *Composite structures* 116 (2014), pp. 235–242.
- [6] R. C. Averill and Y. C. Yip. “Thick beam theory and finite element model with zig-zag sublaminate approximations”. In: *AIAA journal* 34.8 (1996), pp. 1627–1632.
- [7] M. Aydogdu. “Vibration analysis of cross-ply laminated beams with general boundary conditions by Ritz method”. In: *International Journal of Mechanical Sciences* 47.11 (2005), pp. 1740–1755.
- [8] M. Aydogdu and V. Taskin. “Free vibration analysis of functionally graded beams with simply supported edges”. In: *Materials & design* 28.5 (2007), pp. 1651–1656.
- [9] S. Baguet. “Stabilité des structures minces et sensibilité aux imperfections par la méthode asymptotique numérique”. PhD thesis. Université de la Méditerranée-Aix-Marseille II, 2001.
- [10] S. Baguet and B. Cochelin. “On the behaviour of the ANM continuation in the presence of bifurcations”. In: *Communications in numerical methods in engineering* 19.6 (2003), pp. 459–471.
- [11] A. Baker. *Composite materials for aircraft structures*. AIAA, 2004.

- [12] J. R. Banerjee and A. J. Sobey. "Dynamic stiffness formulation and free vibration analysis of a three-layered sandwich beam". In: *International Journal of Solids and Structures* 42.8 (2005), pp. 2181–2197.
- [13] C. Basaglia, D. Camotim, and N. Silvestre. "Post-buckling analysis of thin-walled steel frames using Generalised Beam Theory (GBT)". In: *Thin-Walled Structures* 62 (2013), pp. 229–242.
- [14] K. J. Bathe. *Finite element procedures*. Prentice hall, 1996.
- [15] K. J. Bathe and E. N. Dvorkin. "A formulation of general shell elements - the use of mixed interpolation of tensorial components". In: *International Journal for Numerical Methods in Engineering* 22.3 (1986), pp. 697–722.
- [16] K. J. Bathe and E. N. Dvorkin. "A four-node plate bending element based on Mindlin/Reissner plate theory and a mixed interpolation". In: *International Journal for Numerical Methods in Engineering* 21.2 (1985), pp. 367–383.
- [17] K. J. Bathe, A. Iosilevich, and D. Chapelle. "An evaluation of the MITC shell elements". In: *Computers & Structures* 75.1 (2000), pp. 1–30. ISSN: 0045-7949.
- [18] K. J. Bathe, P. S. Lee, and J. F. Hiller. "Towards improving the MITC9 shell element". In: *Computers & Structures* 81.8 (2003). K.J Bathe 60th Anniversary Issue, pp. 477–489.
- [19] D. Bernoulli. "Commentarii academiae scientiarum imperialis petropolitanae". In: *Petropoli. Chap. De vibrationibus et sono laminarum elasticarum* (1751).
- [20] M. A. Bessa and S. Pellegrino. "Design of ultra-thin composite deployable shell structures through machine learning". In: *IASS Annual Symposium "Interfaces: architecture. engineering. science"*. 2017.
- [21] M. A. Bessa and S. Pellegrino. "Design of ultra-thin shell structures in the stochastic post-buckling range using Bayesian machine learning and optimization". In: *International Journal of Solids and Structures* (2018).
- [22] W. B. Bickford. "A consistent higher order beam theory". In: *Developments in Theoretical and Applied Mechanics* 11 (1982), pp. 137–150.
- [23] C. R. Bowen et al. "Modeling and characterization of piezoelectrically actuated bistable composites". In: *IEEE transactions on ultrasonics, ferroelectrics, and frequency control* 58.9 (2011), pp. 1737–1750.
- [24] T. E. Bruns, O. Sigmund, and D. A. Tortorelli. "Numerical methods for the topology optimization of structures that exhibit snap-through". In: *International Journal for Numerical Methods in Engineering* 55.10 (2002), pp. 1215–1237.
- [25] E. Carrera. "A class of two-dimensional theories for anisotropic multilayered plates analysis". In: *Accademia delle scienze di Torino, Memorie Scienze Fisiche* 19-20 (1995-1996), pp. 1–39.

- [26] E. Carrera. “ C_z^0 Requirements for the two dimensional analysis of multilayered structures”. In: *Composite Structures* 37 (1997), pp. 373–383.
- [27] E. Carrera. “Historical review of Zig-Zag theories for multilayered plates and shells”. In: *Appl. Mech. Rev.* 56 (2003), pp. 287–308.
- [28] E. Carrera. “Theories and finite elements for multilayered plates and shells: a unified compact formulation with numerical assessment and benchmarking”. In: *Archives of Computational Methods in Engineering* 10.3 (2003), pp. 215–296.
- [29] E. Carrera and M. Filippi. “Variable kinematic one-dimensional finite elements for the analysis of rotors made of composite materials”. In: *Journal of Engineering for Gas Turbines and Power* 136.9 (2014), p. 092501.
- [30] E. Carrera, M. Filippi, and E. Zappino. “Analysis of rotor dynamic by one-dimensional variable kinematic theories”. In: *Journal of engineering for gas turbines and power* 135.9 (2013), p. 092501.
- [31] E. Carrera, M. Filippi, and E. Zappino. “Free vibration analysis of rotating composite blades via Carrera Unified Formulation”. In: *Composite Structures* 106 (2013), pp. 317–325.
- [32] E. Carrera and G. Giunta. “Hierarchical closed form solutions for plates bent by localized transverse loadings”. In: *Journal of Zhejiang University SCIENCE A* 8.7 (2007), p. 1026 1037.
- [33] E. Carrera and G. Giunta. “Hierarchical models for failure analysis of plates bent by distributed and localized transverse loadings”. In: *Journal of Zhejiang University SCIENCE A* 9.5 (2008), p. 600 613.
- [34] E. Carrera and G. Giunta. “Refined Beam Theories based on a Unified Formulation”. In: *International Journal of Applied Mechanics* 2.1 (2010), pp. 117–143.
- [35] E. Carrera, G. Giunta, and M. Petrolo. *Beam Structures: Classical and Advanced Theories*. Wiley-Blackwell, 2011.
- [36] E. Carrera, D. Guarnera, and A. Pagani. “Static and free-vibration analyses of dental prosthesis and atherosclerotic human artery by refined finite element models”. In: *Biomechanics and modeling in mechanobiology* 17.2 (2018), pp. 301–317.
- [37] E. Carrera, I. Kaleel, and M. Petrolo. “Elastoplastic analysis of compact and thin-walled structures using classical and refined beam finite element models”. In: *Mechanics of Advanced Materials and Structures* 0.0 (2017), pp. 1–13.
- [38] E. Carrera, M. Maiarú, and M. Petrolo. “Component-wise analysis of laminated anisotropic composites”. In: *International Journal of Solids and Structures* 49.13 (2012), pp. 1839–1851.

- [39] E. Carrera, A. G. de Miguel, and A. Pagani. “Component-wise analysis of laminated structures by hierarchical refined models with mapping features and enhanced accuracy at layer to fiber-matrix scales”. In: *Mechanics of Advanced Materials and Structures* 25.14 (2018), pp. 1224–1238.
- [40] E. Carrera, A. G. de Miguel, and A. Pagani. “Extension of MITC to higher-order beam models and shear locking analysis for compact, thin-walled, and composite structures”. In: *International Journal for Numerical Methods in Engineering* 112.13 (2017), pp. 1889–1908.
- [41] E. Carrera, A. G. de Miguel, and A. Pagani. “Hierarchical theories of structures based on Legendre polynomial expansions with finite element applications”. In: *International Journal of Mechanical Sciences* 120 (2017), pp. 286–300.
- [42] E. Carrera, A. Pagani, and M. Petrolo. “Classical, refined, and component-wise analysis of reinforced-shell wing structures”. In: *AIAA journal* 51.5 (2013), pp. 1255–1268.
- [43] E. Carrera, A. Pagani, and M. Petrolo. “Refined 1D finite elements for the analysis of secondary, primary, and complete civil engineering structures”. In: *Journal of Structural Engineering* 141.4 (2014), p. 04014123.
- [44] E. Carrera, E. Zappino, and G. Li. “Analysis of beams with piezo-patches by node-dependent kinematic finite element method models”. In: *Journal of Intelligent Material Systems and Structures* 29.7 (2018), pp. 1379–1393.
- [45] E. Carrera et al. “A component-wise approach in structural analysis”. In: *Computational methods for engineering science* 4 (2012), pp. 75–115.
- [46] E. Carrera et al. “Recent developments on refined theories for beams with applications”. In: *Mechanical Engineering Reviews* 2.2 (2015), pp. 14–00298.
- [47] T. Cavallo et al. “Effect of localized damages on the free vibration analysis of civil structures by component-wise approach”. In: *Journal of Structural Engineering* 144.8 (2018), p. 04018113.
- [48] A. Chakraborty, S. Gopalakrishnan, and J. N. Reddy. “A new beam finite element for the analysis of functionally graded materials”. In: *International Journal of Mechanical Sciences* 45.3 (2003), pp. 519–539.
- [49] T. Chen, J. Mueller, and K. Shea. “Integrated design and simulation of tunable, multi-state structures fabricated monolithically with multi-material 3D printing”. In: *Scientific reports* 7 (2017), p. 45671.
- [50] S. Chiacchiari et al. “Vibration energy harvesting from impulsive excitations via a bistable nonlinear attachment”. In: *International Journal of Non-Linear Mechanics* 94 (2017), pp. 84–97.

- [51] Y. B. Cho and R. Averill. “An improved theory and finite-element model for laminated composite and sandwich beams using first-order zig-zag sublaminate approximations”. In: *Composite Structures* 37.3 (1997), pp. 281–298.
- [52] J. Cleary and H. J. Su. “Modeling and experimental validation of actuating a bistable buckled beam via moment input”. In: *Journal of Applied Mechanics* 82.5 (2015), p. 051005.
- [53] B. Cochelin. “A path-following technique via an asymptotic-numerical method”. In: *Computers & structures* 53.5 (1994), pp. 1181–1192.
- [54] F. Cottone et al. “Piezoelectric buckled beams for random vibration energy harvesting”. In: *Smart materials and structures* 21.3 (2012), p. 035021.
- [55] G. R. Cowper. “The shear coefficient in Timoshenko beam theory”. In: *Journal of Applied Mechanics* 33.10 (1966), pp. 335–340.
- [56] B. S. Cox et al. “Exploring the design space of nonlinear shallow arches with generalised path-following”. In: *Finite Elements in Analysis and Design* 143 (2018), pp. 1–10.
- [57] M. A. Crisfield. *Non-linear finite element analysis of solids and structures*. Vol. 1. Chichester, England: John Wiley and Sons, 1991.
- [58] A. R. Damanpack and S. M. R. Khalili. “High-order free vibration analysis of sandwich beams with a flexible core using dynamic stiffness method”. In: *Composite Structures* 94.5 (2012), pp. 1503–1514.
- [59] C. Darwin and F. Darwin. *Insectivorous plants*. J. Murray, 1888.
- [60] G. De Pietro et al. “A static analysis of three-dimensional sandwich beam structures by hierarchical finite elements modelling”. In: *Journal of Sandwich Structures & Materials* (2017), p. 1099636217732907.
- [61] G. De Pietro et al. “Hierarchical one-dimensional finite elements for the thermal stress analysis of three-dimensional functionally graded beams”. In: *Composite Structures* (2016).
- [62] C. G. Diaconu, P. M. Weaver, and F. Mattioni. “Concepts for morphing airfoil sections using bi-stable laminated composite structures”. In: *Thin-Walled Structures* 46.6 (2008), pp. 689–701.
- [63] S. A. Emam and D. J. Inman. “A review on bistable composite laminates for morphing and energy harvesting”. In: *Applied Mechanics Reviews* 67.6 (2015), p. 060803.
- [64] A. Entezari, M. Filippi, and E. Carrera. “Unified finite element approach for generalized coupled thermoelastic analysis of 3D beam-type structures, part 1: Equations and formulation”. In: *Journal of Thermal Stresses* 40.11 (2017), pp. 1386–1401.

- [65] L. Euler. “Additamentum I: De Curvas Elasticis”. In: *Methodus inveniendi lineas curvas maximi minimive proprietate gaudentes [...]* (1744), pp. 245–310.
- [66] M. Filippi and E. Carrera. “Bending and vibrations analyses of laminated beams by using a zig-zag-layer-wise theory”. In: *Composites Part B: Engineering* 98 (2016), pp. 269–280.
- [67] M. Filippi, A. Entezari, and E. Carrera. “Unified finite element approach for generalized coupled thermoelastic analysis of 3D beam-type structures, part 2: Numerical evaluations”. In: *Journal of Thermal Stresses* 40.11 (2017), pp. 1402–1416.
- [68] M. Filippi, A. Pagani, and E. Carrera. “Accurate nonlinear dynamics and mode aberration of rotating blades”. In: *Journal of Applied Mechanics* 85.11 (2018), p. 111004.
- [69] Y. Forterre et al. “How the Venus flytrap snaps”. In: *Nature* 433.7024 (2005), p. 421.
- [70] R. Gao et al. “A novel design method of bistable structures with required snap-through properties”. In: *Sensors and Actuators A: Physical* 272 (2018), pp. 295–300.
- [71] L. J. Gibson and M. F. Ashby. *Cellular solids: structure and properties*. Cambridge University Press, 1999.
- [72] G. Giunta, S. Belouettar, and E. Carrera. “A thermal stress analysis of three-dimensional beams by refined one-dimensional models and strong form solutions”. In: *Composite Materials and Structures in Aerospace Engineering*. Vol. 828. Applied Mechanics and Materials. Trans Tech Publications, Apr. 2016, pp. 139–171.
- [73] G. Giunta, S. Belouettar, and A. J. M. Ferreira. “A static analysis of three-dimensional functionally graded beams by hierarchical modelling and a collocation meshless solution method”. In: *Acta Mechanica* 227.4 (2016), pp. 969–991.
- [74] G. Giunta, Y. Koutsawa, and S. Belouettar. “Analysis of three-dimensional piezoelectric beams via a unified formulation”. In: *Advanced Materials Research*. Vol. 745. Trans Tech Publ. 2013, pp. 101–118.
- [75] G. Giunta et al. “A thermal stress finite element analysis of beam structures by hierarchical modelling”. In: *Composites Part B: Engineering* 95 (2016), pp. 179–195.
- [76] G. Giunta et al. “A thermo-mechanical analysis of functionally graded beams via hierarchical modelling”. In: *Composite Structures* 95 (2013), pp. 676–690.
- [77] G. Giunta et al. “A thermo-mechanical analysis of isotropic and composite beams via collocation with radial basis functions”. In: *Journal of Thermal Stresses* 36.11 (2013), pp. 1169–1199.

- [78] G. Giunta et al. "Free vibration analysis of composite beams via refined theories". In: *Composites Part B: Engineering* 44.1 (2013), pp. 540–552.
- [79] G. Giunta et al. "Free vibration and stability analysis of three-dimensional sandwich beams via hierarchical models". In: *Composites Part B: Engineering* 47 (2013), pp. 326–338.
- [80] G. Giunta et al. "Hierarchical models for the static analysis of three-dimensional sandwich beam structures". In: *Composite Structures* 133 (2015), pp. 1284–1301.
- [81] G. Giunta et al. "Static, free vibration and stability analysis of three-dimensional nano-beams by atomistic refined models accounting for surface free energy effect". In: *International Journal of Solids and Structures* 50.9 (2013), pp. 1460–1472.
- [82] M. Grediac. "A finite element study of the transverse shear in honeycomb cores". In: *International journal of solids and structures* 30.13 (1993), pp. 1777–1788.
- [83] R. M. J. Groh and A. Pirrera. "Generalised path-following for well-behaved non-linear structures". In: *Computer Methods in Applied Mechanics and Engineering* 331 (2018), pp. 394–426.
- [84] R. M. J. Groh and P. M. Weaver. "Static inconsistencies in certain axiomatic higher-order shear deformation theories for beams, plates and shells". In: *Composite Structures* 120 (2015), pp. 231–245.
- [85] L. Hanten et al. "Free vibration analysis of fibre-metal laminated beams via hierarchical one-dimensional models". In: *Mathematical Problems in Engineering* (2018).
- [86] R. L. Harne and K. W. Wang. "A review of the recent research on vibration energy harvesting via bistable systems". In: *Smart materials and structures* 22.2 (2013), p. 023001.
- [87] P. R. Heyliger and J. N. Reddy. "A higher order beam finite element for bending and vibration problems". In: *Journal of sound and vibration* 126.2 (1988), pp. 309–326.
- [88] D. H. Hodges et al. "On a simplified strain energy function for geometrically nonlinear behaviour of anisotropic beams". In: *Composites Engineering* 2.5 (1992), pp. 513–526.
- [89] H. Hu et al. "A novel finite element for global and local buckling analysis of sandwich beams". In: *Composite Structures* 90.3 (2009), pp. 270–278.
- [90] H. Hu et al. "Assessment of various kinematic models for instability analysis of sandwich beams". In: *Engineering Structures* 33.2 (2011), pp. 572–579.
- [91] W. Hufenbach and M. Gude. "Analysis and optimisation of multistable composites under residual stresses". In: *Composite structures* 55.3 (2002), pp. 319–327.

- [92] Y. Hui et al. "A free vibration analysis of three-dimensional sandwich beams using hierarchical one-dimensional finite elements". In: *Composites Part B: Engineering* 110 (2017), pp. 7–19.
- [93] Y. Hui et al. "Geometrically nonlinear analysis of beam structures via hierarchical one-dimensional finite elements". In: *Mathematical Problems in Engineering* (2018).
- [94] M. W. Hyer. "The room-temperature shapes of four-layer unsymmetric cross-ply laminates". In: *Journal of Composite Materials* 16.4 (1982), pp. 318–340.
- [95] B. D. Jensen et al. "Design optimization of a fully-compliant bistable micro-mechanism". In: *ASME International Mechanical Engineering Congress and Exposition*. 2001, pp. 1–7.
- [96] R. M. Jones. *Mechanics of composite materials*. CRC press, 2014.
- [97] I. Kaleel et al. "Computationally efficient, high-fidelity micromechanics framework using refined 1D models". In: *Composite Structures* 181 (2017), pp. 358–367.
- [98] I. Kaleel et al. "Micromechanical progressive failure analysis of fiber-reinforced composite using refined beam models". In: *Journal of Applied Mechanics* 85.2 (2018), p. 021004.
- [99] S. Kapuria, P. C. Dumir, and A. Ahmed. "An efficient higher order zigzag theory for composite and sandwich beams subjected to thermal loading". In: *International Journal of Solids and Structures* 40.24 (2003), pp. 6613–6631.
- [100] S. Kapuria, P. C. Dumir, and N.K. Jain. "Assessment of zigzag theory for static loading, buckling, free and forced response of composite and sandwich beams". In: *Composite Structures* 64.3–4 (2004), pp. 317–327.
- [101] J. Kim and S. R. Swanson. "Design of sandwich structures for concentrated loading". In: *Composite Structures* 52.3 (2001), pp. 365–373.
- [102] Y. Koutsawa, G. Giunta, and S. Belouettar. "A free vibration analysis of piezo-electric beams via hierarchical one-dimensional finite elements". In: *Journal of Intelligent Material Systems and Structures* 25.8 (2014), pp. 1009–1023.
- [103] Y. Koutsawa, G. Giunta, and S. Belouettar. "Hierarchical FEM modelling of piezo-electric beam structures". In: *Composite Structures* 95 (2013), pp. 705–718.
- [104] Y. Koutsawa et al. "Static analysis of shear actuated piezo-electric beams via hierarchical FEM theories". In: *Mechanics of Advanced Materials and Structures* 22.1-2 (2015), pp. 3–18.
- [105] D. Krajcinovic. "Sandwich beam analysis". In: *Journal of Applied Mechanics* 39.3 (1972), pp. 773–778.
- [106] E. Lamacchia et al. "Morphing shell structures: a generalised modelling approach". In: *Composite Structures* 131 (2015), pp. 1017–1027.

- [107] A. Laulusa et al. "Evaluation of some shear deformable shell elements". In: *International Journal of Solids and Structures* 43.17 (2006), pp. 5033–5054.
- [108] D. Lentink et al. "How swifts control their glide performance with morphing wings". In: *Nature* 446.7139 (2007), p. 1082.
- [109] L. Léotoing, S. Drapier, and A. Vautrin. "Nonlinear interaction of geometrical and material properties in sandwich beam instabilities". In: *International Journal of Solids and Structures* 39.13-14 (2002), pp. 3717–3739.
- [110] M. Levinson. "A new rectangular beam theory". In: *Journal of Sound and vibration* 74.1 (1981), pp. 81–87.
- [111] P. Litewka and J. Rakowski. "The exact thick arch finite element". In: *Computers & Structures* 68.4 (1998), pp. 369–379.
- [112] A. Mahi et al. "An analytical method for temperature-dependent free vibration analysis of functionally graded beams with general boundary conditions". In: *Composite Structures* 92 (2010), pp. 1877–1887.
- [113] D. S. Malkus and T. J. R. Hughes. "Mixed finite element methods - Reduced and selective integration techniques: A unification of concepts". In: *Computer Methods in Applied Mechanics and Engineering* 15.1 (1978), pp. 63–81.
- [114] R. Masana and M. F. Daqaq. "Relative performance of a vibratory energy harvester in mono-and bi-stable potentials". In: *Journal of Sound and Vibration* 330.24 (2011), pp. 6036–6052.
- [115] K. Mattiasson. "Numerical results from large deflection beam and frame problems analysed by means of elliptic integrals". In: *International Journal for Numerical Methods in Engineering* 17.1 (1981), pp. 145–153.
- [116] F. Mattioni et al. "Analysis of thermally induced multistable composites". In: *International Journal of Solids and Structures* 45.2 (2008), pp. 657–675.
- [117] F. Mattioni et al. "The application of thermally induced multistable composites to morphing aircraft structures". In: *Industrial and Commercial Applications of Smart Structures Technologies*. 2008.
- [118] A. G. de Miguel et al. "Accurate evaluation of failure indices of composite layered structures via various FE models". In: *Composites Science and Technology* 167 (2018), pp. 174–189.
- [119] A. G. de Miguel et al. "Locking-free curved elements with refined kinematics for the analysis of composite structures". In: *Computer Methods in Applied Mechanics and Engineering* 337 (2018), pp. 481–500.
- [120] M. Montemurro et al. "A general multi-scale two-level optimisation strategy for designing composite stiffened panels". In: *Composite Structures* 201 (2018), pp. 968–979.

- [121] F. Nicassio et al. “Low energy actuation technique of bistable composites for aircraft morphing”. In: *Aerospace Science and Technology* 75 (2018), pp. 35–46.
- [122] J. L. Nowinski. *Theory of thermoelasticity with applications*. Sijthoff and Noordhoff, The Netherlands, 1978.
- [123] Y. S. Oh and S. Kota. “Robust design of bistable compliant mechanisms using the bistability of a clamped-pinned beam”. In: *ASME 2008 International Design Engineering Technical Conferences and Computers and Information in Engineering Conference*. American Society of Mechanical Engineers. 2008, pp. 273–282.
- [124] A. Pagani and E. Carrera. “Large-deflection and post-buckling analyses of laminated composite beams by Carrera Unified Formulation”. In: *Composite Structures* 170 (2017), pp. 40–52.
- [125] A. Pagani and E. Carrera. “Unified formulation of geometrically nonlinear refined beam theories”. In: *Mechanics of Advanced Materials and Structures* 25.1 (2018), pp. 15–31.
- [126] A. Pagani et al. “Analysis of laminated beams via Unified Formulation and Legendre polynomial expansions”. In: *Composite Structures* 156 (2016), pp. 78–92.
- [127] A. Paknejad et al. “Analytical solution of piezoelectric energy harvester patch for various thin multilayer composite beams”. In: *Composite Structures* 154 (2016), pp. 694–706.
- [128] S. Park and D. Hah. “Pre-shaped buckled-beam actuators: theory and experiments”. In: *Sensors and Actuators A: Physical* 148.1 (2008), pp. 186–192.
- [129] M. Petrolo et al. “A global-local approach for the elastoplastic analysis of compact and thin-walled structures via refined models”. In: *Computers & Structures* 206 (2018), pp. 54–65.
- [130] C. N. Phan, Y. Frostig, and G. A. Kardomateas. “Analysis of sandwich beams with a compliant core and with in-plane rigidity-extended high-order sandwich panel theory versus elasticity”. In: *Journal of Applied Mechanics* 79.4 (2012), p. 041001.
- [131] G. De Pietro et al. “Hierarchical one-dimensional finite elements for the thermal stress analysis of three-dimensional functionally graded beams”. In: *Composite Structures* 153 (2016), pp. 514–528.
- [132] G. De Pietro et al. “Strong and weak form solutions of curved beams via Carrera’s unified formulation”. In: *Mechanics of Advanced Materials and Structures* 0.0 (2018), pp. 1–12.
- [133] A. Pirrera, D. Avitabile, and P. M. Weaver. “Bistable plates for morphing structures: a refined analytical approach with high-order polynomials”. In: *International Journal of Solids and Structures* 47.25-26 (2010), pp. 3412–3425.
- [134] M. E. Pontecorvo et al. “Bistable arches for morphing applications”. In: *Journal of Intelligent Material Systems and Structures* 24.3 (2013), pp. 274–286.

- [135] P. Portela et al. "Analysis of morphing, multi stable structures actuated by piezo-electric patches". In: *Computers & Structures* 86.3-5 (2008), pp. 347–356.
- [136] G. N. Praveen and J. N. Reddy. "Nonlinear transient thermoelastic analysis of functionally graded ceramic-metal plates". In: *International Journal of Solids and Structures* 35.33 (1998), pp. 4457–4476.
- [137] J. Qiu, J. H. Lang, and A. H. Slocum. "A curved-beam bistable mechanism". In: *Journal of microelectromechanical systems* 13.2 (2004), pp. 137–146.
- [138] J. N. Reddy. *An Introduction to Nonlinear Finite Element Analysis: with applications to heat transfer, fluid mechanics, and solid mechanics*. OUP Oxford, 2014.
- [139] J. N. Reddy. *Energy and variational methods in applied mechanics: with an introduction to the finite element method*. Wiley New York, 1984.
- [140] J. N. Reddy. *Mechanics of laminated composite plates and shells. Theory and Analysis*. 2nd ed. CRC Press, 2004.
- [141] J. N. Reddy, C. M. Wang, and K. H. Lee. "Relationships between bending solutions of classical and shear deformation beam theories". In: *International Journal of Solids and Structures* 34.26 (1997), pp. 3373–3384.
- [142] E. Reissner. "On a certain mixed variational theorem and a proposed application". In: *International Journal for Numerical Methods in Engineering* 20 (1984), pp. 1366–1368.
- [143] D. Restrepo, N. D. Mankame, and P. D. Zavattieri. "Phase transforming cellular materials". In: *Extreme Mechanics Letters* 4 (2015), pp. 52–60.
- [144] M. Santer and S. Pellegrino. "Concept and design of a multistable plate structure". In: *Journal of Mechanical Design* 133.8 (2011), p. 081001.
- [145] M. Savoia, F. Laudiero, and A. Tralli. "A refined theory for laminated beams: Part I—A new high order approach". In: *Meccanica* 28.1 (1993), pp. 39–51.
- [146] G. Scarselli et al. "A novel bistable energy harvesting concept". In: *Smart Materials and Structures* 25.5 (2016), p. 055001.
- [147] S. Shan et al. "Multistable architected materials for trapping elastic strain energy". In: *Advanced Materials* 27.29 (2015), pp. 4296–4301.
- [148] N. Silvestre and D. Camotim. "First-order generalised beam theory for arbitrary orthotropic materials". In: *Thin-Walled Structures* 40.9 (2002), pp. 755–789.
- [149] N. Silvestre and D. Camotim. "Second-order generalised beam theory for arbitrary orthotropic materials". In: *Thin-Walled Structures* 40.9 (2002), pp. 791–820.
- [150] K. P. Soldatos and I. Elishakoff. "A transverse shear and normal deformable orthotropic beam theory". In: *Journal of Sound Vibration* 155 (1992), pp. 528–533.
- [151] V. Steinberg. "Hydrodynamics: Bend and survive". In: *Nature* 420.6915 (2002), p. 473.

- [152] C. Thill et al. "Morphing skins". In: *The Aeronautical Journal* 112.1129 (2008), pp. 117–139.
- [153] T. Timarci and K. P. Soldatos. "Comparative dynamic studies for symmetric cross-ply circular cylindrical shells on the basis of a unified shear deformable shell theory". In: *Journal of sound and vibration* 187.4 (1995), pp. 609–624.
- [154] S. P. Timoshenko. "On the corrections for shear of the differential equation for transverse vibrations of prismatic bars". In: *Philosophical Magazine* 41 (1921), pp. 744–746.
- [155] S. P. Timoshenko. "On the transverse vibrations of bars of uniform cross section". In: *Philosophical Magazine* 43 (1922), pp. 125–131.
- [156] S. P. Timoshenko and J. N. Goodier. *Theory of elasticity*. McGraw-Hill, New York, 1970.
- [157] M. Touratier. "A generalization of shear deformation theories for axisymmetric multilayered shells". In: *International Journal of Solids and Structures* 29.11 (1992), pp. 1379–1399.
- [158] S. W. Tsai. *Introduction to composite materials*. Routledge, 2018.
- [159] E. Tufekci and A. Arpaci. "Analytical solutions of in-plane static problems for non-uniform curved beams including axial and shear deformations". In: *Structural Engineering and Mechanics* 22.2 (2006), pp. 131–150.
- [160] M. Vangbo. "An analytical analysis of a compressed bistable buckled beam". In: *Sensors and Actuators A: Physical* 69.3 (1998), pp. 212–216.
- [161] A. Varello and E. Carrera. "Nonhomogeneous atherosclerotic plaque analysis via enhanced 1D structural models". In: *Smart Structures and Systems* 13.4 (2014), pp. 659–683.
- [162] P. Vidal, L. Gallimard, and O. Polit. "Composite beam finite element based on the proper generalized decomposition". In: *Computers & Structures* 102 (2012), pp. 76–86.
- [163] P. Vidal and O. Polit. "A thermomechanical finite element for the analysis of rectangular laminated beams". In: *Finite Elements in Analysis and Design* 42.10 (2006), pp. 868–883.
- [164] P. Vidal and O. Polit. "Vibration of multilayered beams using sinus finite elements with transverse normal stress". In: *Composite Structures* 92 (2010), pp. 1524–1534.
- [165] V. V. Volovoi et al. "Asymptotic theory for static behavior of elastic anisotropic I-beams". In: *International Journal of Solids and Structures* 36.7 (1999), pp. 1017–1043.

- [166] Y. Wang and X. Wang. “Static analysis of higher order sandwich beams by weak form quadrature element method”. In: *Composite Structures* 116 (2014), pp. 841–848.
- [167] K. Washizu. “Some considerations on a naturally curved and twisted slender beam”. In: *Studies in Applied Mathematics* 43.1-4 (1964), pp. 111–116.
- [168] C. Xu et al. “Bi-stable energy harvesting based on a simply supported piezoelectric buckled beam”. In: *Journal of Applied Physics* 114.11 (2013), p. 114507.
- [169] R. D. Yamaletdinov et al. “Snap-through transition of buckled graphene membranes for memcapacitor applications”. In: *Scientific reports* 8.1 (2018), p. 3566.
- [170] Y. Yan et al. “Exact solutions for the macro-, meso-and micro-scale analysis of composite laminates and sandwich structures”. In: *Journal of Composite Materials* (2018), p. 0021998318761785.
- [171] E. Zappino and E. Carrera. “Thermo-piezo-elastic analysis of amplified piezoceramic actuators using a refined one-dimensional model”. In: *Journal of Intelligent Material Systems and Structures* 29.17 (2018), pp. 3482–3494.
- [172] E. Zappino, G. Li, and E. Carrera. “Node-dependent kinematic elements for the dynamic analysis of beams with piezo-patches”. In: *Journal of Intelligent Material Systems and Structures* 29.16 (2018), pp. 3333–3345.
- [173] G. Zhang, R. Alberdi, and K. Khandelwal. “Analysis of three-dimensional curved beams using isogeometric approach”. In: *Engineering Structures* 117 (2016), pp. 560–574.

This Ph.D. thesis has been typeset by means of the \TeX -system facilities. The typesetting engine was \LaTeX . The document class was `toptesi`, by Claudio Beccari, with option `tipotesi=scudo`. This class is available in every up-to-date and complete \TeX -system installation.